Normal Fault Growth:

Mechanical Controls, Basin Architecture

and Relay Zone Kinematics

A thesis submitted to Imperial College London for

the degree of Doctor of Philosophy in the

Faculty of Engineering

2022

David Redpath BSc MSc

Department of Earth Science and Engineering

Contents

Contents 3

Figures List 8

Abstract 11

Declaration 13

Attribution Licence 13

Acknowledgements 14

The Author 16

1. Chapter 1 - Introduction 17

Preamble 18

1.1 Rationale 19

1.2 Thesis Aims and Objectives 20

1.2.1 Investigating Host Rock Properties' Control on Fault Dimensions 20

1.2.2. Constraining Fault Growth and Segment Linkage in Sediment-Starved Basins 22

1.2.3 Determining the Behaviour of Relay-Breaching Faults 23

1.3 Thesis Overview 25

2. Chapter 2 - Research Context 28

Preamble 29

2.1 Characteristics and Growth of Normal Faults 30

2.1.1 Normal Fault Growth Models 32

2.1.2 Controls on Fault Geometry and Throw 37

2.1.2.1. Mechanical Stratigraphy 38

2.1.2.2. Fault Interactions 38

2.1.3. Fault Growth by Segment Linkage: Relay Zones 39

2.1.3.1. Relay Zone Formation 39

2.1.3.2 Relay Zone and Ramp Geometry 42

2.2 Normal Faulting and Basin Evolution 44

2.2.1 Structural Evolution of Extensional Basins 44

2.2.2 Tectono-stratigraphic Evolution of Rifts 48

2.2.3 Relay Zone Kinematics and Their Control on Basin Architecture and Stratigraphy... 48
2.3 Outstanding controversies related to normal fault growth... 49
2.3.1 Scatter in D-L Data: Mechanical Stratigraphy... 49
2.3.2 Constraining Fault Growth in Underfilled Basins... 50
2.3.3 Relay Zone Kinematics... 51
3. Chapter 3 – Dataset and Methodology... 54
Preamble... 55
3.1 Seismic Reflection Data... 56
3.1.1 Datasets... 56
3.1.2 Seismic Interpretation... 58
3.2 Quantitative Fault Analysis... 59
3.2.1 Throw/Displacement-Length and -Depth Plots... 59
3.2.2 Throw/Displacement Backstripping... 61
3.2.3 3-D Strike Projections... 63
3.2.4 Expansion Indices... 63
3.2.5 Isochrone/Isopach Analysis... 65
3.3 Geomorphological Techniques... 66
3.3.1 Determining Fault Scarp Erosion... 66
3.3.2 Volumetrics and Volume Balancing... 67
4. Chapter 4 - Mechanical Stratigraphy Controls Normal Fault Growth and Dimensions, Outer Kwanza Basin, Offshore Angola... 70
Preamble... 71
Abstract... 72
4.1 Introduction... 73
4.2 Data and Methods... 77
4.2.1 Data... 77
4.2.2 Seismic interpretation and fault characterisation... 79
4.3 Geological Setting... 82
4.3.1 Outer Kwanza Basin... 82
4.4 Results... 83
4.4.1 Planar faults (F1-F5)... 85
4.4.1.1 Observations... 85

4.4.1.2 Interpretation 87
4.4.2 Bifurcating faults (F6-F7) 88
4.4.2.1 Observations 88
4.4.2.2 Interpretation 90
4.4.3 Arcuate faults (A1-A9) 91
4.4.3.1 Observations 91
4.4.3.2 Interpretations 93
4.5 Discussion and Implications 94
4.5.1 Origin and kinematics of planar normal faults; the case for tip restriction by host rock properties 94
4.5.2 Kinematics of bifurcating faults; overcoming tip restriction and continued fault growth 97
4.5.3 Normal fault growth and D-L scaling relationships 98
4.6 Conclusions 99
Acknowledgements 100
5. Chapter 5 - Geomorphological Analysis of Fault-Scarp Degradation Complexes Constrain Style of Normal Fault Growth, Offshore NW Australia 102
Preamble 103
Abstract 104
5.1 Introduction 105
5.2 Regional Geological Overview 108
5.2.1 Exmouth Plateau 108
5.2.1.1.Stratigraphic Framework 111
5.2.1.2 Structural Framework 112
5.3 Dataset and Methodology 113
5.3.1 Dataset 113
5.3.2 Methods 113
5.3.2.1 Variance Attribute Extraction 114
5.3.2.2 Fault throw and eroded volume calculations 114
5.3.2.3 Hangingwall Fan Analysis 117

5.4 Structure of the Thebe Fault Complex 117
5.5 Relay Zone Structure 119
5.6 Footwall Morphology 121
5.7 Hangingwall Structural Style 122
5.8 Hangingwall Stratigraphic Architecture 124
5.9 Across-Fault Balancing of Sediment Volumes 125
5.10 Relay Zones, Footwall Degradation and Fan Deposition: Relay 1 Case Study 128
5.11 Discussion 131
5.11.1 Control of Fault Throw on Footwall Erosion Patterns 131
5.11.2 Constraining Fault Growth Using Fault-Scarp Degradation Complexes 131
5.12 Conclusions 133
Acknowledgements 134
6. Chapter 6 -Throw Rate Variability on Segmented Normal Faults Over Geological Timescales, NW Australia 136
Preamble 137
Abstract 138
6.1 Introduction 139
6.2 Geological Setting of The Exmouth Plateau 141
6.3 Dataset and Methods 145
6.3.1 Dataset 145
6.3.2 Methods 148
6.3.2.1 Throw Calculation and Throw Backstripping 148
6.3.2.2 Throw Rate Calculations 148
6.4 Glencoe Relay Zone: Geometry, Backstripped Throw and Throw Rates 149
6.4.1 Glencoe Relay Zone Geometry 149
6.4.2 Glencoe Backstripped Throw and Throw Rate Analysis 152
6.4.3 Interpretation 156
6.5 Thebe Relay Zone: Geometry, Backstripped Throw and Throw Rates 158
6.5.1 Thebe Relay Zone Geometry 158
6.5.2 Thebe Backstripped Throw and Throw Rate and Analysis 158

6.5.3 Interpretation 162
6.6 Discussion 163
6.6.1 The Role of Breaching Faults and Throw Rate 163
6.6.2 Implications for Fault Growth by Segment Linkage 166
6.6.3 Implications for Potential Seismic Hazards 167
6.7 Conclusions 167
Acknowledgements 168
7. Chapter 7 - Conclusions and Discussion 171
Preamble 172
Overview 173
7.1 Research Aim 1: Investigating Host Rock Properties' Control on Fault Dimensions 173
7.1.1 Mechanical Stratigraphy Controls Fault Geometry and Growth 174
7.1.2 Implications from Thesis Findings On Mechanical Interactions of faults 176
7.2. Research Aim 2: Constraining Fault Growth and Segment Linkage in Sediment-Starved Basins 178
7.2.1 A Discussion of Fault Growth, Footwall Erosion and Volume Balancing 179
7.2.2 Fault Growth Models in Sediment – Starved Settings 180
7.2.3 Implications of my findings on Constraining Fault Growth in Sediment Starved Basins 181
7.3 Research Aim 3: Determining the Behaviour of Relay-Breaching Faults 182
7.3.1 High Throw Rates Exist on Breaching Faults 183
7.4 Potential Societal Impact of Research 185
7.4.1 Potential Geohazard from Increased Throw Rates During Segment Linkage 185
7.4.2 Potential Economic Significance of Research 185
7.5 Future Research Directions 186
7.5.1 Quantifying the influence of mechanical stratigraphy and scatter in D – L datasets 186
7.5.2 Relay Zone Kinematics and Displacement Rates on Breaching Faults 187
7.5.3 The Stratigraphic Response to High Displacement Rates at Sediment Basin Entry Points: Insights from Modelling Breaching Rates 188
7.6 Implications and Concluding Remarks 189
8. References 190

Figures List

Figure 2.1. Stress states for different fault types 30

Figure 2.2. Normal fault geometry and terminology 31

Figure 2.3. A typical throw distribution for normal faulting 32

Figure 2.4. Log-log plot of throw (D) vs. length (L) 33

Figure 2.5. Normal fault growth models 34

Figure 2.6. Stratigraphic predictions for existing fault growth models 36

Figure 2.7. Stages of relay zone maturity 40

Figure 2.8. Breached relay zone geometries 43

Figure 2.9. Seismic examples of breached relay zone geometries 44

Figure 2.10. Stages of rift development and fault network evolution 45

Figure 2.11. Tectono-stratigraphic evolution of extensional settings 47

Figure 3.1. Chapter 4 study location - Kwanza Basin, Offshore Angola 56

Figure 3.2. Chapter 5 and 6 study location - Northern Carnarvon Basin, NW Shelf, Offshore NW Australia 57

Figure 3.3. 3-D Strike Projections 62

Figure 3.4. Parameters for measuring fault scarp degradation 66

Figure 4.1. Study area and location 75

Figure 4.2. Global throw vs. length dataset 76

Figure 4.3. Seismic overview of the key components of the study area 77

Figure 4.4. Depth structure maps 78

Figure 4.5. Seismic cross-section of planar and bifurcating fault groups 79

Figure 4.6. Fault aspect ratio terminology 80

Figure 4.7. Channels eroding upper fault tips 81

Figure 4.8. 3-D strike projections of the planar fault group 84

Figure 4.9. Fault height vs. length plot 85

Figure 4.10. Throw-depth plots for the planar fault group 86
Figure 4.11. Mechanical interactions with a mass-transport complex deposit 86
Figure 4.12. Mechanical stratigraphy and preferential lengthening 88
Figure 4.13. 3-D strike projections for the bifurcating fault group 89
Figure 4.14. Strain accumulation overcoming vertically restricting layer 90
Figure 4.15. Salt bodies influence fault geometry and throw 92
Figure 4.16. Structural kinematic model for fault array development 93
Figure 5.1. Study area location and regional overview 107
Figure 5.2. Stratigraphic column for the Exmouth Plateau, Northern Carnarvon Basin 109
Figure 5.3. Fault scarp degradation thickness 110
Figure 5.4. Thebe Fault Complex: 3-D structure map 112
Figure 5.5. Fault scarp degradation metrics 114
Figure 5.6. Throw-length and degradation factor (DF) - length plots for the Thebe Fault Complex 118
Figure 5.7. Throw-degradation factor (t-DF) plots 120
Figure 5.8. Along strike variability of a footwall-scarp degradation complex 123
Figure 5.9. Across-fault volume balancing of sediment volumes 126
Figure 5.10. The absence of sediment bypass transport systems on the footwall of the Thebe Fault Complex 127
Figure 5.11. Evolution of a fault-scarp degradation complex and accompanying footwall-derived fans 130
Figure 6.1. Fault growth by segment linkage and predictions of elevate throw rates at locations of throw minima over geological timescales 140
Figure 6.2. Study area location and regional overview 142
Figure 6.3. Stratigraphic column for the Exmouth Plateau 143
Figure 6.4. TWT structure and thickness maps 145

Figure 6.5. Map view geometry of studied relay zones 146

Figure 6.6. Glencoe relay zone 150

Figure 6.7. Glencoe relay zone backstripped throw plots 151

Figure 6.8. Glencoe relay zone throw rate variability 153

Figure 6.9. Maximum throw rate locations 154

Figure 6.10. Maximum throw rates on the Glencoe and Thebe relay zone fault segments 155

Figure 6.11. Thebe relay zone 157

Figure 6.12. Thebe relay zone backstripped throw plots 159

Figure 6.13. Thebe relay zone throw rate variability 161

Figure 7.1. Mechanical controls on fault growth and dimensions 176

Abstract

The growth and evolution of normal faults is key to our understanding of rift evolution, the presence and distribution of earth resources and our ability to mitigate earthquake hazards. As such, their growth, geometry, and activity have implications for how we understand earth systems and its resources. Observations from 3D seismic data in sedimentary basins where synkinematic growth strata are present have inspired the propagating, constant-length, and hybrid fault growth models. In developing these models, it is often assumed that the host rock is isotropic and the basin 'filled to spill'- simplifying assessments of fault throw. There has also commonly been an assumption that where two faults link, slip rates are enhanced time but this process is poorly understood and constrained. In this thesis I tackle these outstanding questions by conducting seismic investigations across the Kwanza Basin, offshore Angola and the Exmouth Plateau, NW Shelf, offshore Australia, to improve our understanding of normal fault growth, by addressing three key research topics to: (i) evaluate the conditions under which fault scaling relationships may breakdown, (ii) develop a novel technique to measure fault growth in sediment starved settings and, (iii) analyse the behaviour of throw minima on breaching faults over geological timescales to better understand fault segment linkage.

A high-quality 3D seismic reflection dataset on the Angolan segment of the West African passive margin was analysed. Evidence for mechanical stratigraphy controlling the dimensions of seismic-scale faults was identified, showing that an array of normal faults was vertically and laterally restricted by mechanical stratigraphy. In addition, their aspect ratios and throw distributions did not adhere to fault scaling relationships, despite their geometric data sitting within the parameters of a global D-L dataset. Thus, providing one of a few examples of mechanical stratigraphy's control on seismic-scale fault dimensions using 3D seismic data.

Extensive 3D seismic reflection datasets across the Exmouth Plateau were analysed to study degradation-fan complexes on basin-bounding normal faults. A new method for constraining fault growth in sediment-starved settings was proposed using volume-balancing of the degradation and

fan volumetrics. This technique used the spatio-temporal distribution of footwall-derived fans to determine the evolution of fault tip propagation and mode of fault growth. Thus, developing an additional tool to evaluate fault growth where substantial growth strata are not present.

In addition, 3D seismic reflection datasets were analysed to evaluate the throw rate variability on relay-breaching faults over geological timescales. The results suggest that maximum throw rates on relay-breaching faults exceed those of their adjacent segments but that they persist for a brief period of the faults life. Throw minima were not removed but reduced by throw rate variability on relay-breaching faults that had a strike oblique to their concomitant faults. This study is the first to reconcile observations on active, modern faults that show breaching rates that *could* remove throw minima in as little as < 1 Myr, and those made on ancient, tectonic faults that show the presence of throw minima over geological timescales by suggesting that high throw rates on relay-breaching faults do not persist over geological timescales.

The additional knowledge provided by this thesis: (i) helps to improve the application and understanding of fault scaling relationships by highlighting the need to use such data in context of their host rock properties; (ii) increases the ability to constrain fault growth in sediment starved settings and (iii) advances understanding of relay zone kinematics and informs our understanding of throw rate variability during segment linkage.

Declaration

The material contained in this thesis has not previously been submitted for a degree in this or any other institution. The work presented is that of the authors, except where reference is made.

David Redpath

Attribution Licence (CC BY 4.0)

The copyright of this thesis rests with the author. Unless otherwise indicated, its contents are licensed under a Creative Commons Attribution 4.0 International Licence (CC BY). Under this licence, you may copy and redistribute the material in any medium or format for both commercial and non-commercial purposes. You may also create and distribute modified versions of the work. This on the condition that you credit the author. When reusing or sharing this work, ensure you make the licence terms clear to others by naming the licence and linking to the licence text. Where a work has been adapted, you should indicate that the work has been changed and describe those changes. Please seek permission from the copyright holder for uses of this work that are not included in this licence or permitted under UK Copyright Law.

Acknowledgements

I would like to thank my supervisors Christopher Jackson and Rebecca Bell for their guidance, insights, support, and mentoring, throughout my PhD, and for their ability to bring additional clarity to the scientific questions that have been addresses in this thesis. Their tutoring and support have underpinned my personal development as a research scientist and critical thinker. I would also like to thank Editors and Reviewers of AGU Tectonics for their ideas, critiques and comments which led to the publication of select work in this project. These achievements have been some of the most satisfying parts of my educational pursuits.

I would like to thank the Natural Environment Research Council (NERC) Centre for Doctoral Training (CDT) in Oil & Gas for fully funding this project. Fond memories of my PhD are attached to the people of the 2017 cohort. Thank you, Procter, A. (Imperial College London), and Lloyd, C. (University of Manchester) for friendship that goes beyond the work we have done in our respective research topics and for the good times on awe-inspiring geological field trips.

Thank you to my colleagues in the Basin Research Group for welcoming me and helping me gain much needed skills, many of which constitute the methodologies used in this project. Especial thanks to Steventon, M. and Coleman, A. for their insights as I came to appreciate this project with its ups and downs, and to Pan, S. for discussing all things normal faulting.

Most notably I would like to thank my family. Thank you, Mum and Dad, for encouraging me to look upwards and onwards to life's rich possibilities and to completely reject narrowing views of oneself and others. This way of viewing life has helped me to not only get the best out of the relationships that have mattered most to me throughout the duration of my life but have also allowed me to see beyond the immediate challenges of any worthy endeavour and aspire to the possibilities that are to be seized on the other side of them. I would also like to note, in absolute sentimentality, how grateful I am for my whole family. Truly, all my educational, vocational, and personal hopes have been supported and magnified by the encouraging presence you have all offered throughout my life. I often ponder if I would have been able to become who I am today,

or become anything I could be in the future, without you. The answer is always, categorically: "No".

Thank you to my Wife, Paesha Tuttle Redpath, for absolutely everything I am and can be. I have never felt so inspired and motivated to excel in life as I have been since I met you. Thank you for being courageous in your love for me and frequently flying across the world to fill my life with joy. Times that have led us to the most fulfilling and exceptional marriage. Each day is miraculous. Never has life been so complete and full as it is now. I am eternally grateful for you and for our beautiful marriage. You exceed all my hopes. Thank you for making me the luckiest man and for marrying me when I had nothing to offer but my absolute adoration and love for you and, of course, my highly acclaimed status of a poor PhD candidate! Marriage and life next to you and our new family has already achieved everything that I ever aspired to be.

Finally, I would like to particularly note my thanks and gratitude to God. The critical study of science is equal to the pursuit of truth. Where mystery is present, truth can be pursued. Where truth is revealed, the Divine signature of a Loving and Masterful Creator can be found. So, it has been with me. My course of studies in the Earth Sciences have led me to see patterns, principles and laws that universally result in the wonderful architecture of the natural world.

"All things denote there is a God; yea, even the earth, and all things that are upon the face of it, yea, and its motion, yea, and also all the planets which move in their regular form do witness that there is a Supreme Creator."

(Alma 30:44)

The Author

I hold a first-class BSc (Hons) in Geology from Durham University, as well as an MSc with Distinction in Petroleum Geoscience from the University of Manchester. During my MSc, I completed an internship with Equinor in Oslo, working in the Exploration Asset Team for Tanzania in the Indian Ocean region. In late 2017, I started this PhD studying normal fault growth and investigated controls on their dimensions, normal faulting's implications for basin architecture and the nuances of throw rate variability relating to relay zone kinematics. The project is funded by the Natural Environment Research Council (NERC) Centre for Doctoral Training (CDT) in Oil and Gas. The funding program provided up to 100 days of industry training during my 4.5-year PhD. Having completed a wide range of geoscience and professional development training, this training was suspended due to the COVID-19 crisis, and the length of my PhD extended. In the summer of 2021, I was married to my perfect Wife just weeks after completing an internship with BP. During this internship I worked remotely out of the Sunbury office as a Structural Geology Specialist for the Azeri-Chirag-Gunesli field, Azerbaijan.

The results from this thesis have, thus far, resulted in one first author publication in an international journal (AGU Tectonics), and the other two chapters will soon be prepared for a further publication submissions.

1

Introduction

Preamble

The principal aim of this thesis is to improve our understanding of fault growth and in particular the controls on fault dimension, how we measure fault growth in sediment-starved settings and the behaviour of relay-breaching faults. This chapter will outline the rationale behind this study and detail the research motivations and key aims and objectives of this thesis.

1.1 Rationale

Why Study Normal Fault Growth and Geometry?

Extensional basins are principal locations where subsidence and accommodation creation are sufficient to preserve sediments over geological timescales, and are key settings in which to advance our understanding of the geological mechanisms and history of the earth (e.g. Gupta and Cowie, 2000, Gawthorpe and Leeder, 2000). In these basins, extensional deformation in the lithosphere is chiefly facilitated by normal faults which grow by segment linkage of smaller, precursor segments (e.g. Peacock and Sanderson, 1991, Trudgill and Cartwright, 1994, Cartwright et al., 1995, Cartwright et al., 1996, Crider and Pollard, 1998, Mansfield and Cartwright, 2001, Walsh et al., 2002, Soliva and Benedicto, 2004, Finch and Gawthorpe, 2017, Rotevatn et al., 2019). Main structural styles observed in these basins consequent of normal faulting include: half-grabens (e.g. Northern North Sea) (e.g. Badley et al., 1989, Ziegler, 1992), horst-graben structures (e.g. Basin and Range Province, N America) (e.g. Eaton, 1982); tilted fault blocks (e.g. North Carnarvon Basin) (e.g. Bilal and McClay, 2022); and transfer zones found in many extensional provinces (e.g. Gawthorpe and Hurst, 1993). The temporal and spatial evolution of extensional basins are principally controlled by how normal faults grow and their geometry (e.g., Whipp et al., 2017, Naliboff et al., 2017). In addition, previous studies have also established normal fault growth and geometry as sensitive controls for sediment supply and transport, depositional architecture, and the evolution of extensional basins (McClay, 1990, Gawthorpe and Hurst, 1993, Eliet and Gawthorpe, 1995, Gawthorpe and Leeder, 2000, Jackson et al., 2002, Childs et al., 2003). Despite their importance, questions remain regarding the applicability of normal fault growth models in a variety of geological settings, fault segment linkage and controls on normal fault geometry and growth (e.g., Cowie and Scholz, 1992a). Addressing these questions on the growth and geometry of normal faults is important to i) understand scatter in fundamental fault scaling relationships (Cowie and Scholz, 1992a, Cartwright et al., 1995); ii) improve tectono-stratigraphic predictions based on conceptual, analogue and numerical models that fault growth models (Fossen and

Rotevatn, 2016, Jackson et al., 2017, Rotevatn et al., 2019, Gawthorpe and Leeder, 2000); iii) to evaluate the seismic hazard risk in regions of active faulting, since how faults grow can influence slip event magnitude and periodicity (e.g., Ferrill et al., 1999, Tavarnelli and Pasqui, 2000) and; iv) to assess the viability of sealing faults for trapping mechanism in carbon capture and storage, nuclear waste management and hydrocarbon accumulations (Weber, 1987, Knipe et al., 1998, Dockrill and Shipton, 2010, Manzocchi et al., 2010, Quattrocchi et al., 2013, Miocic et al., 2016).

1.2 Thesis Aims and Objectives

This thesis has three aims directed towards an improved understanding of fault growth and geometry, particularly with regards to fault scaling laws, constraining fault growth patterns, and fault behaviour at fault linkage sites: (i) to investigate the control of host rock properties on fault dimensions, with a focus on mechanical stratigraphy; (ii) to constrain fault growth patterns in sediment starved settings where complete synkinematic sequences are absent to evaluate fault growth and activity; and (iii) determine the behaviour of breaching faults which facilitate fault growth by segment linkage, including their throw rates over geological timescales, and characterise potential implications for fault slip at relay zones.

These aims are motivated by the endeavour to investigate key controls and processes during fault growth and to understand the temporal and spatial development of normal faults. They are also motivated by a desire to evaluate the methodologies which we use to do so in challenging environments. Chapter 2 explores the nuances and remaining controversies regarding these research topics but here we only outline how they will be addressed (See 2.3).

1.2.1 Investigating Host Rock Properties' Control on Fault Dimensions

Aims:

Fault growth models were originally derived from global compilations of throw – length data and the recognition that these two fault measurements where positively correlated over several orders

of magnitude (e.g., Walsh and Watterson, 1988, Cartwright et al., 1995, Walsh et al., 2003, Rotevatn et al., 2019, Nicol et al., 2020b). However, mechanical controls on normal fault growth and geometry can result in deviations from these fault scaling relationships (e.g., Gross et al., 1997, Polit et al., 2009). Thus, I attempt to understand the influence of mechanical stratigraphy on the breakdown of fault scaling relationships and if it can control fault dimensions on seismic-scale, tectonic faults. In addition, I attempt to highlight the potential need to reconsider fault growth models proposed using D-L data that do not indicate the geological setting or mechanical heterogeneity of their faulted sequences. To achieve this aim, the following research topics will be adressed:

- Does mechanical stratigraphy control fault dimensions on seismic-scale faults?
- Quantifying fault dimensions within mechanical stratigraphy.
- Do fault dimensions follow established throw-length scaling relationships for normal faults?
- Testing the hypothesis that global throw-length datasets may hide significant deviations from $D = cL^n$, where c is a constant and n is between 1 and 1.5 that arise from local stress and mechanical conditions.

Objectives:

Undertake seismic interpretation and quantitative analysis of both fault throw and fault geometry of faults located within stratigraphic sequences that are laterally extensive and where a basin-wide unit which has distinctly different mechanical properties to the rest of the stratigraphy is present.

- Describe fault geometry and throw distributions using 3D strike-projections, fault t-x and t-z plots.
- Determine geological controls on these geometric D-L data points for the faults.
- Evaluate the extent to which these data may deviate from global D-L scaling relationships.

- Synthesis observations and interpretation to propose the impact of mechanical stratigraphy on seismic-scale faults in sedimentary basins.

1.2.2. Constraining Fault Growth and Segment Linkage in Sediment-Starved Basins

Aims:

Fault growth models have overwhelmingly been tested in overfilled basins, where syn-kinematic strata are able to be used to constrain fault tip propagation and fault growth (e.g., Jackson et al., 2017, Childs et al., 2017a, Rotevatn et al., 2019, Nicol et al., 2020b). However, clearly, not all faults grow in settings where complete growth strata record fault activity and where techniques such as expansion indices and isochrone analysis can constrain fault growth precisely (e.g., Jackson et al., 2017). To achieve this aim focuses on attempting to use geomorphological techniques to evaluate footwall-derived fans (i.e., deposits typical to sediment-starved settings where footwall scarps are exposed) and analyse their spatio-temporal distribution to constrain fault growth. Thus, I aim to to develop a technique to better constrain fault growth models in sediment-starved basins and address the following topics:

- Can alternative fault analysis techniques be applied in sediment starved settings, where complete synkinematic strata are not present and fault activity cannot be determined solely by analysis of the growth sequence, to aid in constraining fault growth?
- Can we use relay zone observations to constrain the timing of fault tip interaction and therefore lateral propagation?
- Constrain fault growth by applying alternative geomorphological techniques in the subsurface and analysing footwall erosion and hangingwall talus fan distribution during rift activity.

Objectives:

Undertake seismic interpretation, fault throw analysis, and quantitative volumetrics of footwall erosion and hangingwall fans to develop geomorphological techniques capable of constrain fault growth models in sediment starved basins:

- Map stratigraphic horizons characterising fault scarp erosion on the footwall and create a projected pseudosurface for pre-erosion footwall morphology.
- Map horizons bounding degradation fans in the hangingwall to determine their presence, distribution, and volumetrics along the Thebe Fault Complex (TFC).
- Determine sediment redistribution and/or sediment input based on footwall erosion-hangingwall fan volumes.
- Integrate observations from fault throw, and footwall erosion/hangingwall fan volumetrics distributions and constrain fault growth and segment linkage in sediment-starved basins based on temporal and spatial distribution of fans.

1.2.3 Determining the Behaviour of Relay-Breaching Faults

Aims:

Large normal faults typically accumulate length and throw by the process of segment linkage at relay zones. This is facilitated by newly formed breaching faults 'hard-linking' smaller, adjacent precursor faults (e.g.,Dawers and Anders, 1995, Cartwright et al., 1995, Cartwright et al., 1996, Tavarnelli and Pasqui, 2000, Mansfield and Cartwright, 2001, Young et al., 2001, Rotevatn et al., 2019). This process results in, and can be defined by, throw minima at the site of paleo-linkage. (e.g., Peacock and Sanderson, 1991, Huggins et al., 1995, Walsh et al., 2003, Fossen and Rotevatn, 2016, Camanni et al., 2019, Pan et al., 2021) However, Faure Walker et al. (2009) showed that throw rates on active faults in the Apennines, Italy, were higher than their adjacent segments and thus would remove the throw minima across their relay zone in as little as <1 Myr. This is at odds

with observations of throw minima on ancient faults which typically display the persistence of minima over geological timescales. Thus, this work aims to:

- Characterise the throw patterns and behaviour over geological timescales on breaching faults using examples with variable relay zone dimensions and fault maturity.
- Determine the kinematic behaviour of each of the relay zones using throw rates on breaching faults.
- Test the hypothesis that breaching faults may have higher throw rates earlier in their fault life and describe the behaviour of throw minima observed on faults over geological timescales.

Objectives:

Undertake seismic interpretation of three relay zones of varying geometry and conduct quantitative analysis on each of their respective breaching faults which have facilitated segment linkage:

- Describe relay zone geometry and characterise differences between each of the case study relay zones.
- Use relay zone backstripping to characterise breaching fault throw rates over increasingly longer time periods.
- Evaluate the implications for throw minima over relatively short to longer geological timescales using the relay zone observations
- Synthesise interpretations to suggest models for breaching fault and throw minima behaviour over geological timescales.

1.3 Thesis Overview

Chapter 1: *Introduction*

This chapter provides the rationale to the research topic of this thesis including a detailed description of the hypotheses that this thesis addresses and the aims and objectives attached to each research topic.

Chapter 2: *Research Context and Outstanding Controversies*

This chapter provides a literature review of the existing paradigms and prevailing research topics in the study of normal fault growth in sedimentary basins. This chapter initially considers the importance of understanding fault growth in the context of sedimentary basins and their control on rift physiography. This is followed by an overview of fault growth models and a comparison of their implications for the tectono-stratigraphic development of extensional basins. In addition, this chapter highlights the research context and identifies the outstanding controversies in the literature which provide the rationale for the proceeding chapters.

Chapter 3: *Datasets and Methodology*

This provides an outline of the types of data applied in Chapters 4 – 6 and explains the primary methodologies used to achieve research-based conclusions. In Chapters 4 – 6 detailed summaries are provided for the specific data and methodologies used in each of the respective chapters.

Chapter 4: *Mechanical Stratigraphy Controls Normal Fault Growth and Dimensions*

Published in *Tectonics* (Redpath, D., Jackson, C. A.-L., & Bell, R. E. (2022). Mechanical stratigraphy controls normal fault growth and dimensions, Outer Kwanza Basin, offshore Angola. Tectonics, 41, e2021TC006823. https://doi.org/10.1029/2021TC006823), this chapter represents the documentation the control of mechanical stratigraphy on fault growth and dimensions. Specifically, the chapter documents the breakdown of fault scaling relationships because of mechanical stratigraphy in a normal fault array. The findings from this chapter relate to research aim 1 found in 1.2.1.

Chapter 5: *Geomorphological Analysis of Fault-Scarp Degradation Complexes Constrain Style of Normal Fault Growth, offshore NW Australia*

Many sedimentary basins are underfilled and to understand fault growth in these settings we need to use different techniques to those commonly applied in over-filled settings. The chapter combines seismic interpretation and quantitative fault analysis, with geomorphological techniques and volume balancing, to constrain fault growth of large, basin-bounding faults in the Northern Carnarvon Basin on the NW Shelf, Offshore Australia. This chapter is presented in the form of a manuscript prepared for publication submission to Basin Research The results presented here are related to research aim 2 found in 1.2.2.

Chapter 6: *Throw Rate Variability on Segmented Normal Faults over Geological Timescales, NW Shelf, Australia*

This chapter investigates the observations made on active breaching faults that show that they have significantly higher throw rates than the flanking fault segments which they facilitate linkage between (Commins et al., 2005, Faure Walker et al., 2009, Faure Walker et al., 2015). It proposes predictions for the behaviour of throw minima and the implications for fault throw distributions if the observations noted above are correct. It combines detailed seismic interpretation of relay zones which vary in geometry and maturity, with throw backstripping and throw rate analysis to characterise the behaviour of breaching faults over geological timescales. The chapter uses data from the Northern Carnarvon Basin on the NW Shelf, Offshore Australia, and is presented in the form of a manuscript prepared for publication submission. The results in this chapter are related to research aim 3 found in 1.2.3.

Chapter 7: *Discussion and Conclusions.*

This chapter summarises the key findings of the PhD research and highlights its contributions with regards to the field of study. The thesis concludes with a discussion on future work and revealed gaps that our research has uncovered but which are not fully addressed herein.

2

Research Context

Preamble

This chapter introduces fundamental aspects of normal fault growth and the importance of understanding their kinematics, particularly in rift basins. A review of the development of current paradigms and prevailing thoughts on fault growth models and an introduction to each of the fault growth models' respective impacts on the tectono-stratigraphic evolution of extensional basins is given. Finally, we critique the present literature and examine the outstanding controversies that form the rationale for the primary research chapters in this thesis.

2.1 Characteristics and Growth of Normal Faults

All faults share the characteristic function of shortening the crust in one direction and extending it in another; where this compression and extension in the crust occurs perpendicular to one another (Anderson, 1905). In the idealistic Andersonian theory for the dynamics of faulting, normal faulting occurs where the maximum stress is vertical and the minimum stresses in the horizontal plane ($\sigma1 > \sigma2 \geq \sigma3$) (Fig. 2.1) (Anderson, 1905).

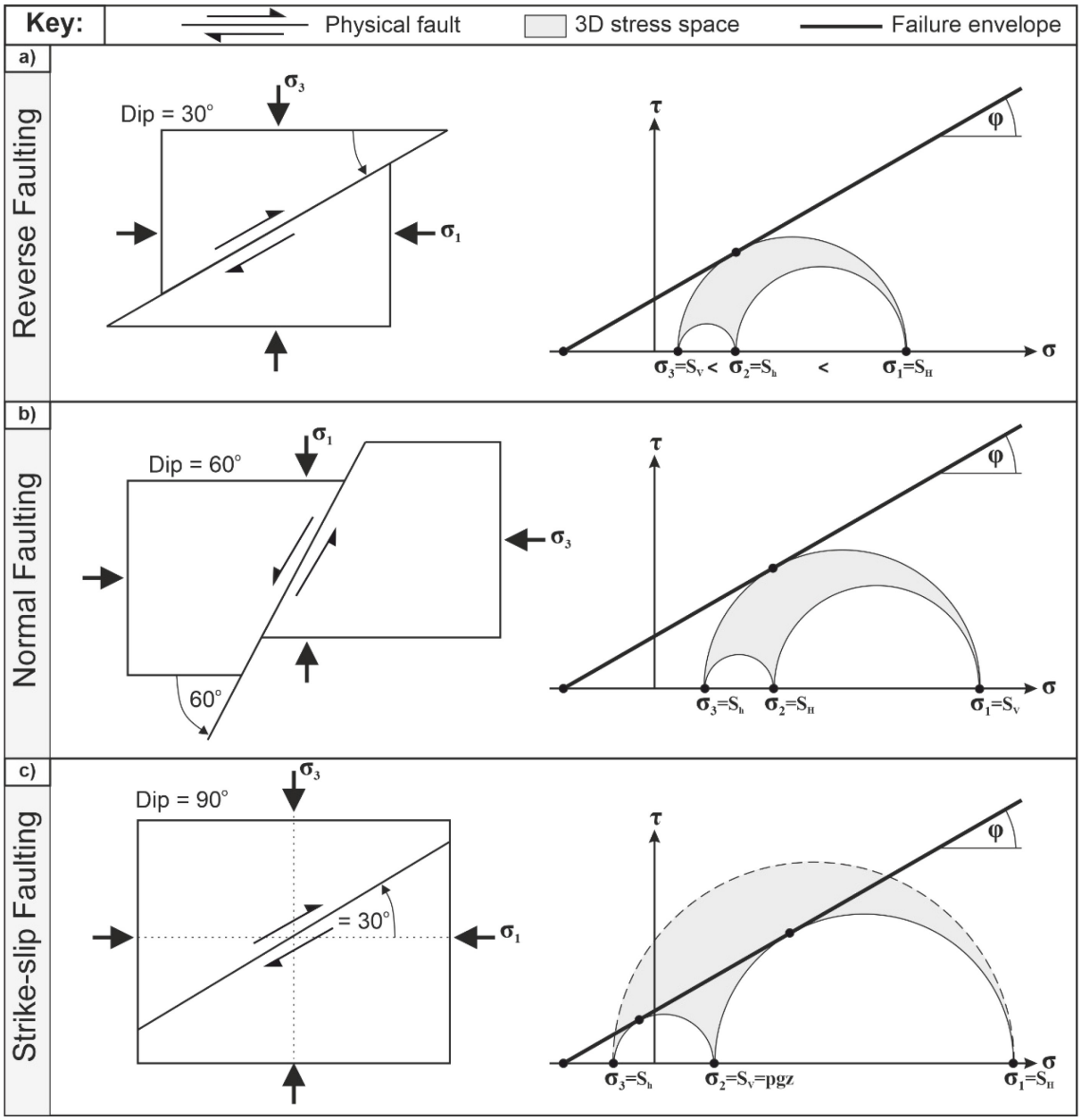


Figure 2.1. Stress states for different fault types | Schematic diagrams of stress states of reverse, normal and strike-slip faults. (a-c) (Left) Schematic diagrams of the orientation of the stress axes for different types of faulting. (Right) The Mohr-Coulomb curve and failure envelope describing the stress state of the associated fault types based on Anderson theory. Modified from Taherynia, Fatemi et al. (2016).

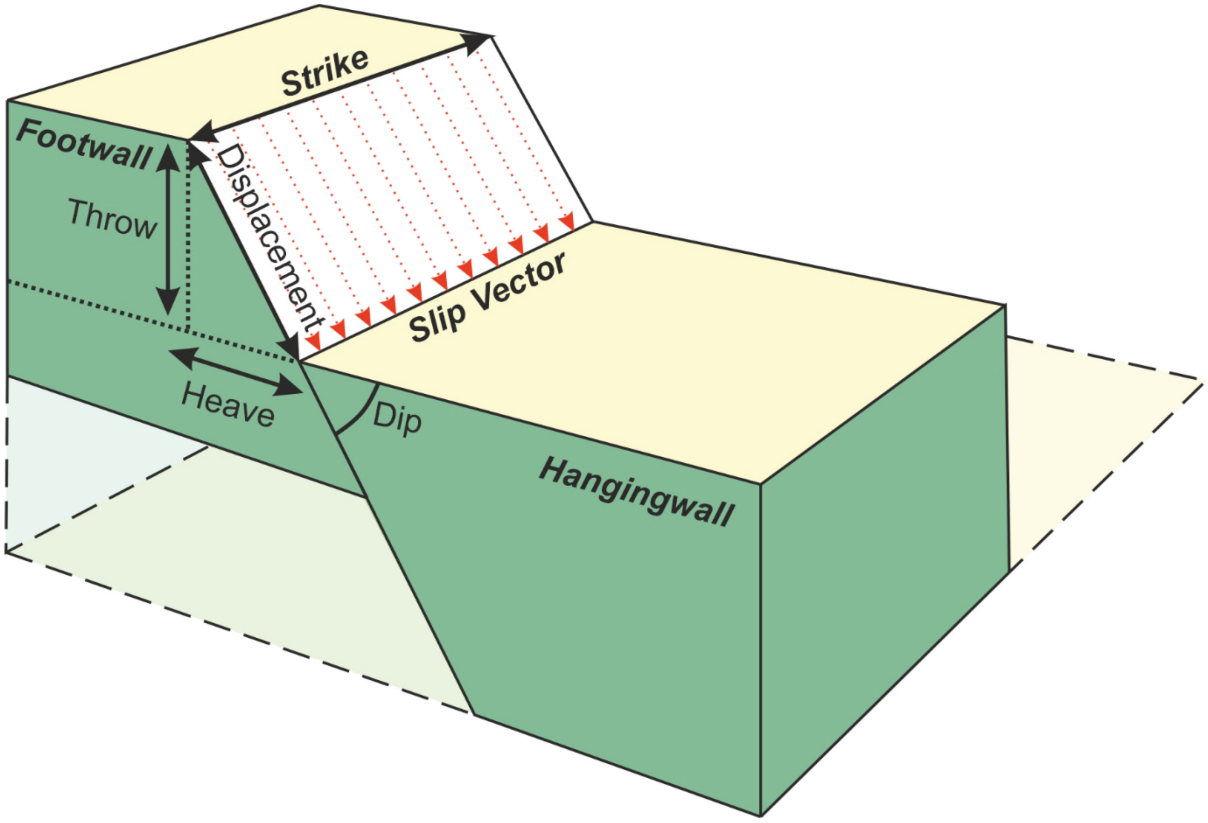


Figure 2.2. Normal fault geometry and terminology | A schematic diagram showing normal fault geometry and key characteristics by which normal faulting can be measure (i.e., throw, throw, heave, strike). Note the distinction that the footwall is downthrown relative to the hangingwall.

Thus, a normal fault plane will strike perpendicular to σ3, parallel to σ2, and dip *c.* 30 degrees from the maximum vertical stress (σ1) (Anderson, 1905) (Fig. 2.1). Anderson's theory (1905) was idealistic in at least the following ways: i) oblique slip is not accounted for and ii) it assumes isotropy in the host rock and that slip is orientated on optimal fault surfaces, which in a significant amount of cases is not so (Célérier, 2008) (Fig. 2.1).

Natural normal faults occur as planes of deformation across which the hangingwall is translated downwards relative to the footwall, resulting in extension of the crust (e.g., Jackson and McKenzie, 1983, Jackson, 1987a, Wilkins and Gross, 2002, Walsh et al., 2003, Childs et al., 2017b, Rotevatn et al., 2019). The direction and extent to which the hangingwall moves along the fault plane is called slip and is described by its horizontal (heave) and vertical (throw) components (Fig. 2.2). Where the slip vector is known the term throw can be used. While normal faults extend the crust, they are not restricted to extensional basins or passive margin settings and can be found

accommodating extension in a variety of basins (e.g., Boronkay and Doutsos, 1994, Joshi and Hayashi, 2010, Roure et al., 1992, Waldron, 2005).

2.1.1 Normal Fault Growth Models

Normal faults grow by increases in their fault slip and length (e.g., Cowie and Scholz, 1992a, Dawers and Anders, 1995, Wilkins and Gross, 2002, Childs et al., 2017a, Rotevatn et al., 2019). As a result an isolated normal fault plane will typically assume a quasi-elliptical geometry with maximum throw at the segment's centre, which will decrease radially towards the fault tips (Childs et al., 2017b).

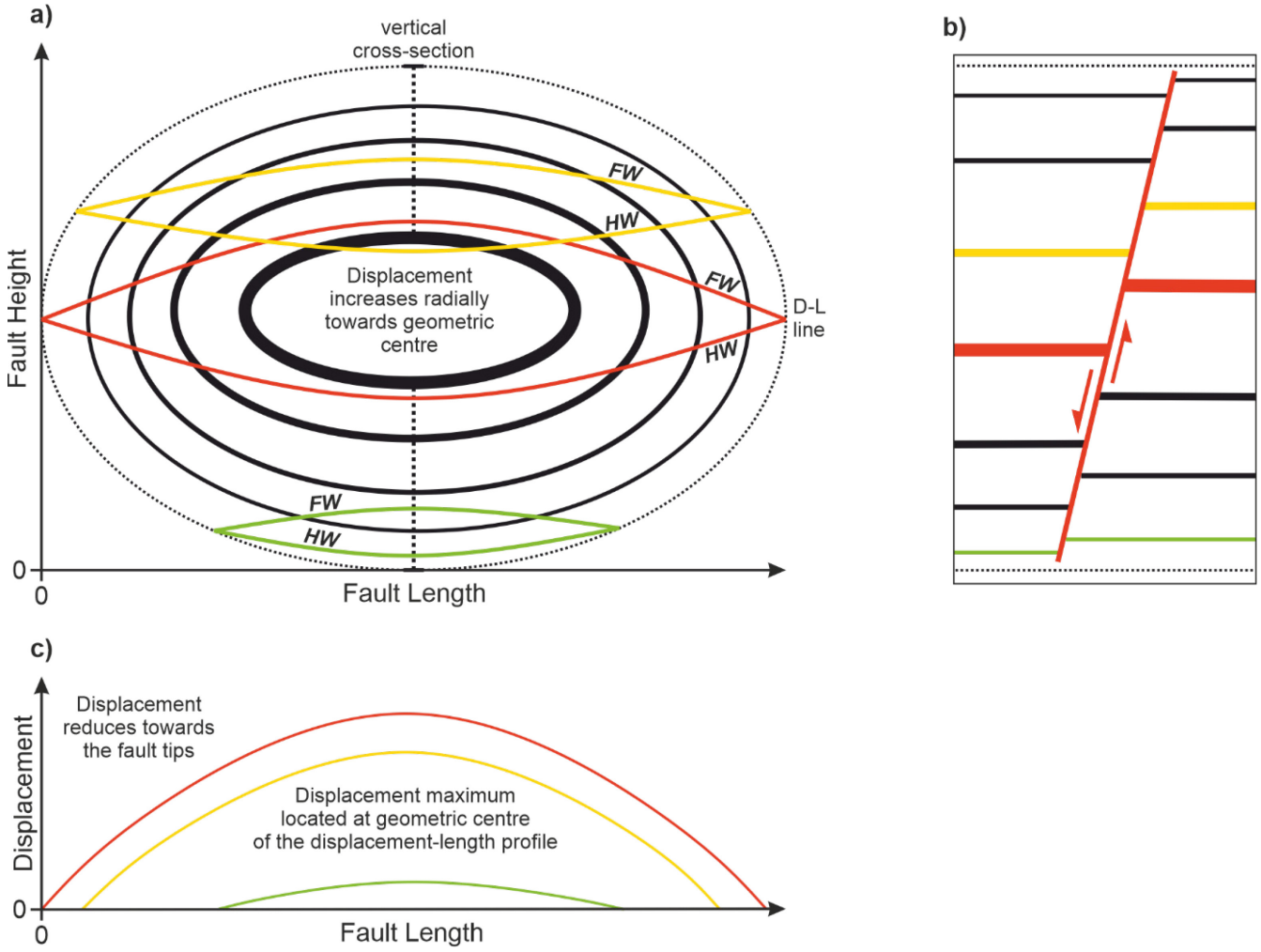


Figure 2.3. A typical throw distribution for normal faulting | (a) A schematic diagram showing the quasi-elliptical to circular geometry of normal fault planes. Also showing the intersection of the fault plane with the footwall and hangingwall of three offset surfaces. (b) A schematic cross-section of a normal fault showing a typical pattern of reducing throw towards tips. The coloured surfaces correspond to those in (a-c). (c) A schematic throw-length plot showing decreasing throw towards the fault tips and the throw maxima on each of the surfaces at the geometric centre of the fault.

This pattern can be characterised by throw-length plots which for isolated faults will assume a profile which increases from zero at fault tips to the maximum throw at the centre of the fault segment (Fig.2.3). Fault growth models which attempt to describe normal fault growth are fundamentally derived from global compilations of throw (D) and length (L) data (Fig. 2.4). More specifically, fault geometric data shows examples of faults throw and length across several orders of magnitude and have led to the establishment the relationship between a normal faults' maximum throw (D) and length (L) characterised by:

$D = cL^n$

here c is a constant and n is between 1 and 1.5 and defines the throw-length scaling relationship for faults (Fig. 2.4; e.g.Schlische et al., 1996).

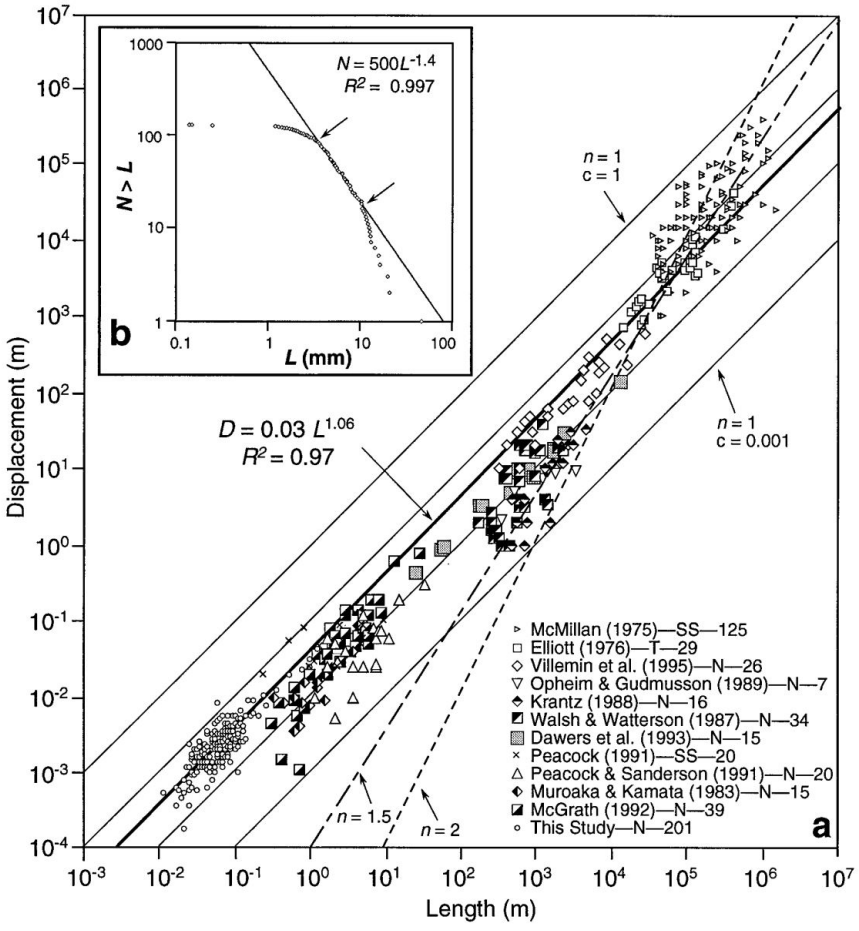


Figure 2.4. Log-log plot of throw (D) vs. length (L) |D-L plot for various published fault populations. Abbreviations: N, normal faults; T, thrust faults; SS, strike-slip faults. Note the positive correlation between throw and length that underpins fault scaling relationships. Taken from Schlische et al. (1996).

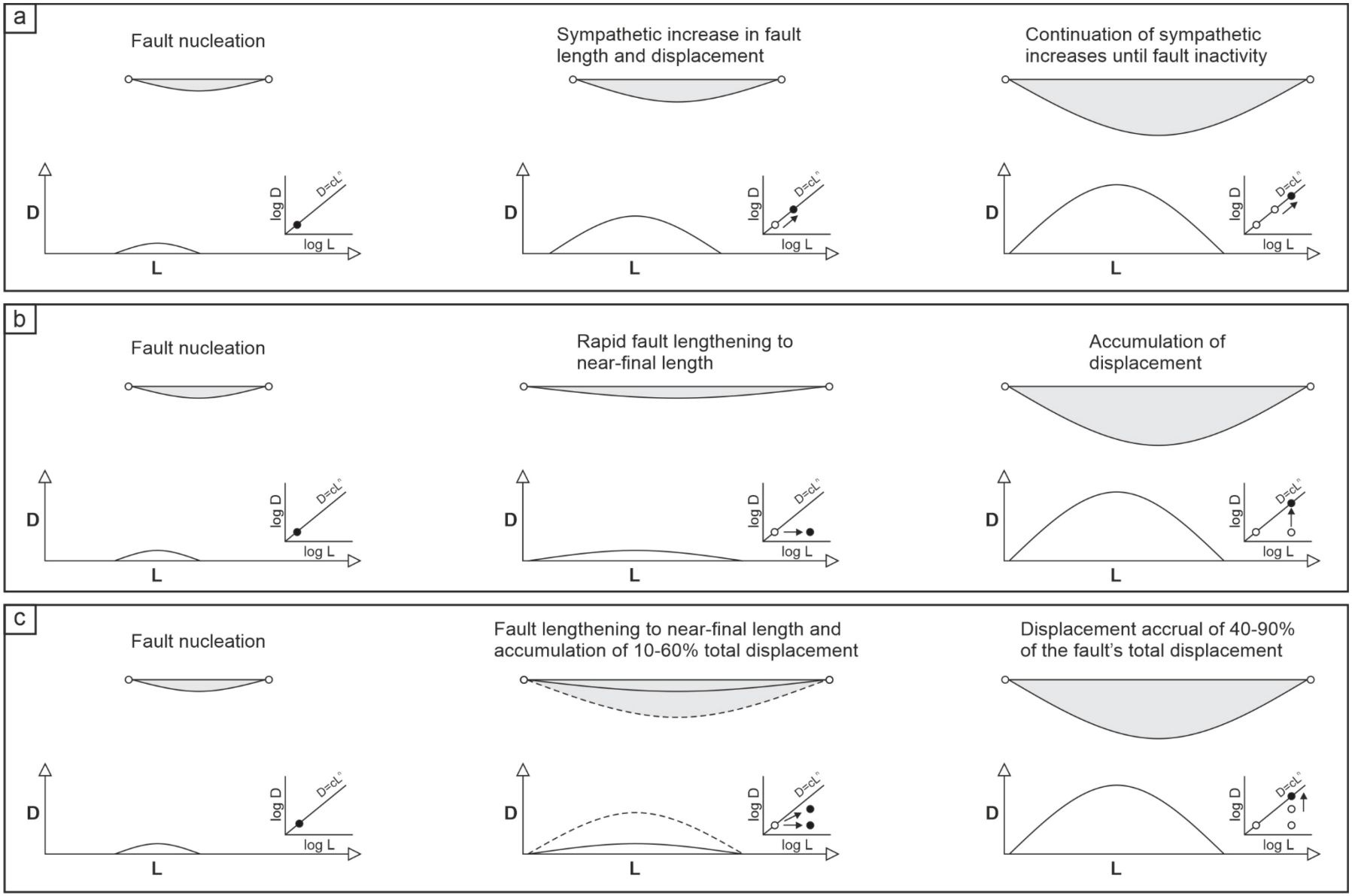


Figure 2.5. Normal fault growth models| A schematic diagram showing the key progressive stages of each fault growth model with their respective throw-length plots and log-log D-L predictions. (a) Propagating fault model (Watterson, 1986, Walsh and Watterson, 1987, Walsh and Watterson, 1988); (b) Constant-length model (Walsh et al., 2002); and (c) Hybrid model (Rotevatn et al., 2019).

Three distinct models exist for ultimately achieving this pattern for the final geometry and throw of faults, namely: i) the propagating fault model; ii) the constant length model and most recently; iii) the hybrid fault growth model (Fig. 2.5) (Watterson, 1986, Walsh and Watterson, 1988, Walsh et al., 2002, Rotevatn et al., 2019).

Initially, the observations from D-L data led to the development of the 'propagating' fault model normal faults grow by a sympathetic increase in their throw and length (Fig. 2.4 and 2.5a) (e.g., Jackson and McKenzie, 1983, Walsh and Watterson, 1987, Walsh and Watterson, 1988, Cowie and Scholz, 1992a, Dawers and Anders, 1995). With the advent of 3D seismic reflection data this hypothesis was able to be tested on ancient fault systems in the subsurface. Observations made primarily using 3D seismic reflection data supported an alternative model for normal fault growth called the 'constant length' model in which faults rapidly establish their near-final early on in the fault life before accumulating significant throw (Fig. 2.5b) (Walsh et al., 2002, Jackson et al., 2017, Rotevatn et al., 2019). These fault growth models have been tested primarily in the subsurface on normal faults located in sedimentary basins allowing for the observation of fault tip behaviour and throw accrual over geological timescales using techniques such as: expansion indices, isochrone analysis, throw distribution plots and throw backstripping (e.g., Jackson et al., 2017). Most recently, the advancement of the quality of 3D seismic reflection data has allowed for astute observation of normal fault growth and allowed the proposal of a third fault growth model, the so-called 'hybrid' fault growth model (Fig. 2.5c) (Rotevatn et al., 2019). This model is characterised by rapid fault lengthening by tip propagation and segment linkage to its near-final length during the first 20 – 30 % of the fault life (Stage 1). During this stage significant throw (10 – 60% of total end-of-life fault throw) can also accumulate, and may be achieved by characteristics most congruent with the propagating fault model (i.e., tip propagation, relay breaching and segment linkage) (Rotevatn et al., 2019).

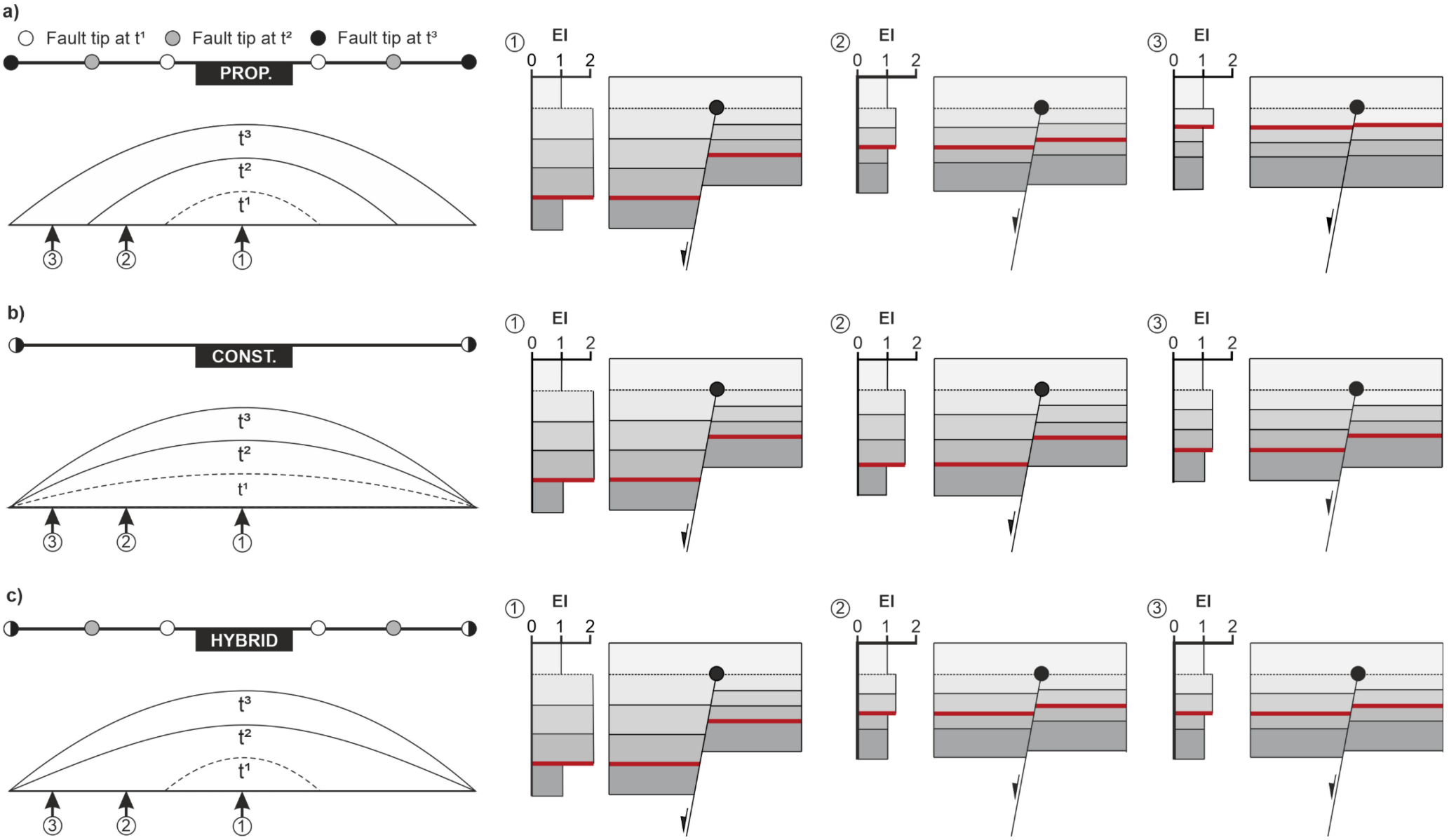


Figure 2.6. Stratigraphic predictions for existing fault growth models| (Left) (a-c) Schematic diagrams showing the lateral tip propagation and throw accumulation at progressive time periods according to the (a) propagating fault model; (b) constant-length model and; (c) hybrid fault growth model. (Right) (a-c) Schematic diagrams showing stratigraphic predictions of across fault thickening at locations along strike (i.e., 1,2,3) for each fault growth model. The red line indicates the base syn-kinematic surface at each location along strike. Modified from Jackson et al. (2017)

This fault-lengthening stage is followed by a stage dominated by throw accrual (70 – 80 % of fault life), during which time the fault does not significantly lengthen, a characteristic of the constant-length model (Fig. 2.5c) (Rotevatn et al., 2019, Pan et al., 2021, Lathrop et al., 2021, Redpath et al., 2022). The advent of the hybrid fault growth model highlighted how each of the previously established fault growth models can be applicable when describing specific stages of fault growth. Each of these fault growth models have significant implications for understanding the temporal and spatial development of extensional settings since each model can make predictions regarding the structural and tectono-stratigraphic evolution of rift basins (Fig. 2.6).

2.1.2 Controls on Fault Geometry and Throw

In agreement with fault growth concepts, the faults growth models previously mentioned maintain a fault geometry characterised by a planar fault surface with quasi-elliptical tip-lines, and a throw distribution where maximum throw is located at the centre of the fault and decreases towards the fault tip-lines (Fig. 2.3 and 2.5). However, this is rarely the case and faults inevitably become non-planar as they experience interactions with the inherent heterogeneities in nature, which control both their throw and geometry (e.g., Bürgmann et al., 1994, Nicol et al., 1996, Martel, 1999, Soliva and Benedicto, 2005, Soliva et al., 2008, Polit et al., 2009, Duffy et al., 2015, Finch and Gawthorpe, 2017). For example, a propagating isolated fault may change its orientation, throw, length and dip due to interactions with any one of the following: mechanical stratigraphy (Martel, 1999, Wilkins and Gross, 2002, Soliva et al., 2005a, Polit et al., 2009, Laubach et al., 2009, Ferrill et al., 2017, Redpath et al., 2022), other faults (e.g., Bürgmann et al., 1994, Nicol et al., 1996, Crider and Pollard, 1998, Soliva et al., 2008, Duffy et al., 2015, Finch and Gawthorpe, 2017, Nicol et al., 2017), and non-uniform near- and far- stress fields (e.g., Tvedt et al., 2013a).

2.1.2.1. Mechanical Stratigraphy

Mechanical stratigraphy encompasses: i) the varying material properties of host-rock (e.g., Young's Modulus, compressive and tensile strengths) ii) the thickness of mechanical layers, and iii) the character and frictional properties of the transition boundaries between heterogenous mechanical layers (e.g. sharp vs. gradational boundaries, and smooth vs. rugose contacts; cf., Ferrill and Morris, 2008, Ferrill et al., 2017, Laubach et al., 2009) (See 3.2.1). Mechanical stratigraphy can control the presence, geometry, and throw distribution of faults, and can do so on a variety of scales (i.e., centimetres to kilometres) (e.g., Martel, 1999, Wilkins and Gross, 2002, Ravaglia et al., 2004, Soliva et al., 2005b, Soliva et al., 2005a, Soliva et al., 2006, Polit et al., 2009, Bastesen and Rotevatn, 2012). The influence that mechanical stratigraphy can impose on fault growth and dimensions has implications for fault growth and D-L scaling relationships. For example, these implications may be but are not exclusive to: i) vertically restricted faults, resulting in preferential lateral fault tip propagation or controlling dip-linkage causing faults to appear 'underdisplaced' (Soliva and Benedicto, 2005, Wilkins and Gross, 2002) and; ii) laterally restricted faults where high throw gradients exist at the restricted tips and causing faults to appear 'overdisplaced' (e.g., Wilkins and Gross, 2002, Laubach et al., 2009, Ferrill et al., 2017). Such is the control of mechanical stratigraphy on fault growth and dimensions that it can lead to significant deviations from fault scaling relationships and produce scatter in global D-L datasets (e.g., Gross et al., 1997).

2.1.2.2. Fault Interactions

As discussed earlier, uninterrupted interaction between adjacent fault segments results in throw transfer at relay zones. We simplified phases of interaction between into stages of i) underlap (Fig. 2.7a), ii) overlap (i-ii = 'soft-linkage') (Fig. 2.7b) and iii) the formation of breaching faults (Fig. 2.7c) and iv) breaching of the relay ramp (iii-iv = 'hard-linkage') (Fig. 2.7d) (Cartwright et al., 1996, Mansfield and Cartwright, 2001, Peacock, 2002, Soliva and Benedicto, 2004, Fossen and Rotevatn, 2016). These phases were introduced in context of relay zone and ramp formation during

continued extension. However, more precisely defined, hard linkage is when faults physically interact and soft linkage is when faults interact only through their stress fields and not all fault interactions which control fault growth, their dimensions and impact the D-L scaling relationship result in hard linkage and breached relay zones (e.g., Crider and Pollard, 1998, Gupta and Scholz, 2000, Soliva and Benedicto, 2004, Soliva et al., 2008, Finch and Gawthorpe, 2017). Published works explore a variety of fault tip interaction scenarios and their implications for: throw distribution (e.g., Bürgmann et al., 1994, Willemse et al., 1996), fault dimensions (e.g., Nicol et al., 1996), and landscape evolution (e.g., Duffy et al., 2015, Nicol et al., 2017, Whipp et al., 2017). Normal faults can show a wide variety of types of fault interactions (e.g., Peacock et al., 2017). Despite this, some key implications of fault interaction are that: (i) when fault tips interact it results in an asymmetric throw distribution skewed towards the interacting tips (e.g., Walsh and Watterson, 1988, Bürgmann et al., 1994, Nicol et al., 1996), (ii) high throw gradients occur at the interacting tip of each of the faults (Cowie and Shipton, 1998, Peacock, 2002); (iii) fault propagation can become inhibited at interacting tips due to high can become 'overdisplaced' on a particular segment due fault propagation being inhibited by fault interaction (e.g., Peacock and Sanderson, 1996, Peacock, 2002); and (iv) that fault interaction can be geometrically complex and occur at the vertical tips, lateral tips and when faults intersect one another's the fault surface (e.g., Nicol et al., 1996, Finch and Gawthorpe, 2017, Naliboff et al., 2017, Maerten et al., 1999, Peacock et al., 2017). Indeed, where faults interact, they control the dimensions and throw distribution of fault surfaces and fault interaction becomes a key control for throw-length scaling relationships (See 3.2.1).

2.1.3. Fault Growth by Segment Linkage: Relay Zones

2.1.3.1. Relay Zone Formation

Irrespective of fault growth model, large normal fault systems result from the linkage of precursor fault segments, and in doing so release large strains and maintain scaling relationships during the

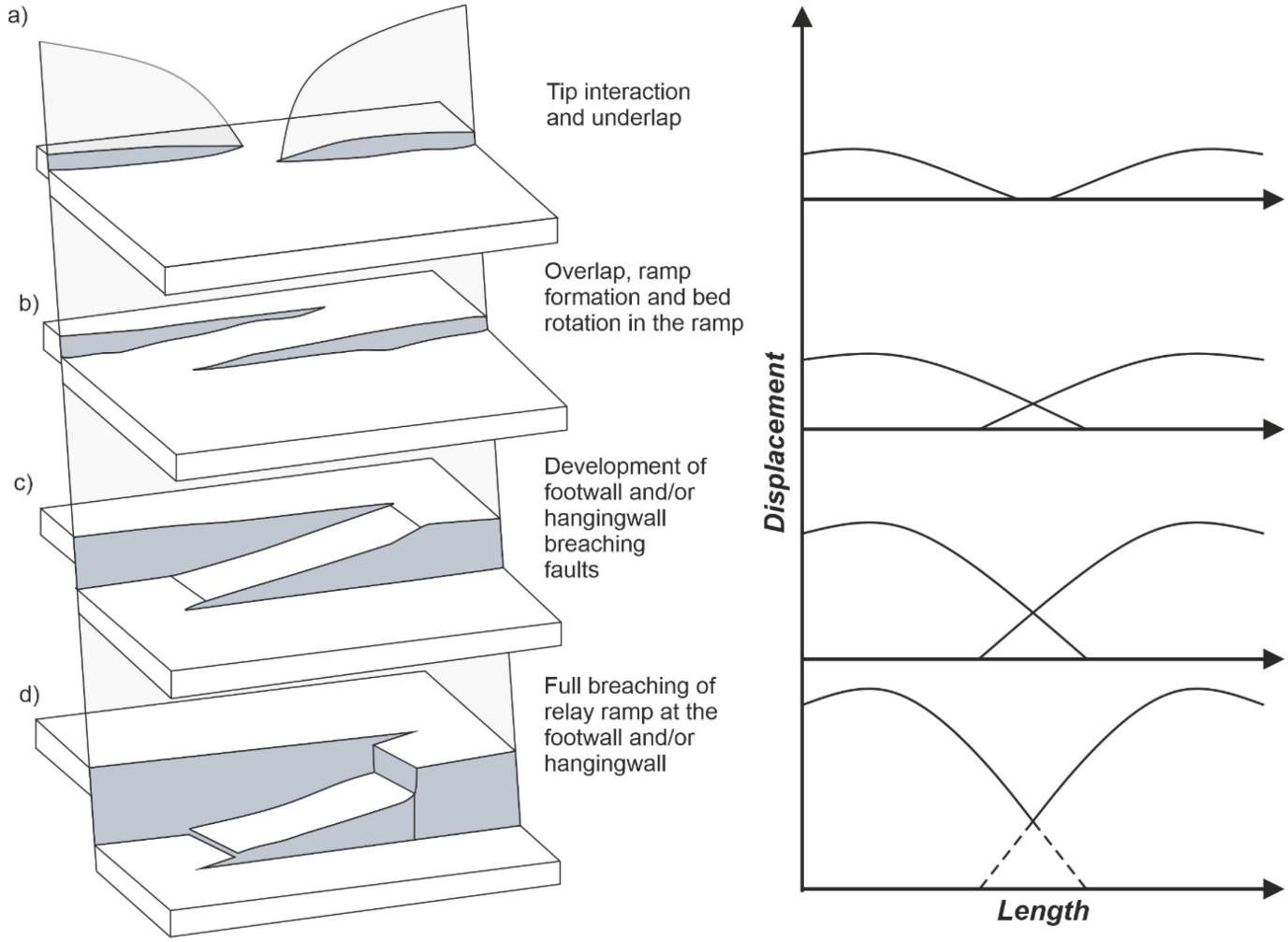


Figure 2.7. Stages of relay zone maturity| Schematic diagrams showing key stages of relay zone maturity that facilitate fault growth by segment linkage, with their respective throw-length plots. (a) Fault tip interaction and underlap; (b) overlap and relay ramp formation; (c) the initiation of relay-breaching faults at the ramps hangingwall and footwall extremities and (d) a fully breached relay zone with examples of hangingwall-breaching and footwall-breaching faults that facilitate the formation of the new larger fault. Modified from Cunningham et al. (2021).

growth of fault systems (Dawers and Anders, 1995, Cartwright et al., 1996, Mansfield and Cartwright, 2001, Peacock, 2002, Soliva and Benedicto, 2004, Rotevatn et al., 2019). As faults grow by segment linkage, adjacent fault segments interact with one another at their respective tips and form transfer and relay structures (Trudgill and Cartwright, 1994, Peacock and Sanderson, 1994, Huggins et al., 1995, Walsh et al., 1999, Fossen and Rotevatn, 2016). The main difference between the two are that transfer zones are more broadly described as being major relay zones that involve a number of faults and relay zones which commonly transfer throw across extensional basins, while relay zones indicate a more simple structure normally involving two fault structures whose

tips are interact (Fossen and Rotevatn, 2016). When fault structures - each with their individual throw and geometry - interact and form these structures' throw is 'transferred' or 'relayed' from one fault to the other, hence the usage of the terms relay or transfer zones (Bosworth, 1985, Morley et al., 1990, Gawthorpe and Hurst, 1993). This process of linkage is characterised by several distinct phases (Fig.2.7):

(i) *Underlap - Overlap:* As two subparallel faults propagate close enough towards their surrounding stress and strain fields interact with one another. During continued lateral growth and interaction, the result of high throw gradient at each of the respective fault tips, results in a skewed throw-length profile (Fig. 2.7a) While the propagating tips of adjacent faults do not overlap one another this phase is called 'underlap'. Intuitively, 'overlap' occurs during the stage at which interacting fault tips overlap one another. The geometry of the tips in plan view begin to curve towards one another in the overlapping zone as the fault propagates into the stress shadow beyond the increased stress region at the fault tips (e.g., Crider and Pollard, 1998, Fossen and Rotevatn, 2016).

(ii) *Relay Ramp Formation:* Relay ramps are characterised by zones of rotated bedding located between the two overlapping, unlinked adjacent fault segments in a relay zone (Fig. 2.7b) (e.g., Gawthorpe and Hurst, 1993, Peacock and Sanderson, 1994, Crider and Pollard, 1998, Xu et al., 2011, Long and Imber, 2012, Whipp et al., 2017, Childs et al., 2017c). As faults overlap and extension continues the decrease in throw but increase in stress at the fault tips results in the deformation of the host-rock between the fault tips (Ferrill and Morris, 2001). Bedding is reoriented and the consequent relay ramp connects the footwall and hangingwall of the fault segments along the relay zone

(Fig. 2.7b) (e.g., Peacock and Sanderson, 1994, Peacock, 2002, Soliva and Benedicto, 2004, Childs et al., 2017c).

(iii) *Relay Zone Breaching:* In the presence of ongoing extension and strain accumulation breaching faults nucleate in the relay and physically link the adjacent fault segments (Fig. 2.7c-d) (e.g., Trudgill and Cartwright, 1994, Gawthorpe and Leeder, 2000, Fossen and Rotevatn, 2016, Rotevatn et al., 2019). The precursor segments now form a coalesced fault surface with its own distinct throw-length data (Fig. 2.7c-d).

2.1.3.2 Relay Zone and Ramp Geometry

Fault interaction and linkage, and therefore the consequent geometry of relay zones and their structures, are not solely dependent on strain (Fossen and Rotevatn, 2016). Such factors as: the distribution and spacing of faults (e.g., Whipp et al., 2017) , mechanical properties of the host-rock (e.g., Ravaglia et al., 2004, Soliva et al., 2006, Camanni et al., 2019), and pre-existing structures (e.g., Conneally et al., 2014, Duffy et al., 2015, Collanega et al., 2018) all influence the formation, localisation and geometry of relay zones. Extensive studies using both observational and modelling techniques suggest a plethora of relay zone and ramp geometries in their respective boundary conditions (e.g, Ravaglia et al., 2004, Long and Imber, 2012, Conneally et al., 2014, Fossen and Rotevatn, 2016, Childs et al., 2017c, Finch and Gawthorpe, 2017). However, for research context we present relay zone and ramp geometries which include key observations rather than an extensive review of boundary conditions and their control on relay zone structure (Fig. 2.8 and 2.9). Controls on the relay ramp geometry in the examples presented are the dip direction, arrangement, and kinematics of adjacent fault segments (e.g., Gawthorpe and Hurst, 1993, Whipp et al., 2017) (Fig. 2.8 and 2.9).

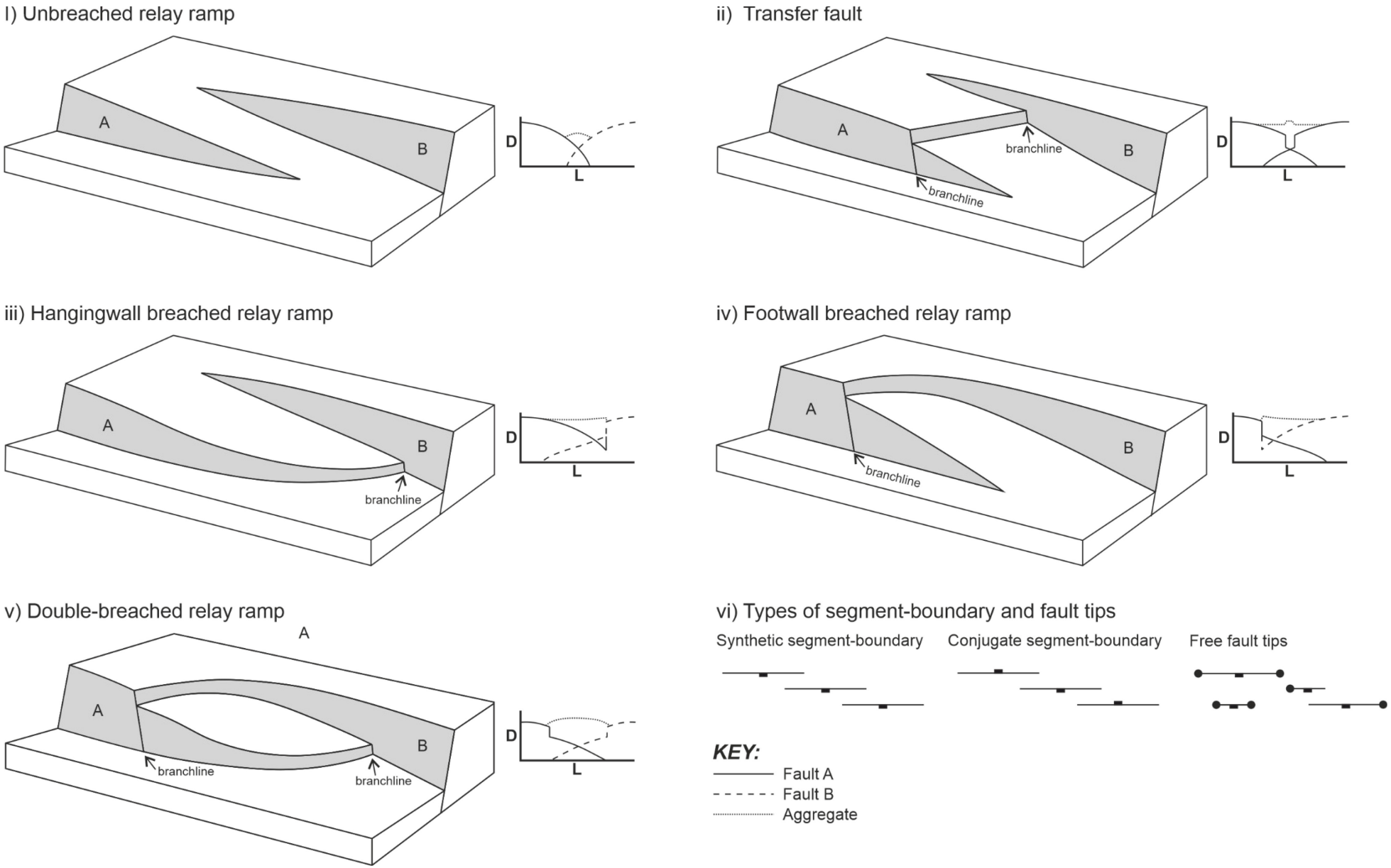


Figure 2.8. Breached relay zone geometries | Schematic diagrams highlighting the principal locations of relay-breaching faults and their associated breached relay zone geometries. (i-v) A classification scheme for the location of relay-breaching faults which occur at fault segment boundaries and their respective throw-length (D-L) plots. (vi) A map view geometry of the types of normal fault segment boundaries and their dip directions. Modified from Whipp et al. (2017).

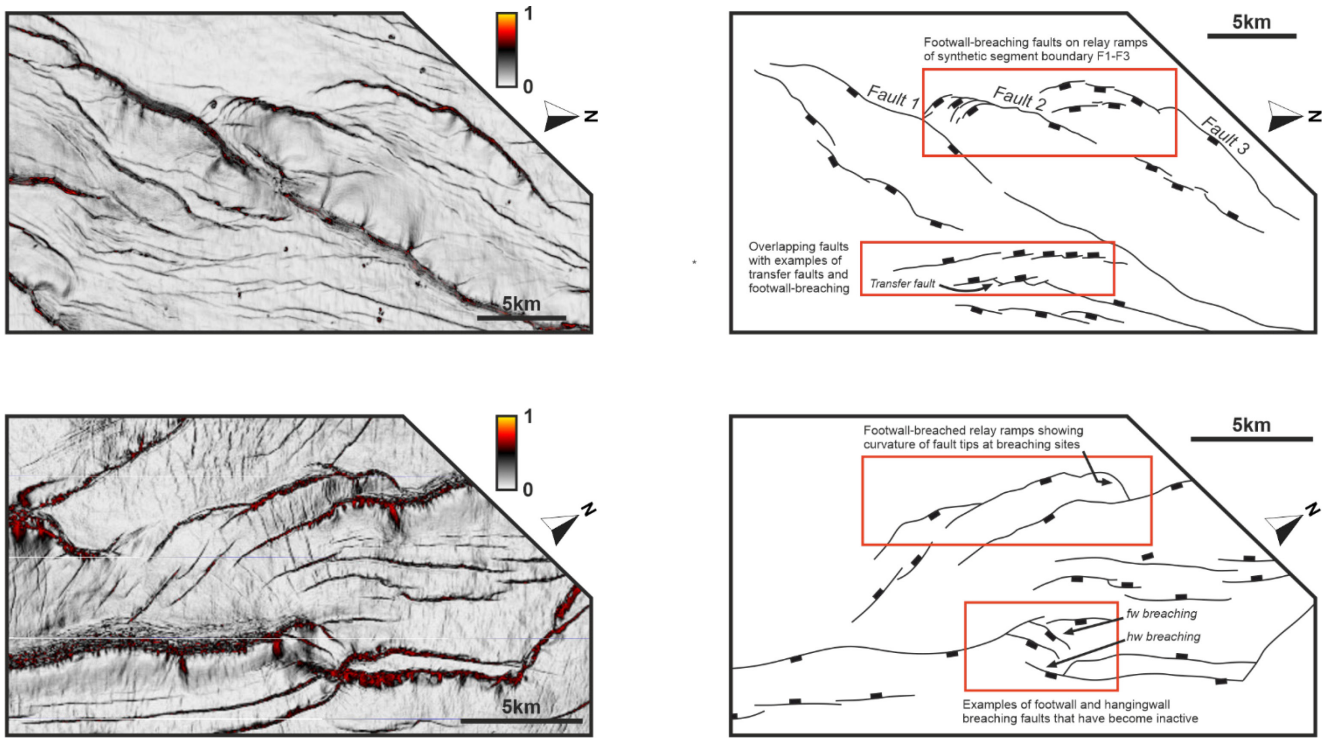


Figure 2.9. Seismic examples of breached relay zone geometries| (Left) Variance extractions on base syn-rift surfaces at two separate locations on the Exmouth Plateau, NW Shelf, offshore Australia. These extractions show the pattern of normal faulting in their areas and examples of relay zone breaching geometries. (Right) A map view interpretation of the variance extractions highlighting some of the relay zone geometries described in figure 2.8.

2.2 Normal Faulting and Basin Evolution

2.2.1 Structural Evolution of Extensional Basins

The formation of extensional basins is controlled by the development of normal faults (Fig. 2.10) (e.g., Gibbs, 1984, Leeder and Gawthorpe, 1987, McClay, 1990, Gawthorpe and Hurst, 1993, Gawthorpe and Leeder, 2000). In such settings, large fault arrays form by the nucleation, propagation, and linkage of small, precursor segments (e.g., Duffy et al., 2015, Whipp et al., 2017, Finch and Gawthorpe, 2017). During continental rifting large faults and *fault arrays* develop by four main stages: i) fault nucleation, ii) fault propagation, (iii) linkage; and iv) strain localisation (Fig. 2.10) (e.g., Peacock and Sanderson, 1991, Dawers and Anders, 1995, Cartwright et al., 1995, McLeod et al., 2000, Gupta and Cowie, 2000, Gawthorpe and Leeder, 2000, Young et al., 2001, Finch and Gawthorpe, 2017, Pan et al., 2021).

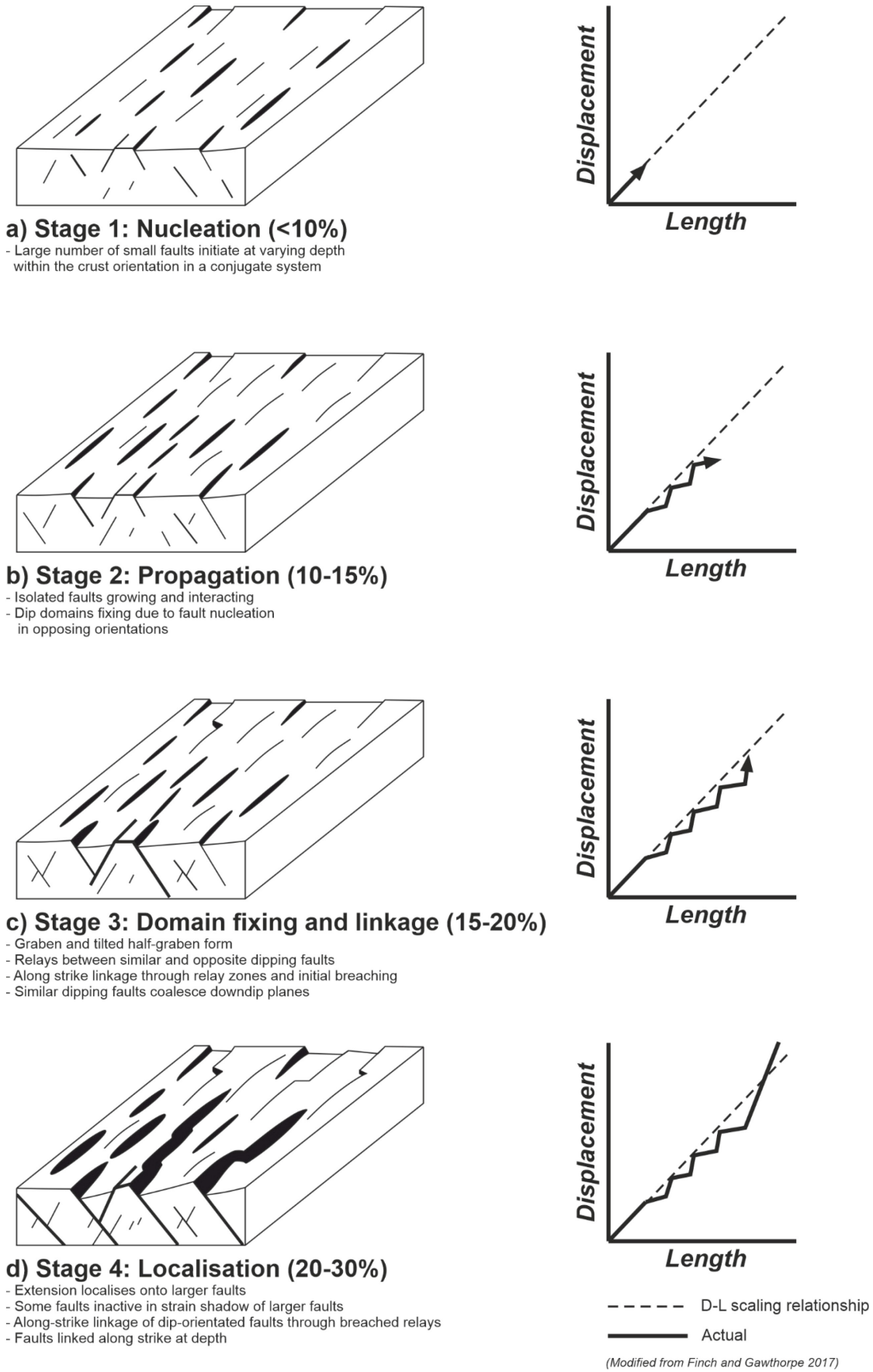


Figure 2.10. Stages of rift development and fault network evolution|(a-d) Schematic diagrams showing the four stages of rift development, outlining the evolution of fault networks within extensional basin settings. The throw-length plots show the progression of maximum throw and fault trace length present in the basin at each stage of rift development. Modified from Finch and Gawthorpe (2017)

Numerical, modelling and observational studies have identified the role of active faults in the pattern of throw accumulation, strain localisation and fault abandonment constituting the complex fault interactions that result in a few large, long basin-bounding faults that determine the structural evolution of extensional basins (e.g., Fig. 2.10; McClay, 1990, Cowie and Scholz, 1992a, Pan et al., 2021). In addition, these studies have determined that constituent fault segment and arrays become kinematically linked and create *fault networks* which begin to no longer act solely as their constituent parts (e.g., Cowie and Shipton, 1998, Gawthorpe and Leeder, 2000, Naliboff et al., 2017, Finch and Gawthorpe, 2017). Rather, as the evolution of extensional basins progress, fault arrays change from many short, low-throw segments to few large, long basin-bounding faults with high maximum throw and they begin to respond to extensional stress feedbacks via 'strain localisation' (Fig. 2.10) (e.g., Gupta et al., 1998, Gawthorpe and Leeder, 2000, Cowie et al., 2000, Walsh et al., 2001, Pan et al., 2021). Together existing studies seem to broadly agree on a sequential process of fault initiation and rift saturation (e.g., Mansfield and Cartwright, 2001, Peacock, 2002, Childs et al., 2003), strain localisation (e.g., Frederiksen and Braun, 2001, Kogan et al., 2012), the development of large basin-bounding faults (e.g., Finch and Gawthorpe, 2017, Nicol et al., 2020b), and cessation of fault activity on faults located in stress shadows of larger structures (e.g., Pan et al., 2021) (Fig. 2.10). These existing findings conclusively highlight the importance of studying normal faulting across the range of scales in which they have influence, and the potentially crucial insights that can yet come from understanding normal faulting and its influence on the overall structural development, and subsequent tectono-stratigraphic evolution, of extensional basins (e.g., Fig. 2.11; Gawthorpe and Leeder, 2000).

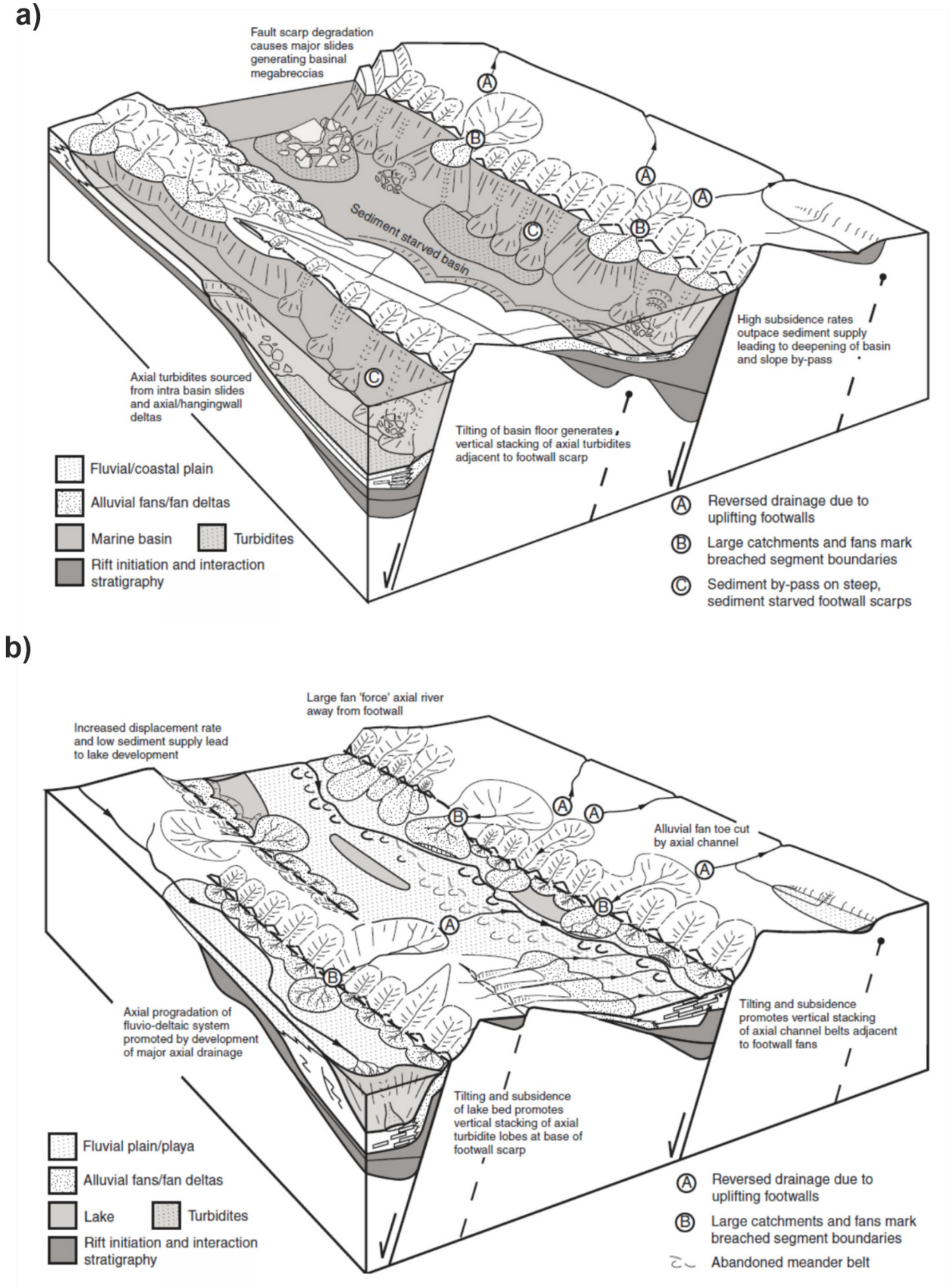


Figure 2.11. Tectono-stratigraphic evolution of extensional settings| (a) The tectono-stratigraphic evolution of extensional basins in coastal/marine depositional environments. (b) The tectono-stratigraphic evolution of extensional basins in continental depositional environments. From Gawthorpe and Leeder (2000).

2.2.2 Tectono-stratigraphic Evolution of Rifts

Basin architecture depends on the relationships between i) accommodation creation and changes in base level; ii) the development of drainage catchments and iii) the structural evolution of the basin (e.g., Leeder and Gawthorpe, 1987, Gawthorpe and Leeder, 2000, Gawthorpe et al., 2018). Each of these relationships are underpinned by the process of fault propagation, growth, linkage, and cessation of fault activity (e.g., Gawthorpe and Leeder, 2000, Gupta and Cowie, 2000, Cowie et al., 2000, Densmore et al., 2004). To understand the tectono-stratigraphic evolution of sedimentary basins, early theoretical and experimental models of rift basins and their implications for landscape evolution in rift basins were tested by Gawthorpe and Leeder (2000) based on observations from natural rifts in end members of coastal/marine (Fig. 2.11a) and continental rift settings (Fig. 2.11b). In both settings sediment supply is derived primarily from the rift-margin hinterland and sediment transport and drainage networks are organised by fault-controlled rift topography and bathymetry (Fig. 2.11) (e.g., Leeder and Gawthorpe, 1987, Gawthorpe and Leeder, 2000, Gupta and Cowie, 2000, Cowie et al., 2000, Densmore et al., 2004, Commins et al., 2005).

2.2.3 Relay Zone Kinematics and Their Control on Basin Architecture and Stratigraphy

Across all stages of rift basin development, and all scales of fault growth by segment linkage, the evolution of relay zones, relay ramps and large transfer zones are fundamental to the tectono-stratigraphic evolution of rift basins (e.g., Gawthorpe and Hurst, 1993, Peacock, 2002, Athmer and Luthi, 2011, Wiebke et al., 2010, Fossen and Rotevatn, 2016, Moustafa and Khalil, 2016). The extent to which they control sediment routes deposition in rifting margins depends on the interplay of various factors such as: sedimentation rate, fault activity, ramp geometry and base level fluctuations (e.g., Athmer and Luthi, 2011). However, it is largely established that where these factors are preferable, relay and/or transfer zones control sedimentation and deposition in extensional basins in several dominant mechanisms, for example: (i) by establishing large catchments in their footwalls (Fig. 2.11) (e.g., Gawthorpe and Hurst, 1993, Eliet and Gawthorpe,

1995, Gawthorpe and Leeder, 2000, Goldsworthy and Jackson, 2000, Densmore et al., 2003), (ii) by acting as basin entry points for sedimentary systems such as: river channels, fans and fan-deltas, and turbidites (Fig. 2.11b) (e.g., Wiebke et al., 2010, Athmer and Luthi, 2011, Ma et al., 2021), and (iii) by being the principal mechanism for basin linkage by which hydrologically closed basins evolve into open rift settings (Fig. 2.11a) (e.g., Gawthorpe and Leeder, 2000). Unravelling relay zone kinematics which facilitate growth by segment linkage is thus key to being able to understand the structural evolution along rift margins in active and ancient examples (See 2.3.3)

2.3 Outstanding controversies related to normal fault growth

2.3.1 Scatter in D-L Data: Mechanical Stratigraphy

Global compilations of throw - length (D – L) geometric data underpin fault scaling relationships and consequently the paradigm fault growth models, which are in part based on global fault geometric data (e.g., Watterson, 1986, Walsh and Watterson, 1987, Cowie and Scholz, 1992a, Cladouhos and Marrett, 1996, Walsh et al., 2002, Rotevatn et al., 2019). The throw - length data include normal fault data which each have resulted from their own unique growth conditions, such as mechanical stratigraphy (e.g., Martel, 1999, Wilkins and Gross, 2002, Laubach et al., 2009), among others (e.g., Bürgmann et al., 1994, Nicol et al., 1996, Soliva et al., 2008, Nicol et al., 2017). As discussed in the research context chapters, mechanical stratigraphy can influence fault geometric data. Yet, since the geometric data does not discriminate between boundary conditions of the faults and due to the enormity of the amount of data points in global D-L compilations, the impact that mechanical stratigraphy has on scatter within the datasets and on fault scaling relationships is often masked. Research has focussed on field outcrop and modelling studies to determine the impact that mechanical stratigraphy has on fault dimensions and growth, but little regarding its impact on seismic-scale faults has been published.

This gap in knowledge presents questions such as:

- Does mechanical stratigraphy control fault dimensions and growth on large, seismic-scale faults ?
- Are D – L global data compilations lacking by not analysing geometric data in context of the conditions in which faults grow ?

Therefore, in Chapter 4, I address research aim 1 in 1.2.1 and investigate whether seismic-scale fault dimensions and growth can be influenced by mechanical stratigraphy, In addition, I present the potential impact on the applicability of these data compilations when fault geometric data is not analysed in context of the boundary conditions in which individual faults grow.

2.3.2 Constraining Fault Growth in Underfilled Basins

The testing and proposing of fault growth models has been overwhelmingly conducted in rift basins where sedimentation rates are equal to or exceed slip rates creating accommodation space, in part because reliable, developed techniques to determine fault growth require such conditions (e.g., Jackson et al., 2017, Rotevatn et al., 2019). However, not all faults grow in ideal basin conditions, while determining fault growth and proposing fault growth models is a requirement for a range of geoscience disciplines that operate in a range of non-idealistic conditions (i.e., 'underfilled' or sediment-starved basins). Geomorphological techniques have been extensively used in many active rift settings where footwall geomorphology is used to determine fault growth history such as: footwall topography (Densmore et al., 2004, Alves et al., 2009), drainage basin morphology and patterns (Goldsworthy and Jackson, 2000, Tsodoulos et al., 2008), knickpoint analysis (Commins et al., 2005), and geomorphological indices (Verroios and Zygouri, 2021). However, we rarely see such techniques applied in the subsurface in sediment-starved basins where conventional fault growth techniques previously highlighted are insufficient to constrain fault growth due to the lack of complete synkinematic strata in the hangingwall.

This gap in methodology results in questions such as:

- How can fault growth be constrained in underfilled basins ?
- Can geomorphological techniques be applied in the subsurface ?
- Can an integration of subsurface and geomorphological techniques progress our understanding of how faults grow in sediment-starved settings ?

Thus, in Chapter 5, I address research aim 1 in 1.2.2 and propose a new technique, using footwall geomorphological analyses and fault throw data, to constrain fault growth in a sediment-starved basin.

2.3.3 Relay Zone Kinematics

Fault growth by segment linkage controls the development of rift physiography and the stratigraphic architecture of extensional basins (e.g., Fig. 2.11; Gawthorpe and Hurst, 1993, Finch and Gawthorpe, 2017). As discussed earlier, relay zones are the sites segment linkage and are primary structures controlling sediment transport systems along rifted margins (e.g., Gawthorpe and Leeder, 2000, Gupta and Cowie, 2000, Athmer and Luthi, 2011). Thus, understanding relay zone kinematics allow us to resolve how faults grow by segment linkage and the structural and stratigraphic architecture of extensional basins.

Despite widespread agreeance on the influential role of relay-breaching faults during segment linkage, little is known regarding their kinematic behaviour during and post segment linkage. In particular, the evolution of throw minima on breaching faults over geological timescales are somewhat overlooked and only a few works have been published on the kinematics of relay zones throughout the life of the breaching fault (e.g., Commins et al., 2005, Faure Walker et al., 2009). Recent geometric and geomorphic observations from relatively young (kyr) active faults suggest that breaching faults exhibit markedly higher throw rates than concomitant faults' throw maxima, despite being the area of lowest total throw (Faure Walker et al., 2009). Despite such observations, examples in seismic data of large tectonic faults which have been active for millions of years display

distinct throw minima and suggest this is not the case (e.g., Huggins et al., 1995, Pan et al., 2021). As of yet, none of these hypotheses have been thoroughly tested on faults which have been active over geological timescales. If such breaching fault behaviour were present over geological timescales, this would have a significant impact on rift development as throw minima would be removed at locations of paleo-fault segmentation and linkage impacting landscape evolution at these key basin entry points for sediments.

This gap in knowledge prompts questions such as:

- Is this the case ? If not, what is the behaviour of throw minima over geological timescales?
- What are the throw rates on breaching faults over geological timescales ?

Therefore, in Chapter 6, I address research aim 1 in 1.2.3 and focus on the quantification of throw rates on breaching faults over geological timescales. I conduct this study using relay zones of varying maturities and geometries to determine more consistent principles governing the behaviour of throw minima and breaching faults.

3

Dataset and Methodology

Preamble

This Chapter outlines the datasets and methodologies which constitute the multi-disciplinary approach to the research aims highlighted in Chapter 1. These methodologies include reflection seismic interpretation; quantitative techniques used to determine fault dimensions and kinematics and geomorphological analysis. In this chapter detailed descriptions of these data and methods are given. Given that Chapter 4 is a published paper and chapters 5 and 6 have been written as papers there will be some inevitable repetition between this chapter and the 'Datasets and Methodology' sections of chapters 4,5 and 6.

3.1 Seismic Reflection Data

3.1.1 Datasets

The dominant datasets used in Chapters 4 – 6 largely consist of 3D-seismic reflection datasets. Below, I describe these datasets briefly given that Chapters 4 – 6 go further into describing each dataset and their parameters in detail.

Kwanza Basin, Offshore Angola

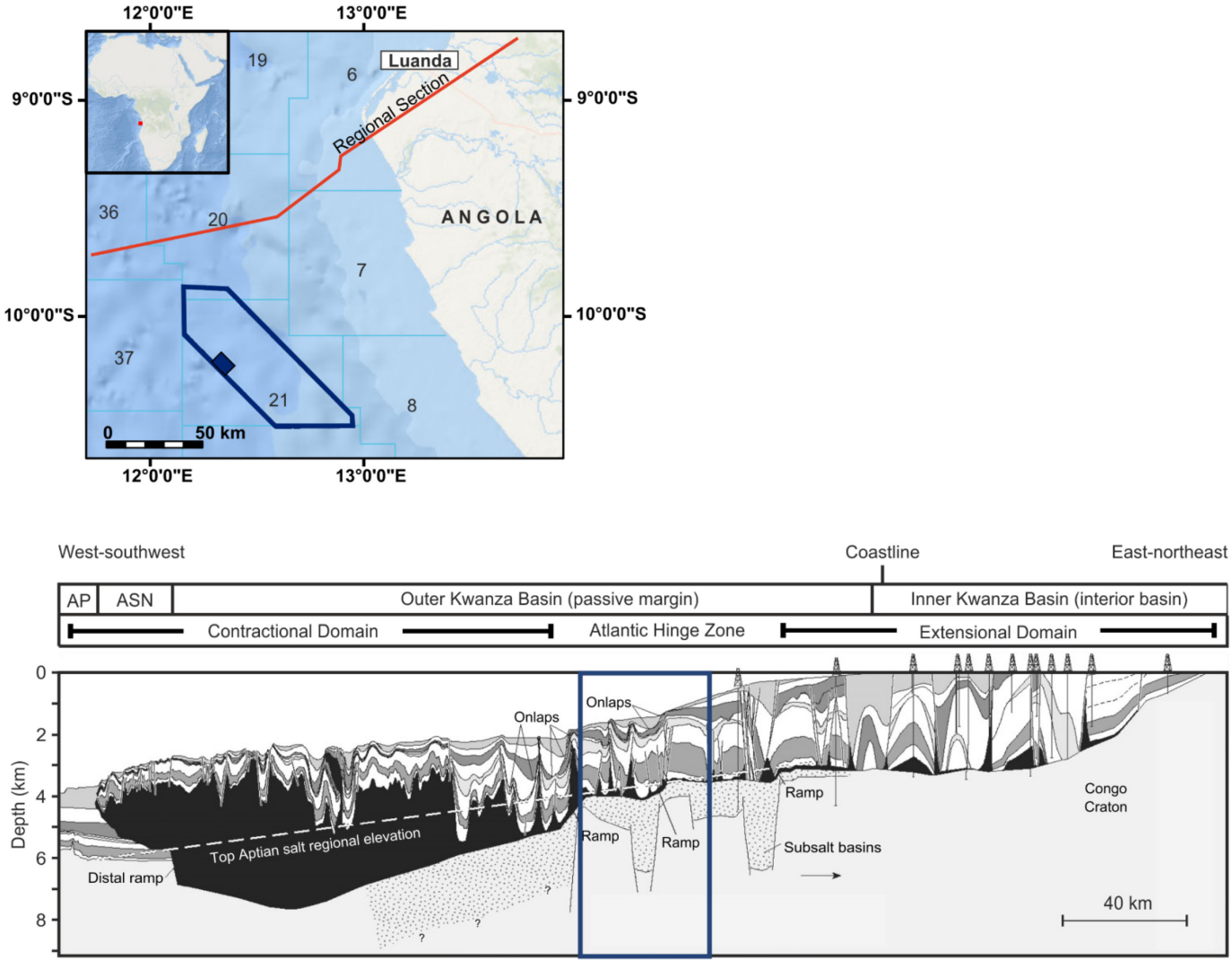


Figure 3.1. Chapter 4 study location - Kwanza Basin, Offshore Angola | (Top) A map view of the Angolan sector of the West African Passive Margin and location of the dataset used in chapter 4 (dark blue box). The red line shows the location of the regional section. (b) A regional cross-section of the study area used in Chapter 4.

In Chapter 4, we use high-quality, pre-stack, depth-migrated (PDSM) BroadSeis™ 3D- seismic reflection data acquired by Compagnie Générale de Géophysique (CGG) from the Outer Kwanza Basin, offshore Angola in Block-21 (Fig. 3.1). The survey has an areal extent of 2915 km^2. Since the data are depth-migrated we could measure fault geometry and displacement directly from the seismic data. There are no well-data in this area, so regional stratigraphic surfaces are used from existing literature to provide age control (See Chapter 4, 'Data and Methods').

Northern Carnarvon Basin, Offshore Australia

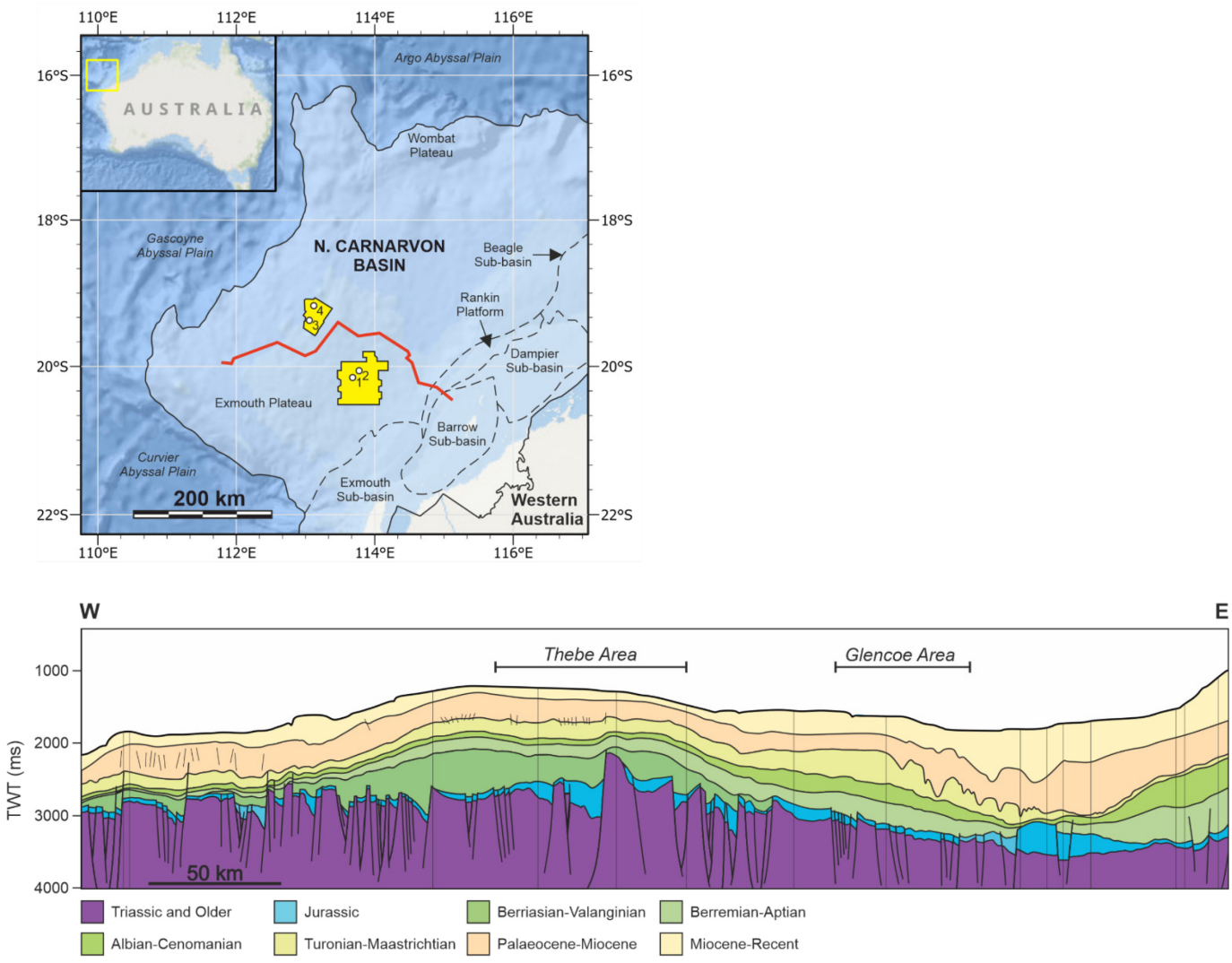


Figure 3.2. Chapter 5 and 6 study location - Northern Carnarvon Basin, NW Shelf, Offshore NW Australia | (Top) A map view showing the location of the chapter 5 and chapter 6 study area (see chapters 5 and 6). (Below) A regional cross-section, outlined in the above by the red section line, of the Northern Carnarvon Basin showing the key structural and stratigraphic framework.

In Chapters 5 and 6 we use two different high-quality, pre-stack, time migrated (PTSM) 3-D seismic reflection surveys, both located in the Northern Carnarvon Basin on the Exmouth Plateau, NW Shelf, offshore Australia (Fig. 3.2). For Chapter 5 we use the HEX07B survey located in the WA-346-P permit area. The survey has an areal extent *c.* 1800 km^2 and a maximum penetration of 4610 ms TWT. This seismic survey is accompanied by well-data from the Thebe-1 and Thebe-2 wells. In addition, formation tops from these wells are used to constrain horizon interpretations and provide control to our seismic tectonostratigraphic frameworks (See Chapter 5, 'Dataset and Methodology'). In Chapter 6 we also use the HEX07B survey described above and formation tops from the Thebe-1 and Thebe-2 wells in a similar manner. In addition, we use high-quality, pre-stack, time migrated (PTSM) 3-D seismic reflection data from the Glencoe survey located in the WA-360-P permit area and *c.* 100 km to the SE of the Thebe HEX07B survey (Fig. 3.2). The survey has an areal extent of *c.* 4000 km^2 and a maximum penetration of 8000 ms TWT. This seismic survey is accompanied by well-data from the Nimblefoot-1 well and formation tops from this well is also used to constrain horizon interpretation to constrain our tectonostratigraphic framework for Chapter 6 (See Chapter 6, 'Dataset and Methodology').

3.1.2 Seismic Interpretation

The primary method of investigation in this study focused on fault surface interpretation of normal faults and horizon interpretation of the stratigraphic surfaces which interacted with the fault surfaces. All seismic datasets used through Chapters 4 – 6 are zero-phased (i.e. central peak or trough aligned at time zero, see Simm and Bacon (2014), allowing for a more accurate interpretation of key stratigraphic surfaces. Seismic reflection data presented in this thesis are presented in the Society of Exploration Geophysicists (SEG) normal polarity; i.e. US Standard, where an peak indicates a downward increase in acoustic impedance (Brown, 2011). In all chapters the vertical resolution achieved in each of the datasets is based on the limit of separability: Tuning Thickness = ¼ (λ_D)

; where λ_D is the dominant wavelength (Bacon et al., 2003).

Throughout Chapters 4 – 6 Schlumberger's Petrel™ suite has been used as the seismic interpretation software.

3.2 Quantitative Fault Analysis

Our understanding of fault growth is underpinned by geometric criteria such as along-strike variations in displacement, fault aspect ratio (i.e., the ratio of maximum fault height and length), and displacement distribution on a faults surface among others (Jackson et al., 2017). Quantitative fault analysis techniques can allow us to make key observations on topics such as i) periods of fault slip and lengthening; ii) fault geometry and; iii) displacement distribution on fault surfaces (e.g., Childs et al., 2003, Jackson et al., 2017). When applied appropriately, these techniques ultimately allow for the observation of key geometric criteria and become powerful tools which can determine fault dimensions, fault kinematics and test fault growth models. In this section we give an overview of each of these techniques, potential errors when applying them and uncertainties associated with their use.

3.2.1 Throw/Displacement-Length and -Depth Plots

Faults typically grow by accumulating displacement and length (Walsh and Watterson, 1987, Walsh and Watterson, 1988, Marrett and Allmendinger, 1990, Cowie and Scholz, 1992b, Needham et al., 1996, Kim and Sanderson, 2005, Torabi et al., 2019, Rotevatn et al., 2019). Displacement does not accrue uniformly on fault surfaces resulting in along-strike and down-dip variations (e.g., Nicol et al., 1996, Soliva et al., 2008). To understand such along-strike and down-dip variations in displacement we construct displacement-length (D-x) and displacement-depth (D-z) plots. Where the slip vector is *not* known, we construct these plots using the vertical component of slip (i.e., throw) to construct throw-length (T-x) and throw-depth (T-z) plots (Jackson et al., 2017). For simplicity, we will use the term 'throw' when describing how to construct these plots below.

However, the term 'displacement' could be inserted in its place for cases where the slip vector is known.

Throw-length (T-x) plots comprise systematic measurements of throw along strike for the full length of the fault trace in map view (e.g., Cowie and Scholz, 1992a, Cowie and Scholz, 1992b, Meyer et al., 2002). They are constructed by measuring the depth of a correlative surface across a fault surface and provide a measurement of the amount of throw on the correlative surface (i.e., seismic reflections) (e.g., Barnett et al., 1987, Peacock and Sanderson, 1991, Mansfield and Cartwright, 2001, Walsh et al., 2003, Kim and Sanderson, 2005)

Throw-depth (T-z) plots comprise systematic measurements of throw along fault dips for several correlative surfaces (e.g., Baudon and Cartwright, 2008a, Baudon and Cartwright, 2008b, Tao and Alves, 2019). They differ from T-x plots in that rather than measuring throw along the length of a fault for a given correlative surface, T-z plots measure throw for several correlative surfaces at a given point along the length of the fault.

They are constructed by measuring the depth of correlative surfaces across a fault surface and provide a measurement of the amount of throw on the selected correlative surfaces (i.e., seismic reflections). Along-strike and down-dip variations in throw can be indicators of fault geometry and kinematics, therefore, making T-x and T-z plots useful when observing normal faults (e.g., Hongxing and Anderson, 2007, Jackson et al., 2017). For example: throw minima exist at the site of relay zones indicating displacement transfer (e.g., Huggins et al., 1995, Peacock, 2002), or successive pronounced increases in throw on increasingly older or deeper correlative surfaces could indicate periods of fault activity where the majority throw was accumulated on a fault surface (e.g., Hongxing and Anderson, 2007).

T-x and T-z plots are constructed from numerous correlative surfaces (i.e, stratigraphic surfaces, or seismic reflections) which span the length and depth of a fault. Often seismic-scale faults observed in seismic reflection data can reach up to the order of kilometres in both length, down-dip height and displacement (See Chapter 5 – 6). Taking throw measurements for such faults on

multiple correlative surfaces introduces the possibility of error while using this method. In addition, correlative surfaces can undergo deformation (e.g., fault-related folding, normal drag) and result in changes to the actual throw measured at a given point. The accuracy and veracity of interpretations made for fault kinematics using this method is dependent upon the accuracy of mapping and number of horizons used (e.g., Tao and Alves, 2019). In order to maintain the validity of interpretations using this method, we ensure that we: i) use a consistent spacing interval for measurements; ii) take sufficient measurements of throw along strike by measuring at least every 150 m along strike of faults that are over 10 km long; iii) take measurements on numerous correlative surfaces with depth at any given point along fault length and; iv) remove the effect of strain in correlative surfaces, in order to achieve the coverage of measurements needed to appropriately interpret fault kinematics using this method. This method is used throughout Chapters 4 – 6.

3.2.2 Throw/Displacement Backstripping

In Chapter 6, the "original" method outlined by Jackson et al. (2017) is used. This method includes subtracting throw/displacement measured on a shallower horizon from throw measured across a deeper horizon (e.g., Jackson et al., 2017). By so doing on successively deeper horizons the original method of throw/displacement backstripping reveals the throw/displacement on a horizon at the age of the horizon to which it is backstripped. Thus, backstripped throw/displacement can reveal fault activity along the strike of the fault and constrain the position of faults tips at different time periods. This method is particularly useful when attempting to evaluate fault growth models, which are in part determined by the lateral propagation of fault tips (e.g., Jackson et al., 2017, Rotevatn et al., 2019). Another way of measuring this is using the modified method, in which displacement/throw is calculated bat the time of deposition of a given horizon by subtracting the maximum displacement along the horizon from the fault surface (e.g., Rowan et al., 1998). The method assumes that faults grew in accordance with the isolated fault growth model, and thus, the

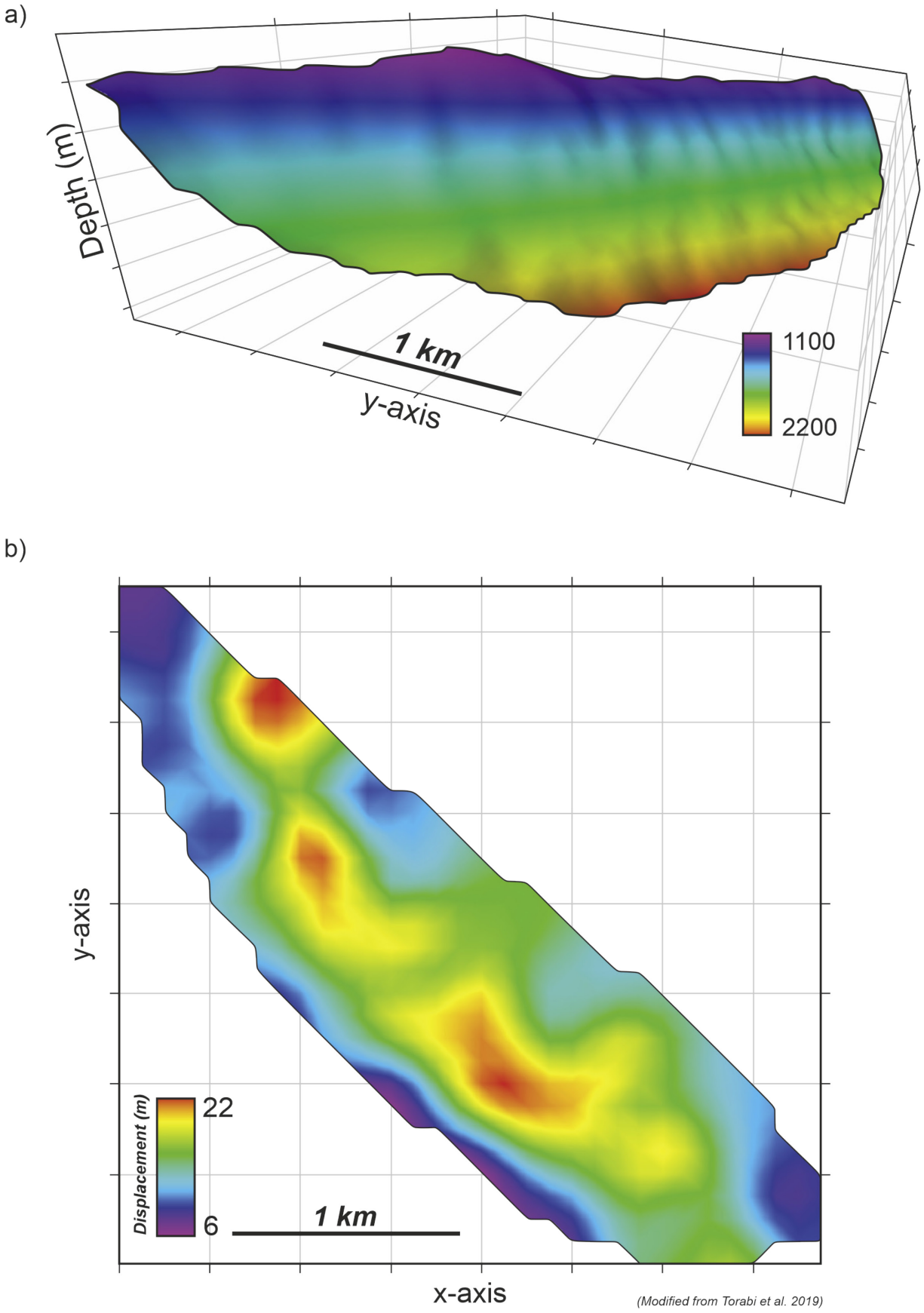


Figure 3.3. 3-D Strike Projections | (a) The initial fault surface projection. (b) The map view of the throw projected onto the 3D fault surface projection shown in (a). Modified from Torabi et al. (2019).

original method is used in this thesis as it aims to test different fault growth models where backstripping is used.

3.2.3 3-D Strike Projections

Throw-length and throw-depth plots do not allow for visualisation of the 3D distribution of throw/displacement on the fault surfaces, however, 3-D strike projections do (e.g., Torabi et al., 2019). 3-D strike projections achieve this by 'projecting' displacement values onto the interpreted 3-D fault surface geometry (Fig. 3.3). Firstly, to construct 3-D strike projections an interpretation of the fault surface is needed. This is achieved by interpreting the geometry of the fault – which appears as a discontinuity in seismic reflections – along the length of the fault. The fault geometry can then be converted into a surface using the Petrel™ surface tool (Fig. 3.3a). In addition, displacement measurements for correlative surfaces that are offset by the fault plane are taken at consistent intervals along the length of the fault. This can be achieved using either the displacement length or displacement-depth plot methodology. These displacement measurements are then converted into a surface using the Petrel™ surface tool. Finally, this displacement distribution surface is added to the fault surface as an attribute (Fig. 3.3b). This allows for the 3-D display of the distribution of displacement on the fault surface (Fig. 3.3b). The errors that can be incurred using this method are identical to potential errors found in the displacement – length plots (i.e., accuracy and precision of displacement measurements and fault geometry) as are the precautions to ensure reliable results (see 3.2.1).

3.2.4 Expansion Indices

Faults that intersect the free surface cause differential subsidence and create accommodation space in their hangingwall basins, thus influencing basin physiography and the stratigraphic evolution of the basin (e.g., Leeder and Gawthorpe, 1987, Gawthorpe and Leeder, 2000, Childs et al., 2003). For such faults, when their slip rate is less than or equal to the sedimentation rate across-fault

thickening of synkinematic strata occurs and therefore records the initiation and cessation of fault activity (e.g., Tvedt et al., 2013b, Jackson et al., 2017). The Expansion Index (EI) calculates the magnitude and timing of this across-fault thickening in the following manner:

$$\text{Expansion Index (EI)} = H_t \; / \; H_o$$

; where H_t = hangingwall thickness and H_o = footwall thickness for a specific stratal unit.

It follows then that: i) values >1 indicate periods of across fault-thickening; ii) values = 1 indicate no across-fault thickening and; iii) values < 1 indicate stratal thinning from the footwall to the hangingwall and can indicate either erosion in the hangingwall or error in the measurement of the expansion index (Jackson et al., 2017). Thus, when EI is applied to a syn-sedimentary fault against a geological period or a proxy such as depth, we can constrain the timing of fault activity (e.g, Fig. 2.6; Jackson et al., 2017, Childs et al., 2017a). The EI gives a 1-D insight to periods of across fault-thickening, however, if for example it was applied along the length of a fault it can indicate regions where across-fault thickening was occurring and therefore constrain the location of fault tips during a specific timeframe (e.g., Fig. 2.6). Measuring the expansion index across a fault surface accurately depends on several factors. Firstly, mapping across-fault thickening inaccurately, or miscorrelating surfaces will introduce artificial thickening or thinning across a fault surface, reducing the reliability and repeatability of resulting fault growth histories being unreliable. In addition to error that may be introduced by human measurement, error can be introduced by not appropriately compensating for geological phenomena. These may include but are not limited to: strain-related changes in rock thickness in the hangingwall (Delogkos et al., 2020), and burial-compaction of pre-, syn- and post-kinematic sediments resulting in changes to fault displacement and stratigraphic thickness (Taylor et al., 2008). As a result, EI values that deviate slightly away from 1 may be because of such mentioned events rather than actual across-fault changes in stratal thickness. Thus, the inputs to EI values must be carefully mapped and EI output values considered in context of geological factors (i.e., sediment compaction, footwall/hangingwall strain) (Jackson et al., 2017).

3.2.5 Isochrone/Isopach Analysis

Along strike variations in slip result in the formation of hangingwall depocentres characterised by fault-normal synclines with axes that plunge towards the location of maximum displacement on the fault surface (e.g., Gupta et al., 1998, Gupta et al., 1999, Cowie et al., 2000, Khalil and McClay, 2009, Khalil and McClay, 2017). In line with the common along strike displacement distribution, accommodation space created is greatest at the centre of the fault and decreases towards its tips. As growth strata are deposited into depocentres, their thickness also follows this pattern (e.g., Giba et al., 2012, Jackson and Rotevatn, 2013). Isopach (m)/isochrone (TWT) maps record the variations in thickness of growth strata in the hangingwall depocentre between seismically constrained upper and lower bounding surfaces (i.e., thickness change between the base syn-kinematic and post-kinematic surfaces), while isopach maps' units of measurement are in metres or feet, isochrone maps' units are in milliseconds (ms) or seconds (s) TWT (Jackson et al., 2017). When used for syn-kinematic stratigraphic intervals these maps can be used to determine the shape and location of hangingwall depocentres for a specified time-interval and, when applied for successive intervals, the migration of depocentres (e.g., Pan et al., 2021). Thus, aiding in constraining the location of fault tips during fault growth and therefore allowing for the observation of lateral tip propagation through time.

While isopach/isochrone analysis effectively measures the along-strike and across-fault variations in thickness of strata, changes in thickness of stratigraphy are not solely caused by fault-driven accommodation creation in extensional basins. Thickness variations can also occur as a result of point-sourced sedimentary systems such as fan deltas, slope aprons or footwall-derived degradation-fan complexes (see Chapter 5; e.g., Barrett et al., 2021).

Our novel application of geomorphological methods for constraining fault growth in Chapter 5, illustrates the potential for determining fault growth by manipulating the potential pitfalls when using isopach/isochrone analysis (i.e., point-sourced sedimentary systems and underfilled basins)

to use these exact pitfalls as sources of chronostratigraphic and tectonostratigraphic information to constrain fault growth in underfilled basins (see Chapter 5).

3.3 Geomorphological Techniques

3.3.1 Determining Fault Scarp Erosion

In Chapters 5 and 6 footwall degradation is widespread on the footwalls of large, extensional, basin-bounding fault arrays (see Chapters 5 - 6; e.g., Bilal et al., 2020, Bilal and McClay, 2022). The two components of footwall degradation which can be measured are: i) vertical erosion – the difference between actual throw and a projected pseudosurface and ii) headward erosion – the distance between the footwall cut-off and the most headward point of erosion (Fig. 3.4) (e.g., Leeder and Gawthorpe, 1987, Yielding, 1990, Elliott et al., 2012, Bilal et al., 2020, Barrett et al., 2021).

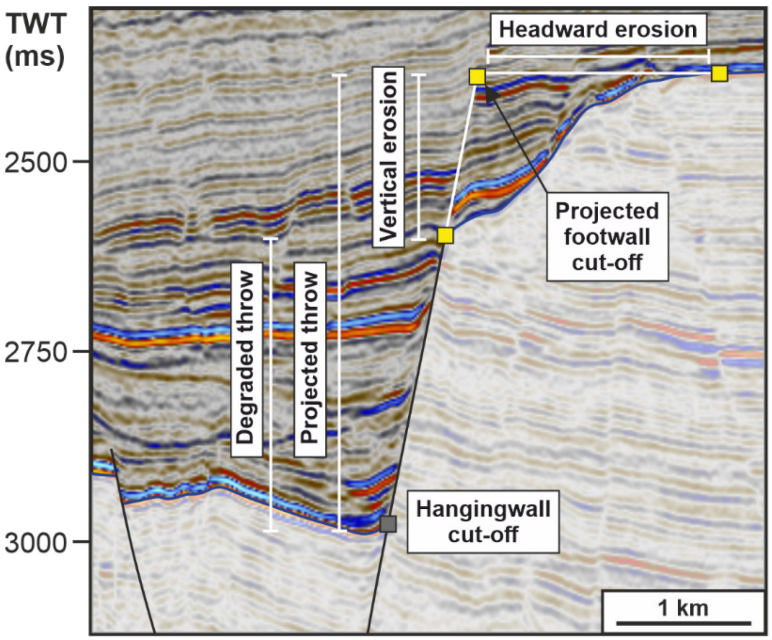


Figure 3.4. Parameters for measuring fault scarp degradation | A schematic diagram overlain onto a seismic cross-section of a degraded fault scarp showing the definitions of the different parameters used when measuring fault scarp erosion and throw on such eroded scarps.

To understand the along-strike variability of erosion and determine its impact on displacement/throw we construct vertical/headward erosion – length plots. This method differs in that when measuring throw on a correlative surface across the fault plane the footwall geometry is already present, whereas in this case the footwall geometry is eroded (e.g., Yielding, 1990,

Yielding and Roberts, 1992, Elliott et al., 2012, Alves and Cupkovic, 2018, Barrett et al., 2021). First, to best assess the geometry of the uneroded fault scarp, a pseudosurface is extrapolated by projecting the fault plane and the dip trend of the uneroded footwall surface. This pseudosurface represents the geometry of the footwall *prior* to erosion. Vertical erosion – length plots are constructed by measuring the vertical distance between the pseudosurface footwall cut-off and the actual footwall cut-off, at consistent spacing along the length of the fault. Headward erosion is measured by calculating the distance between the pseudosurface footwall cut-off and the most headward point of erosion (Fig. 3.4). We can also estimate erosion thickness and the areal extent of erosion by using isochrone analysis to measure between the eroded surface and the uneroded pseudosurface (see 3.2.5). If the pseudosurface has been judiciously mapped, then the area where the isochrone shows thickness is the areal extent of the footwall erosion and the thickness difference shown represents the 2-D distribution of vertical erosion.

Reliable results of vertical and headward erosion on the footwall depends on the precision and accuracy taken when mapping the eroded and pseudosurface and the same aspects for their associated footwall cut-offs. In Chapters 5 – 6. Carefully mapping these surfaces on closely spaced intervals along the length of fault strike can reduce the error and uncertainty associated with the measurements of vertical and headward erosion (*c.* 50 m spacing; see Chapter 5; 'Datasets and Methodology').

3.3.2 Volumetrics and Volume Balancing

To calculate volumetrics, two seismic reflections are mapped on at least 5 inlines and crosslines to constrain the structure of each of the surfaces (see 5.3). The volume between these two surfaces represents the volume for a given stratigraphic unit. The volume calculation can be done using the Petrel™ volumetric calculation functions. Where volume balancing calculations are performed, the methods of Barrett et al. (2021) are used as the primary reference for performing these techniques, in which the volume of eroded material of the footwall is balanced with the volume of

hangingwall fans to determine the fans' origin (see 5.3.2). Moreover, this volume balancing approach can also be used in source-to-sink studies. First, when applying this method using seismic reflection data, the volumetric calculations outlined above are applied between the base and top surfaces for both the 'source' and the 'sink' - in the case of Chapter 5 the focus is the base and top surfaces of the eroded footwall sequence and the degradation fans, respectively. Second, because of along-strike variation in source and sink volumetrics the fault system is compartmentalised into several sections to measure source – sink volumetrics more precisely. Volume balancing is then performed by analysing the differences between source and sink volumes, allowing for investigation of possible causation (e.g., Elliott et al., 2012, Barrett et al., 2021).

Time – Depth conversion is a key step in volumetric calculations and volume balancing when using seismic reflection data in TWT (milliseconds or seconds). Depth conversion uncertainties will clearly impact the volumetric calculations and therefore volume balancing. Where the source and sink are at different depths in TWT, accurate corresponding measurements of interval or average seismic velocities are required to calculate representative volumetrics in conceivable units (i.e., metres or feet). In addition to time – depth conversion, since volumetrics and volume balancing are inherently linked to the bounding top and base surfaces of the stratigraphic volume in question, precise mapping of these surfaces is imperative.

4

Mechanical Stratigraphy Controls Normal Fault Growth and Dimensions, Outer Kwanza Basin, Offshore Angola

Preamble

DR interpreted the data, wrote the manuscript, and drafted the figures presented in this chapter. CALJ and RB provided insightful input into the interpretations and the development of analytical methods and contributed excellent feedback when writing the final manuscript.

This manuscript is published in the journal *Tectonics:*

Redpath, D., Jackson, C. A. L. & Bell, R. E., 2022, Mechanical Stratigraphy Controls Normal Fault Growth and Dimensions, Outer Kwanza Basin, Offshore Angola. *Tectonics*, 41, e2021TC006823. *https://doi.org/10.1029/2021TC006823*

Mechanical Stratigraphy Controls Normal Fault Growth and Dimensions, Outer Kwanza Basin, Offshore Angola

David Redpath[1], Christopher A.-L Jackson[2], Rebecca E. Bell[1]

[1] Basins Research Group (BRG), Department of Earth Science & Engineering, Imperial College, Prince Consort Road, London, SW7 2BP, UK

[2] Department of Earth and Environmental Sciences, The University of Manchester, Oxford Road, Manchester, M13 9PL, UK

Abstract

Mechanical stratigraphy controls the growth patterns and dimensions of relatively small normal faults, yet how it influences the development of much larger structures remains unclear. Here we use 3D seismic reflection data from the Outer Kwanza Basin, offshore Angola to constrain the geometry and kinematics of several normal faults formed in a deep-water clastic succession. The faults are up to 6.3 km long and 1.9 km tall and have up to 44 m of throw. Aspect ratios and lower-tip throw gradients are greater for faults that terminate downwards at a c. 100 m thick, mass-transport complex (MTC) (up to 5.2 and 0.12) than for those that offset it (up to 2.7 and 0.01). Faults that offset the MTC invariably have >30 m of throw. Based on their geometric properties and throw patterns, we interpret that the faults nucleated above the MTC and propagated down toward it. Upon encountering this unit, which we infer behaved in a more ductile manner than encasing strata, tip propagation was halted until tip stresses were sufficiently high (corresponding to minimum throw of c. 30 m) to breach it. Faults with smaller throw were unable to breach the MTC. We argue that using only geometric criteria to determine fault growth patterns can mask the significant control mechanical stratigraphy has on fault kinematics. Mechanical stratigraphy is therefore a key control on the growth of large, seismic-scale normal faults, in a similar way to that observed for far smaller structures.

4.1 Introduction

Understanding the geometry and growth of normal faults is crucial for a range of geoscience disciplines. For example, these structures control landscape evolution and sediment transport pathways in areas of continental extension (e.g. Gibbs, 1984, Leeder and Gawthorpe, 1987, McClay, 1990, Gawthorpe and Hurst, 1993, Trudgill and Cartwright, 1994, Peacock and Sanderson, 1994, Eliet and Gawthorpe, 1995, Gawthorpe and Leeder, 2000, Childs et al., 2003), the magnitude and recurrence interval of potentially hazardous earthquakes (e.g. Cowie and Scholz, 1992b, Walsh et al., 2002, Soliva et al., 2008, Wilkinson et al., 2015), and the occurrence and viability of hydrocarbon and geothermal resources (e.g. Bodvarsson et al., 1982, Fairley and Hinds, 2004, Rotevatn et al., 2007, Athmer and Luthi, 2011, Corbel et al., 2012, Serié et al., 2017).

Fault growth models were originally derived from global compilations of throw (D) and length (L) data. More specifically, the recognition that D and L were positively correlated over several-orders-of-magnitude in the form $D = cL^n$, where c is a constant and n is between 1 and 1.5, led to the development of the so-called "propagating" fault model, in which faults grow via a broadly synchronous increase in their throw and length (e.g. Walsh and Watterson, 1988, Cartwright et al., 1995, Walsh et al., 2003, Nicol et al., 2005, Rotevatn et al., 2018, Nicol et al., 2020a). More recent observations, primarily from 3D seismic reflection data imaging sedimentary basins, support an alternative model for normal fault growth, the so-called "constant-length" fault model. In this model, faults rapidly establish their near-final length *before* accumulating significant throw (e.g. Walsh et al., 2002, Rotevatn et al., 2018). Rotevatn et al. (2018) also propose a hybrid growth model in which rapid fault lengthening by tip propagation, and ultimately segment linkage (characteristics most consistent with the propagating fault model) principally occurs during the initial 20-30% of the fault lifespan (Stage 1), with this period followed by a second, more prolonged period of throw accrual, during which time the fault does not significantly lengthen (characteristics more characteristic of the constant-length model; Stage 2).

Fault geometry and growth can be controlled by the so-called "mechanical stratigraphy" of the host rock, although this is not explicitly illustrated in global D-L datasets, which incorporate faults formed in a wide range of lithologies. The term "mechanical stratigraphy" encompasses: (i) the varying material properties of rock strata (e.g., measured properties such as compressive and tensile strengths, Young's modulus), (ii) the thicknesses of the mechanical layers, and (iii) the character and frictional properties of the transitions or boundaries between mechanical layers (e.g., sharp vs. gradational boundaries, and smooth vs. versus rugose contacts) (c.f. Groshong, 2006, Ferrill and Morris, 2008, Laubach et al., 2009, Ferrill et al., 2017). In this context, "strong", "stiff", or "competent" units (e.g., igneous rock, cemented sandstone or carbonate) tend to resist deformation, maintain bed length and thickness during deformation, accommodate little deformation before brittle failure, or have low ductility, whereas "weak", "soft", or "incompetent" strata (e.g., mudstone, salt) tend to deform relatively easily, change bed length and thickness during deformation, accommodate significant deformation before brittle failure or have high ductility (see Ferrill et al., 2017). Within this framework, the vertical and lateral propagation of faults that nucleate in "strong" layers can be impeded vertically and laterally as they approach, deform, and mechanically interact with "weak" layers, a situation common in heterogeneous sedimentary sequences. This behaviour can result in anomalous fault aspect ratios (i.e., the ratio between maximum fault height and length) and a deviation from the expected D-L relationship (Wilkins and Gross, 2002, Soliva and Benedicto, 2005, Soliva et al., 2005a). For example, a fault may preferentially propagate along-strike (i.e., laterally) in competent layers, thereby restricting its vertical height and increasing its aspect ratio, as well as restricting its ability to accumulate throw; such faults may thus appear "under-displaced". Short- and long-range stress interactions between salt bodies and faults (e.g., Tvedt et al., 2013b), and between neighbouring faults (e.g., Peacock and Sanderson, 1991, Dawers and Anders, 1995, Martel, 1999, Peacock, 2002, Soliva et al., 2006), can also influence fault growth and geometry. To-date, however, most studies have focused on the control of mechanical stratigraphy on the geometry and growth of relatively small normal faults

(i.e., throws of <1 m and <100 m long; e.g., Soliva and Benedicto (2005), Soliva et al. (2005a), Wilkins and Gross (2002), and it is not clear if and how this control might scale with increasing mechanical unit thickness and size.

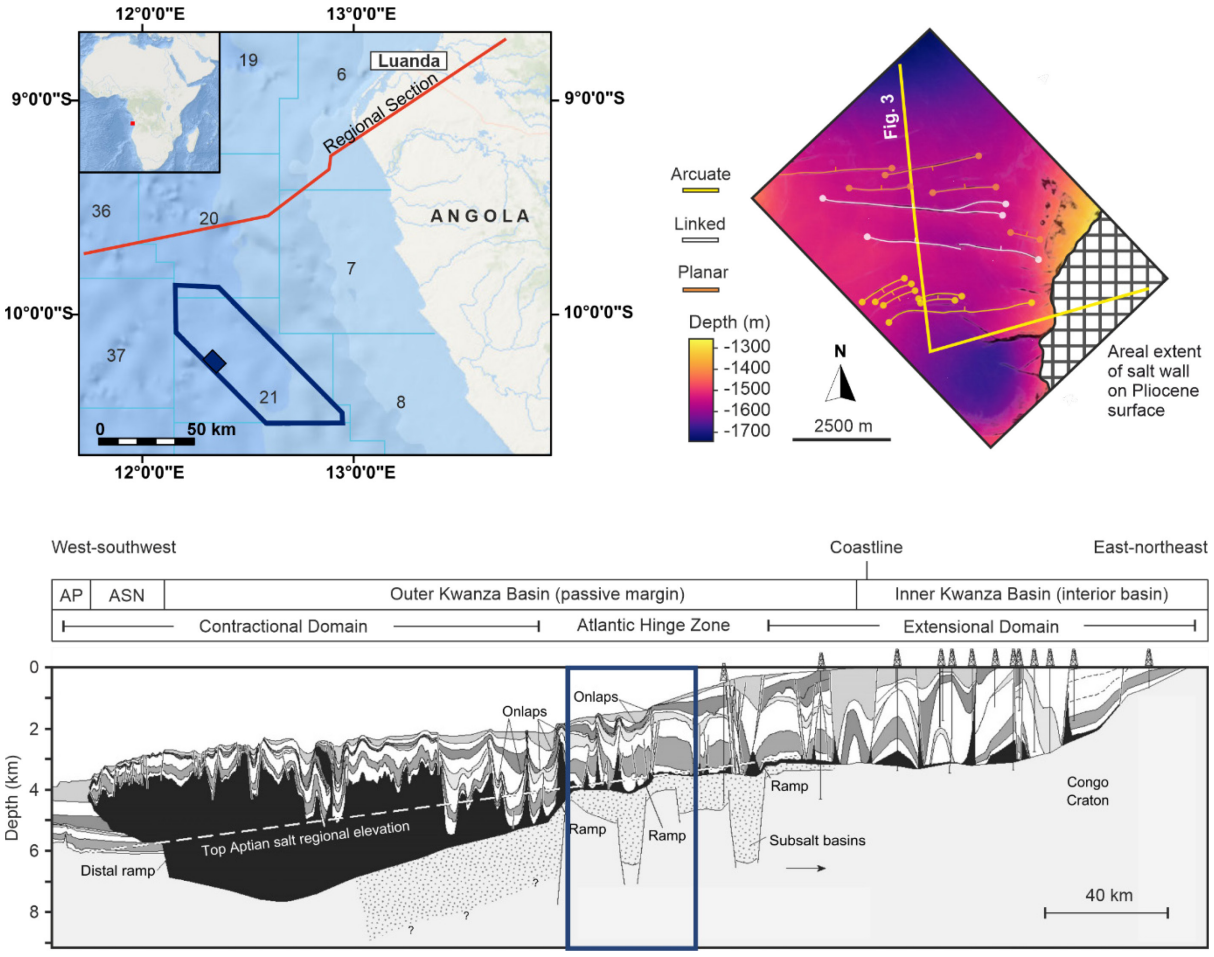


Figure 4.1. Study area and location | (Top left) A location map of the CGG 3D PDSM survey showing the 70 km2 study area and the regional section. (Top right) A Pliocene depth structure map highlighting the planform geometry of studied faults and showing the presence of the N-S trending salt wall and the minibasin on its western flank, which characterise our study area. (Bottom) A regional cross-section outlining the structure and location of our study area in the Outer Kwanza Basin on the Angolan passive margin.

In this study, we use high-quality 3D seismic reflection data acquired by Compagnie Générale de Géophysique (CGG) from the Outer Kwanza Basin, offshore Angola to quantify the geometry of and throw patterns on several normal faults (Fig. 4.1 and 4.2). These data allow us to assess how host rock mechanical properties, inferred from seismic facies analysis, influence fault growth and ultimate geometry, thereby allowing us to test fault growth models. These faults occur in a

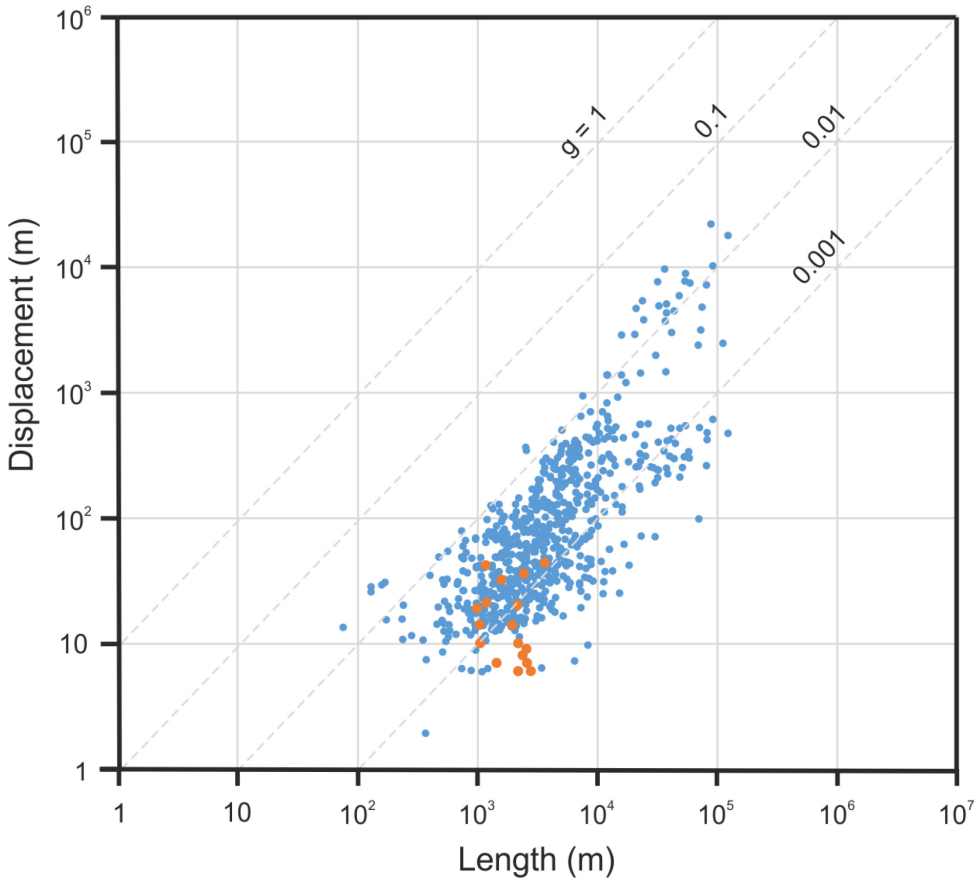


Figure 4.2. Global throw vs. length dataset | D-L data for extensional faults on a log-log plot extracted from global studies (blue): (Nicol et al., 1996, McLeod et al., 2000, Young et al., 2001, Nicol et al., 2005, Morley, 2007, Baudon and Cartwright, 2008a, Xu et al., 2011, Tvedt et al., 2013a, Whipp et al., 2014, Reeve et al., 2015, Duffy et al., 2015, Tvedt et al., 2016, Ghalayini et al., 2016, Reilly et al., 2016, Khalil and McClay, 2017, Morley, 2017, Worthington and Walsh, 2017, Torabi et al., 2019). The D-L fault data presented within this study are also shown (orange). Note that the D-L data sit within global D-L patterns and, that on this scale, adhere to scaling laws (i.e., $D = cL^n$), despite the data presented revealing deviations from D-L scaling relationships in their geometry and growth histories (see text for full discussion).

mudstone host rock, within which mechanical layering is imposed by a regionally developed mass-transport complex (MTC). We reveal marked differences in the geometry and kinematics of the faults and explore the role of host rock heterogeneity and local mechanical interactions on their growth patterns. We show that the aspect ratios and throw patterns vary on even closely spaced faults forming in the same host rock. We explore why faults can deviate from *D-L* scaling laws as they grow, even when they presently have *D-L* scaling relationships that broadly adhere to global compilations ($D = cL^n$; Fig. 4.2). Our study shows that *D-L* scaling (i.e., geometric) data alone does not allow us to determine the style of fault growth; detailed kinematic analysis using growth strata

(e.g., Childs et al., 2003, Tvedt et al., 2013b, Jackson and Rotevatn, 2013), and the analysis of faults of varying scales within a single population, together provide more robust kinematic constraints.

4.2 Data and Methods

4.2.1 Data

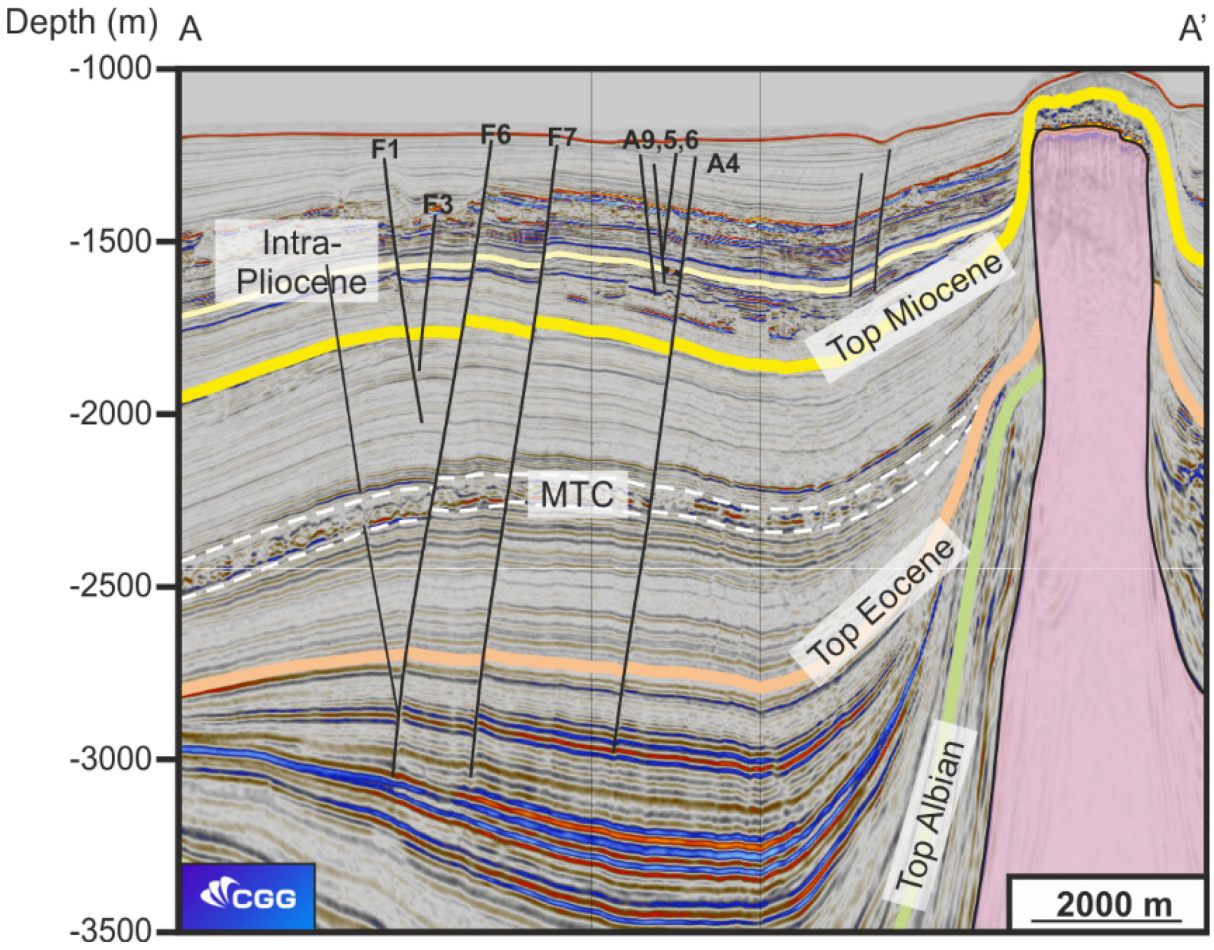


Figure 4.3. Seismic overview of the key components of the study area| A seismic overview of the structure and stratigraphy of the study area, highlighting the key stratigraphic and structural elements in this study. Data courtesy of CGG Multi-Client

The study area is imaged by a high-quality, pre-stack, depth-migrated (PDSM) 3D survey with an aerial extent of 2915 km^2 (Fig. 4.1). The inline and crossline spacing for the survey is 25 m, with a vertical sampling interval of 2 m. The data are normal polarity (a peak indicates a downward increase in acoustic impedance) and zero phase, with a vertical resolution of c. 6 m at the seabed and c. 30 m at a depth of 3.5 km, approximated by a quarter of the dominant wavelength of the

data (assuming average P-wave velocity of 2500 m/s) (see discussion by Evans and Jackson, 2019). In the absence of well-data, the lithology and absolute ages of the mapped seismic-stratigraphic units are constrained by using seismic facies analysis, seismic-stratigraphic principles, and by correlating their bounding horizons with three regionally mapped horizons (the Top Albian, Top Eocene and Top Miocene) presented by Hudec and Jackson (2004) (See also Spathopoulos, 1996, Marton et al., 2000, Hudec and Jackson, 2003, Hudec and Jackson, 2004, Jackson et al., 2005, Jackson and Hudec, 2008, Serié et al., 2017). The ages of other mapped horizons are inferred relative to these regional surfaces and documented geological events (e.g. periods of continental uplift and related salt tectonics). We use these age estimates to infer at which stratigraphic levels fault throw maxima occur, which may relate to the depth at which the faults nucleated (e.g. Hongxing and Anderson, 2007).

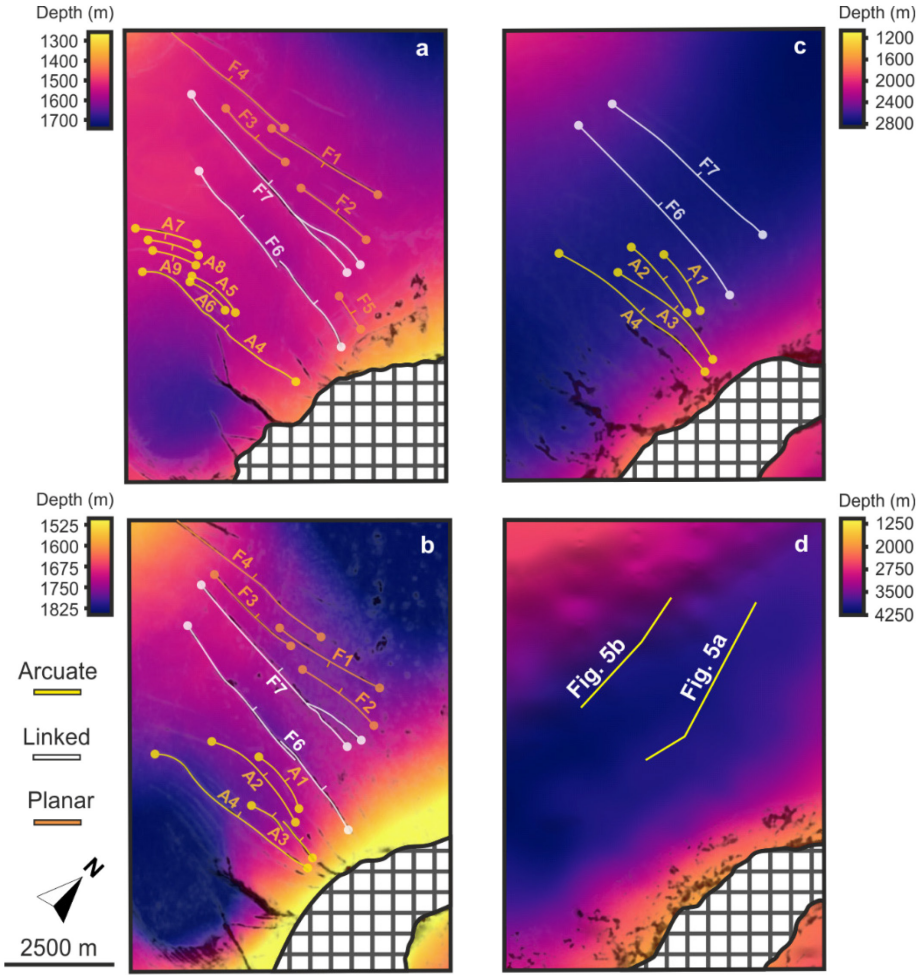


Figure 4.4. Depth structure maps (a-d) Depth structure maps of the Intra-Pliocene, Top Miocene, Top Eocene and Top Albian surfaces, respectively. The temporal and spatial presence of each of the studied faults is also highlighted on each of the structure maps. The Top Albian surface is not offset by any of the faults and shows the locations for seismic sections 4.5a and 4.5b in figure 4.5.

4.2.2 Seismic interpretation and fault characterisation

We study a c. 70 km2 area that is located between a c. 10 km elongate ridge of salt (i.e., salt wall) and a sub-circular dome of salt that has pierced the overlying strata (i.e., salt stock), the latter only being partially imaged along the western edge of the seismic survey (Fig. 4.1 and 4.3). Within this area we focus on sixteen, exceptionally well-imaged normal faults that form part of a larger array (Fig. 4.4 and 4.5).

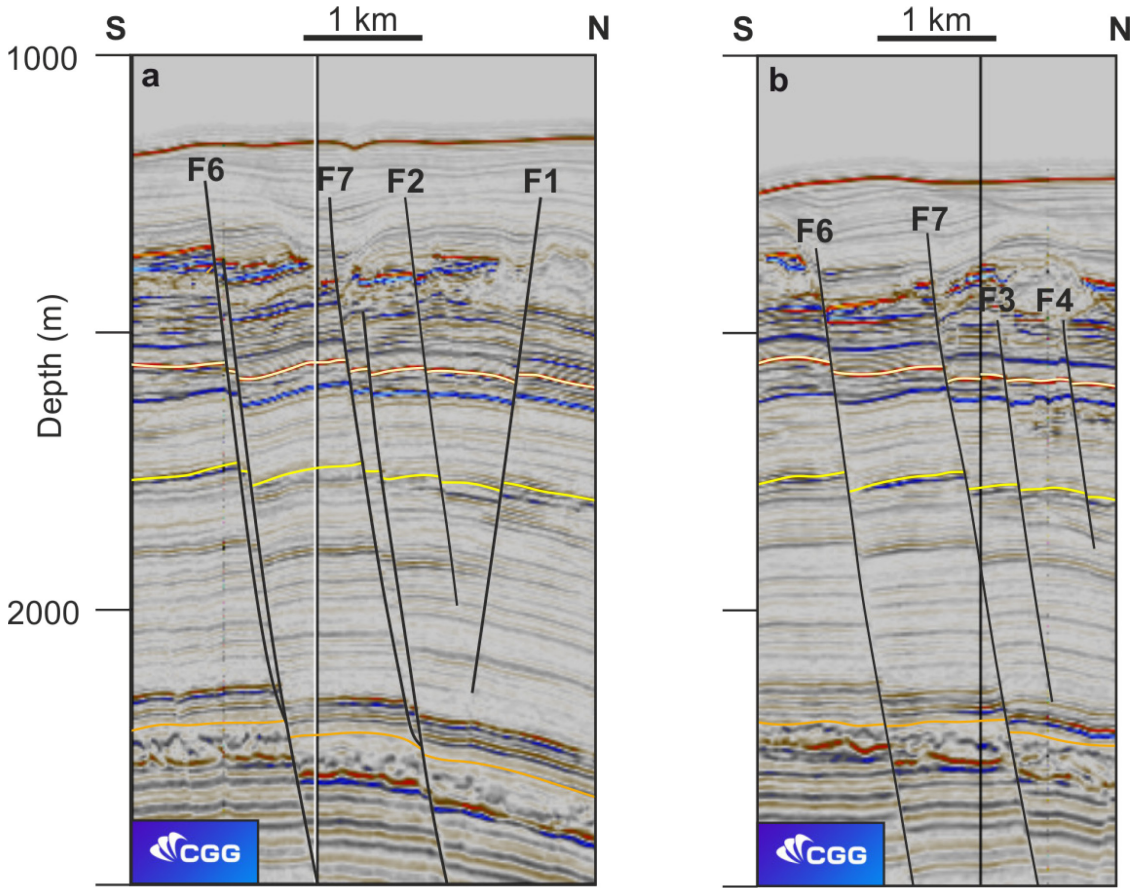


Figure 4.5. Seismic cross-section of planar and bifurcating fault groups | (a) Seismic-cross section of the planar (F1-4) and bifurcating (F6-7) fault groups, specifically showing the down-dip linkage in the bifurcating group (F6-7). (b) Seismic cross-section of planar (F1-4) and bifurcated (F6-7) fault groups. In addition, each section shows their fault dip and interaction with each of the key Intra-Pliocene, Top Miocene and Top MTC surfaces, shown with depth respectively. Here, the bifurcated faults show bifurcating upward fault segments with narrow relay zones and offset the Top MTC horizon. Data courtesy of CGG Multi-Client.

These faults are also selected because we can comprehensively map numerous (18) horizons in their flanking host rocks and, therefore, generate 3D throw strike-projections that allow us to

constrain throw distributions across their surfaces (e.g. Walsh et al., 2003, Baudon and Cartwright, 2008a, Duffy et al., 2015). We accurately mapped the faults on closely spaced (*c.* 50 m) seismic sections trending normal to fault strike. We therefore constrain their three-dimensional geometry, including their aspect ratio (i.e. length/down-dip height), with reasonable precision (Fig. 4.6) (Nicol et al., 1996, Polit et al., 2009). Where fault-related folding of the host rock is present adjacent to the fault surfaces, the cut-offs are extrapolated to remove the effects of this ductile or continuous deformation (e.g. Walsh and Watterson, 1987, Hongxing and Anderson, 2007, Jackson et al., 2017).

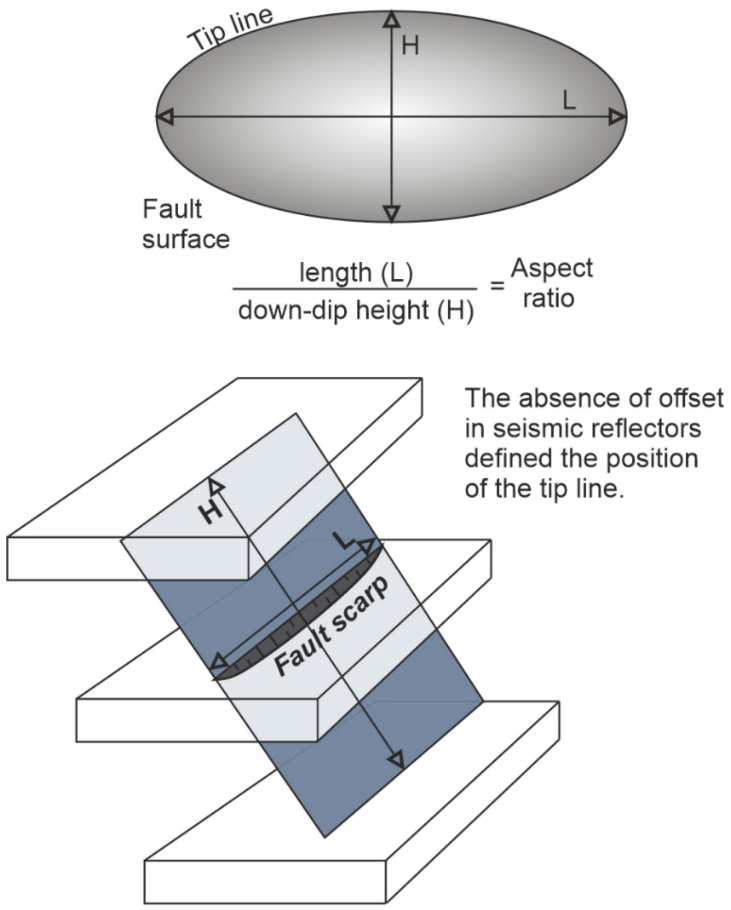


Figure 4.6. Fault aspect ratio terminology | A schematic diagram giving an overview of fault terminology; including the defined terms for calculating aspect ratio (top) and determining the geometry of a fault (bottom).

Shallow stratigraphy (*c.* 0-300 m below seabed) in the study area contains deep-water channels that incise up to 200 m into underlying stratigraphy (Fig. 4.7). This makes it difficult to confidently and regionally map near-seabed growth sequences that are now eroded (i.e., F6 and 7) (Fig. 4.7).

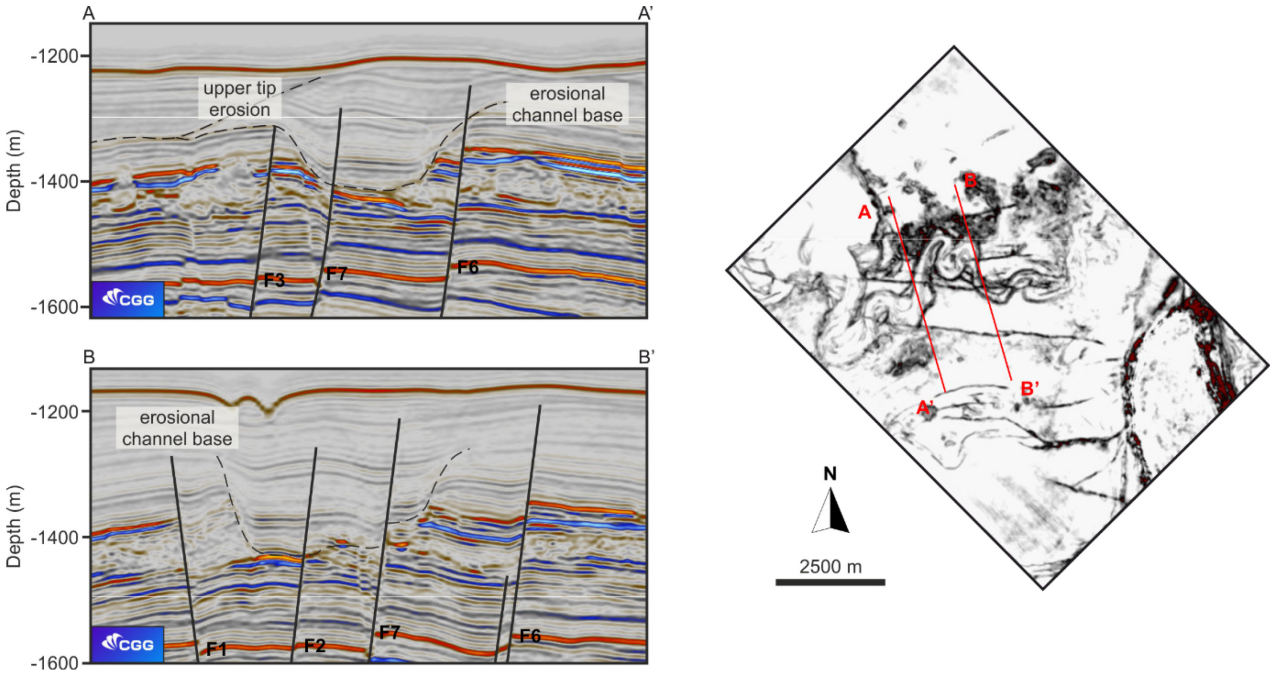


Figure 4.7. Channels eroding upper fault tips| (Right) A variance extraction (−1400 m) of meandering channels. (Left) Seismic sections of the erosional channels observed in the variance extraction within the shallow stratigraphy of the area (c. 200–250 m below seabed). The erosional bases of these channels erode the upper tips of faults (e.g., F3). In the case where upper fault tips offset the channel deposits (e.g., F4, F6, and F7), it is likely any previous growth packages of near-seabed growth have been eroded. Data courtesy of CGG Multi-Client.

Since many of the faults in the study area have shallow upper tips, where extensive channel-driven erosion occurs at the top of the fault (i.e., F3), it may be the case that aspect ratios become slightly higher than the original fault geometry (Fig. 4.6). We follow the method of Walsh and Watterson (1991) to construct throw-distance (T-x) plots that show how throw varies along-strike on a given horizon, as well as strike-projections that show the throw distribution across the fault surface (e.g. Fig. 4.8) (Tvedt et al., 2013b, Duffy et al., 2015, Collanega et al., 2018, Torabi et al., 2019). We also calculate throw gradients (i.e. change in throw/distance on fault surface over which the change occurs) across the fault surface, noting that relatively high gradients (> 0.15) may reflect retardation of fault tip propagation due to mechanical interactions with adjacent faults or host rock layers (e.g. Walsh and Watterson, 1988, Nicol et al., 1996). To determine where faults intersected the free surface during their growth, we calculate the expansion indices (EI) of packages of growth strata. EI is calculated by dividing the hanging-wall thickness of the package by its adjacent footwall

thickness (e.g. Tvedt et al., 2013b, Jackson et al., 2017). Finally, we define down-dip fault height (H) as the (sub)vertical distance from the fault upper to lower tip, and fault length (L) as the maximum (sub)horizontal distance between the fault's lateral tips (Fig. 4.6). Using these geometric data we determine fault aspect ratio (fault length/down-dip height of fault), which again can be used to infer whether the growth of a fault has been inhibited by mechanical interactions with adjacent faults or changes in host rock mechanical properties (Nicol et al., 1996, Soliva et al., 2005b).

4.3 Geological Setting

4.3.1 Outer Kwanza Basin

The formation of the Inner and Outer Kwanza basins, offshore Angola initiated in the Early Cretaceous when rift pulses between the African and South American plates, and ultimately the breakup of Gondwana, resulted in the opening of the South Atlantic Ocean (Brice et al., 1982, Jackson et al., 2005, Hudec and Jackson, 2004) (Fig. 4.1).

During the Early Cretaceous, intermittent marine incursions resulted in restricted marine conditions and the deposition of thick, Aptian-Albian evaporites in the Inner and Outer Kwanza basins (e.g. Bate et al., 2001, Karner and Gambôa, 2007). Flow of this evaporite sequence from the Late Cretaceous until present controlled the overall, post-breakup structural evolution of the Kwanza Basins (Marton et al., 2000, Hudec and Jackson, 2004, Jackson and Hudec, 2008). For example, basinward tilting of the margin during the Late Cretaceous initiated the first post-salt phase of extension, causing the formation of predominantly seaward-dipping, salt-detached normal faults (Jackson et al., 2005). Post-salt deposition was initially dominated by relatively fine-grained deep-water sediments of the Iabe Group (Hudec and Jackson, 2003, Hudec and Jackson, 2004, Jackson and Hudec, 2008, Serié et al., 2017).

The second phase of significant post-salt extension occurred during the Neogene, triggered by onshore cratonic uplift (Jackson et al., 2005, Hudec and Jackson, 2004). Basement-involved uplift

of the continental shelf and upper slope in the Miocene resulted in an increase in the rate of seaward translation of the salt and its overburden, from *c.* 0.2 to 1 mm/yr (Jackson and Hudec, 2008, Jackson et al., 2005, Hudec and Jackson, 2004, Evans and Jackson, 2019). This resulted in a further 20 km of extension in the Outer Kwanza Basin (Hudec and Jackson, 2003, Jackson and Hudec, 2008, Evans and Jackson, 2019). This regional extension may have driven the faulting studied here, although local extensional stresses triggered by coeval diapir rise and minibasin subsidence may also have played a role. Since the Miocene, sedimentation in the Outer Kwanza Basin has been dominated by hemipelagic clays and silts, with coarser-grained sediments being deposited in the basin in turbidite-fed channels and lobes (Serié et al., 2017, Howlett et al., 2020). Seismically chaotic, sharp-based, low-amplitude bodies of unknown composition are also observed in the post-Miocene sedimentary sequence; these are geophysically distinct from the fine- and coarse-grained slope deposits described above, which are typically characterised by moderate-to-high amplitude, continuous seismic reflections (Fig. 4.3) (see Serié et al., 2017, Howlett et al., 2020). Based on these seismic expressions and the deep-water depositional setting, we suggest that these bodies represent mass-transport complexes (MTCs) (Moscardelli and Wood, 2008, Wu et al., 2019). We lack borehole data to constrain their lithology, but we tentatively suggest that they may be mudstone-dominated, based on the fact that the post-Miocene slope of Angola comprise very fine-grained rock types (e.g., Fraser et al., 2005).

4.4 Results

The normal fault array studied here sits within the axis of a N-trending minibasin (Fig. 4.3 and 4.4). The largest faults dip to the north and offset Cenozoic stratigraphy (Fig. 4.3 and 4.4). The D-L data for the faults broadly fit within global D-L trend, sitting in the lower part of the dataset (Fig. 4.2). Within the fault array we can define three distinct fault groups based on their geometrical characteristics and inferred kinematic behaviour.

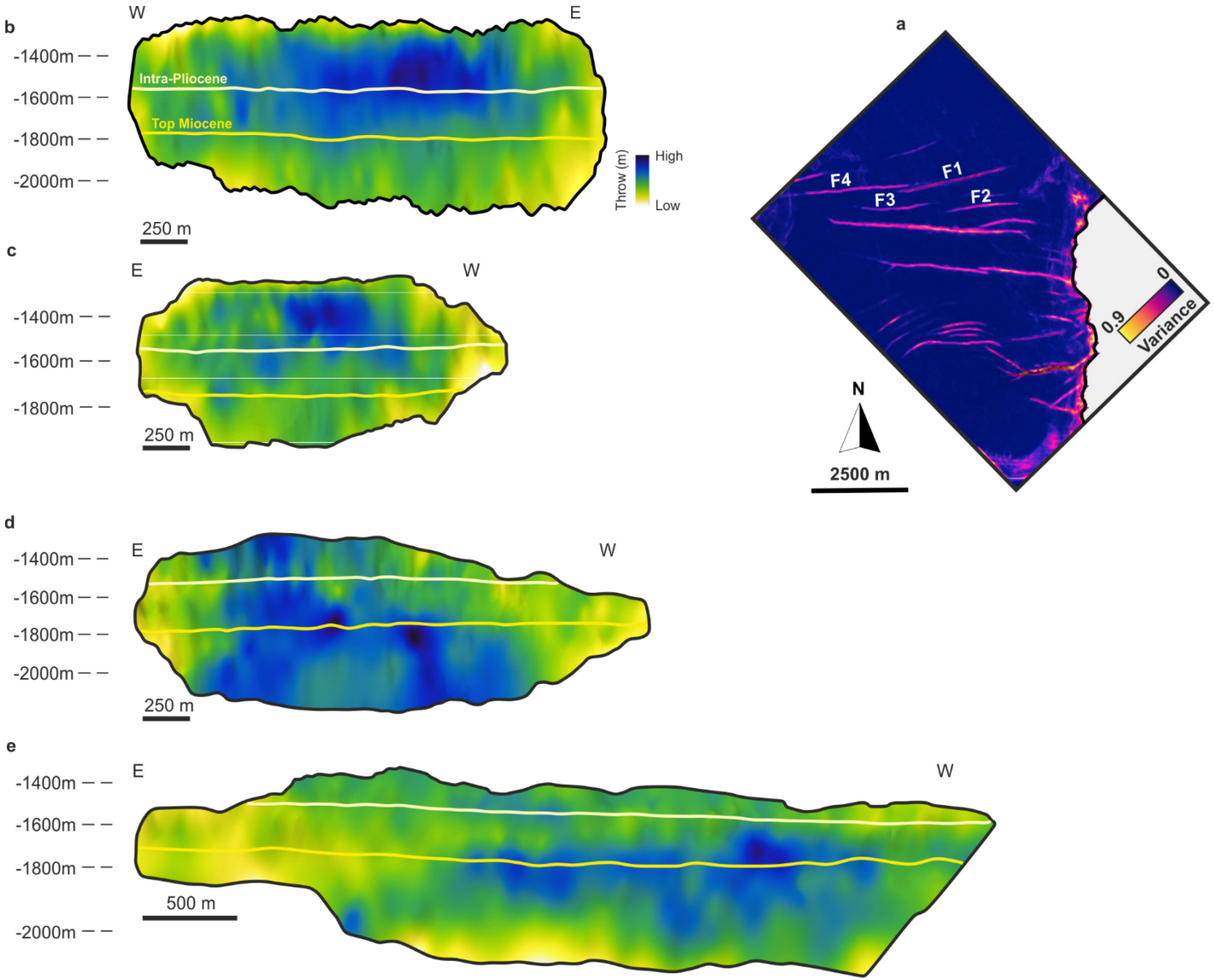


Figure 4.8. 3-D strike projections of the planar fault group| (a) A variance extraction of the Intra-Pliocene surface and the locations of F1-4. (b-e) Strike projections for F1-4, respectively. They display the geometry of, and throw distribution on, the fault surfaces with the Intra-Pliocene and Top Miocene surfaces, respectively with depth. Unrestricted faults (F1-2; b-c) display throw maxima in Pliocene stratigraphy which decrease towards their tips. Restricted faults (F3-4; d-e) display throw maxima positioned towards their lower tips in Miocene stratigraphy. The aspect ratios for F1-2 (b-c) are 0.01 and are 0.12 and 0.11 for F3-4 (d-e), respectively. The aspect ratios for F1-2 are 2.7, while F3 and F4 have greater aspect ratios of 3.7 and 5.2, respectively.

4.4.1 Planar faults (F1-F5)

4.4.1.1 Observations

Planar faults are developed in the north of the study area, striking E-W and dipping 54-58° (Fig. 4.4 and 4.5). Striking orthogonal to the trend of adjacent salt wall, all of the faults dip northwards, with the exception of a single antithetic fault that dips southward (F1). The faults are 750–950 m tall and have maximum trace lengths of 1.8–4 km (Fig. 4.9). The maximum throw in this group is ~ 20 m, with the throw maxima occurring in Pliocene stratigraphy (Fig. 4.8 and 4.10). The upper tips of the planar faults are in Pliocene stratigraphy and their lower tips are located in Miocene stratigraphy (Fig. 4.5). F1 and F2 are quasi-elliptical, whereas F3 and F4 are elliptical (Fig. 4.8b - e). The throw maxima for F1 and F2 are located near their centres, with throw ultimately decreasing towards their tips (Fig. 4.8b and c).

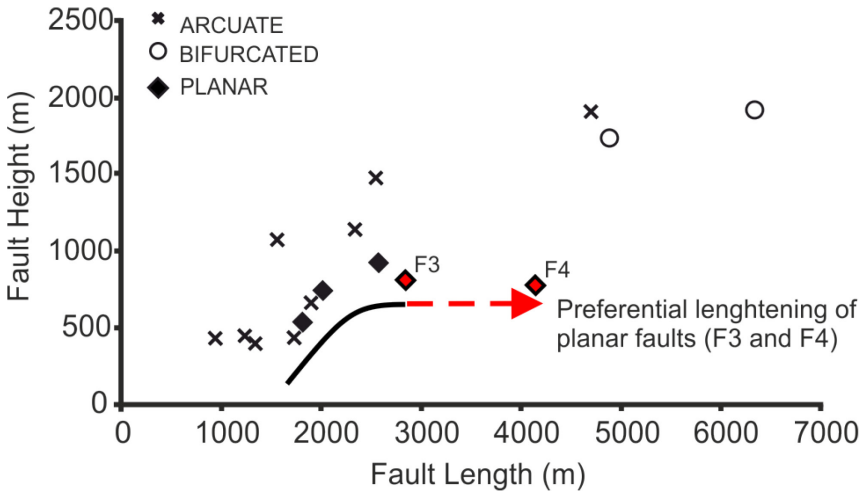


Figure 4.9. Fault height vs. length plot | Fault height - length data for all fault groups within the studied array. Overall, a trend is observed of fault height increasing proportionally with fault length. However, faults which tip out down dip at the Top MTC surface and have high aspect ratios (F3-4) show increasing fault length without a proportional increase in fault height (red), as predicted for vertically restricted faults (Fig. 14.2).

In contrast, throw maxima for F3 and F4 are slightly offset towards their lower halves (Fig. 4.8d and e). This difference in the position of throw maxima is reflected in the lower tip throw gradients. F1 and F2 show a relatively low throw gradient of 0.01, whereas F3 and F4 display throw gradients that are an order of magnitude greater (i.e. 0.12 and 0.11, respectively). The aspect ratio for planar faults with a throw maximum occurring along the Top Miocene horizon (i.e., F3 and F4) ranges

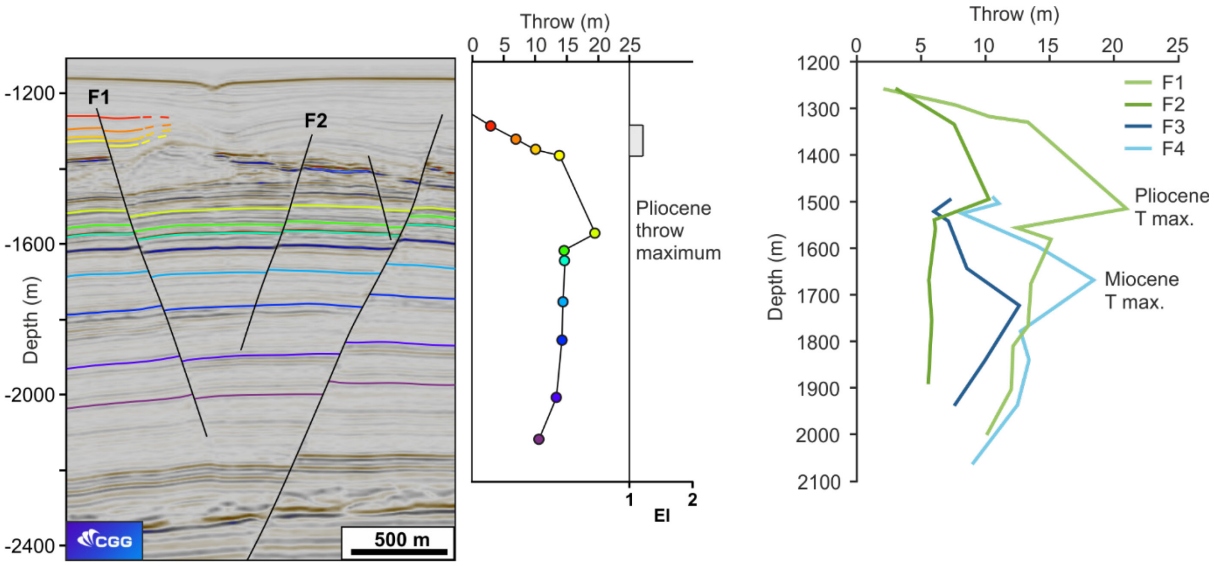


Figure 4.10. Throw-depth plots for the planar fault group| A seismic section of the position of unrestricted faults (F1-2) within the stratigraphy. Their lower tips do not interact with the MTC layer. A t-z plot for F1 where the EI on the upper tip is c. 1.2 (left). T-z plots (F1-4) showing that restricted faults exhibit throw maxima in Miocene stratigraphy and unrestricted faults exhibit throw maxima in Pliocene stratigraphy (right). Data courtesy of CGG Multi-Client.

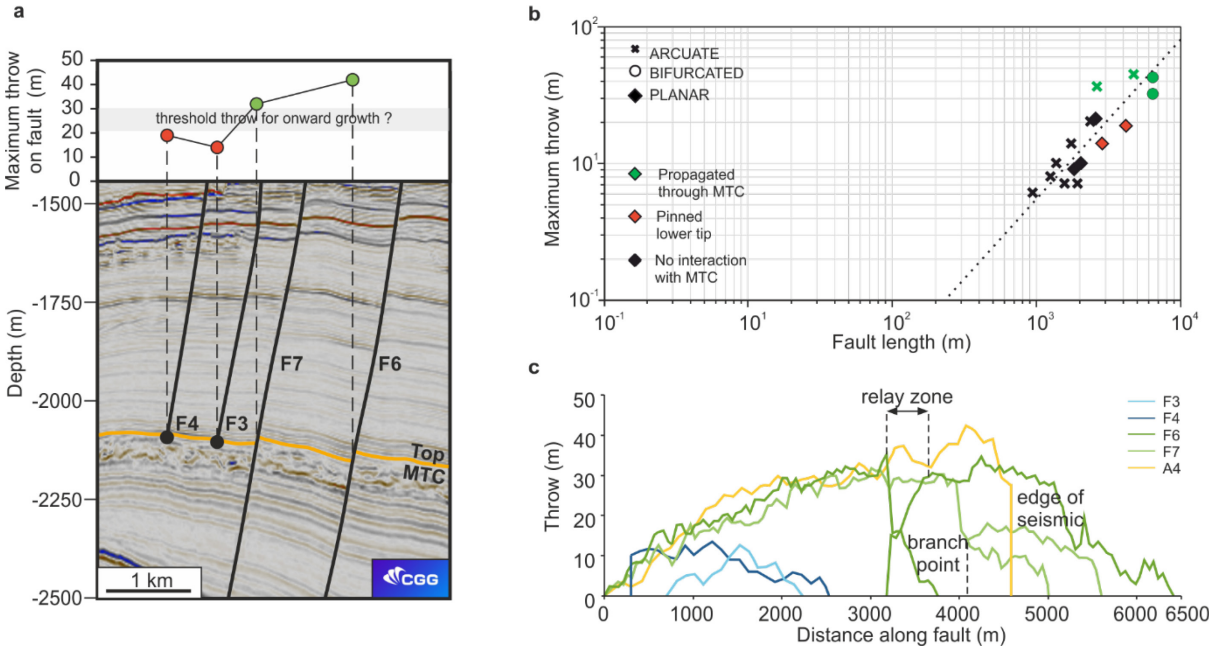


Figure 4.11. Mechanical interactions with a mass-transport complex deposit| (a) A seismic cross-section showing the tips of F3-4 tipping out downdip on top of the MTC surface and the adjacent bifurcating faults (F6-7) offsetting the Top MTC surface. Above, the maximum throw of the respective faults are displayed and the proposed accumulated strain needed to overcome the threshold for onward growth through the MTC (grey box). (b) Throw-length data for the fault array displaying that faults with maximum throws > 30 m offset the MTC, while faults with throw values < 30 m which interact with the MTC are vertically restricted. T-x regression analysis for the array's data also suggests the constant length model for fault growth [i.e. T>0 where L=0]. (c) T-x plots for faults restricted by the MTC (F2-3) and some which achieve onward propagation (F6-7, A4). Data courtesy of CGG Multi-Client.

from 3.5-5.2, whereas the ratio for those with a throw maximum in shallower, Pliocene stratigraphy is 2.7 (F1 and 2) (Fig. 4.8 and 4.10). The lower tips of faults that exhibit relatively high aspect ratios (> 3.5), and which have maximum throws of < 20 m, are located at the top of a laterally extensive, seismically chaotic unit that we interpret as an MTC (F3 and F4; Fig. 4.11 a) (Moscardelli and Wood, 2008).

Only F1, which has the largest throw and shallowest upper tip of all the planar faults, is associated with growth strata. In this case, Pliocene growth strata have an EI of 1.2 (Fig. 4.10). Stratigraphic packages adjacent to all of the other faults in the planar fault group have EI <1.1 making it difficult to determine if these structures were ever growth faults that breached the free surface, or whether they grew as so-called 'blind' structures (e.g. Baudon and Cartwright, 2008a, Jackson et al., 2017).

4.4.1.2 Interpretation

Their quasi-elliptical geometry, relatively low aspect ratio, and concentric throw distribution suggest F1 and F2 grew as mechanically unrestricted structures (cf. F3 and F4 below; see also Fig. 4.8) (Nicol et al., 1996). Fig. 4.11a shows that the lower tips of F3 and F4 coincide with the MTC. Furthermore, these faults have aspect ratios greater than those of F1 and F2. Given that these relatively closely spaced faults formed in similar host rock in response to broadly similar driving stresses, one plausible interpretation for the greater aspect ratios of F3 and F4 is that their basal tips mechanically interacted with the MTC near the base of the faulted sequence. This could have resulted in their tips being pinned, inducing the preferential lengthening of these faults and thus giving rise to the development of relatively high aspect ratios (Fig. 4.9; 4.11a and 4.12). This interpretation is supported by the observation that the throw maxima for F3 and F4 are slightly offset towards their lower tips, and that lower-tip throw gradients are higher for these faults than F1 and F2 (Fig. 4.8d and e). These geometrical characteristics are consistent with enhanced strain accumulation in these areas as a function of vertical tip restriction during fault propagation (Fig. 4.8 and 4.12) (Wilkins and Gross, 2002).

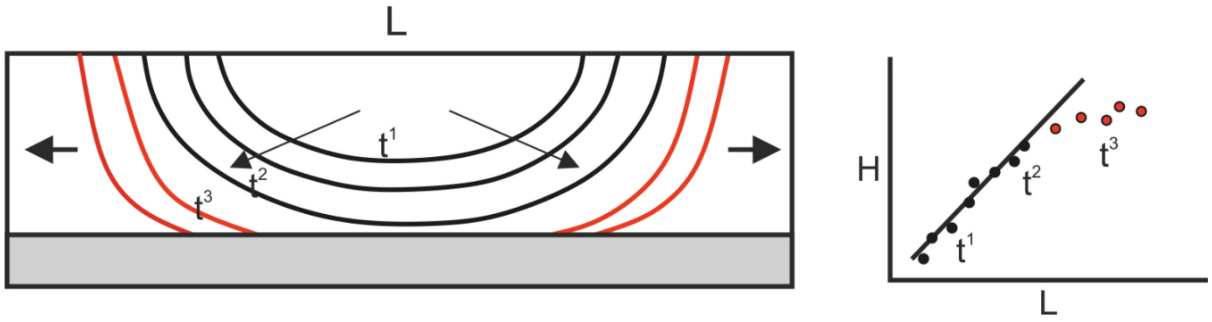


Figure 4.12. Mechanical stratigraphy and preferential lengthening| A schematic diagram portraying the effects of vertical restriction by a mechanical layer (MTC) during fault growth, and its effect on fault geometrical data as a result of growth with preferential lengthening. Modified from Soliva and Benedicto (2005).

4.4.2 Bifurcating faults (F6-F7)

4.4.2.1 Observations

These faults are the longest in the studied array (> 5 km). They are characterised by a single fault segment at depth and two segments within shallower stratigraphy (F6 and F7; Fig. 4.4; 4.5 and 4.13). Bifurcating faults (F6 and F7) strike WNW-ESE and dip 54-60° northward (Fig. 4.4 and 4.5). The bifurcating faults contrast with the planar faults in two key ways; (i) they have larger throws (> 30 m; Fig. 4.11); and (ii) their basal tips lie beneath rather than above the MTC (Fig. 4.3 and 4.13).

F7 bifurcates upwards with a sub-horizontal, c. 1.2 km long branchline coinciding with the top of the MTC (Fig. 4.4; 4.5 and 4.13b). Maximum throw on F7 (c. 32 m) is also located near the top of the MTC and the throw gradient below the MTC is relatively low (0.08; Fig. 4.13b). The maximum down-dip height and trace length of F7 are 1.75 km and 6.4 km respectively, resulting in an aspect ratio of 3.6 (Fig. 4.9 and 4.13b). At the structural level of the Pliocene, F6 consists of two parallel, overlapping fault segments separated by a narrow (~70 m) relay zone (Fig. 4.4 and 5). At depth these segments link and form a single fault surface (Fig. 4.4c; 4.5 and 4.13a). Similar to F7, the c. 1 km long, sub-horizontal branchline for the two upper segments of F6 coincides with the top of the MTC (Fig. 4.13a). In contrast to F7, the throw maximum for F6 occurs beneath (rather than above) the MTC, within Oligocene-Miocene stratigraphy (Fig. 4.13a).

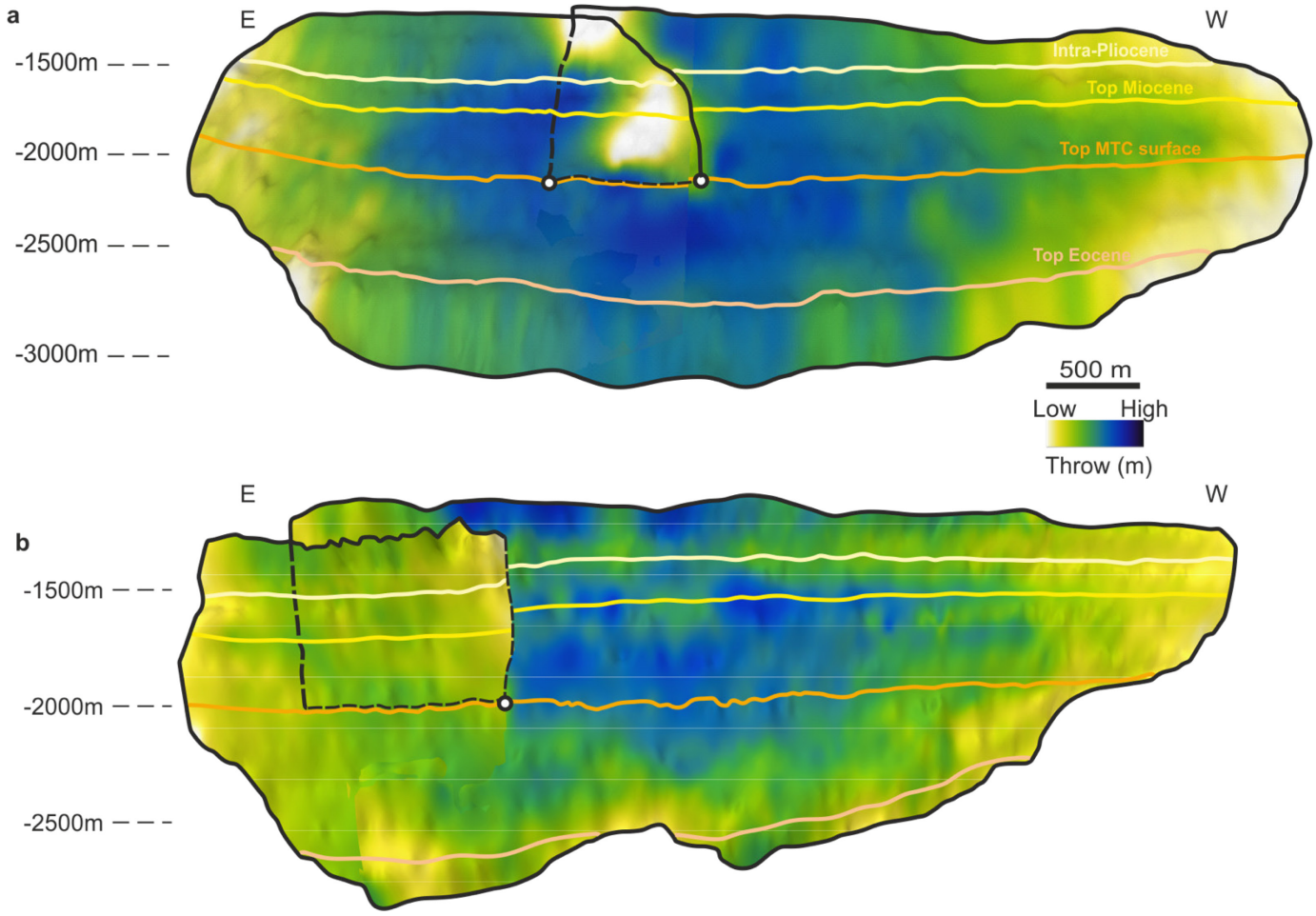


Figure 4.13. 3-D strike projections for the bifurcating fault group| 3-D strike projections for the bifurcating faults (F6 and F7) displaying their geometry and the throw distribution on their fault surfaces, showing the Intra-Pliocene, Top Miocene, Top MTC and Top Eocene surfaces, respectively with depth. (a) F6: Maximum throw lies beneath the Top MTC surface and relay branchline (blue area). Overall, greater throw values encircle the relay zone which is associated with a throw minimum (white area). High throw gradients (c. 0.2) are present at the transition from the fault surface to the relay zone (sharp transition from blue to white area). (b) F7: Maximum throw lies coincident with the Top MTC surface on the main fault surface. Overall, greater throw values are present along strike at the structural level of the Top MTC surface.

The distribution of throw on F6 defines a broad, U-shaped (depth) throw maximum that encircles the relay zone and its associated throw minimum, and which extends below the MTC and beneath the branchline (blue area; Fig. 4.13a). Relatively high throw gradients of up to c. 0.2 occur in the relay zone where the faults overlap (sharp transition from blue to white; Fig. 4.13a). F6 has a maximum down-dip height and length of 1.9 km and 6.3 km, respectively, resulting in an aspect ratio of 3.3.

4.4.2.2 Interpretation

The position of the maximum throw on F7 at the top of the MTC suggests the fault: (i) nucleated at this structural level; and/or (ii) nucleated elsewhere, possibly within the shallower stratigraphy, with the position of maximum throw migrating downwards with time. Irrespective of where the fault nucleated, it was able to propagate through the MTC (Fig. 4.13b). This observation, coupled with the distinct decrease in throw and throw gradient immediately below the MTC, suggest that the MTC may have initially retarded downward or upward propagation of F7, causing strain to accumulate along the top of the MTC before the fault could propagate onward (Fig. 4.13b and 4.14a). We therefore suggest that in a similar way to F3 and F4, the tips of smaller, precursor segments were initially vertically restricted along the top of the MTC (Fig. 4.14a). However, unlike in the case of F3 and F4, the accumulation of additional throw meant tip stresses around F7 became high enough to allow the fault to breach the MTC (Fig. 4.14a) (Wilkins and Gross, 2002).

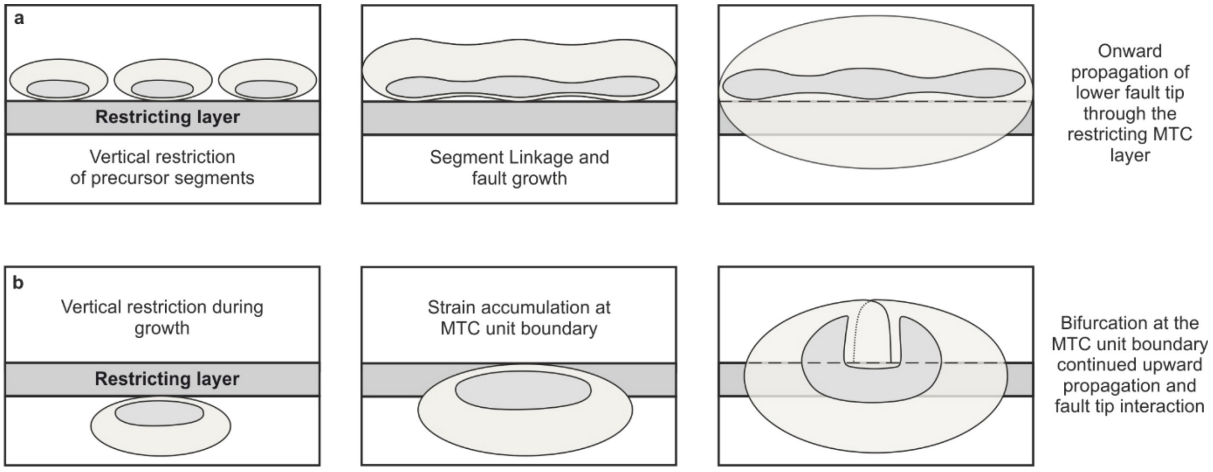


Figure 4.14. Strain accumulation overcoming vertically restricting layer | Sketch diagrams of proposed growth histories for bifurcating faults. (a) F7: Individual precursor fault segments become vertically restricted by the regionally extensive MTC during downward propagation. As a result of this restriction precursor faults preferentially lengthen via segment linkage and the throw maxima migrate downwards as strain accumulation occurs at the restricted tip. Eventual strain accumulation overcomes the MTC restricting influence and continues downward propagation. (b) F6: Similarly, to F7, an initial vertical restriction results in strain accumulation and throw maxima migration towards the MTC. Following overcoming the MTC's restricting influence, bifurcation at the MTC boundary occurs.

In contrast to F7, we suggest F6 nucleated below (rather than above) the MTC based on the fact that maximum throw on the structure occurs at least partly below the MTC (Fig. 4.13a). Having

nucleated below the MTC, F6 was then able to propagate upwards towards and ultimately through the MTC, locally bifurcating as it did (Fig. 4.14b). The throw distribution presently observed on F6 is consistent with numerically modelled throw distributions where a bifurcating planar frontal segment is present (Fig. 4.13a) (Soliva et al., 2008). We therefore suggest that the high throw values broadly encircling the relay zone, which is also associated with relatively high throw gradients (0.2), are as a result of tip interaction between the overlapping shallow segments during bifurcation and upward growth (Fig. 4.13a and 4.14b) (Nicol et al., 1996, Soliva et al., 2008, Nicol et al., 2017).

4.4.3 Arcuate faults (A1-A9)

4.4.3.1 Observations

The group is characterised by faults defined by smooth, along-strike changes in their orientation, resulting in a bow-shaped, convex trace in map-view (Fig. 4.4). This group of faults are concentrated in the south of the study area, on the northern rim of a locally deep part of the minibasin on the west of the salt wall; this deep area is best expressed at the Pliocene and Miocene structural level (Fig. 4.4a and b, respectively). Close to the salt wall these faults strike E-W, perpendicular to the salt-sediment interface, changing to a NE-SW strike ≥ 2 km away from the salt wall; this change in strike defines their plan-view geometry, with the faults following the overall shape of the deep part of the minibasin (Fig. 4.4a and b). Maximum throws on arcuate faults decrease with increasing distance from the salt wall; for example, A4 has a maximum throw of 44 m, whereas A9 has a maximum throw of ~10 m at 0.8 km and 3.5 km distance from the salt wall, respectively (Fig. 4.15a; see also Fig. 4.4a and b). We also note that arcuate faults appear overdisplaced, achieving similar maximum throws at only 60-70% of the strike length of other fault types (Fig. 4.15b). For example, A3 is 2.6 km long and has c. 35 m maximum throw, whereas F6 has comparable throw (c. 38 m) but is significantly longer (6.3 km) (Fig. 4.15b). Arcuate faults

also have notably lower aspect ratios (i.e., 1.4-2.7) compared to the linked and planar faults (i.e., 2.7-5.2) (Fig. 4.9).

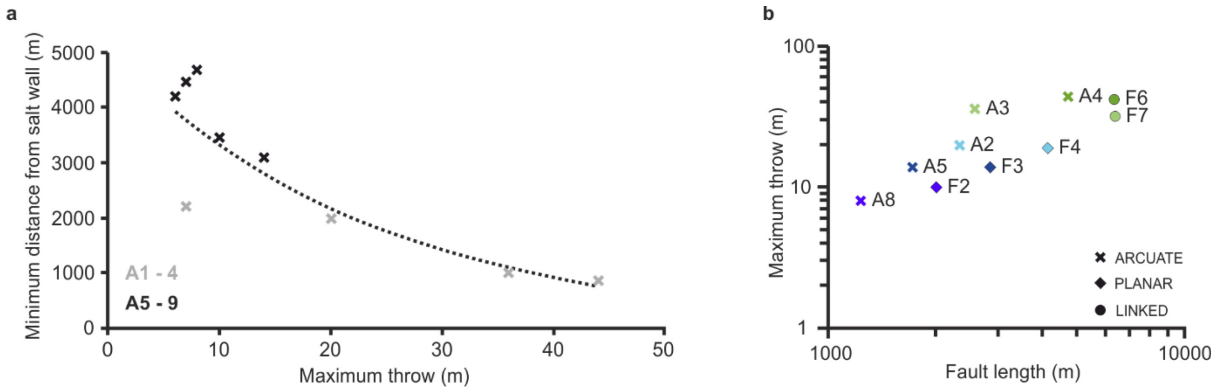


Figure 4.15. Salt bodies influence fault geometry and throw| (a) A plot showing the relationship between the maximum throw on arcuate faults and their distance from the salt wall. In this fault group, the maximum throw observed on faults increases as the faults become more proximal to the salt wall. The deeper arcuate subgroup (A1-4) exhibits greater throws than the shallower (A5-9) subgroup. (b) A comparative plot of throw - length data between arcuate faults and that of other groups which exhibit similar maximum throw values. This plot highlights that, in comparison to other fault groups, arcuate faults are overdisplaced.

We can sub-divide the arcuate fault group based on the depth at which they occur, the detailed fault geometry, and the overall throw distribution. The first subgroup faults strike broadly E-W (i.e., similar to the overall trend of the fault array) and are present at greater depths (i.e., below -1900 m) than the second subgroup (A1-4; Fig. 4.4a - c). They exhibit down-dip heights of 1–1.9 km and maximum lengths of 1.5–4.7 km, yielding aspect ratios of 1.4 – 2.4 (Fig. 4.9). The largest faults in this subgroup, A3 and A4, have maximum throw values of 36 and 44 m, respectively, and offset the MTC, whereas those with throws < 30 m do not (Fig. 4.11b and c; and Fig. 4.15). The second subgroup occurs at a shallower depth, in post-Miocene stratigraphy (A5-9; Fig. 4.3 and 4.4a). The upper tips of faults in this subgroup are located just 100 m beneath the seabed and they typically tip out ~150 m above the Top Miocene horizon (Fig. 4.16). Four faults in this subgroup dip towards the south, towards the centre of the deep part of the minibasin described above, whereas one dips to the north (Fig. 4.4). A5-9 have down-dip heights which range between 400–670 m and maximum lengths of 930–1730 m, yielding aspect ratios of 2.1 – 3.9

(Fig. 4.9) The maximum throw on these faults are generally less than that observed on A1-4 (i.e., maximum throws of ~10 - 15 m; Fig. 4.15 a).

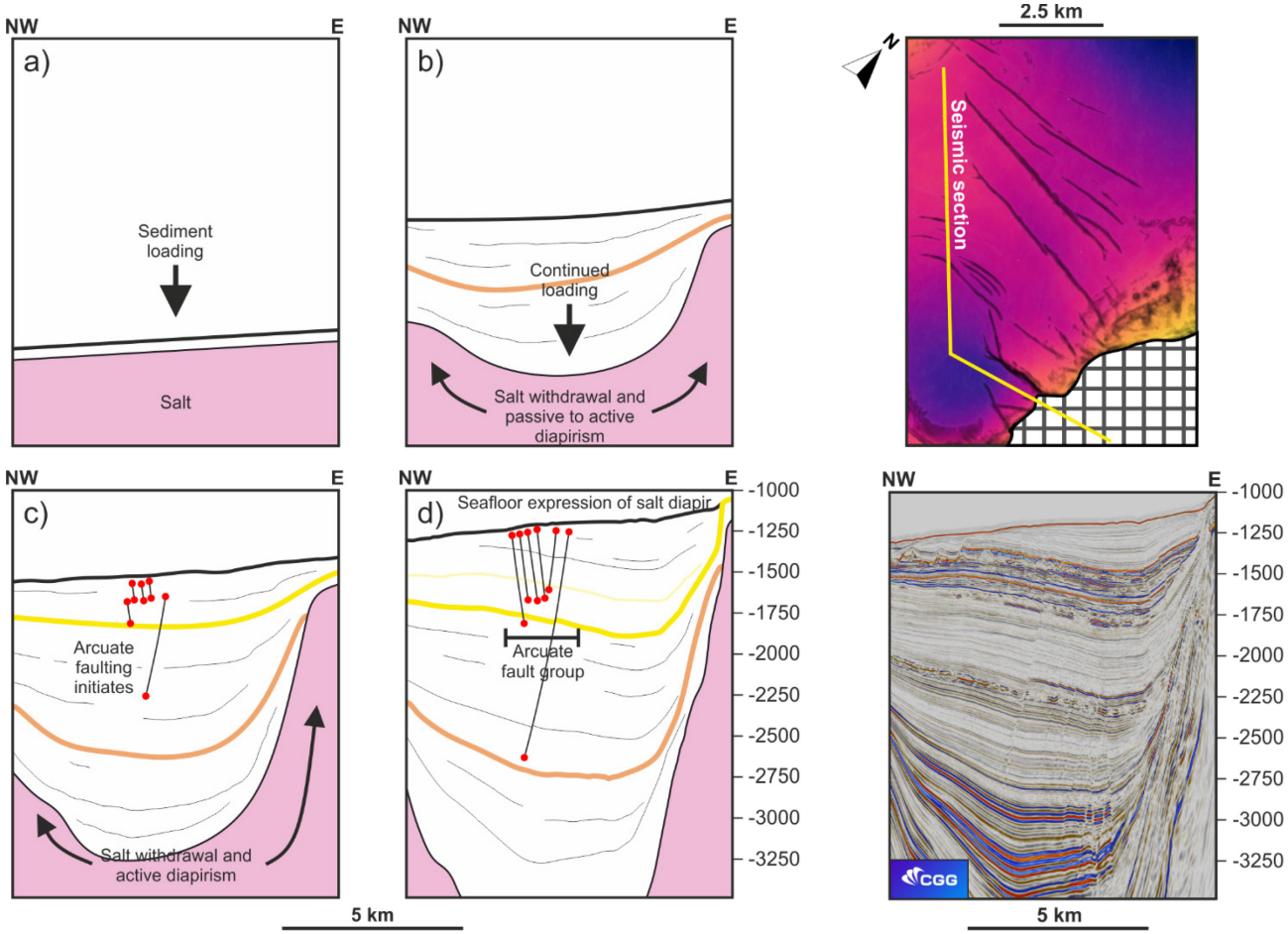


Figure 4.16. Structural kinematic model for fault array development| A variance co-blended depth structure map of the Intra-Pliocene surface (top right) showing the location of the seismic section of the present-day structure of the salt minibasin (bottom right). The structure map also highlights the deeper part of the minibasin in the south and the onlap surface onto the salt wall. Hatched = presence of salt wall at this structural level. (a-d) A sketch diagram of the evolution of the minibasin in relation to the arcuate fault group. Evolution includes: a) sediment loading, b) salt withdrawal, diapirism, c-d) outer-arc bending and the subsequent onset of the nucleation of extensional arcuate faults. Data courtesy of CGG Multi-Client.

4.4.3.2 Interpretations

Since the arcuate faults closely parallel the outer rim of the deep part of the minibasin (Fig. 4.4) we suggest they formed to accommodate outer arc-style bending and stretching of the minibasin-fill during differential subsidence and salt withdrawal (Fig. 4.16); geometrically similar faults are observed in association with mobile mud withdrawal (Stewart, 2006). We propose these faults

became overdisplaced for two reasons. Firstly, the larger faults in the first subgroup (A1 - 4) terminate very near the salt-sediment interface suggesting that these faults became restricted laterally due to not being able to propagate into the weak salt (e.g. Tvedt et al., 2013b). Thus, resulting in these faults becoming overdisplaced as throw accrual continues under laterally restricted tips. Secondly, the shallower second subgroup are more closely spaced than other faults within the extensional array and are sub-parallel (Fig. 4.4a). We propose that these faults experienced mechanical interactions between their fault tips, which resulted in lateral restriction of their growth and overthrow. While the cause (i.e., fault interaction) for fault restriction differs to that of the larger arcuate faults (i.e. salt interaction), the result of overthrow is the same (e.g. Crider and Pollard, 1998, Martel, 1999, Nicol et al., 2017).

4.5 Discussion and Implications

4.5.1 Origin and kinematics of planar normal faults; the case for tip restriction by host rock properties

The occurrence of throw maxima within Miocene and Pliocene strata suggest the planar faults nucleated within Neogene stratigraphy (Fig. 4.10) (Hongxing and Anderson, 2007). Whereas all other planar faults propagated as blind structures, F1 represented a surface-breaching growth fault during at least the Pliocene (Fig. 4.10). During the Middle Miocene, salt and overburden translation rates increased significantly from *c.* 0.2 to 1 mm/yr within the Outer Kwanza Basin, principally due to margin uplift (Hudec and Jackson, 2004, Evans and Jackson, 2019). Depending on the structural position on the margin, this resulted in extensional (i.e. typically in up-dip, proximal locations) or contractional (i.e. typically in downdip, distal locations) deformation of salt and its overburden (Hudec and Jackson, 2004, Evans and Jackson, 2019). Despite our study area being in the present-day transitional domain (Fig. 4.1), increases in downdip salt flux could have resulted in local extension of this area due to outer-arc bending and translation across the base-salt relief (Evans and Jackson, 2019). The planar faults may therefore have formed in the Middle Miocene

in response to this increased rate of basinward translation of salt and its overburden, eventually breaching the seabed in the Pliocene, as evidenced by the presence of the growth strata in the hanging wall of F1 (Evans and Jackson, 2019).

Field-based studies and modelling results show that mechanical stratigraphy can influence the growth and ultimate geometry of normal faults; e.g. multi-layered sequences defined by different rock competencies controls, down-dip linkage, fault restriction and fault aspect ratio (e.g. Wilkins and Gross, 2002, Soliva and Benedicto, 2005, Schöpfer et al., 2006). For example, Nicol et al. (1996) suggest vertically restricted faults display greater aspect ratios. More recent work proposes various mechanisms by which vertical restriction might occur, showing that faults growing in mechanically more homogenous host rocks assume circular to elliptical shapes throughout their lives, whereas those in multi-layered sequences can have their vertical growth impeded, thus growing from a circular to an elliptical geometry, resulting in an increase in aspect ratio (Fig. 4.12) (Soliva et al., 2005a, Soliva and Benedicto, 2005, Soliva et al., 2006). One consequence of the latter style of fault growth is the development of high throw gradients at the restricted (vertical) tip (Fig. 4.8d and e) (Wilkins and Gross, 2002). Within the planar fault group, F3 and F4 have relatively high aspect ratios (3.5 and 5.2, respectively) and high throw gradients (0.12 and 0.11, respectively) at their lower tips; these values are an order-of-magnitude greater than those of F1 and F2 (0.01). The migration of throw to the restricted tip and consequent high throw gradients is shown by the presence of their throw maxima being slightly offset towards their lower tips, which is characteristic of mechanically bound faults (Fig. 4.8d and e; and 4.10) (e.g. Wilkins and Gross, 2002, Soliva and Benedicto, 2005, Soliva et al., 2005b). In contrast, relatively closely (< 1 km) spaced faults within the bifurcating fault group, which have throw maxima of > 30 m and that offset the MTC, do not have these geometric characteristics (Fig. 4.11). This pattern, where only faults with T_{max} > 30 m offset the MTC, can be observed in the arcuate fault group in the extensional array (Fig. 4.11b). An important observation is that despite being < 1 km from F3 and 4 and although they offset similar stratigraphy (Fig. 4.5), the lower tips of F1 and 2 lie above the

MTC; as a result, these faults do not have the same high aspect ratios or throw gradients at their lower tips (Fig. 4.5, 4.7 and 4.9).

The variable geometric relationships between the faults and the MTC suggests that it acted as a mechanical layer, restricting the downward and upward propagation of the fault tips and overall enlargement of the surfaces of faults that ultimately only accumulated only < 30 m maximum throw (Fig. 4.11b). This resulted in higher aspect ratios and lower tip throw gradients on those faults not able to propagate, as well as influencing the growth, geometry and throw distribution of bifurcating faults (Fig. 4.12 and 4.14). Because drilling data are not available to determine the MTC lithology or mechanical properties, we do not know if this unit retarded tip propagation by: (i) acting as a relatively stiff layer that was hard to strain; or (ii) acting in a ductile manner, with strain being internally distributed in more diffuse manner. The latter case has been observed in field-based studies of normal faulted, mechanically layered host rocks, with faults seemingly nucleating and propagating only in more competent, stiff layers (typically >0.5 m thick) (Soliva et al., 2005b). Underlying and overlying, more compliant layers (<0.5 m thick) behave in a ductile manner and are characterised by diffuse strain and high strain gradients. Faults essentially decouple in these layers, with high aspect ratios and underdisplaced fault populations arising as a function of 'forced' propagation within the stiff layers. We propose that this case may also apply at a substantially larger, seismic-scale, such as that documented here. Deep water MTC's are predominantly mudstone-dominated (Wu et al., 2019) meaning that it could be the case that they act in a ductile manner with strain being more diffuse, as documented in mechanically heterogeneous faulted sequences (e.g. Bürgmann et al., 1994, e.g. Nicol et al., 1996, Wilkins and Gross, 2002, Soliva and Benedicto, 2005, Soliva et al., 2005b, Soliva et al., 2005a, Roche et al., 2012). In the absence of drilling data, we propose that either of these hypotheses could be the case for the MTC's mechanical control on fault growth.

4.5.2 Kinematics of bifurcating faults; overcoming tip restriction and continued fault growth

Fault linkage and bifurcation control throw distributions on normal fault surfaces (Peacock and Sanderson, 1991, Dawers and Anders, 1995, Mansfield and Cartwright, 2001, Peacock, 2002, Soliva and Benedicto, 2004, Soliva et al., 2008). We noted that the laterally restricted branchline of F7 occurs at the top of the Miocene MTC, and that the throw maximum also lies at this structural and stratigraphic level. The throw maximum is restricted to the larger, rearward (i.e., footwall side) fault and does not continue onto the frontal (i.e. hangingwall side) splay (Fig. 4.13b). In section 5.1 we discussed that the vertical restriction of the lower tips within the planar fault group resulted in high throw gradients (Wilkins and Gross, 2002, Jackson et al., 2014). If a similar process occurred during growth of the fault F7, which bifurcates upwards, it could follow that pinned precursor segments nucleated above the MTC as physically separate structures, with high stressing building-up at their lower tips before they were able to link and propagate onward, resulting in the present throw pattern (Fig. 4.13b and 4.14a). The same process could occur for a segmented fault system nucleating *below* and ultimately propagating upwards through a mechanical layer (Wilkins and Gross, 2002).

An alternative interpretation for the throw patterns on F7 is based on our observation that the main, rearward segment accommodates a laterally extensive, sub-horizontal throw maxima, whereas the frontal splay has overall lower throw values and lacks a discrete throw maximum (Fig. 4.13). Thus, we may interpret that the main fault surface nucleated above the MTC and started to grow before the splay, becoming temporarily mechanically pinned along the MTC, resulting in the development of throw maxima before propagating further downwards (Wilkins and Gross, 2002) (Fig. 4.13). The splay segment, which also nucleated above the MTC, may not have achieved the critical tip stresses required for onwards propagation, instead linking down-dip with the main fault surface near the top of the MTC (Wilkins and Gross, 2002, Soliva and Benedicto, 2005, Soliva et al., 2005b) (Fig. 4.13).

Bifurcating fault F6 shows a distinct concentration of high throw near the MTC (Fig. 4.13a); this is consistent with the hypothesis of stress and strain concentration at the MTC prior to onward fault propagation (Fig. 4.14). Moreover, a second distinct area of high throw occurs on the frontal fault of F6, immediately east of the relay zone (Fig. 4.13a). This is consistent with throw distributions typically seen within relay zones, where tip interaction occurs between adjacent, upward-propagating segments (Peacock and Sanderson, 1991, Trudgill and Cartwright, 1994, Peacock and Sanderson, 1994, Peacock, 2002, Long and Imber, 2012, Freitag et al., 2017). Fault bifurcation can occur as a result of stress field reorientation or non-uniformity, as well as irregular tip-line propagation due to intra-host rock mechanical heterogeneities, such as an intra-stratal MTC (Soliva et al., 2008). This would explain the bifurcation and position of the branchline on the top of the MTC (Fig. 4.5a and 4.13). Our data suggest that only faults that accumulated > 30 m of throw were able to propagate through the MTC; below this value, the tips were pinned due to the build-up of insufficient tip stresses to allow onward propagation (Fig. 4.11a and b) (Wilkins and Gross, 2002).

4.5.3 Normal fault growth and D-L scaling relationships

D-L scaling relationships derived from global datasets have historically been used to support a normal fault growth model by synchronous lengthening and throw accumulation (i.e. 'propagating model'; Childs et al., 2017b, Rotevatn et al., 2018); (See also e.g. Watterson, 1986, Walsh and Watterson, 1988, Walsh et al., 2002). More recently, however, studies using 3D seismic reflection data have integrated stratigraphic data in an otherwise purely geometrical analysis. This has given rise to an alternative fault growth model that states fault lengthening (which may include linkage of initially isolated segments) occurs before the accumulation of significant throw (i.e. 'constant-length model'; Jackson and Rotevatn, 2013, Childs et al., 2017b, Rotevatn et al., 2019, Nicol et al., 2020a).

We show here that host-rock heterogeneities, and near- and far-field stress regimes and their interactions, can all result in the formation of under- or over-displaced faults (i.e. faults that significantly deviate from global D-L scaling relationships and thus produce scatter within these datasets), and/or faults with anomalously low or high aspect ratios (Cowie and Scholz, 1992a, Dawers and Anders, 1995, Peacock, 2002, Soliva and Benedicto, 2005, Soliva et al., 2005b, Soliva et al., 2005a). This is in addition to fault linkage, which typically results in underdisplaced faults likely characterised by anomalously low aspect ratios (Cartwright et al., 1995). Our study shows how detailed analysis of largely blind faults of varying sizes developing within the same overall tectono-stratigraphic setting can shed light on the kinematics of fault growth; such studies can complement those focused on growth faults flanked by syn-kinematic strata (e.g. Tvedt et al., 2013b, Duffy et al., 2015, e.g. Jackson et al., 2017). A key observation is that the studied faults would fall within the general scatter present in global D-L scaling datasets (Fig. 4.2), and that this would mask the not insignificant variability in their geometric properties (i.e. D-L relationship, aspect ratio) and inferred growth patterns, and the relationship of these to local stratigraphic factors (i.e. an intra-stratal MTC).

4.6 Conclusions

3D seismic reflection data from the Outer Kwanza Basin, offshore Angola image a basement-decoupled normal fault population that deform a clastic-dominated, deep-water succession. These faults are up to 6.3 km long, 1.9 km tall, and have up to 44 m of throw. Aspect ratios (i.e., fault height to fault length), maximum throw, and lower-tip throw gradients vary between faults, being greater (aspect ratio up to 5.2; maximum throw <30 m; throw gradients up to 0.12) for faults that terminate downwards at an intra-stratal mass-transport complex (MTC) than those that offset it (aspect ratio up to 3.6; maximum throw >30 m; throw gradients up to 0.08). We interpret that the faults nucleated above and propagated down towards the MTC. Upon encountering this unit, which we infer was weaker than the encasing strata, tip propagation was halted until tip stresses

were sufficiently high to breach it. We suggest that such stresses were reached when a fault accumulated a maximum throw of at least 30 m. The throw-length (D-L) relationship for all faults fall within the general scatter present in global D-L scaling datasets, regardless of their geometry or growth patterns. In the absence of growth strata, D-L scaling relationships must be used with caution when studying fault kinematics, given the role mechanical stratigraphy plays in controlling fault propagation, size, finite throw (or throw), and geometry. Mechanical stratigraphy therefore has a key control on the growth of large, seismic-scale normal faults in a similar way to that observed for far smaller structures

Acknowledgements

We would like to thank the significant guidance and comments of the reviewers and editors, notably C. J. Ebinger and Andy Green. We thank the NERC Centre for Doctoral Training in Oil and Gas for the provision of funding to the PhD research of David Redpath. We also thank CGG for making these data available for academic use. The data can be accessed by direct request to CGG (https://www.cgg.com/multi-client-data/multi-client-seismic), upon signing of a confidentiality agreement. We also thank Schlumberger for providing access to Petrel software.

5

Geomorphological Analysis of Fault-Scarp Degradation Complexes Constrain Style of Normal Fault Growth, Offshore NW Australia

Preamble

DR interpreted the data, wrote the manuscript, and drafted the figures presented in this chapter. CALJ and RB provided insightful input into the interpretations and the development of analytical methods and contributed excellent feedback when writing the final manuscript.

This manuscript is prepared and formatted for submission to Journal *Basin Research*.

Abstract

Normal faults accommodate crustal extension, with their kinematics determining the physiography, seismic hazard, and resource potential of rift basins. The patterns and long-term (10^6 Myr) tempo of the growth of large (>10 km long) normal faults has been most accurately constrained in overfilled sedimentary basins, where synkinematic (growth) strata preserve a record of fault slip, lengthening, interaction, and linkage. Over comparable length-scales, the geomorphological analysis of fault scarps and related drainage systems exposed at the Earth's surface in areas of active extension can also constrain the patterns and timing of faulting, typically over substantially shorter timescales (<10^5 Myr). However, geomorphological methods are not yet widely used when studying the growth of buried and seismically imaged, now-inactive faults in sediment-starved rifts; in such settings, traditional methods, such as isopach analysis and throw backstripping, cannot be effectively applied. Here we use 3D seismic reflection and well data from the Exmouth Plateau in the North Carnarvon Basin, NW Australia to determine the style and timing of growth of the Thebe Fault Complex, a large (at least 45 km-long and with up to 0.8 km of throw), segmented normal fault that formed during Late Triassic – Late Jurassic rifting. Geomorphological analysis of the fault's footwall and hangingwall suggest it rapidly attained its near-final length (c. 45 km) within 10 Ma of the rift initiation, which is equivalent to only 12 % of the total rift history. Fault interaction, relay zone formation, and footwall uplift and erosion occurred during this time, with degradation accounting for up to 49% of initial footwall relief, on faults with as little as *c.* 250 m throw. We also show that the magnitude, pattern, and dominant fault scarp erosion mechanism on the Exmouth Plateau is related to fault throw and related footwall relief.

5.1 Introduction

The style and pace of growth of normal faults controls rift basin geometry and landscape development in areas of continental extension (e.g., Gawthorpe and Leeder, 2000; Whittaker, 2012). Understanding how normal faults grow also plays a vital role across a range of geoscience disciplines, including earthquake forecasting, the exploration for and extraction of a range of natural resource (e.g., hydrocarbons, geothermal energy), and the locating of storage sites for CO_2. Growth models for normal faults are at least partly rooted in the scaling relationship between fault throw (D) length (L):

$$D = cL^n$$

; where c is a constant and n is between 1 and 1.5 (e.g.Watterson, 1986, Walsh and Watterson, 1988, Walsh and Watterson, 1987, Leeder and Gawthorpe, 1987, Jackson and McKenzie, 1983, Jackson, 1987b). This formed the basis for the 'propagating' fault model which states that faults grow by coeval increases in their length and throw (Watterson, 1986, Cartwright et al., 1996, Childs et al., 2003, Rotevatn et al., 2018). Since the late-1990s, studies of fault growth using seismic reflection data, which image synkinematic (growth) sequences that record fault length and throw over geological time, provide support for the 'constant-length model'. In this model, faults grow by rapid tip propagation and establish their near-final length prior to accumulating the majority of their throw (Walsh et al., 2002, Jackson et al., 2017, Childs et al., 2017b, Rotevatn et al., 2018). More recently, the 'hybrid model' fault growth model proposes that rapid fault lengthening to its near-final length by tip propagation and segment linkage, consistent with the propagating fault model, largely occurs during the first 20 – 30 % of the faults life. Then follows a prolonged period (70 – 80 % of fault life) of throw accumulation, during which time the fault does not significantly lengthen, in a manner consistent with the constant-length model (Rotevatn et al., 2019, Pan et al., 2021, Lathrop et al., 2021, Redpath et al., 2022).

Studies that have provided the most robust constraints on the geometrical and temporal evolution of long (i.e., >10 km long), large throw (i.e., >1 km) normal faults that grew over geological timescales (i.e., $>10^6$ Myr) have typically focused on: (i) now-inactive normal faults imaged in seismic reflection data; and (ii) normal faults that formed in balanced or overfilled extensional basins, in which sediment accumulation rate is equal to or ideally exceeds fault slip rate (e.g. Walsh et al., 2002, Childs et al., 2003, Ziesch et al., 2017, Childs et al., 2017b, Rotevatn et al., 2018). This is because growth strata provide a record of fault activity, which can be investigated using techniques such as: i) expansion index (EI) analysis; ii) throw and relay zone backstripping; and iii) isopach/isochron analysis (Jackson et al., 2017). Clearly, however, not all faults grow in such settings, i.e., in some settings, growth strata, in particular that preserved in the hangingwall, are accessible or poorly exposed (i.e., in the field), or are poorly imaged (i.e., in the subsurface).

In many modern extensional settings, growth strata are deeply buried within the hangingwall basin fill of active normal faults, which typically form prominent topographic relief at the basin margin. In these cases, the footwall geomorphology can be used to determine fault growth history. More specifically, the morphological analysis of the area, relief, and outlet spacing associated with footwall-hosted catchments (Densmore et al., 2004, Alves et al., 2009, Goldsworthy and Jackson, 2000, Tsodoulos et al., 2008), as well as rivers cross-cutting active faults ((e.g., knickpoint analysis; Commins et al., 2005, Verroios and Zygouri, 2021), all help constrain the growth and linkage of normal faults over relatively short timescales (e.g., $<10^5$ Myr). However, such techniques are rarely applied to subsurface data from underfilled or sediment-starved basins where, like in active rift settings, the hangingwall fill is buried.

In this study we use high-resolution 3D seismic reflection and borehole data from the Exmouth Plateau, NW Shelf, offshore Australia to undertake a quantitative analysis of the geometry and growth of a large, segmented normal fault. To do this, we study the geomorphology of a fault-scarp degradation complex imaged in its footwall, and depositional patterns in its hangingwall (Fig. 5.1). By doing this we can highlight how geomorphological methods developed in active rifts can

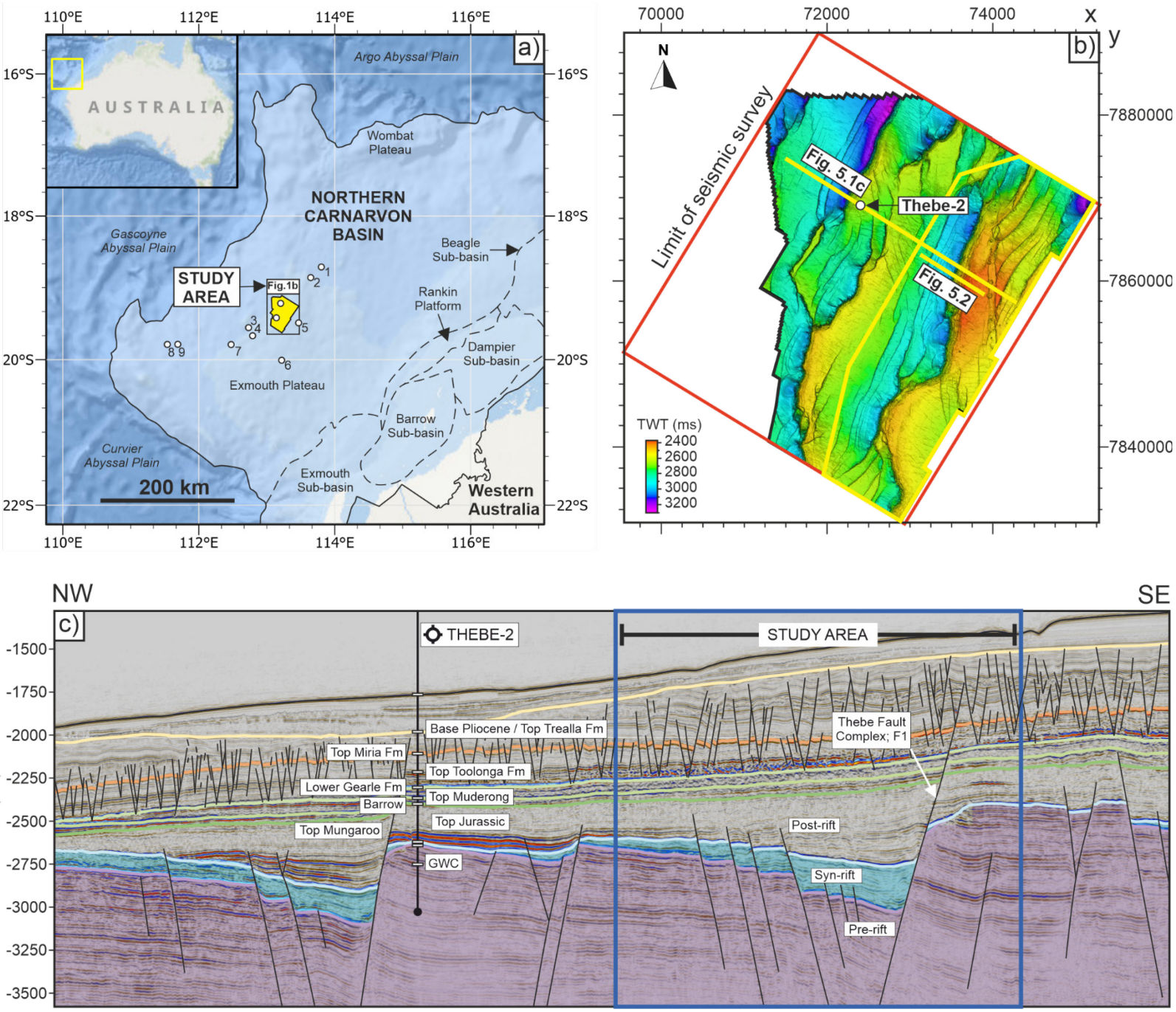


Figure 5.1. Study area location and regional overview| (a) A location map of the North Carnarvon Basin showing the i) location of the Thebe seismic survey study area and ii) significant wells in the surrounding area: 1 = Belicoso-1; 2 = Dalia South-1; 3 = Guardian-1; 4 = Kentish Knock South-1; 5 = Jupiter-1; 6 = Blake-1; 7 = Arnhem-1; 8 = Cadwallon-1; 9 = Genseric-1. (b) A time structure map of the Top Rheatian surface highlighting rift physiography. Yellow polygon indicates the extent of Figure 4. (c) Seismic dip-section across the region of the study area, with the position of Thebe-2 well, from which regional surfaces where mapped and the pre-, syn-, and post-rift as defined in this paper. Section position shown in B. Pre-rift = Pink shaded zone. Syn-rift = Blue shaded zone. Syn-kinematic extends to Top Miria / Base Tertiary (see Fig. 5.2).

be applied to assess the long-term evolution of large normal faults now deeply buried in sedimentary basins. We suggest that where traditional analytical methods cannot be applied due to the absence or poor imaging of growth strata, geomorphological methods can be applied.

5.2 Regional Geological Overview

The North Carnarvon Basin is an epicratonic basin and the westernmost province in a series of Paleozoic-Cenozoic basins comprising the Westralian Superbasin, NW Australia. The basin covers an offshore area of 535,000 km^2, incorporating a set of inboard and outboard sub-basins separated by the NE-trending Rankin Platform (Fig. 5.1) (Bilal and McClay, 2022). The Exmouth, Barrow, Dampier and Beagle sub-basins constitute the central inboard zone and represent failed rift systems, whereas the outboard area of the basin is defined by the Exmouth Plateau. Beyond these sub-basins, the adjoining Argo, Cuvier and Gascoyne abyssal plains define the oceanward limits of the North Carnarvon Basin (Pan et al., 2021, Bilal and McClay, 2022) (Fig. 5.1).

5.2.1 Exmouth Plateau

The Exmouth Plateau is a NW-trending block of thinned (*c.* 20 km) continental crust (Exon and Willcox, 1978, Driscoll and Karner, 1998). It covers an area *c.* 150,000 km^2, with an average water depth of *c.* 1.6 km (Fig. 5.1). In contrast to the inboard sub-basins, the Exmouth Plateau underwent limited extension and subsidence during the rifting of Gondwana from the Australian continental margin during the latest Triassic – early Jurassic rift phase, which was also related to the opening of the Ceno-Tethys Ocean (Exon and Willcox, 1978, Bilal and McClay, 2022). The Argo, Cuvier and Gascoyne abyssal plains, which now bound the plateau, initially formed during the onset of seafloor spreading during the Late Jurassic –Early Cretaceous (Fig. 5.1) (Exon and Willcox, 1978, Driscoll and Karner, 1998, Stagg, 2004, Reeve et al., 2016, Pan et al., 2021, Bilal and McClay, 2022) The syn-rift structural fabric of the Exmouth Plateau formed during Late Triassic – Early Cretaceous rifting and is dominated by N- to NNE-trending, domino-style fault blocks (Fig. 5.1).

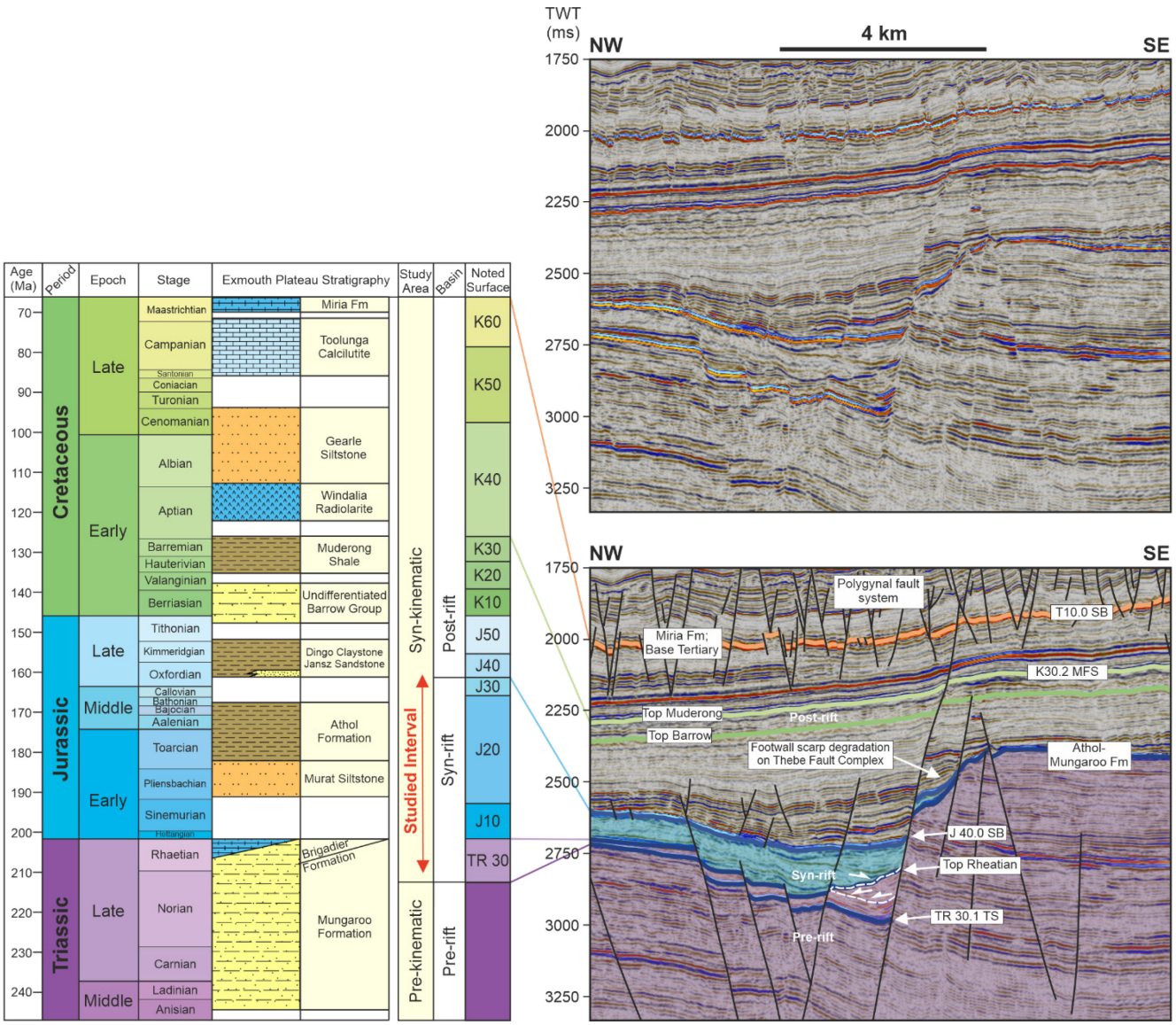


Figure 5.2. Stratigraphic column for the Exmouth Plateau, Northern Carnarvon Basin| Stratigraphy of the Northern Carnarvon basin and the mains stratigraphic surfaces of the studied interval extrapolated from the Thebe-2 well in the NW and displayed on a NW-SE seismic section at the studied Thebe Fault Complex (TFC). The studied interval lies between the TR30.1 TS and J40.0 SB. TS, Transgressive surface; MFS, Maximum flooding surface; SB, sequence boundary. Hangingwall fans are outlined by the white dashed line. Stratigraphic noted surfaces are from McArthur, Hartley, et al. (2016)

The syn-kinematic stratigraphy is relatively thin in half-graben depocentres across the Exmouth Plateau and is thin to seemingly absent on structurally high footwalls of rift-related normal faults, indicative of the basin being sediment-starved during at least some of the rift event. As a result, many of the fault footwalls, which are typically comprised of the Mungaroo Formation (Triassic) (see below), were exposed during rifting, such that widespread and prominent footwall degradation

scarps are present on the major N- to NNE-trending fault scarps (Fig. 5.2 and 5.3) (Bilal et al., 2020, Barrett et al., 2021, Bilal and McClay, 2022). Previous studies highlight that: (i) the magnitude of fault-scarp degradation is broadly and positively correlated to the magnitude of fault throw (e.g., Elliott et al., 2012); (ii) fault-scarp degradation was associated with the deposition of hangingwall fans (e.g., Scarselli et al., 2015, Bilal et al., 2020); and (iii) volumetric analysis of the material eroded from the footwall vs. that deposited in the hangingwall reveal areas of sediment bypass and the position of sediment input points (e.g., Barrett et al., 2021). However, none of these studies quantify the relationship between footwall degradation, hangingwall deposition, and the style and timing of fault growth.

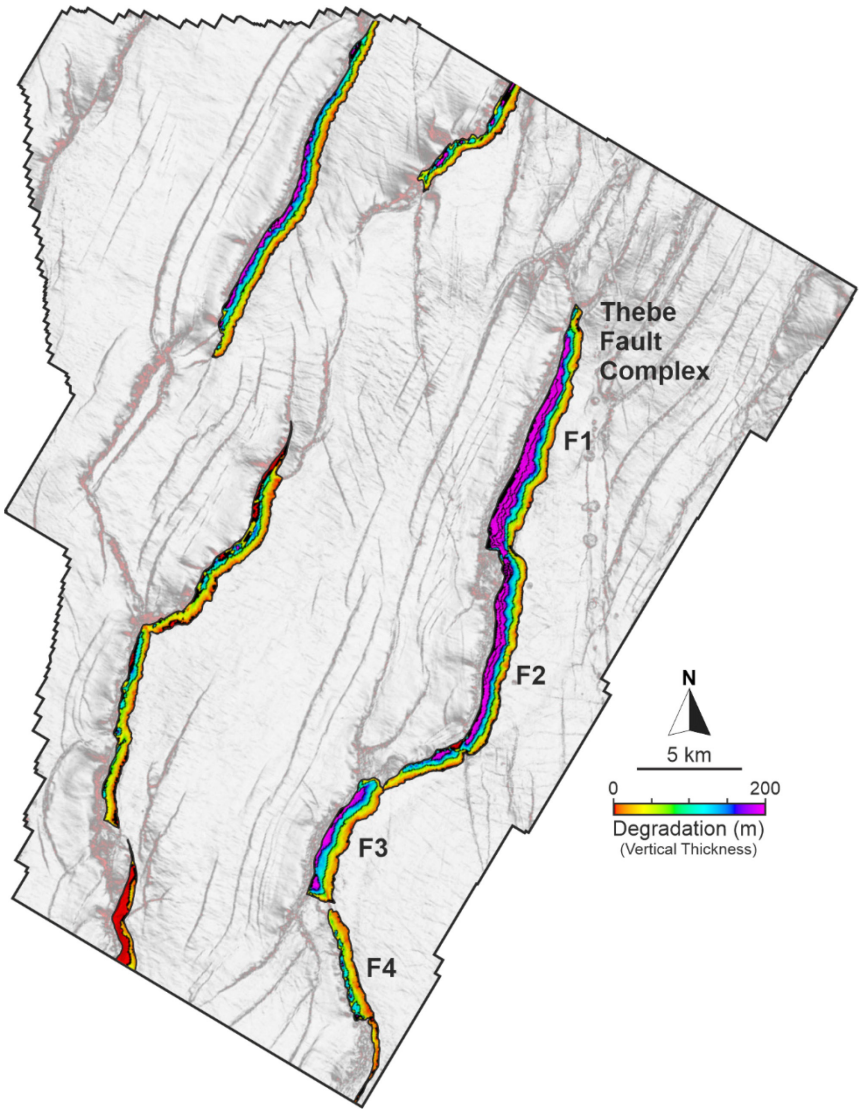


Figure 5.3. Fault scarp degradation thickness| A shaded variance extraction of the base syn-kinematic surface (TR 30.1 TS) within the Thebe seismic survey, showing the footwall degradation extent and thickness. Degradation is present on all the major NE-SW trending domino style fault blocks. The Thebe Fault Complex shows the greatest amount of degradation. (Degradation key is contoured at 50 m intervals.)

5.2.1.1.Stratigraphic Framework

Three megasequences define the stratigraphic framework of the study area (Fig. 5.2). The pre-rift megasequence consists of the non-marine Mungaroo Formation, which comprises interbedded sandstones, siltstones, and claystones. The top of the Mungaroo Formation is defined by the TR 30.1 TS surface (Fig. 5.2).

The syn-rift megasequence represents the main rift stage and it is bounded below and above by the TR 30.1 TS (209.5 Ma) and J 40.0 SB (162.5 Ma) surfaces, respectively (Fig. 5.2). The oldest syn-rift sediments belong to the marine Brigadier Formation (*c.* 205 – 201.3 Ma) (Fig. 5.2). Immediately adjacent to the degraded fault scarps, hangingwall fan deposits in the lowermost part of the Murat Siltstone downlap the Brigadier Formation (Fig. 5.2). The fans are onlapped by syn-rift shelfal-offshore marine siltstones and claystones of the (upper) Murat Siltstone and overlying Athol Formation (*c.* 189.9 – 165 Ma) (Fig. 5.2). These age constraints and stratal patterns show that between the latest Rhaetian (i.e., end of deposition of the Brigadier Formation) and earliest Pliensbachian (i.e., early during deposition of the Murat Siltstone) (i.e., a period of *c.* 10 Ma), fault-related footwall relief and hangingwall accommodation had already developed in association with many of the rift-related faults (Fig. 5.2) (e.g., Scarselli et al., 2015, Bilal et al., 2020).

The Oxfordian J 40.0 SB (162.5 Ma) unconformity marks the cessation of the initial and main rift phase, with fault reactivation then occurring in the Early Cretaceous (Pan et al., 2021, Bilal and McClay, 2022) (Fig. 5.2). During reactivation, progradation of the Barrow Group resulted in the basin becoming overfilled. The Valanginian K 20.2 SB marks the end of fault activity (Bilal and McClay, 2022) (Fig. 5.2). The Winning Group, Toolonga Calcilutite, and Miria Formation represent a substantial part of the post-rift megasequence, and they are capped by the Base Tertiary (T 10.0 SB) (Fig. 5.1c and 5.2). The remaining post-rift megasequence consists of relatively fine-grained, marine sediments (Fig. 5.1 and 5.2).

5.2.1.2 Structural Framework

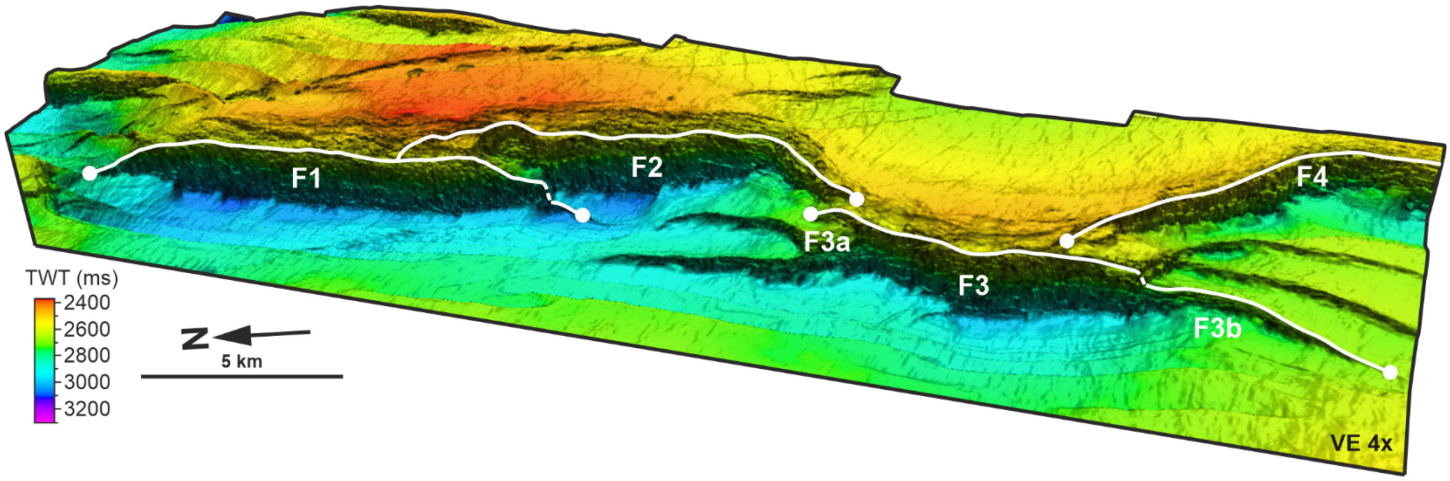


Figure 5.4. Thebe Fault Complex: 3-D structure map | TWT (ms) structure map for the Top Mungaroo (TR 30.1 TS) surface showing the Thebe Fault Complex (Fault 1 - 4). Vertical exaggeration = 4.

The study area contains five major, NW-dipping extensional faults, defining a series of tilted fault blocks that are *c.* 5 – 12 km wide (Fig. 5.1). These structures formed in response to Late Triassic – Early Cretaceous continental extension (Fig. 5.2) (Pan et al., 2021, Bilal and McClay, 2022). The faults are 10 to at least 45 km long, with maximum throws of 0.4 – 0.8 km (Fig. 5.4). Of the five main tectonic faults, four exhibit footwall degradation (Fig. 5.3). For the purpose of this study, we focus on the Thebe Fault Complex (Fig. 5.3) because: i) initial observations of the base synkinematic surface (TR 30.1 TS) show that the greatest amount of fault-scarp degradation occurs along this fault complex, meaning it is the best-imaged (Fig. 5.3); and ii) this is the longest fault within the study area, meaning we can assess the relationship between fault geometry (e.g., relay zones, fault-related folds) and throw, and related patterns of erosion and syn-rift deposition, associated with a structure of comparable dimension to those described in active rifts (Fig. 5.4).

5.3 Dataset and Methodology

5.3.1 Dataset

We use a high-quality, pre-stack, time migrated (PSTM) 3D seismic reflection survey (HEX07B) located in the WA-346-P permit area of the Exmouth Plateau, North Carnarvon Basin, offshore NW Australia. The survey has an areal extent of *c.* 1800 km^2 and images down to 4610 ms TWT, with NW-trending inline and NE-trending crossline intervals of 25 m and 12.5 m, respectively. The data are displayed with normal polarity (a peak indicates a downward increase in acoustic impedance). The nearest well to our study is Thebe-2, which is situated on a footwall high of another major fault block in our study area (Fig. 5.1). Within the rift sequence, the focus of our study, the seismic frequency ranges from 15 to 65 Hz, with an average of 40 Hz. To estimate the seismic resolution for our seismic survey we use the checkshot data from Thebe-2, which gives a maximum vertical resolution of 8.5 m for the interval of interest ($\Lambda/4$) (Fig. 5.1) (Barrett et al., 2021). Key stratigraphic tops for the study (i.e., TR 30.1 TS and J 40.0 SB) were interpreted from well-log data in the NW of the survey, with a synthetic seismogram showing these are represented by high-amplitude, soft (i.e., TR 30.1 TS) or hard (i.e., J 40.0 SB) reflections (Fig. 5.2). These two surfaces provided a basis for regional mapping of other key stratigraphic surfaces. We mapped a total of six regional horizons that define the structural style and stratigraphic framework of the study area (e.g., fault complex geometry, morphology of the footwall, thickness patterns in syn-rift strata; Fig. 5.2 - 5.4).

5.3.2 Methods

To constrain the style and timing of fault growth in a sediment-starved rift basin using the relationship between fault throw, footwall geomorphology, and the temporal and spatial distribution of hangingwall fans, we need to: i) determine the relationship between fault throw and the volume of material eroded from the fault footwall deposited in the fault hangingwall; and ii) assess the spatial and temporal distribution of hangingwall fans.

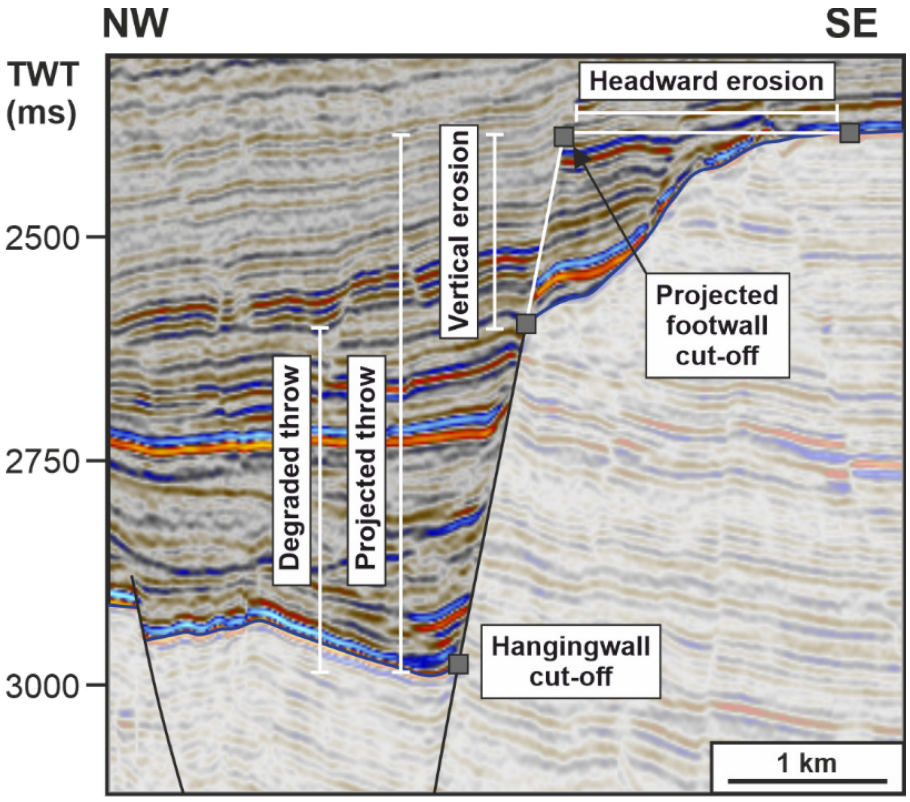


Figure 5.5. Fault scarp degradation metrics | Definitions for fault throw and footwall degradation terms used in projected throw and degradation factor. The projected footwall cut-off marks the intersection of the projected footwall (headward erosion) and fault scarp (vertical erosion) surfaces, that forms the pseudo-surface for the Top Mungaroo Surface.

5.3.2.1 Variance Attribute Extraction

We use the variance method which indicates the degree to which seismic traces vary by identifying the isolating edge and discontinuities from the seismic dataset, to visualise the presence and along-strike variation of the Thebe Fault Complex in the seismic reflection data (Chopra and Marfurt, 2018, Chopra and Marfurt, 2005).

5.3.2.2 Fault throw and eroded volume calculations

In order to constrain fault throw along the Thebe Fault Complex, we undertook regional seismic mapping of the Top Mungaroo surface, which defines the base of the syn-rift succession and thus records the cumulative rift-related strain. This surface also acts as the interface the degraded fault scarps and the onlapping, younger sediments that preserve them (Fig. 5.1 and 5.2). To define the

fault geometry, we accurately mapped four major faults (Fault 1-4) on closely spaced (*c.* 50 m) seismic sections perpendicular to strike, along the total (imaged) length of the Thebe Fault Complex. We then measured footwall and hanging wall cut-offs at Top Mungaroo to calculate fault throw in ms (TWT). To account for fault-related folding (i.e., continuous deformation; sensu Walsh and Watterson, 1988) in our throw calculations, we measured the footwall and/or hangingwall cut-off where the projected regional dip of the footwall/hangingwall strata, beyond the inflection point of the fold, intersected the fault plane. We then converted throw measurements from ms (TWT) to metres by taking the checkshot data from Thebe-2 and calculated the best-fit polynomial relationship between time and depth. This equation was then used to convert the footwall and hangingwall cut-off depths from TWT to metres. We then calculated the throw in metres (i.e., HW cut-off in metres – FW cut-off in metres) (Fig. 5.5). There may be potential error inherent in this calculation since the Thebe-2 well was drilled into a different footwall high located within Thebe HEX07B, adjacent to the Thebe Fault Complex in this study (Fig. 5.1). In the absence of well data on the footwall high of the Thebe Fault Complex - and therefore checkshot data to perform a TWT-Depth conversion directly for our study area - we assume that the stratigraphy found in the fault scarp that the Thebe-2 well penetrates to be similar to that of the Thebe Fault Complex scarps (e.g. Scarselli et al., 2015, Bilal et al., 2020, Barrett et al., 2021, Bilal and McClay, 2022). From these throw data, we finally produced throw-distance (T-x) plots to illustrate how throw varied along the length of the fault complex and to determine the position of structural features of interest such as relay zones (Fig. 5.6a – c) (e.g. Dawers and Anders, 1995, Duffy et al., 2015, Jackson et al., 2017).

To determine the magnitude of fault-scarp degradation, we: (i) extrapolated the trajectory of the fault plane upwards above its upper tip; and (ii) projected the Top Mungaroo surface up dip, above where it is presently eroded at the base of the degradation complex, to where it intersects (i.e., is cut-off against) the fault (Fig. 5.5). The vertical height difference between the throw measured on this pseudo-surface and the equivalent throw calculated by using the present (i.e., degraded) Top

Mungaroo surface was used to estimate the magnitude of vertical erosion (Fig. 5.5). By using the projected Top Mungaroo surface we were also able to generate an isopach and constrain the true volume of material eroded from the footwall scarp. The magnitude of headward erosion is the horizontal distance from the present cut-off of the Top Mungaroo surface against the fault and the position of the onset of erosion of the Mungaroo Formation (Figs 3 and 5) (e.g., Barrett et al., 2021). To calculate the volume of footwall-derived material potentially in the basin and the volume of hangingwall fans, we used the TWT - depth conversion to depth convert the upper and lower bounding surfaces of the pre-erosion fault scarp and the hangingwall fans. We then calculated the volumes of the footwall-erosion and hangingwall fans on the Thebe Fault Complex. Since the depth conversion was performed using Thebe-2 well data only analogous to the Thebe Fault scarp, we assume some uncertainty in our volume calculations. We determine this uncertainty by calculating the volumes using checkshot data from both the Thebe-2 and the nearby Thebe-1 well. We found that the volume varied by approximately ±15% when using the depth conversion data from Thebe-1 with respect to Thebe-2 and define this as the uncertainty within these measurements.

In addition to directly measuring the volumes of material eroded from the footwall, we calculated a ratio that we here call the *degradation factor* (DF):

$$\text{DF} = \text{Projected Throw} / \text{Degraded Throw}$$

; where projected throw is the vertical distance from the hangingwall cut-off and the pseudo footwall cut-off (i.e., true fault throw), and degraded throw is throw presently observed (i.e., including the throw lost due to footwall erosion) at the Top Mungaroo level (Fig. 5.5). DF therefore indicates the ratio between true throw and fault-scarp degradation. Thus, DF shows how the magnitude of vertical erosion varies along strike relative to projected throw, and therefore helps us to understand the relationship between fault throw and footwall degradation (Fig. 5.6c and 5.7). In particular, we show the value of DF in cases where the magnitude of vertical erosion is anomalously high compared to the total fault throw (Fig. 5.7).

5.3.2.3 Hangingwall Fan Analysis

To calculate the volume of material deposited in the immediate hangingwall of the Thebe Fault Complex, and the relationship this has to fault throw and the volume of material eroded from the footwall, we follow the method of Barrett et al. (2021), i.e., we mapped the top and base of these units on every inline and crossline, from which we created an isochron map (Fig. 5.2) (Table 5.1). We then subdivided the fault into eight sections using areas of low thickness as the dividing lines between areas of greater thickness; by doing so, we attempted to identify individual fan-shaped depositional bodies, which are expressed as locally thick accumulations of sediment.

5.4 Structure of the Thebe Fault Complex

The Thebe Fault Complex is at least 45 km long, extending beyond the southern limit of our seismic dataset (See Fault 4; Fig. 5.4 and 5.6). It comprises four distinct segments (Faults 1 – 4) defined at the ends by distinct throw minima, relay zones (Relays 1-3; see below), and along-strike bends in the fault trace (Fig. 5.4 and 5.6). Fault 1 is the northernmost segment in the Thebe Fault Complex and is 14.7 km long. Throw is greatest (0.78 km) at the fault centre, decreasing towards the fault tips, except for a local throw minimum at the site of transverse folding in the hangingwall (Fig. 5.6b) (see section 5.4.8). Fault 2 is 15.1 km long and exhibits three 'plateaus' of relatively consistent throw (i.e., 15 – 18 km, 18-21 km, and 21 – 27 km along strike) that correlate to relay 1, the centre of the fault segment, and relay 2, respectively (Fig. 5.6b). Fault 2 has a throw maximum of 0.76 km that is located near its centre (Fig. 5.6b). Fault 3 consists of a main fault and two splays (Faults 3a and 3b) and has a total length of 14.6 km (Fig. 5. 4 and 6). Fault 3 forms the central segment of the fault and has a throw maximum of 0.64 km (Fig. 5.6). Fault 3a is distinguished from the main fault segment by a significant and marked increase in throw, whereas 3b is also characterised by a marked increase in throw toward the main fault segment. Throw is greater on Fault 3b (178 m) than Fault 3a (75 m) (Fig. 5.6). Fault 4 is the southernmost segment in the Thebe Fault Complex and is at least 11.1 km long.

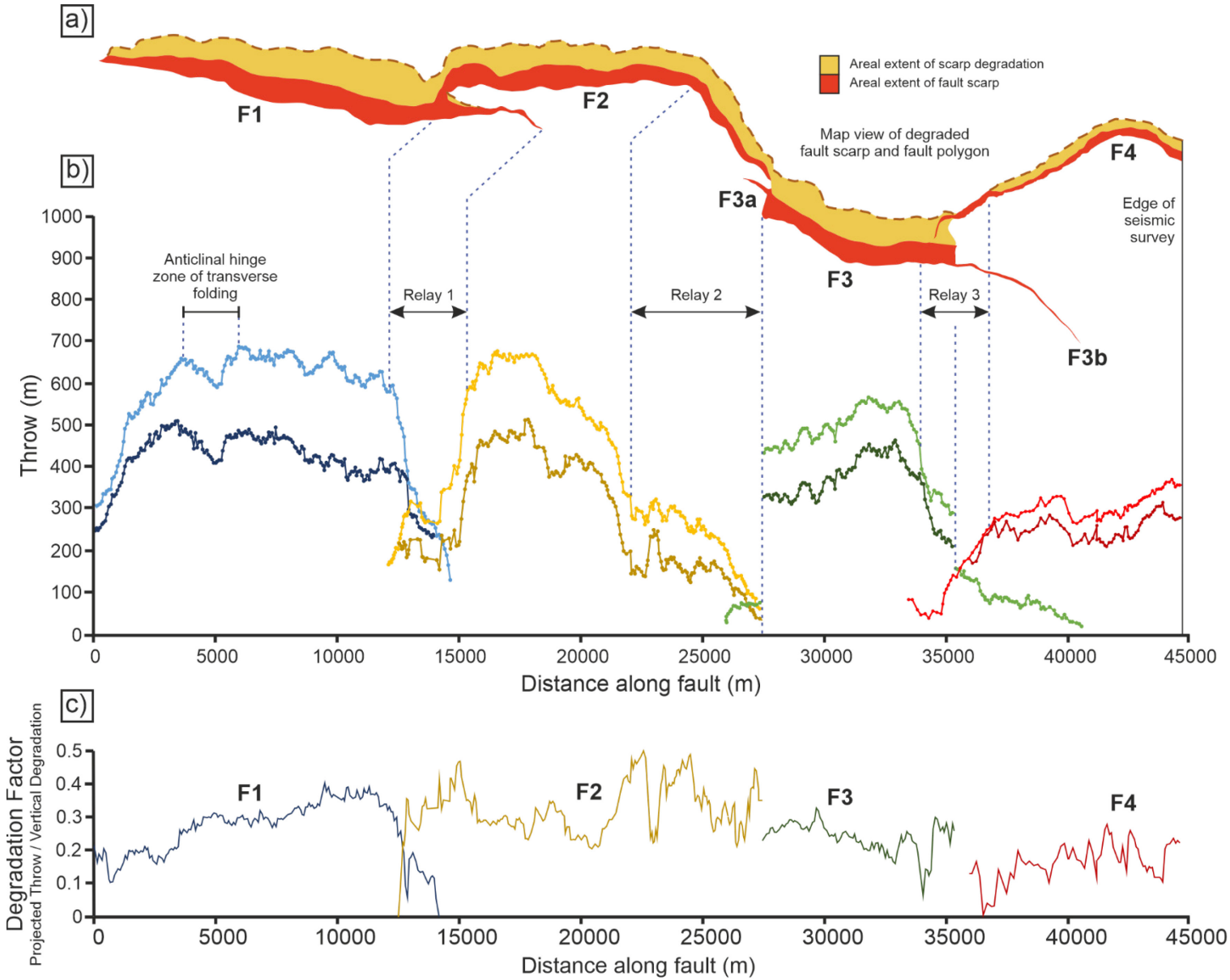


Figure 5.6. Throw-length and degradation factor (DF) - length plots for the Thebe Fault Complex| (a) Map view of fault scarp erosion (orange) and fault throw (red) along the Thebe Fault Complex. (b) A throw-length plot of the projected throw (lighter colours) and post-erosional throw (darker colours) along the length of the Thebe Fault Complex. (c) A DF-length plot showing the fraction of projected throw eroded by footwall degradation for F1-F4 along the Thebe Fault Complex. Degradation factor data is absent where footwall erosion equals zero at the fault tips (See Fig. 5.3).

Throw increases southwards away from its northern tip to a maximum of 0.42 km (Fig. 5.6b). Note that the throw maxima and geometric centre of Fault 4 may lie to the south of our seismic dataset (Fig. 5.4 and 5.6).

5.5 Relay Zone Structure

The four main segments of the Thebe Fault Complex are separated by three relay zones (Fig. 5.4 and 5.6a-b). Relay 1 is a footwall-breached relay ramp located between faults 1 and 2 (Fig. 5.4 and 5.6a-b). The ramp is *c.* 2.5 km long and 1 km wide. Up-dip on the relay ramp, several relatively small (maximum throw of *c.* 75 m) faults strike perpendicular to the ramp, facilitating geometrical or 'hard' fault linkage of faults 1 and 2 (Fig. 5.4 and 5.6) (Whipp et al., 2017). Typical of relay zones, Relay 1 is associated with a local throw minimum of *c.* 400 m, even when strain accommodated by the overlapping tips of faults 1 and 2, and the small, ramp-breaching faults, is summed (Fig. 5.6a and 5.b) (e.g. Peacock and Sanderson, 1991, Cartwright et al., 1996, Mansfield and Cartwright, 2001, Peacock, 2002, Soliva and Benedicto, 2004, Fossen and Rotevatn, 2016).

Relay 2 is a footwall-breached relay located between Faults 2 and 3. It occurs at a *c.* 5 km long bend in the map-view trend of the Thebe Fault Complex. This bend is associated with a local reduction in throw of *c.* 220 m and defines a clear change from the dominant N-S-to-NNE-SSW strike to a E-W-to-ESE-WSW strike (Fig. 5.4 and 5.6a). The bend is also spatially related to one of three throw 'plateaus' observed on Fault 2 (Fig. 5.6b). Relay 2 is spatially related to a marked increase in throw of *c.* 400 m at its southern end where it meets the predominant N-S-to-NNE-SSW-striking, northernmost part of Fault 3 (*c.* 27.5 km along the fault; see Fig. 5.6a and b).

Relay 3 is located between Fault 3 and 4 and appears to define a footwall-breached relay. Itis associated with a *c.* 3 km long fault bend, with the local fault strike changing from N-S-to-NNE SSW to NNW-SSE. Relay 3 is also spatially related to a local throw reduction of *c.* 130 m (*c.* 34 – 37 km along the fault; see Fig. 5.6a and b).

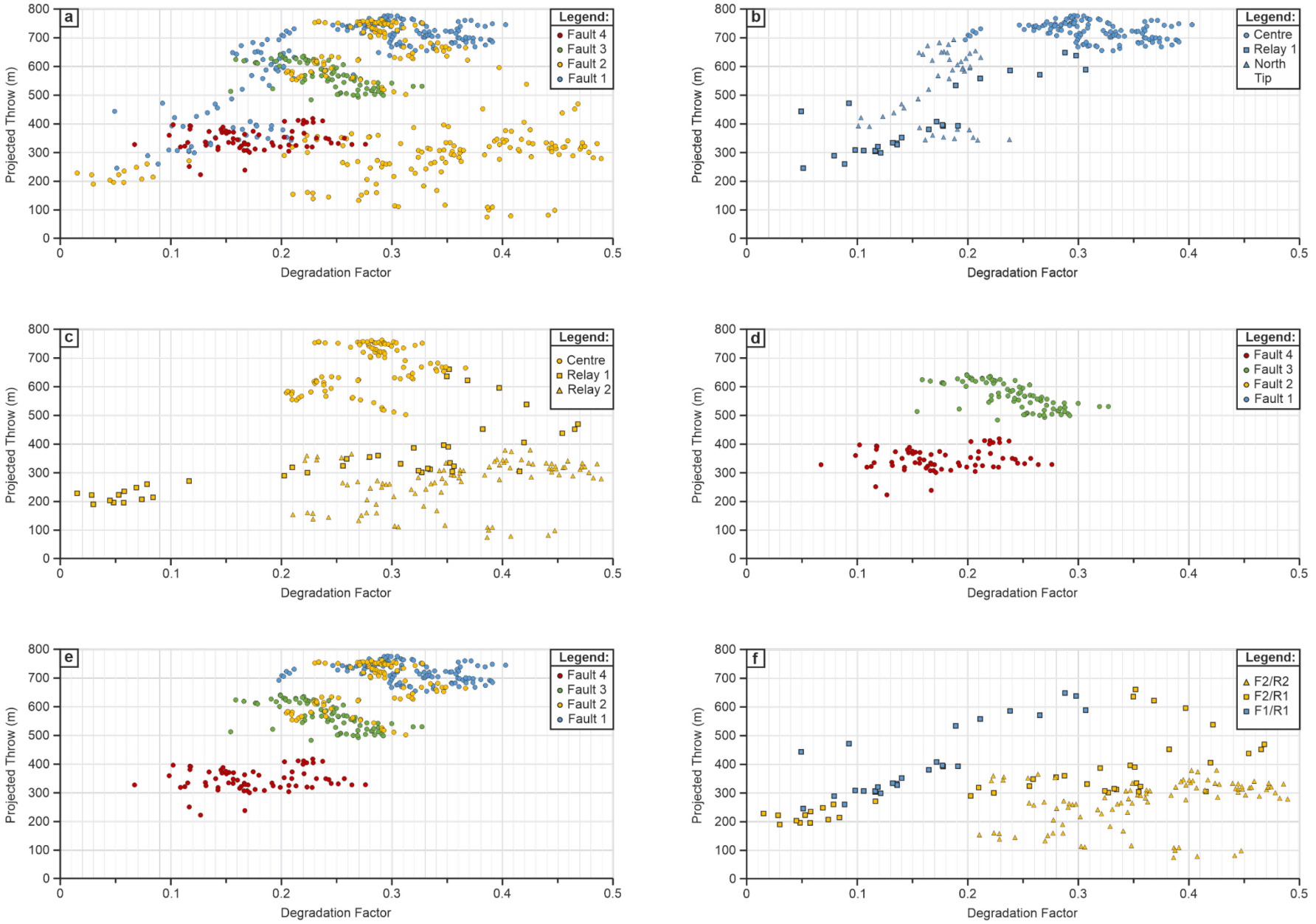


Figure 5.7. Throw-degradation factor (t-DF) plots| Projected throw-degradation factor plots for the Thebe Fault Complex. (a) t-DF data for the degradation-fan complexes of the TFC. (b) t-DF plot for Fault 1. (c) t-DF plot for Fault 2 (d) t-DF plot for Faults 3 and 4. (e) t-DF plot for all data located at the centre of fault segments 1-4. (f) t-DF for relay zone 1 and 2.

5.6 Footwall Morphology

Fault-scarp degradation is widespread in the footwall of the Thebe Fault Complex (Fig. 5.3 and 5.6b). This footwall erosion is characterised by a high-amplitude, concave, low angle (6°) reflection that truncates the Mungaroo Formation. Erosion extends up to 1.6 km into the footwall although as we now describe, this, as well as the vertical (and total) amount of erosion, vary as a function of structural position (i.e., fault segment centre vs. relay zone) and fault throw (Fig. 5.2, 5.3, 5.6b and Fig. 5.7). DF on the Thebe Fault Complex range from 0 (i.e., where degradation is not present, typically towards the fault tips) to *c.* 0.5 (i.e., the magnitude of degradation is 50% of the true fault throw).

Throw on Fault 1 is 200-800 m, with DF values ranging from 0.05 – 0.41 (Fig. 5.7). Fault 1 displays a broadly positive relationship between throw and degradation factor, i.e., degradation factor and thus total erosion increases as a function of increasing fault throw (Fig. 5.7b). The highest throw and DF values for Fault 1 are > 700 m and *c.* 0.2 – 0.4 DF, respectively, occurring at the centre of the fault segment (Fig. 5.7b).

Throw on Fault 2 varies from *c.* 75 to 760 m, with associated DF values ranging from 0.01 – 0.49 (Fig. 5.7c). In a similar manner to Fault 1, Fault 2 displays a broadly positive relationship between throw and degradation factor (Fig. 5.7b and c), with the highest throw (500 – 760 m) and DF (0.2 – 0.37) values also occurring at the centre of the fault segment (Fig. 5.7c). The sections of Relays 1 and 2 associated with Fault 2 are notably anomalous in that they are the only sections with DF >0.4, despite not being associated with the highest projected throw values for either Fault 2 or the Thebe Fault Complex as a whole (Fig. 5.7a and c).

For faults 3 and 4, footwall degradation occurs exclusively at the centre of the fault segments and is absent at fault tips (Fig. 5.6b). Throw on Fault 3 varies from *c.* 500 to 640 m, with associated DF ranging from 0.15 – 0.33 (Fig. 5.7d), whereas throw on Fault 4 is smaller, varying from *c.* 200 – 420 m, with associated DF values ranging from 0.07 – 0.28 (Fig. 5.7d).

In summary, t-DF plots reveal that greatest fault throw and magnitude of footwall erosion (as expressed by DF) are typically being encountered towards the geometric centre of the fault segments. More specifically, Faults 1 and 2, which exhibit the greatest throws, are the only segments with DF values >0.4, whereas faults 3 and 4, which have lower maximum throws, have DF values <0.35 (Fig. 5.7). We thus interpret that the magnitude of footwall degradation is broadly controlled by fault throw and the related footwall relief (Fig. 5.7). There are two key exceptions to this general relationship, at the north and southern tips of Fault 2, in relays 1 and 2. Here, anomalously large degradation factors are observed, given these are locations of relatively modest throw (Fig. 5.7a and c). We discuss potential reasons for this later, after we assess the relationships between the footwall erosion and the hangingwall fans' depositional architecture.

5.7 Hangingwall Structural Style

The hangingwall of Fault 1 contains a fault-perpendicular anticline that separates two synclinal depocentres (Fig. 5.4 and 5.6b). The anticline corresponds to local minima in throw and vertical erosion; however, DF does not show a local minimum (Figs 4 and 6b and c). In addition to fault-perpendicular folding, the hangingwall of the Thebe Fault Complex is deformed by numerous, relatively small (maximum throw of 80 m and 2-17 km long) normal faults that strike sub-parallel to, but which are antithetic (i.e., SE-dipping) to, the main structure (Fig. 5.4 and 5.8). Notably, these faults display no evidence of fault scarp degradation, despite their relatively long trace lengths (Fig. 5.3, 5.4 and 5.8) (Pan et al., 2021).

We interpret that fault-perpendicular folding in the hangingwall of Fault 1 occurred in response to fault growth, defining the position of linkage between the two smaller, precursor segments now forming Fault 1. This interpretation is supported by the observation that this is also the location of a throw minimum (Fig. 5.4 and 5.6). As we explore further below, we propose that folding did not impact the style or magnitude of footwall degradation, because segment linkage occurred

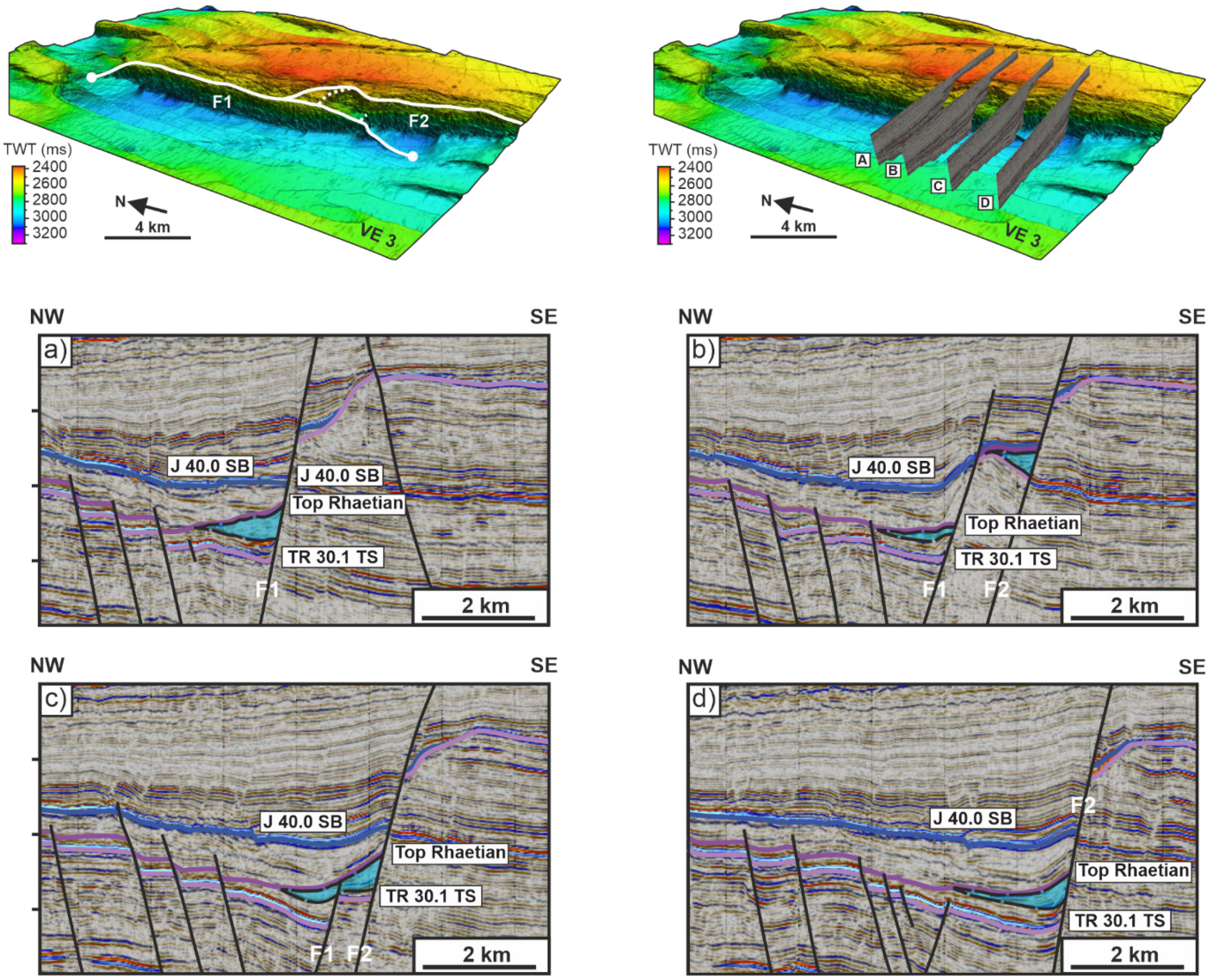


Figure 5.8. Along strike variability of a footwall-scarp degradation complex| (Top left) TWT structure map of F1, F2 and their breached relay zone. (Top right) location of seismic type sections along strike and down-dip of the relay ramp (a-d). (Below) (a-d) Type seismic sections showing the variability in hangingwall fan thickness along strike and down-dip of the F1/F2 breached relay ramp. Moreover, highlighting (a) thicker fan deposits in the F1 hangingwall; (b) the presence of basin-dipping reflections downlapping onto the relay ramp and (c) F1 cross-cutting the base of the hangingwall fan. Degraded fan material = blue shade.

prior to the onset of major footwall uplift and erosion. If there were any along-strike variations in magnitude of erosion, related to along-strike variations in fault throw, we interpret that these were essentially smoothed out as the fault accumulated throw, and its footwall was uplifted and more deeply eroded. The lack of erosion of the footwalls of the low-throw, antithetic faults also suggests that the presence and amount of fault-scarp degradation is directly controlled by the amount of fault throw (see section 6).

5.8 Hangingwall Stratigraphic Architecture

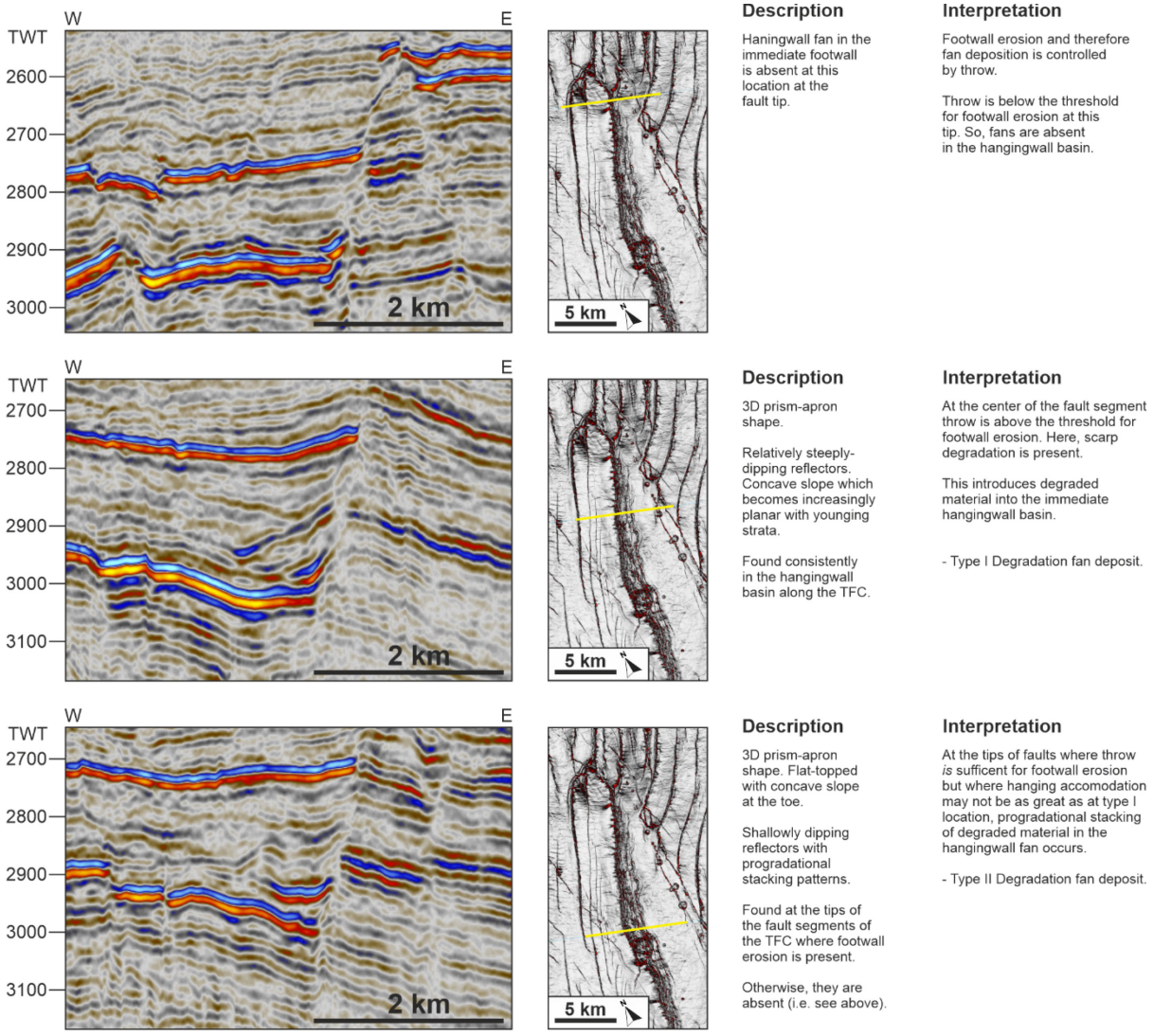


Table 5.1. Seismic facies analysis of footwall-derived fans | Table showing key seismic cross-sections of the fault-scarp degradation complex and presenting results from the seismic facies analysis conducted on the hangingwall fans.

Hangingwall fan deposits are best developed along the northernmost segments of the Thebe Fault Complex (i.e., faults 1 and 2), where throw, vertical erosion, and degradation factor are greatest (Fig. 5.6b, 5.7, 5.8; see also Table 5.1). Fans are absent at the northernmost tip of Fault 1, where throw (and accordingly footwall uplift and erosion) decreases to zero. The fans downlap the Top Brigadier Formation along the entire length of the fault complex, suggesting geologically synchronous deposition (see below; see also Figs 2 and 8) (Table 5.1). The upper surface of the

fans dip basinward, creating a wedge-shaped geometry in cross-section that thins basinward (Figs 2 and 8) (Table 5.1). The fans are classified into two types; type I and II (Table 5.1). Type I fans consist of relatively steep, basinward-dipping reflections and a concave upper surface. (Table 5.1). Type II fans are defined by progradational stacking pattern and exhibit distinctly flat-topped geometries on their clinoforms; these types of fans are located exclusively towards the southernmost tip of Fault 1, within Relay 1 (Table 5.1).

We interpret that the Type I deposits to have been deposited in base levels which could accommodate the rate of deposition of footwall-derived hangingwall fans. However, towards fault tips where throw is lower Type II deposits have distinct flat-topped geometries, potentially due to their upper surfaces being closer to base level. We also suggest that due to their spatial distribution being exclusive to the immediate hangingwall of Fault 1 and 2 and both Type I and II displaying basinward dipping reflections, that material from scarp degradation is deposited as footwall-derived fan deposits in the hangingwall basin (Fig. 5.2 and 5.8) (Table 5.1). We now test this hypothesis via across fault volume balancing of material eroded from the footwall and deposited in the hangingwall.

5.9 Across-Fault Balancing of Sediment Volumes

Volume balancing allows us to investigate the relationship between the amount of material eroded from the footwall of the fault complex and the amount deposited in the hangingwall (V_{hw}). (Fig. 5.9). V_{fw} is defined as the volume between the pre-erosion scarp surface and the present day fault scarp surface and V_{hw} is defined by the volume between the top and base fan surfaces (Fig. 5.5). Where $V_{fw}>V_{hw}$, we consider that eroded material bypassed and was perhaps redistributed away from the immediate hangingwall of the fault complex, perhaps even being transported outside of the half-graben bound by the Thebe Fault Complex (Fig. 5.9). In contrast, where the volume of material deposited in the hangingwall fan deposits exceeds that of the local footwall erosion (i.e., $V_{hw}>V_{fw}$), we infer these are areas in receipt of material redeposited from elsewhere within the hangingwall (or perhaps the broader study area) (Fig. 5.9).

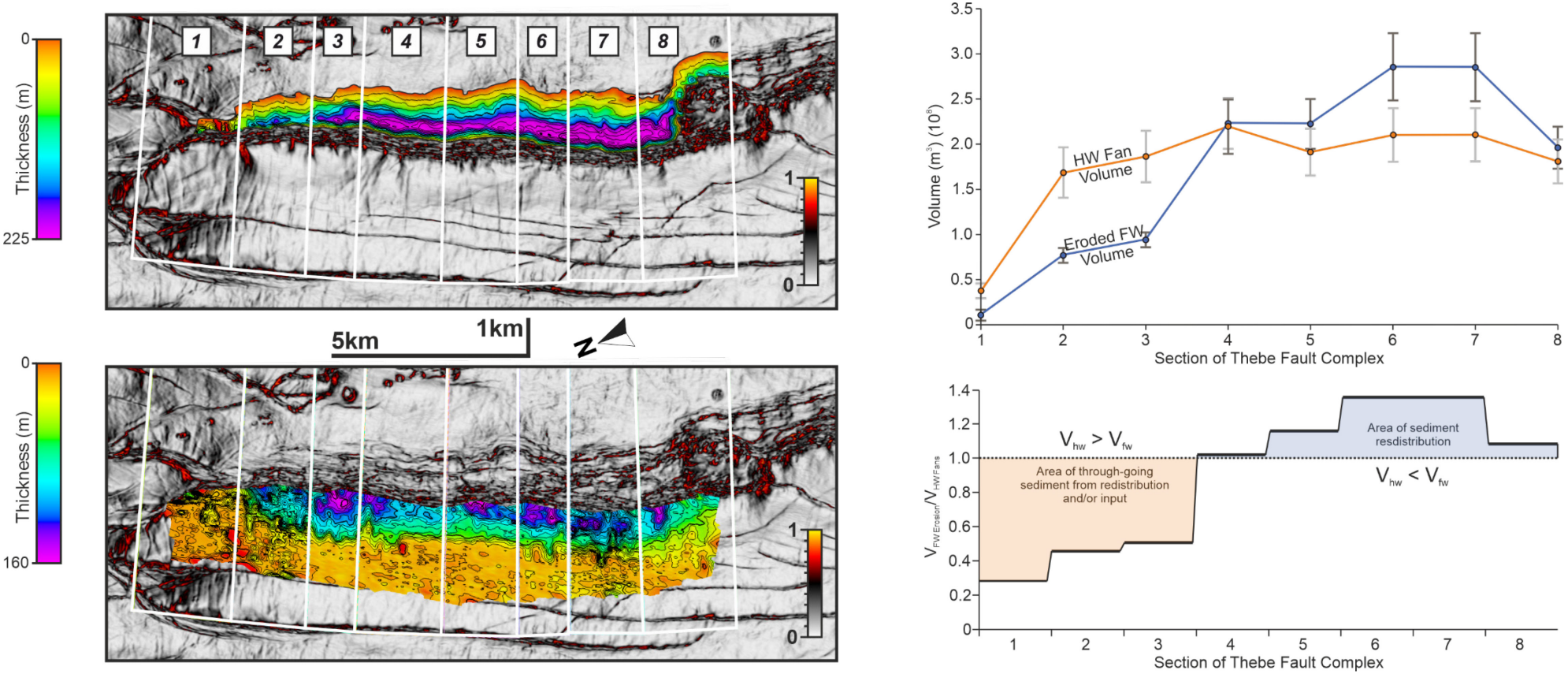


Figure 5.9. Across-fault volume balancing of sediment volumes| (Left) Map view of the thickness and areal extent of footwall degradation (top); and the thickness of the degraded hangingwall fan deposits along Fault 1 (see Fig.1). Section 8 constitutes the northernmost area of Relay 1 and Fault 2. (Right) Hangingwall fan and footwall erosion comparative volumes along strike for sections 1-8 (top); and a V_{fw}/V_{hw} ratio graph depicting areas of through-going sediment from redistribution and/or input (orange) and areas of sediment redistribution (blue) for section 1-8 (bottom).

We focus our analysis on fault 1, where hangingwall fans are best-developed, sub-dividing this portion of the Thebe Fault Complex into eight areas (see reasoning and methods above in section 5.3.2.3). Areas 1 – 3 have V_{fw}/V_{hw} ratios < 1 with values of 0.29, 0.46 and 0.51, respectively (Fig. 5.9). Areas 6 and 7 have Vfw/Vhw ratios > 1, each having identical values of 1.36 (Fig. 5.9). Areas 4, 5 and 8 are the only locations where V_{fw}/V_{hw} *c.* 1.0, with values of 1.00, 1.16 and 1.08, respectively (Fig. 5.9). For areas 1-4, where $V_{hw}>V_{fw}$, the volume of hangingwall fan-deposited material exceeds that of material degraded from the footwall by 1.953 x 10^8 m^3 (Fig. 5.9). In contrast, for areas 5-8, where $V_{fw}>V_{h}w$, the volume of material eroded from the footwall exceeds that of hangingwall fan-deposited material by 1.907 x 10^8 m^3 (Fig. 5.9).

The amount by which total hangingwall fan volume exceeds total footwall eroded volume within areas 1 – 4, is c. 98% of the amount by which footwall eroded volumes exceeds hangingwall fan volume within areas 5 – 8. Thus, we suggest along-strike redistribution of footwall-derived material northwards from areas 5 – 8 to areas 1 – 4 (Fig. 5.9). However, we note that the total volume of sediment eroded from the footwall (V_{fw} = 1.292 x 10^9 m^3) broadly balances with the total amount of material deposited in the hangingwall fans (V_{hw} = 1.296 x 10^9 m^3), meaning that 99.6% of the former was essentially captured in the immediately adjacent depocentres within the fans. In addition to these observations, the footwall does not exhibit bypass transport systems (Fig. 5.10).

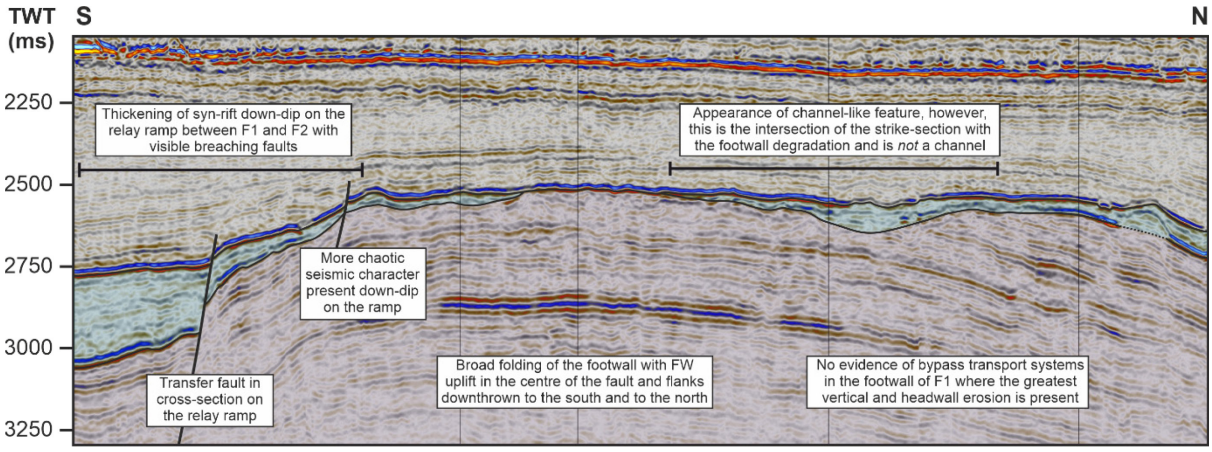


Figure 5.10. The absence of sediment bypass transport systems on the footwall of the Thebe Fault Complex| Along strike section of the F1 footwall in the Thebe Fault Complex and down-dip section of the relay ramp and stratal thickening in the hangingwall of F2. Pre-rift (purple shade) Syn-rift (Blue shade) and Post-rift (no shade).

We thus interpret that the hangingwall fans in the immediate footwall of the Thebe Fault Complex are almost completely footwall-derived. To put it another way, the source-to-sink system was relatively closed, suggesting footwall morphology, fault geometry and growth, and hangingwall stratigraphic architecture are linked. In addition, we suggest that the volume imbalance between the footwall and hangingwall indicates potential axial transport of footwall-derived sediment in the hangingwall basin, which could have been accomplished by a combination of surface currents and hangingwall architecture. We suggest that surface currents in a submarine environment may be a viable mechanism to achieve along-strike redistribution of footwall-derived material northwards. In addition, we suggest that this redistributed material may have been structurally trapped in the northern end of the basin because the thickest fans in the hangingwall are found on the boundary of section 3 and 4, abutting against a prominent hangingwall anticline (Fig. 5.9 and 5.11).

5.10 Relay Zones, Footwall Degradation and Fan Deposition: Relay 1 Case Study

Having established that throw controls the broad patterns of footwall erosion and that hangingwall fans are seemingly exclusively footwall-derived (see 4.1 and 4.2), we here focus on Relay 1 to more precisely establish the timing of faulting, footwall erosion, and hangingwall fan deposition (Fig. 5.8 and 5.9). We focus on Relay 1 given the related section (i.e., section 8) is characterised by V_{fw}/V_{hw} *c.* 1 (Fig. 5.9), suggesting sediment deposition in this location is principally governed by local faulting, and related footwall and uplift and erosion.

Along the length of Relay 1, fan deposits are present both in the hangingwall of the main segments (i.e., faults 1 and 2) and on the footwall-breached relay ramp (Fig. 5.9a-d). Immediately north of the relay zone at cross-section A, Type I fans downlap the Top Brigadier Formation and younger strata onlap their upper surface (Fig. 5.2 and 5.8a-d). At cross-section B, which is located *c.* 2 km further south, vertical erosion on the footwall is significantly less compared to that observed

further north (i.e., cross-section A; Fig. 5.6a-b and 5.8b). This is accompanied by a reduction in the cross-sectional area of fan material observed in the hangingwall (Fig. 5.8a and b). The fan deposits also downlap onto the breached relay ramp, forming 'perched' fan deposits. The upper surface of these deposits are coincident with the J 40.0 SB surface on the eroded Fault 1 scarp (Fig. 5.8b and 5.9b). At the southern, downdip end of Relay 1, at cross-section C, throw on Fault 1 is greatly reduced, and Fault 2 represents the main, basin-bounding fault (Fig. 5.8c). Here, the perched fan deposits observed *c.* 2 km further north are absent (Fig. 5.8c). The cross-sectional area of the hangingwall fan again increases, as does the vertical erosion occurring on the footwall, with both being greater than observed up-dip on the ramp on cross-section B (Fig. 5.8b and c). The upper surface of the fan is coincident with the Top Rhaetian surface, with its base surface offset by the southern tip of Fault 1 (Fig. 5.8c). At cross-section C, Type I fans downlap the Top Brigadier Formation. Beyond Relay 1 at cross-section D, Fault 2 defines the main, basin-bounding fault, and the fan is geometrically similar to that observed at cross-section A (Fig. 5.8a and d).

We interpret that relay zone formation and therefore overlap between Faults 1 and 2 occurred broadly coeval with or immediately prior to, the onset of footwall degradation given footwall-derived fans form 'perched' deposits on the now-breached relay ramp (Fig. 5.8). This interpretation is based on the observation that at cross section B the top and base surfaces of the fans are completely offset by Fault 1, but that at cross-section C only the base of fan is offset and the fan has not been rotated post-depositionally (Fig. 5.8). We suggest that the fault dissected the fan at cross-section C relatively later than at cross-section B, and that fan deposition potentially occurred prior to the fault tip propagating to the location of cross-section C. Given that these perched deposits are not supplied by by footwall channels to those at the fault segment centres and are similar in seismic facies (i.e., Type I; Table 5.1 and Fig. 5.2, 5.8 and 5.10), we interpret them to be derived from material eroded from the immediate footwall (Gawthorpe and Leeder, 2000). Finally, the observation that perched fans are present on the early-formed relay ramp suggest that Faults 1

and 2 had to have achieved fault segment growth, tip interaction and relay ramp formation somewhat synchronous with, and potentially prior to, the onset of degradation (Fig. 5.11).

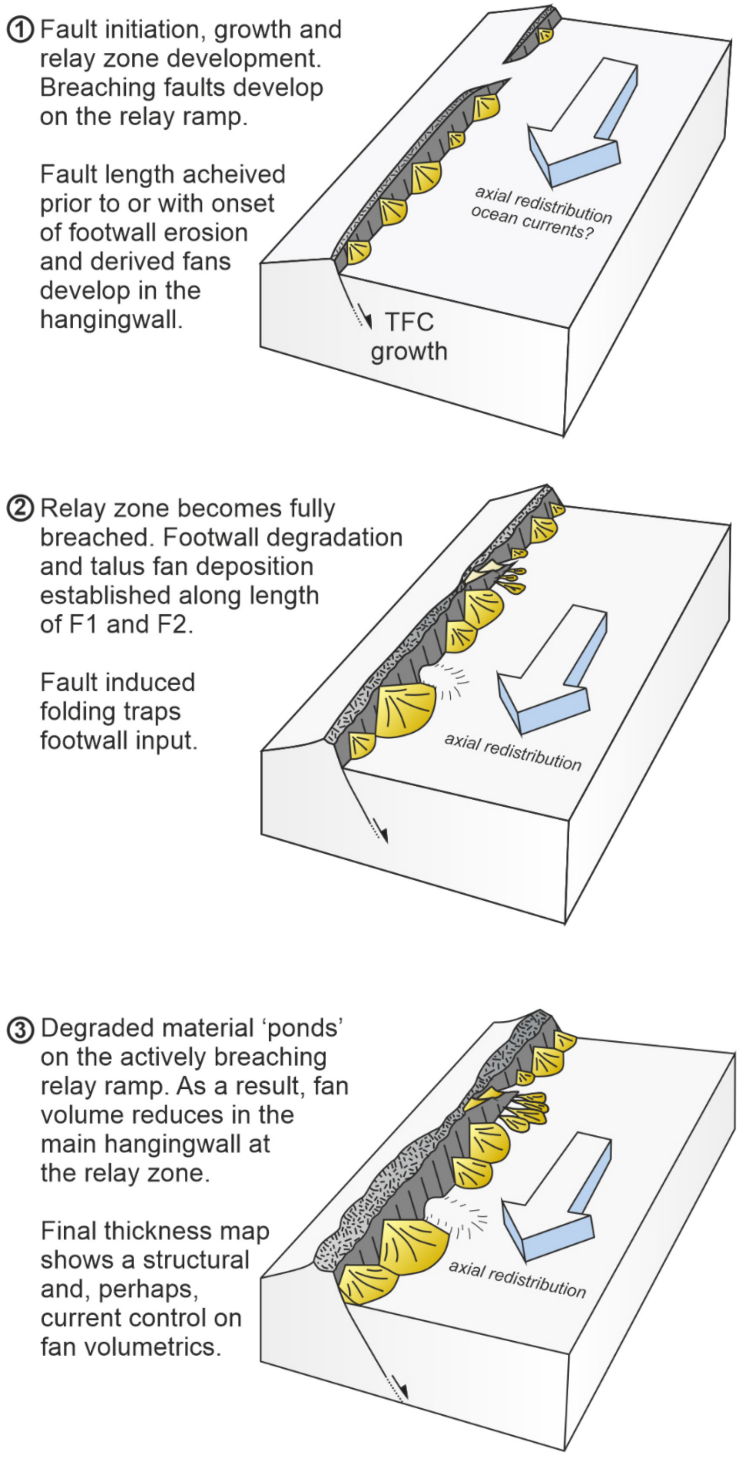


Figure 5.11. Evolution of a fault-scarp degradation complex and accompanying footwall-derived fans| Schematic diagrams of the evolution of the Thebe Fault Complex and its footwall-derived hangingwall fans showing: (i) all base surfaces of hangingwall fans downlap onto the same surface (2); (ii) footwall degradation was active during relay zone formation evidenced by 'ponded' degraded material on the relay ramp (3); and (iii) headwall erosion decreases towards fault tip (4)(See Fig. 5.6). This model occurred within *circa* 10Ma based on the observation that all the base surfaces of the fans downlap onto the top brigadier, in addition to the fans' upper surfaces being onlapped by the Murat siltstone (10 Ma older).

5.11 Discussion

5.11.1 Control of Fault Throw on Footwall Erosion Patterns

Throw and erosion are positively correlated, being greatest at the geometric centre of fault segments, and decreasing towards the tips (Fig. 5.6). This suggests a coupled relationship between throw accrual, footwall uplift and the erosive process that modified the fault scarp. Studies of active faults in the Basin and Range Province, USA (Densmore et al., 2004) and Spercheios Basin, Greece (Whittaker and Walker, 2015), and subsurface studies of now-inactive, buried faults in the Halten Terrace, Offshore Mid-Norway (Elliott et al., 2012) have previously established that the magnitude and along-strike distribution of fault throw are a first-order control on footwall relief and footwall erosion patterns. Spatial variations in the bedrock lithology may also control the patterns and magnitudes of footwall erosion (e.g., Eliet and Gawthorpe, 1995, McLeod and Underhill, 1999, Bilal et al., 2020). In the case of the Thebe Fault Complex, we lack sufficient well data to truly assess the role of footwall lithology. However, if this was the key control, we might expect a weaker relationship between fault throw and erosion magnitude (Fig. 5.6, 5.7 and 5.10). We therefore suggest that footwall erosion is intrinsically linked to total throw on the basin-bounding fault system, in a similar way to that seen in other field and subsurface geomorphological analyses of footwall erosion along seismic-scale faults (e.g., Elliott et al., 2012, Whittaker and Walker, 2015).

5.11.2 Constraining Fault Growth Using Fault-Scarp Degradation Complexes

Quantitative analysis of the geomorphology of normal fault footwalls has been used to constrain fault kinematics in areas of active continental extension (Goldsworthy and Jackson, 2000, Tsodoulos et al., 2008, Whittaker and Walker, 2015), but has only rarely been applied to the study of buried, inactive structures imaged in the seismic reflection data (e.g., Elliott et al., 2012). By applying some geomorphological techniques to seismic reflection data, we have shown that patterns and more specifically, the magnitude of footwall erosion is linked to total throw on the

basin-bounding fault system (Fig. 5.6, 5.7 and 5.9). We can also constrain the timing of fan deposition and related fault growth, using our case study of Relay 1. First, fans downlap on the same seismic reflection (top Brigadier Formation) along the length of the fault complex, suggesting deposition was geologically synchronous (Fig. 5.2 and 5.8). Second, the stratigraphic architecture of fan deposits on at Relay 1 suggest deposition syn- or immediately post-linkage of faults 1 and 2 on the intervening relay ramp, indicating that fault lengthening and tip overlap had occurred by this time (Fig. 5.8). Finally and perhaps most critically, the Murat Siltstone and Athol Formation onlap onto the (Top Rhaetian) surface capping the fans, indicating deposition (and thus degradation, fault growth, and footwall uplift within the first *c.* 10 Ma of rifting history (Fig. 5.2 and 5.8). This corresponds to the time elapsed between the Latest Rhaetian (i.e., the top Brigadier Formation, defining downlap surface for fans) and the latest Sinemurian (i.e., strata onlapping onto the fans top surface) (Fig. 5.2 and 5.8), representing only *c.* 12% of the total *ca.* 85.5 Myr rift history (Pan et al., 2021). Given this, we argue that growth of the Thebe Fault Complex was more consistent with the hybrid fault growth model (Walsh et al., 2002, Jackson et al., 2017, Rotevatn et al., 2019, Pan et al., 2021). This model would facilitate an early period of fault-lengthening in which relay zone formation and segment linkage can occur early in fault life as we observe for Relay 1. In addition, this model also accommodates sufficient throw accrual to facilitate the footwall uplift and erosion, required for deposition of the degraded fan deposits on the relay ramp, early in the fault life as seen for the Thebe Fault Complex (Within initial < 10 Myr and < 12% of rift history) (Fig. 5.11)

Using fault-scarp degradation complexes to constrain fault growth is a technique which has, to our knowledge, not been applied in the subsurface. Applying this technique requires the prerequisites that: (i) footwall erosion is correlated to fault throw; and (ii) fan deposits are footwall-derived. These two prerequisites can be evaluated by: (i) calculating headward and/or vertical erosion along the length of the fault scarp; and (ii) across-fault volume balancing of footwall erosion and fan deposits, respectively, as demonstrated in this study. The prerequisites mean that the spatial and

temporal distribution of footwall-derived fans is related to fault lengthening and throw. In such settings, critical fault growth characteristics can be deduced using this method. For example, the presence of fans increasing along the length of the fault with younging strata would indicate fault lengthening and constrain the period over which it occurred.

5.12 Conclusions

- Throw distribution along the Thebe Fault Complex shows throw maxima at the centre of fault segments and decreasing throw towards fault tips. Throw minima show the loci of precursor segment linkage points as the fault grew.
- Scarp degradation mimics fault throw along the length of the Thebe Fault Complex. The absence of scarp degradation on Faults 3 a and b and the antithetic faults in the hangingwall basin - which have significantly lower throw than those faults where scarp degradation is widespread - indicate to accumulative throw being a primary control on footwall erosion.
- Given these patterns and the absence of footwall incisional channels, accumulated throw is established as the main control on scarp degradation and the amount of degraded material input into the hangingwall basin. Thus, concluding that fault scarp degradation is inherently linked to throw and structural variations along strike.
- The case study of Relay 1 highlights that the processes required for deposition of degradation fans into the sediment-starved basin such as throw accumulation, footwall uplift/erosion, and deposition either preceded or occurred in-tandem with the onset of relay zone formation and fault linkage. Given the relationship of the upper fan deposits' surface to the onlapping Athol Formation these processes must have occurred in < 10 Ma from the onset of rifting – only < 12% of the rift history.
- Thus, the fault-lengthening required for fault tip interaction and relay zone formation, in addition to the throw accrual for footwall erosion and subsequent deposition of degraded

fans, also occurred within < 12% of the fault life. Thus, the Thebe Fault Complex and in particular Faults 1 and 2 grew in a manner most conducive to the hybrid fault growth model.

- Finally, the geomorphological techniques applied here, namely footwall geomorphology, volume balancing of the associated degraded fan deposits, and analysis of their temporal and spatial distribution have been able to constrain fault growth of seismic-scale, basin-bounding faults in a sediment-starved setting. We propose that this method can be used in any sediment-starved setting where fault scarp-degradation complexes are present.

Acknowledgements

The work contained in this publication contains work conducted during a PhD study undertaken as part of the Natural Environment Research Council (NERC) Centre for Doctoral Training (CDT) in Oil & Gas and is fully funded by NERC whose support is gratefully acknowledged. We also thank Geoscience Australia for their ongoing commitment to making these and a plethora of other data available for academic use. We thank Schlumberger for providing access to Petrel software.

6

Throw Rate Variability on Segmented Normal Faults Over Geological Timescales, NW Australia

Preamble

DR interpreted the data, wrote the manuscript, and drafted the figures presented in this chapter. Billy Andrews from University of Plymouth provided the computational code and method for the calculation of fault throw and throw rates. CALJ, RB and BA provided insightful input into the interpretations and the development of analytical methods and contributed excellent feedback when writing the final manuscript.

This manuscript is prepared and formatted for submission to the Journal of *Structural Geology*.

Abstract

A key process during fault growth by segment linkage is the development and breaching of relay zones, with the newly formed breaching fault facilitating linkage of precursor segments. Despite the importance of breaching faults, little is known about the throw rates present on breaching faults and how they may influence the presence and persistence of local throw minima at relay zones. Recent studies on young (15kyr) active faults suggest that breaching fault throw rates result in the removal of throw minima in as little as <1 Myr. However, this is at odds with observations of ancient, tectonic faults that show that throw minima persist over geological timescales. Here we use the Glencoe and Thebe 3D seismic reflection surveys from the NW Shelf, offshore Australia to constrain throw rate variability on breaching faults and their adjacent segments over geological timescales. We investigate this using two examples of relay zones, one that is partially breached in the Thebe survey and one that is double breached in the Glencoe survey. We find that the maximum throw rates on the Thebe and Glencoe relay zones are found on their breaching segments (13.4 m/Myr and 47.9 m/Myr, respectively) and that this represents a 48-58% increase in maximum throw rates from their adjacent segments. However, we also find that these rates only persist for a short period of time relative to the overall fault life over geological timescales (4-13% of the total rifting period, respectively). We argue that high throw rates on breaching faults persist for only a short period of the faults lifespan and that we reconcile and explain why active, young faults show breaching fault throw rates that could remove throw minima in as little as < 1 Myr, despite commonly observing throw minima in ancient examples of relay zones that were active over geological timescales.

6.1 Introduction

Normal faults grow by segment linkage (Peacock and Sanderson, 1991, Cartwright et al., 1995, Mansfield and Cartwright, 2001, Jackson et al., 2002, Fossen and Rotevatn, 2016). During this process, relay ramps form between adjacent, overlapping fault segments, with the breaching of ramps leading to the formation of longer structures (Peacock and Sanderson, 1991, Gawthorpe and Hurst, 1993, Cartwright et al., 1995, Huggins et al., 1995, Mansfield and Cartwright, 2001, Peacock, 2002, Jackson et al., 2002, Fossen and Rotevatn, 2016). Breached relay ramps (i.e., zones of paleo-linkage) are often defined by, and can thus be detected by, local throw minima (Fig. 6.1a) (Peacock and Sanderson, 1991, Peacock and Sanderson, 1994, Trudgill and Cartwright, 1994, Giba et al., 2012, Soliva and Benedicto, 2004). Extensive literature on relay zones have studied a breadth of concepts such as: relay zone geometry (e.g., Peacock and Sanderson, 1994, Huggins et al., 1995, Kristensen et al., 2008, Camanni et al., 2019), relay bed rotation and folding (e.g.,Trudgill and Cartwright, 1994), relay structural elements (i.e., relay bends, branch-lines and transfer faults) (e.g.,Gawthorpe and Hurst, 1993, Walsh et al., 1999) and throw transfer and segment linkage (e.g., Peacock and Sanderson, 1991). However, considering they are a fundamental structural element in the growth of large, seismogenic, normal faults, comparatively little research has focused on the kinematics of relay-breaching faults. In particular, the way in which throw rates vary over geological time (i.e., $>10^5$-10^6 Myr) on relay breaching faults is poorly constrained. The importance of understanding throw rate variability is clear when we consider their control on the occurrence of seismic hazards on active faults and their influence on the geometric development of faults, which controls landscape evolution (e.g., Faure Walker et al., 2009, Cowie et al., 2012, Carafa et al., 2022). Additionally, since fault grow by segment linkage, the rate at which relay breaching occurs has implications for fault growth models (e.g., Walsh et al., 2002, Jackson et al., 2017, Rotevatn et al., 2019).

Where throw rates on relay-breaching faults have been studied, it has been done using geometric and geomorphic observations from relatively young (i.e., <20 kyr), active faults. These studies

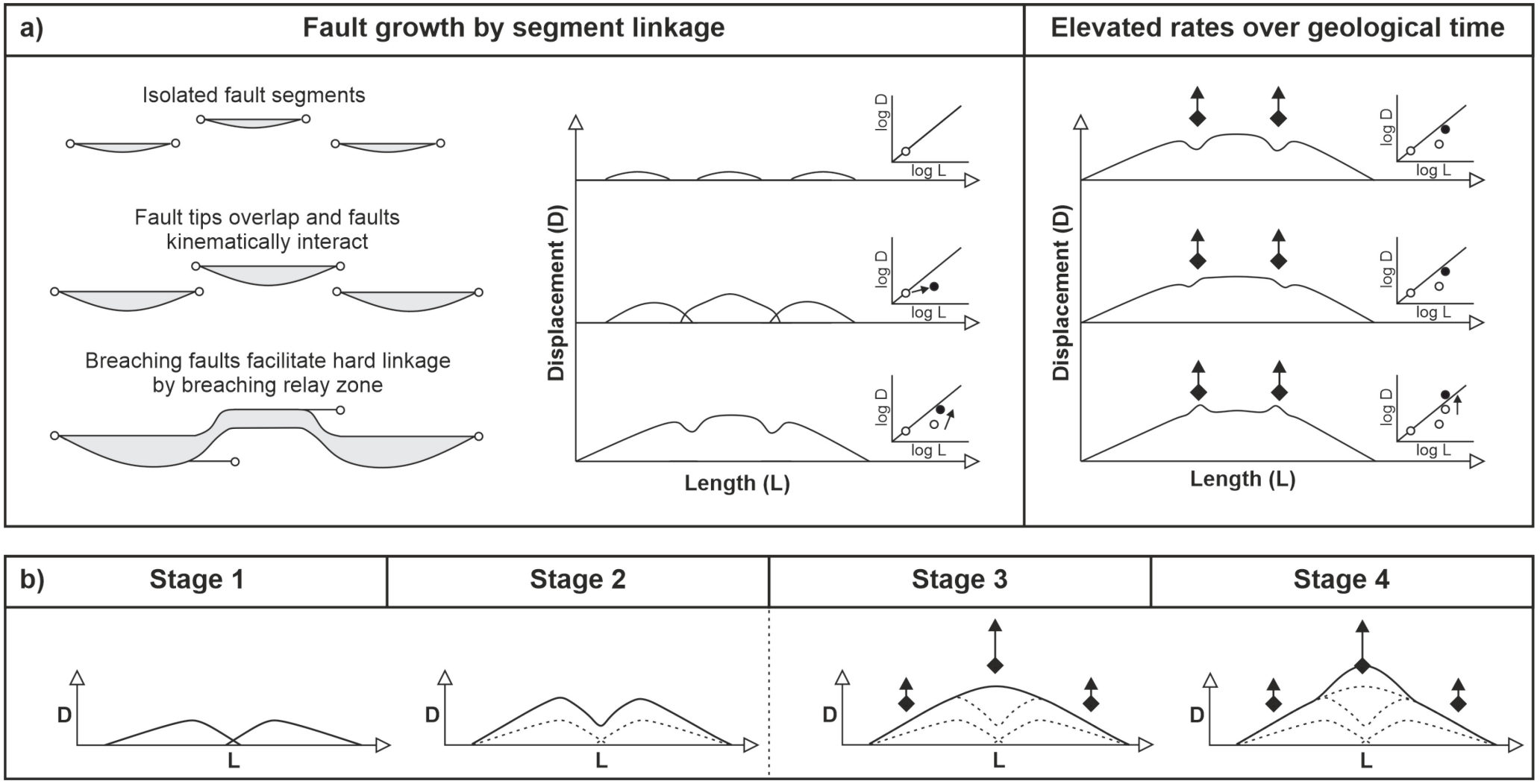


Figure 6.1. Fault growth by segment linkage and predictions of elevate throw rates at locations of throw minima over geological timescales| (a) (Left) Schematic diagrams showing the displacement length development during fault growth by segment linkage. (Right) Schematic diagrams showing the development of displacement minima if breaching faults were to attain higher displacement rates than their concomitant faults over geological timescales. (b) A schematic diagram of growth by segment linkage and the end member profile for D-L, if higher displacement rates on breaching faults persisted over geological timescales

show that over these relatively short timescales, relay-breaching faults exhibit markedly higher throw rates than their adjacent segments, despite still being defined as areas of lower total throw (e.g., Faure Walker et al., 2009, Faure Walker et al., 2015). If such kinematics were to persist over geological timescales, it is possible that throw minima could be removed at locations of paleo-fault segmentation and linkage (e.g., Commins et al., 2005), and that breached relays could even become local throw maxima (Fig. 6.1b). This prediction, however, appears at odds with observations from seismic reflection data imaging large, ancient tectonic faults that were active for millions to tens-of-millions of years, which indicate that breached relays are still defined by well-developed throw minima (e.g., Huggins et al., 1995, Pan et al., 2021; Fig. 6.1a). There is, therefore, a discrepancy between the post-linkage fault throw rates observed over relatively short timescales on still-active structures, and the geological record of total throw on ancient structures imaged in geophysical data.

In this study we investigate temporal and spatial changes in geological throw rates on relay-breaching faults and their flanking segments. We select the Glencoe and Thebe Relay Zones, Exmouth Plateau, offshore NW Australia, because (i) they differ in their maturity, insomuch that the Glencoe Relay Zone is a double-breached relay zone and the Thebe Relay Zone is a partially hangingwall-breached relay zone; (ii) both are very well-imaged in high-quality, 3D seismic reflection data; and (iii) nearby wells provide age constraints on syn-rift stratigraphy, allowing us to constrain the timing and tempo of fault growth, and relay formation and breaching (Fig. 6.2 and 6.3). Crucially, the geometries of these relay zones approximate those studied by Faure Walker et al. (2009), allowing for the key findings from their study regarding throw rates over timescales of thousands of years to be tested over geological timescales.

6.2 Geological Setting of The Exmouth Plateau

The North Carnarvon Basin is an epicratonic basin covering 535,000 km^2 in the westernmost region of the Paleozoic-Cenozoic basins comprising the Westralian Superbasin, NW Australia (Fig.

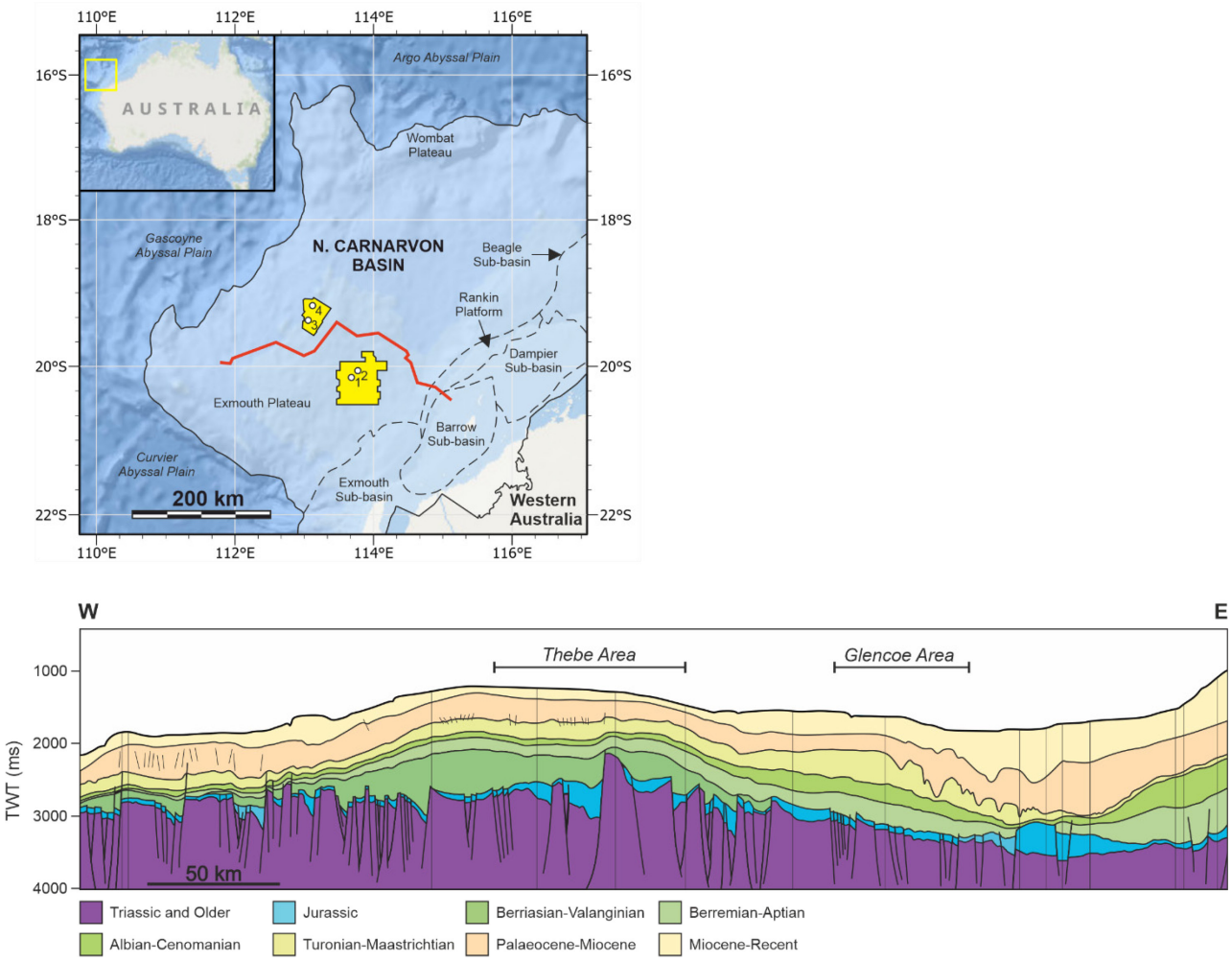


Figure 6.2. Study area location and regional overview| (Above) A location map of the North Carnarvon Basin showing the: (i) location of the Glencoe and Thebe seismic surveys and significant wells located within the study areas: 1 = Nimblefoot-1; 2 = Glencoe-1; 3 = Thebe-1 and; 4 = Thebe-2. (Below) A regional dip-section showing the structure and stratigraphy of the Exmouth Plateau and the area of the Plateau where the Thebe and Glencoe surveys are located. Section position is shown by the red section line on the geographic location map.

6.2). The major tectonic components of the North Carnarvon Basin are four NE-trending, sub-basins in the east and the 400 km-wide Exmouth Plateau in the west, which are separated by the Rankin Platform and Kangaroo Syncline (e.g., Deng and McClay, 2020, Lathrop et al., 2021) (Fig. 6.2).

The Exmouth Plateau is a NE-trending Mesozoic-Cenozoic plateau. The boundaries of the Exmouth Plateau to the south are defined by the inboard basins, whereas its outboard boundaries are defined by the Argo, Cuvier, and Gascoyne abyssal plains (Fig. 6.2) (Longley et al., 2002, Stagg, 2004, Bilal and McClay, 2022). Two main periods of extension controlled the structural evolution

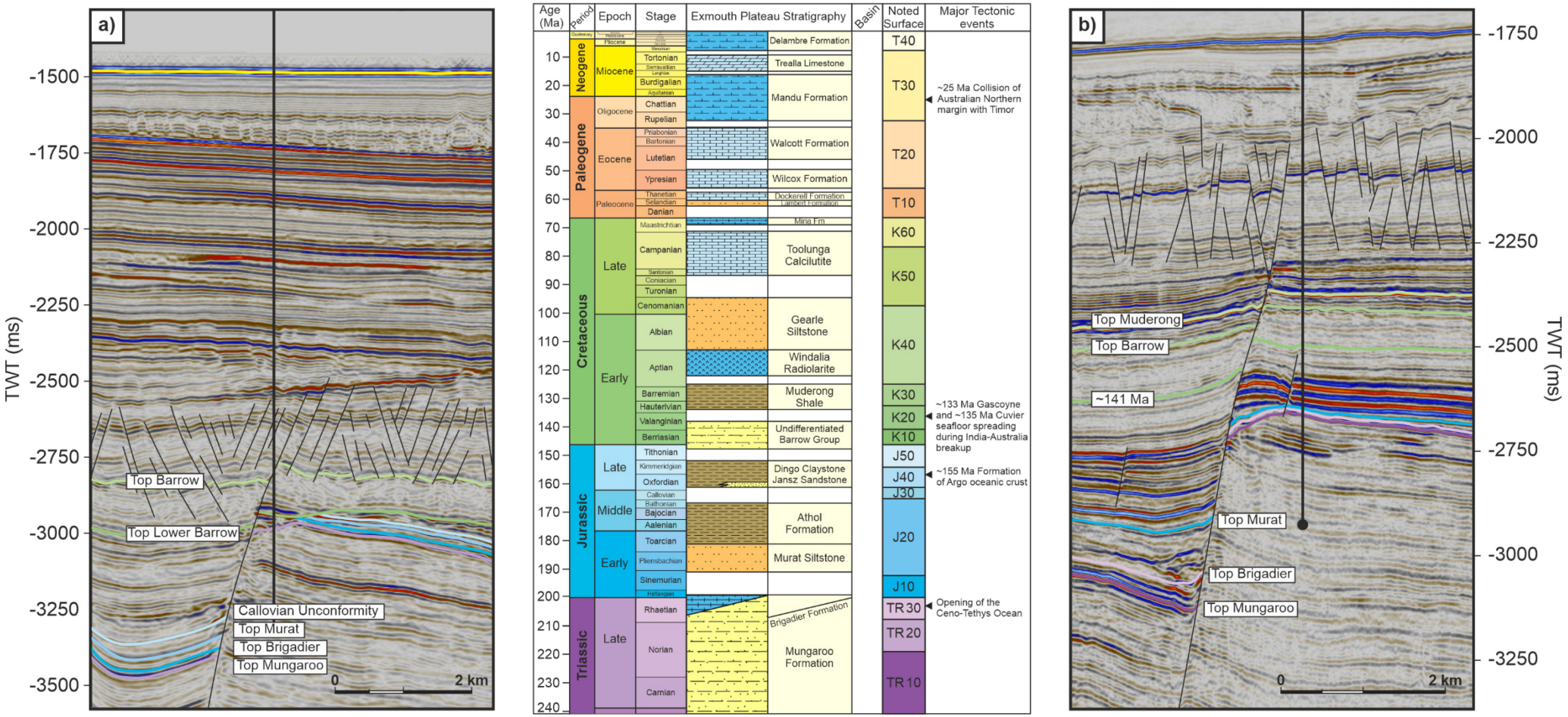


Figure 6.3. Stratigraphic column for the Exmouth Plateau | (a) A seismic cross-section at the Nimblefoot-1 well located on the footwall of relay zone studied in the Glencoe survey and showing the key stratigraphic surfaces used in our study. The surfaces are taken from well data for Nimblefoot-1 and Glencoe-1 wells, and Lathrop et al. (2021). (b) A seismic cross-section at the Thebe-1 well located on adjacent fault block to the relay zone studied in the Thebe survey and showing the key stratigraphic surfaces used in our study. The surfaces are taken from well data at Thebe-1 and from Pan et al. 2021. (Middle) A stratigraphic column for the Exmouth Plateau. Key tectonic events are taken from Barrett et al. (2021) and Bilal and McClay (2022).

of the Exmouth Plateau, namely the: i) a main syn-extensional phase, which occurred during the opening of the Cen-Tethys Ocean during the Latest Triassic – Earliest Jurassic, and that resulted in the formation of N-S to NNE-SSW-trending major fault blocks and bounding normal faults, and; ii) a reactivation phase, which occurring during the Early Cretaceous after a short period of tectonic dormancy in the Late Jurassic (Fig. 6.3) (Pan et al., 2021, Bilal and McClay, 2022).

The initial syn-extensional phase occurred during a period of sediment-starvation across the Exmouth Plateau, resulting in the deposition of a relatively thin (< 400 m) synkinematic sequence consisting of the Brigadier (shallow marine claystone and limestones), Athol and Murat formations (marine claystones) (Fig. 6.3) (Exon and Willcox, 1978, Longley et al., 2002, Reeve et al., 2016, Pan et al., 2021, Lathrop et al., 2021, Bilal and McClay, 2022). During Early Cretaceous, extension and reactivation of normal faults was accompanied by mantle plume-related resulting uplift, which drove progradation of the Barrow Group across the Exmouth Plateau (Black et al., 2017, Longley et al., 2002, Bilal and McClay, 2022). Following this phase of continued extension, the Exmouth Plateau developed into a passive margin and deposition was subsequently dominated by hemipelagic and pelagic carbonate (Fig. 6.3) (Gibbons et al., 2012, Lathrop et al., 2021, Bilal and McClay, 2022).

Age Framework		
Horizon Age (Ma)	**Glencoe Dataset**	**Thebe Dataset**
123 ± 1.0		Top Muderong
137.7 ± 0.3	Top Barrow	Top Barrow
142.3 ± 3.0	Top Lower Barrow	
141 ± 3.3		~141 Ma (Barrow)
165.5 ± 3.0	Callovian Unconformity	
181.3 ± 1.3	Top Murat	Top Murat
192 ± 4.5	~192 Ma (Murat)	
201.3 ± 1.3	Top Brigadier	Top Brigadier
209.5 ± 1.0	Top Mungaroo	Top Mungaroo

Table 6.1. Age framework for the Glencoe and Thebe datasets| A table showing the age framework for the Glencoe and Thebe datasets. Theses time periods are used to calculate throw rates over given periods and constrain the temporal evolution of throw rates on the relay-breaching faults. The uncertainty (±) associated with the ages of these surfaces is determined by the range of ages found in publications and well data on the Exmouth Plateau (Bilal and McClay, 2022, Barrett et al., 2021, Lathrop et al., 2020, Scarselli et al., 2015).

6.3 Dataset and Methods

6.3.1 Dataset

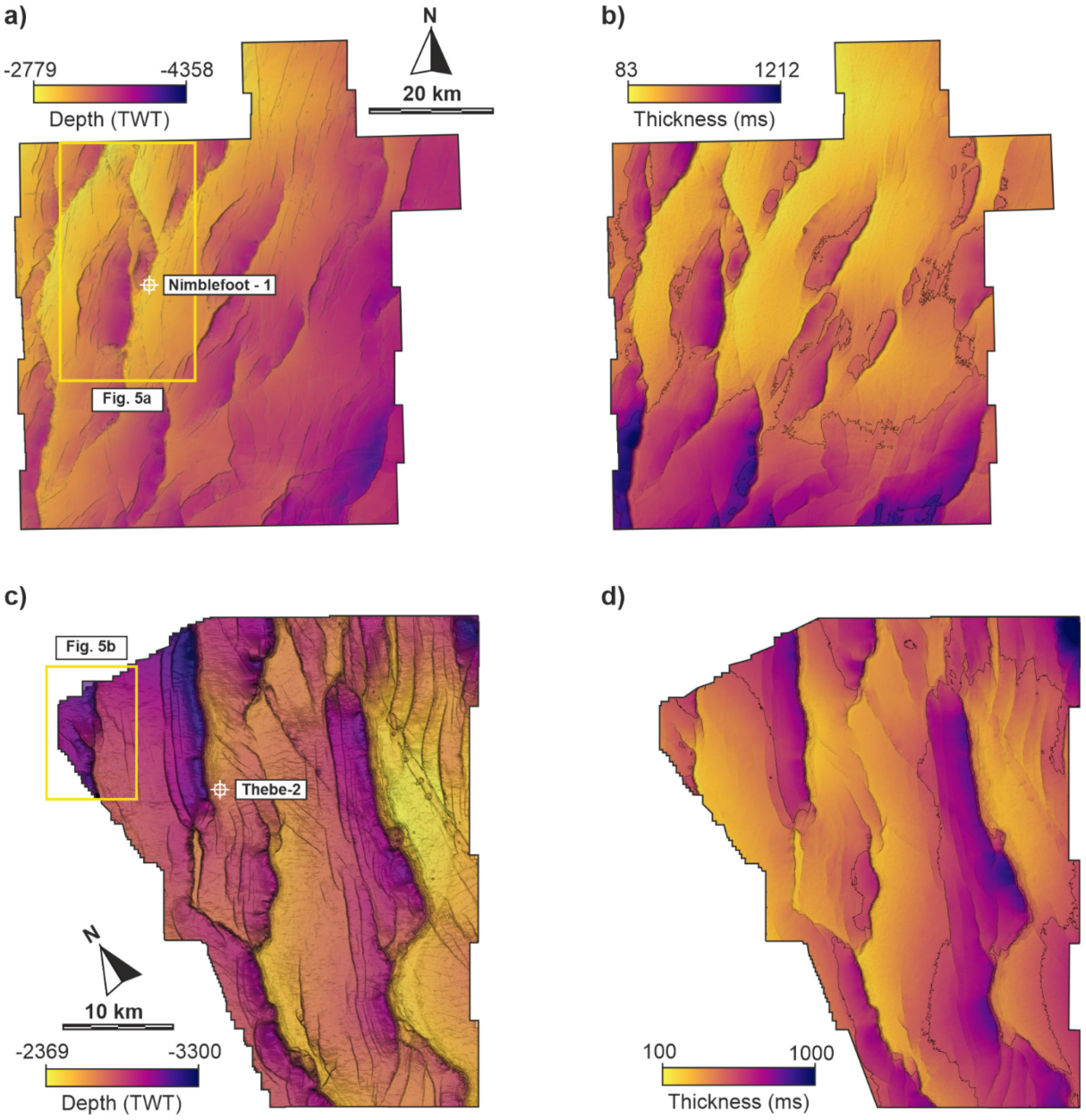


Figure 6.4. TWT structure and thickness maps| (a-b) Glencoe Study Area. (c-d) Thebe study area. (a) A TWT structure map of the Top Mungaroo (base syn-rift) surface highlighting rift physiography and (b) A thickness map from the Top Mungaroo to Top Barrow surfaces (see Fig. 6.3a), with 500 ms contours. (c) A TWT structure map of Top Mungaroo (Base Syn-Rift) surface highlighting rift physiography and (d) A thickness map from the Top Mungaroo (base syn-rift)to Top Muderong (see Fig. 6.3.b), with 500 ms contours.(a) and (c) show the locations of figures 6.5a and 6.5b, respectively.

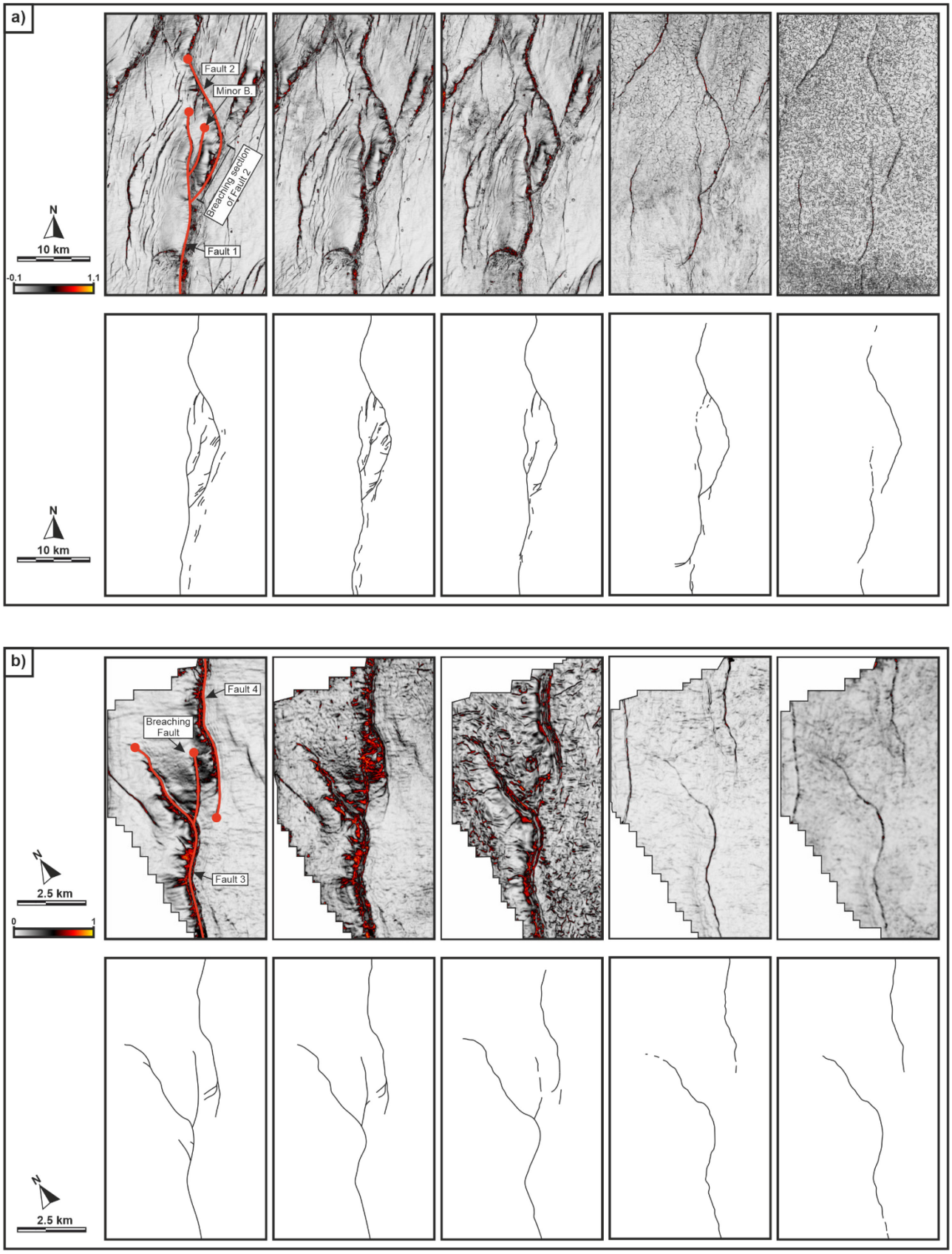


Figure 6.5. Map view geometry of studied relay zones | (a) Glencoe Relay Zone. (Above) Left to Right. Variance extractions on the Top Brigadier; Top Murat; Callovian Unconformity; Top Lower Barrow and Top Barrow surfaces. Also highlight the faults studied in this area. (Bottom) Left to Right. Sketch diagrams of relay zone structure and

geometry on the respective surfaces showing the spatio-temporal geometry of the relay zone. (b) Thebe Relay Zone. (Above) Left to Right. Variance extractions on the Top Mungaroo; Top Brigadier; Top Murat; Top Barrow and Top Muderong surfaces. Also highlight the faults studied in this area. (Bottom) Left to Right. Sketch diagrams of relay zone structure and geometry on the respective surfaces showing the spatio-temporal geometry of the relay zone.

We study both double-breached (i.e., Fig. 6.4a and 6.5a) and partially-breached (i.e., Fig. 6.4c and 6.5b) synthetic relay zones, located in the North Carnarvon Basin, Exmouth Plateau, NW Shelf Offshore Australia (Fig. 6.2 and 6.4). For the study of the double-breached synthetic relay zone (Fig. 6.5a), we use high-resolution (pre-stack time migrated) 3-D seismic reflection data from the Glencoe survey, located *c.* 100 km to the SE of the Thebe survey, within the WA-390-P permit area (Fig. 6.2). This example is located in the fault block penetrated by the Nimblefoot-1 well and covers *c.* 4000 km^2 (Fig. 6.2 and 6.4a). It has a maximum penetration of 8000 ms TWT, with E-W trending inlines and with a bin spacing of 25 m. The data are in normal polarity (i.e., a peak indicates a downward increase in acoustic impedance) and within the interval of interest has a maximum vertical resolution of 6.6 m ($\Lambda/4$) (Brown, 2011, Lathrop et al., 2021). In the Glencoe area we have mapped six regional seismic horizons. The age of the Top Mungaroo, Callovian Unconformity and the Top Lower Barrow and Top Barrow surfaces are age constrained using biostratigraphic data from Nimblefoot-1, and correlating them with results from existing literature which used biostratigraphy from 1,500 wells across the North Carnarvon Basin to constrain stratigraphic ages, published by Marshall and Lang (2013). We additionally used age constraints for the Glencoe study area from Lathrop et al. (2021) for surfaces (i.e., Top Brigadier and Top Murat) which were not age constrained by the above methods and were estimated assuming a constant sedimentation rate between horizons of known ages (Fig. 6.3; Table 6.1).

To study the partially-breached synthetic relay zone (Fig. 6.5b), we use high-resolution (PSTM) 3-D seismic reflection data from the Thebe HEX07B survey, within the WA-346-P permit area (Fig. 6.2 and 6.4c-d). This relay zone is located on the fault block immediately to the NNE of the Thebe-2 well (Fig. 6.2 and 6.4c). The HEX07B survey covers *c.* 1800 km^2. Its maximum penetration is 4610 ms TWT, with NW-trending inline and NE-trending crossline intervals of 25 and 12.5 m,

respectively. The data are displayed with normal polarity (i.e., a peak indicates a downward increase in acoustic impedance), and within the interval of interest the maximum vertical resolution is 8.5 m ($\Lambda/4$) (Brown, 2011, Barrett et al., 2021). For the Thebe relay zone case study, we have mapped six regional seismic horizons (Fig. 6.3). The ages of all surfaces were constrained using the same method applied in the case of the Glencoe relay zone, by correlating them with existing literature from Marshall and Lang (2013), except for the '~141 Ma' surface whose age is constrained assuming a constant rate of sedimentation (e.g., Pan et al., 2021).

6.3.2 Methods

6.3.2.1 Throw Calculation and Throw Backstripping

We used the six key stratigraphic surfaces mapped in the Glencoe and Thebe study areas to calculate throw on the relay-breaching faults and adjacent segments (Fig. 6.3 and Table 6.1). To calculate throw, footwall and hangingwall cut-offs were measured for key surfaces at closely spaced (*c.* ~125 m) intervals along the length of the faults. The vertical distance between the footwall and hangingwall cut-offs equals throw (e.g., Hongxing and Anderson, 2007, Jackson et al., 2017, Lathrop et al., 2021, Redpath et al., 2022). We used the 'original method' for throw backstripping, which subtracts throw measured across a shallower, younger surface from a deeper, older surface (e.g., Jackson et al., 2017). We then constructed backstripped throw plots for the relay-breaching faults and adjacent segments constituting the relay zone. For both the Glencoe and Thebe datasets, we converted throw from TWT (ms) to metres using time-depth conversion velocity models from the Nimblefoot-1 and Glencoe-1 well, and Thebe-1 and -2 wells, respectively.

6.3.2.2 Throw Rate Calculations

The above methods and the calculation of throw rates are applied to our dataset using a code-based technique. This technique calculated fault parameters from seismic interpretation inputs using a python script by: (i) inputting footwall and hangingwall cut offs and determining mid-

points for geospatial plotting; (ii) calculating mid-depth, throw and heave for each fault and; (iii) creating a geospatially oriented plot of the chosen parameter (i.e., backstripped throw and throw rate). This technique then included a QC phase where we input the above data into QGIS to find areas where throw = 0m but where horizons also existed, which was particularly important for creating the backstripped throw plots. This method calculated throw rates (m/Myr) by using the backstripped throw values (in metres) on a surface and dividing it by the length of time over which the backstripped throw was calculated (Myr) (Table 6.2). The time periods considered are calculated by using the difference in the ages of key surfaces identified and mapped in the Glencoe and Thebe datasets (e.g., Top Barrow – Top Lower Barrow period lasts 4.6 Myr) (see Table 6.1). This method is applied to each period between the key surfaces in the age framework (Table 6.1).

Glencoe				Thebe			
Time Period (Ma)	Max. Throw Rate (m/Myr)			Time Period (Ma)	Max. Throw Rate (m/Myr)		
	Fault 1	Fault 2	Minor Breaching		Fault 3	Fault 4	Breaching
Top Barrow - Top L. Barrow	33.0	24.8	0.0	Top Muderong - Top Barrow	1.7	0.9	0.0
Top L. Barrow - Callovian U.	27.6	23.7	12.3	Top Barrow - 141	5.0	8.8	13.4
Callovian U. - Top Murat	6.9	7.3	4.3	141 - Top Murat	5.0	4.0	2.4
Top Murat - 192	6.9	47.9	1.3				
192 - Top Brigadier	14.7	4.8	1.3	Top Murat - Top Brigadier	6.0	4.6	2.9
Top Brigadier - Top Mungaroo	8.8	4.9	2.2	Top Brigadier - Top Mungaroo	9.4	8.4	3.5
Maximum Throw (m)	992.0	840.0	336.0	**Maximum Throw (m)**	460.0	310.0	127.0

Table 6.2. Throw rate calculations for the Glencoe and Thebe relay zones| A Table showing the throw rates found on each of the faults in the Glencoe and Thebe dataset.

6.4 Glencoe Relay Zone: Geometry, Backstripped Throw and Throw Rates

6.4.1 Glencoe Relay Zone Geometry

The Glencoe relay zone is a synthetic, double-breached relay zone (Fig. 6.5a and 6.6). It consists of two broadly N-S-striking major fault segments (i.e., Fault 1 and 2) (Fig. 6.5a and 6.6). Fault 1 defines the south-western boundary of the Glencoe relay zone and is comprised of two distinct segments separated by a narrow relay zone (Fig. 6.5a and 6.7g). It is ~40 km long with a maximum throw of ~990 m (Fig. 6.7g; Table 6.2). Fault 2 defines the north-eastern boundary of the Glencoe

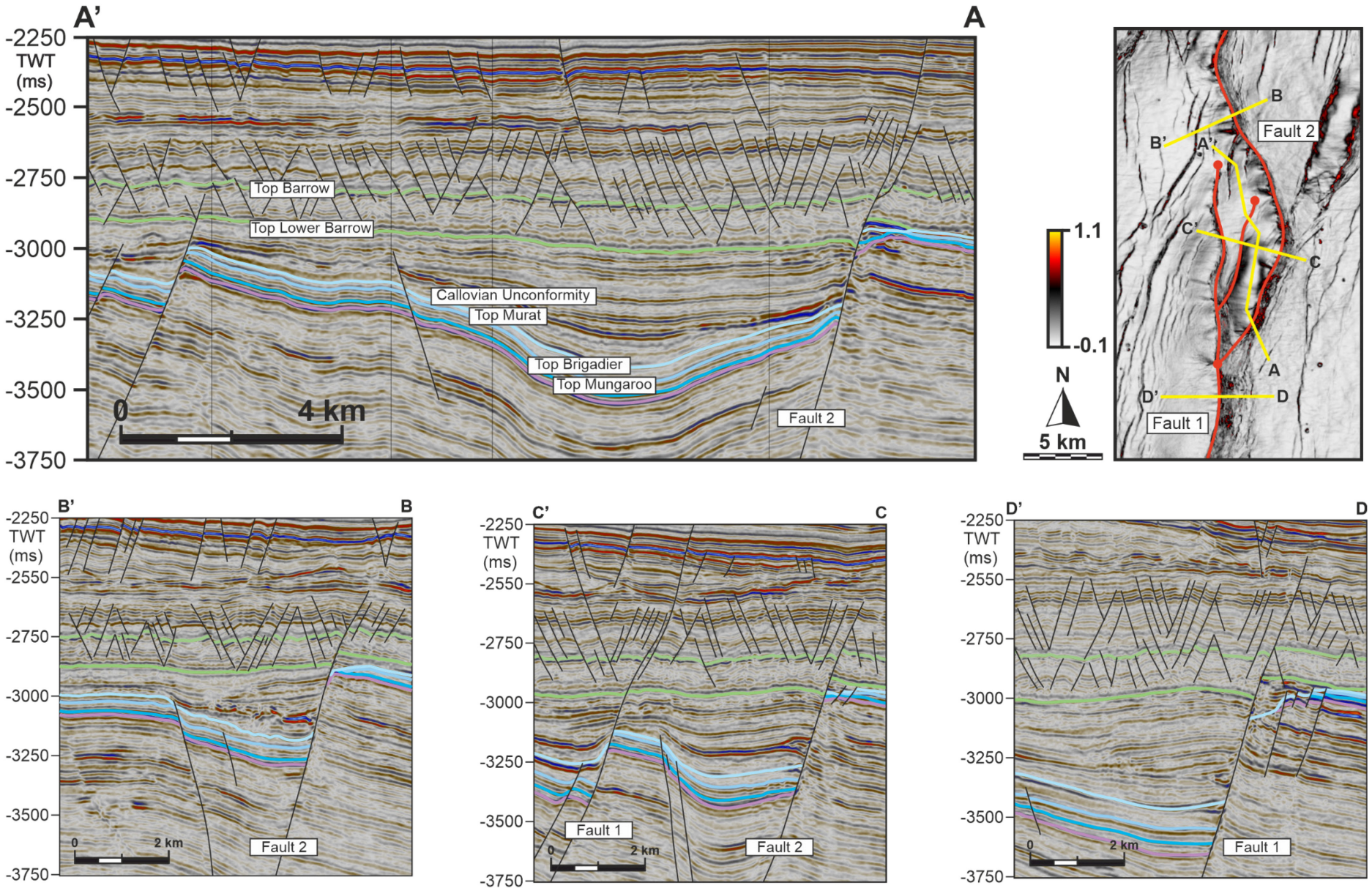


Figure 6.6. Glencoe relay zone | (Top Left) A seismic cross section showing the down-dip structure of the Glencoe relay ramp (A-A'). (Top Right) A variance extraction of the Top Brigadier surface showing the location of each of the cross-sections. (Bottom) Seismic cross sections of sections B-D showing the relay zone structure.

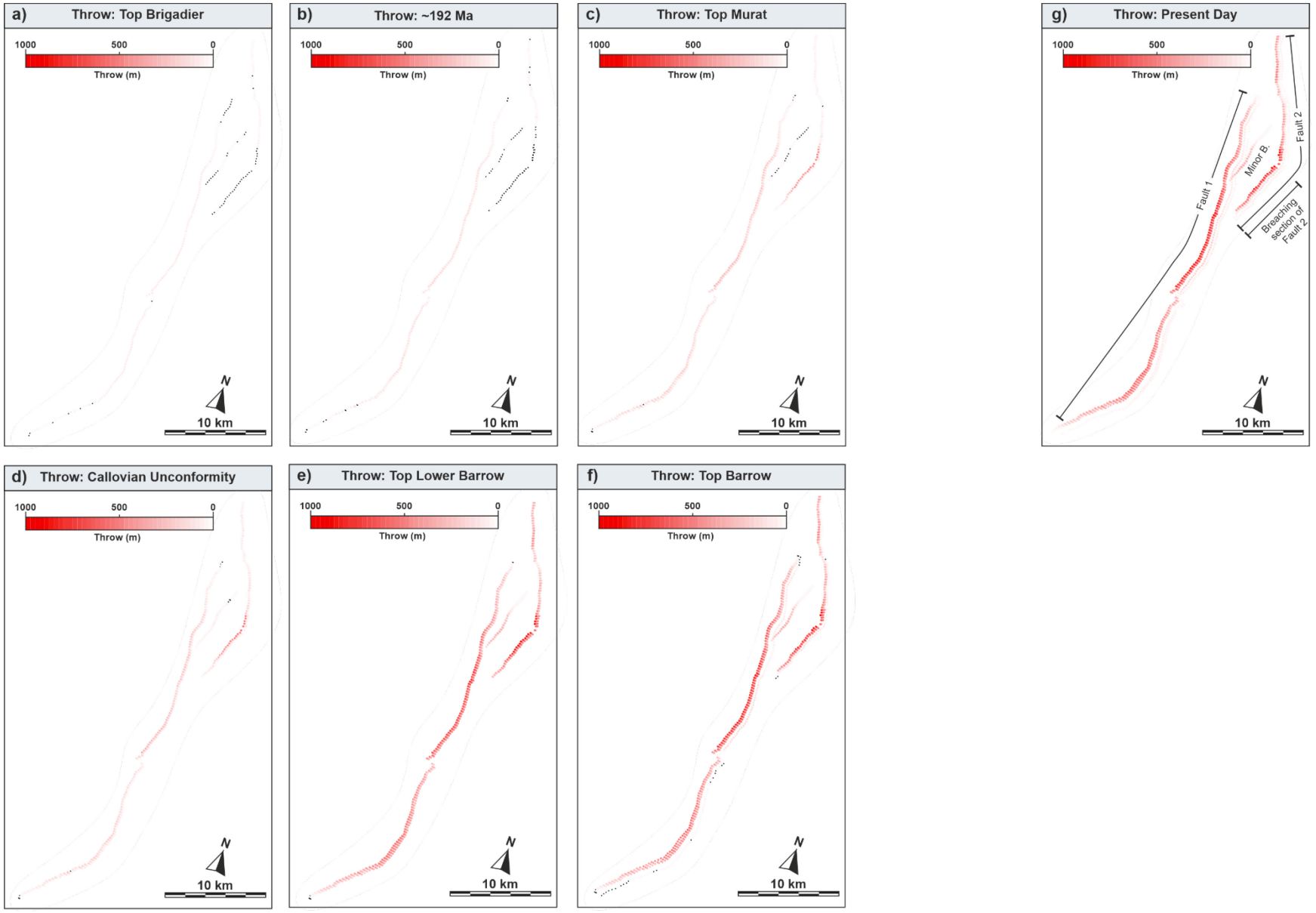


Figure 6.7. Glencoe relay zone backstripped throw plots| (Right) The present day throw on Faults 1 and 2 for the Glencoe relay zone. (Left) Backstripped throw for Faults 1 and 2 of the Glencoe relay zone. Each respective 2D map is backstripped to noted surface on the GIS map. Black dots indicate a value of 0m on the surface when backstripped to the noted time.

relay zone and is ~ 20 km long with a maximum throw of ~840 m on its NNE-trending section (Fig. 6.7g and Table 6.2). Faults 1 and 2 are hard-linked by NNE-SSW-striking segment, which represents the initial ~8 km of Fault 2 northward from its branchline with Fault 1, and that strikes obliquely to Fault 1 (~30°) and the N-S striking section of Fault 2 (~60°) (Fig. 6.5a, 6.6 and 6.7g). The relay ramp is ~4 km wide and ~10 km long and contains a secondary, antithetic, hangingwall-breaching fault that extends ~7 km north-northeastwards into the relay zone from its southern branchline with Fault 1 (Fig. 6.5a and 6.6; i.e., C'-C).

6.4.2 Glencoe Backstripped Throw and Throw Rate Analysis

Backstripped Throw plots for the Glencoe relay zone indicate that Faults 1 and 2 were active from the earliest phase of rifting and that they had accumulated throw along much of their entire length by the deposition of the Top Brigadier (Fig. 6.7a). During the following measured period, throw increased slightly with only minor changes to the locations where throw was present on Fault 1 and 2 (Fig. 6.7b). A distinct change in the length of Fault 2 occurred by the Top Murat in which the NNE-SSW striking section becomes active at its southern end and accumulates ~400m throw (Fig. 6.7c). Moreover, the antithetic hangingwall-breaching fault is seen to accumulate throw along its entire length by the Callovian Unconformity, thus establishing the double-breached geometry observed in the present day. From the time of the Callovian Unconformity, the backstripped throw plots show that all faults in the Glencoe relay zone were active along their entire length until they reached the present day throw distribution (Fig. 6.7d-g). The present day throw shows that Fault 1 has maximum throw near its geometric centre, with throw decreasing towards its tips of ~990 m (Fig. 6.7g; Table 6.2). Maximum throw on Fault 2 which is ~840m is skewed slightly south of its geometric centre, on the NNE-SSW-striking part of the fault bounding the relay (Fig. 6.7g; Table 6.2). Finally, the minor hangingwall relay-breaching fault decreases in throw away from its branchline with Fault 1 towards its northern tip and has a maximum throw of ~336m (Fig. 6.7g, Table 6.2).The Glencoe relay zone throw rate analysis supports the observations from the backstripped throw above. The earliest throw rates show that Fault 1 and 2

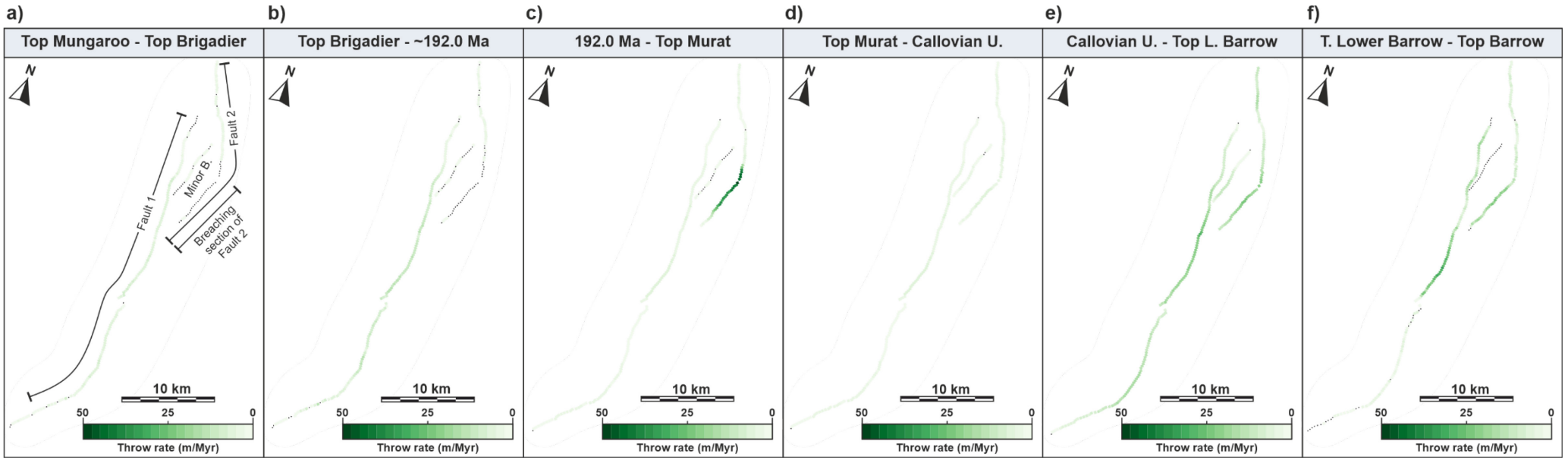


Figure 6.8. Glencoe relay zone throw rate variability| 2D GIS throw rate maps showing the throw rate on the faults constituting the Glencoe relay zone for each noted time period between noted key stratigraphic surfaces (a-f). Black dots indicate a value of 0 m/Myr (i.e., faults are inactive during respective time period).

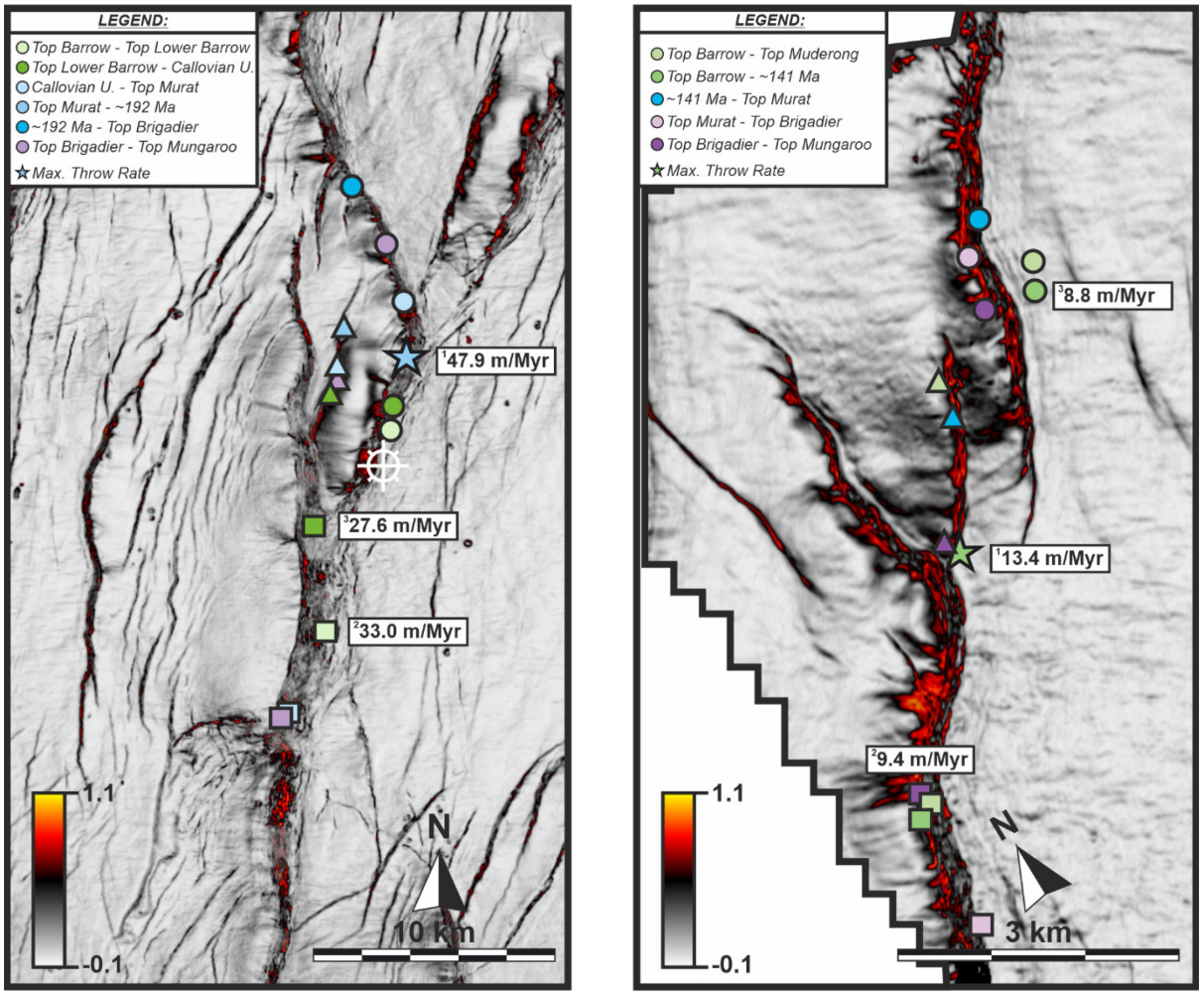


Figure 6.9. Maximum throw rate locations| (Left) A variance extraction map showing the location of the maximum throw rates on each of the faults during each time period for the Glencoe relay zone (see Table 1). (Right) A variance extraction map showing the location of the maximum throw rates on each of the faults during each time period for the Thebe relay zone (see Table 1). The highest three throw rates are marked by 1-3 next to the location along the faults where they occurred during the corresponding time period.

were active during the Top Mungaroo – Top Brigadier and that the NNE-SSW breaching section of fault 2 did not have any accumulated throw (Fig. 6.8a). This remains so until the 192 Ma- Top Murat period which shows that the maximum throw rate on Fault 2 and for the whole Glencoe relay zone occurred during this time (Fig. 6.8a, 6.9 and 6.10b, i.e., 47.9 m/Myr). This correlates to the period in which throw became present along this section of Fault 2 in the backstripped throw plots (Fig. 6.7c and 6.8c). In addition, the throw rates also agree with backstripped throw plots for the next measured period (Top Murat – Callovian U.), by showing that the antithetic hangingwall

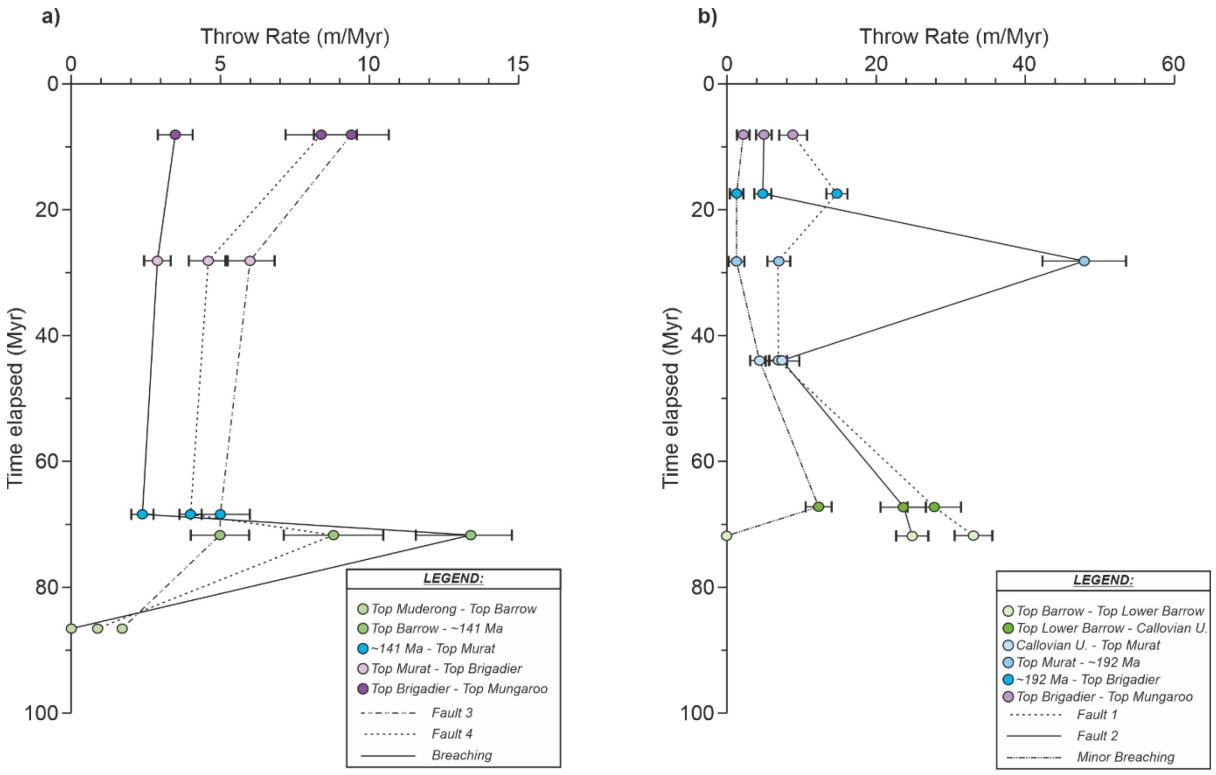


Figure 6.10. Maximum throw rates on the Glencoe and Thebe relay zone fault segments| Plots showing maximum throw rate vs. time elapsed since the start of deformation. (a) shows the data for the Thebe relay zone, while (b) shows this data for the Glencoe relay zone. Error bars indicate uncertainty originating from ranges of ages for the surfaces that were used to calculate the time periods over which throw rates were active, as shown in the figure.

minor breaching fault introduced throw rates along its entire length at the same time in which backstripped throw plots show the accumulation of throw along its entire length (Fig. 6.7d and 6.8d). During this same period (Top Murat – Callovian Unconformity) the throw rates reduce on all faults except on this minor hangingwall-breaching fault (Fig. 6.8d and 6.10b). Following this period, throw rates on all faults increase during the Callovian U. – Top Lower Barrow (Fig. 6.10b). During the Callovian U. – Top Lower Barrow, Fault 1 and 2 both achieve the second highest throw rate observed on them, and the minor breaching fault achieves the highest throw rate in its fault history (Fig. 6.9 and 6.10b). Finally, the Top Lower Barrow – Top Barrow period shows increasing maximum throw rates on Faults 1 and 2, but also that that throw rates became 0 m/Myr along the entire length of the minor, antithetic hangingwall-breaching fault and at the tips of Fault 1 (Fig. 6.8f).

These observations definitively show that the highest throw rate for the Glencoe relay zone occurred during the ~192.0 Ma – Top Murat period on the footwall relay-breaching section of Fault 2 with a maximum throw rate of 47.9 m/Myr, 58% higher than the highest throw rates on its adjacent faults (Fig. 6.8c, 6.9 and 6.10b;Table 6.2).

6.4.3 Interpretation

We interpret that Faults 1 and 2 established their near-final length early on within the first 8.2 Mry of fault activity and the first 11% of their total life, during the Rhaetian to Earliest Jurassic (Fig. 6.3, 6.7a and 6.8a). We also suggest that due to the NNE-SSW trending section of Fault 2 propagating *after* the establishment of Fault 2's near final-length, and that it forms a branchline with Fault 1, that this section is the footwall-breaching fault of the relay zone. This occurred during the Early Jurassic (i.e., 192 Ma – Top Murat period), only 10.7 Myr and 15% of Faults 1 and 2 lifespans (Fig. 6.7c and 6.8c; Table 6.1). Moreover, it had the highest throw rates (i.e., 47.9 m/Myr) of any of the structures associated with the Glencoe relay zone occurring during this period of the Early Jurassic (i.e., 192 Ma – Top Murat period) (Fig.6.8c, 6.9 and 6.10b; Table 6.2).

Although, the Glencoe relay zone clearly shows that the maximum throw rate is achieved on the footwall relay-breaching segment (Fig. 6.9), a key result is that this period of accelerated throw rates does not persist over the life of the relay-breaching fault, rather we see it over a period of 9.7 Myr at most (192 Ma – Top Murat; Table 6.2), just 13 % of the total rift period. We thus interpret that it may be the case that even where maximum throw rates are present on relay-breaching faults for a time, the throw minima may not be removed if the throw deficit with the adjacent faults is equal to or more than the maximum throw rate observed on the breaching fault multiplied by the relatively brief period - when compared to the life of adjacent faults 1 and 2 - over which these throw rates occurred. We suggest that this is the case with the throw minima on the Glencoe relay zone on which the maximum throw on the relay-breaching section is ~840m (Fig. 6.7f), only ~150m less than, and 85% of, the throw maximum (~990m) of its adjacent Fault 1. We interpret

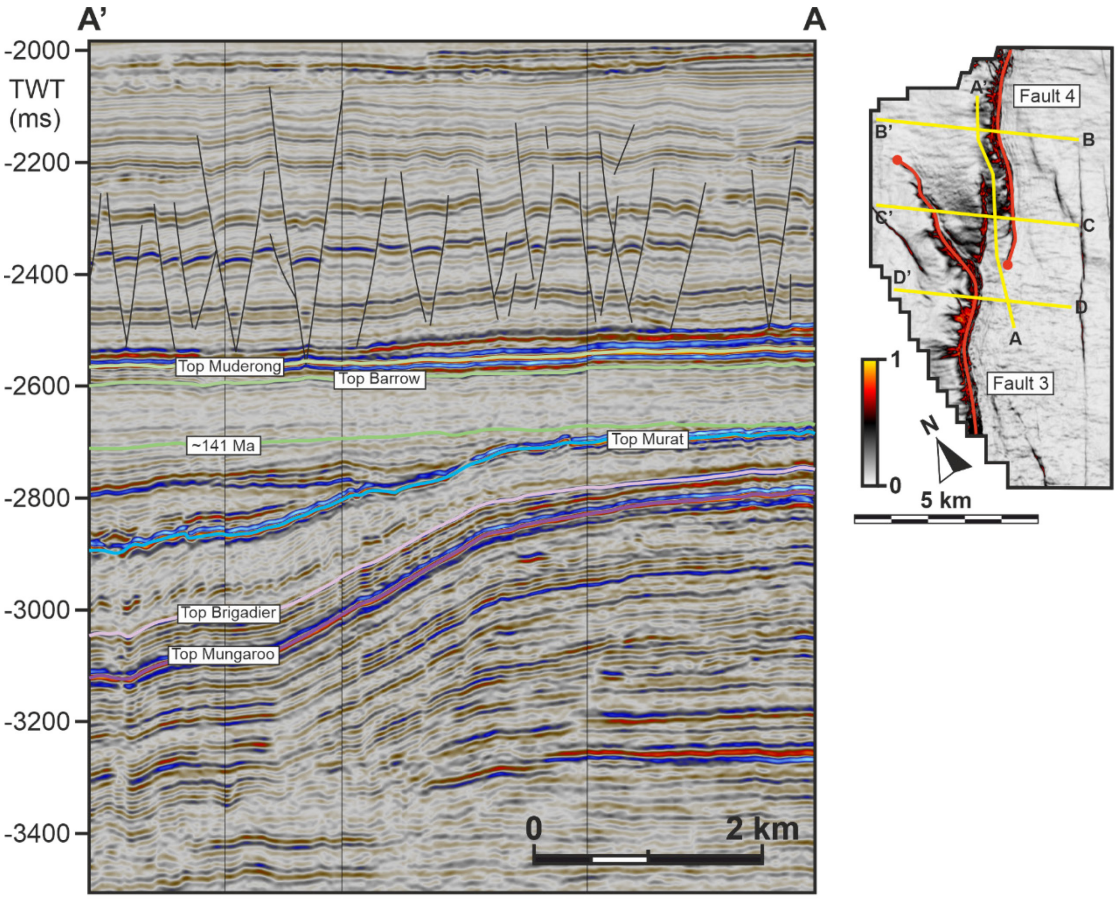


Figure 6.11. Thebe relay zone| (Left) A seismic cross section showing the down-dip structure of the Thebe relay ramp (A-A'). (Middle) A variance extraction of the Top Brigadier surface showing the location of each of the cross-sections. (Right) A series of seismic cross sections for B-D showing the relay zone structure.

that it may thus be the case that the high throw rate on the breaching fault reduced the throw minimum with Fault 1 and the non-breaching section of Fault 2 rather than removing it.

6.5 Thebe Relay Zone: Geometry, Backstripped Throw and Throw Rates

6.5.1 Thebe Relay Zone Geometry

The Thebe relay zone is a synthetic, hangingwall-breached relay zone (Fig. 6.5b and 6.11). It is defined by two broadly N-S-striking fault segments (i.e., Fault 3 and 4) (Fig. 6.5b, 6.11 and 6.12f). Fault 3 defines the south-western edge of the Thebe relay zone and is ~9.5 km long with maximum throw of ~460 m (Fig. 6.5b, 6.11 and 6.12f; Table 6.2). Fault 3 strikes NW-SE in the north and N-S in the south (Fig. 6.5b, 6.11 and 6.12f). Fault 4 defines the north-eastern margin of the Thebe relay zone and is at least 7.5 km long with a maximum throw of ~310 m (Fig. 6.5b, 6.11 and 6.12f; Table 6.2). Faults 3 and 4 are not hard-linked; instead, a synthetic, ~3 km-long partially breaching fault extends northwards from its branchline with Fault 3. We state that this fault partially breaches the hangingwall since the NW-SE trending section is the continuation of Fault 3 and that it offsets the ramp at its down-dip end (Fig. 6.11). This hangingwall-breaching fault strikes approximately parallel to the adjacent faults and has a throw maximum of ~130 m (Fig. 6.5b and 6.12f; Table 6.2). The relay ramp is ~2 km wide and 3.5 km long (Fig. 6.5b and 6.11).

6.5.2 Thebe Backstripped Throw and Throw Rate and Analysis

Backstripped throw plots for the Thebe relay zone indicate that all faults (i.e., 3, 4 and breaching fault) were active from the earliest phase of rifting and that they had accumulated throw along much of their entire length by the deposition of the Top Brigadier (Fig. 6.12a). During the following measured period, throw increased slightly up to the Top Murat (Fig. 6.12b). By ~141 Ma the backstripped throw plots show that throw maxima began to be distinctly established at the

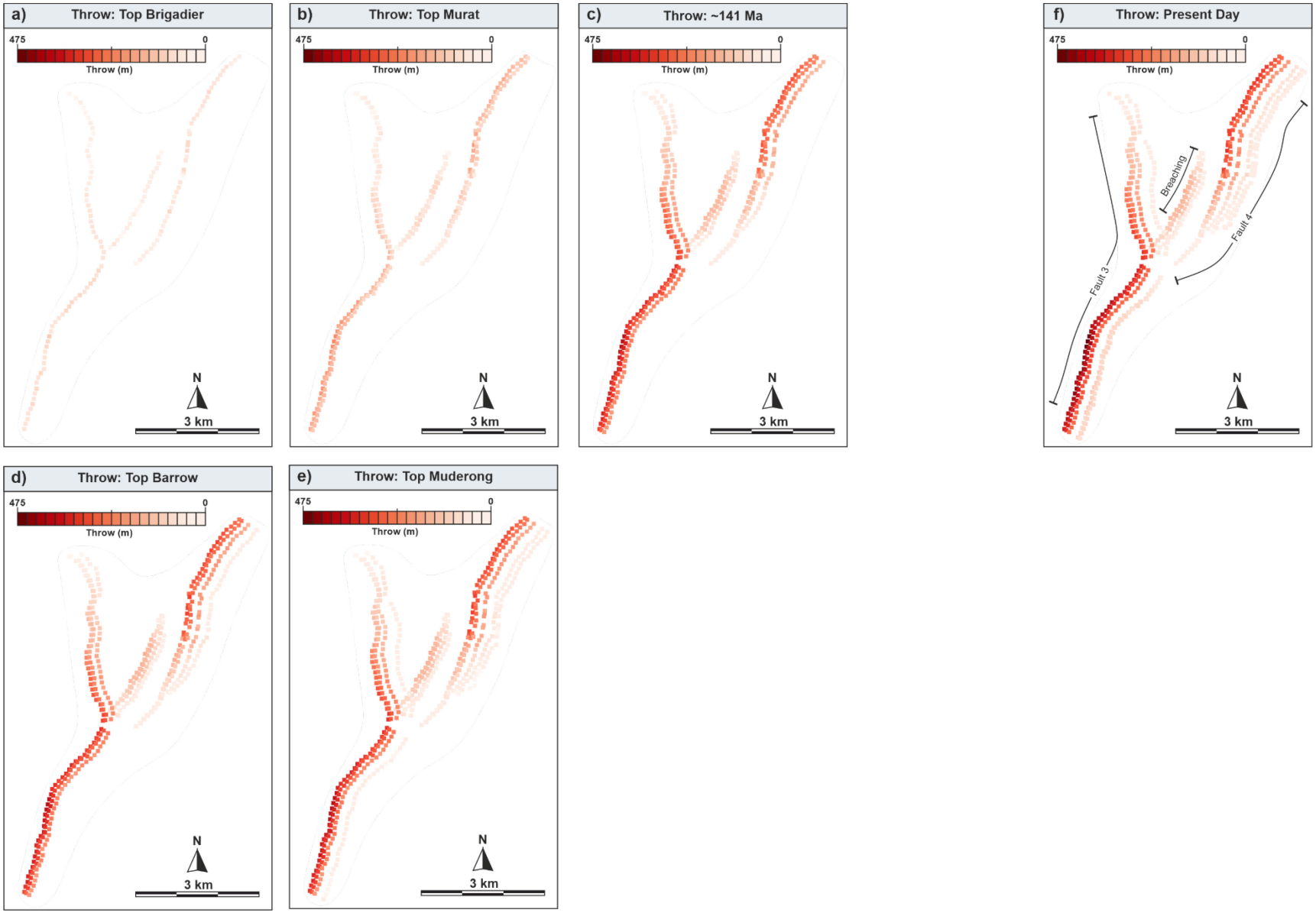


Figure 6.12. Thebe relay zone backstripped throw plots | (Right) The present day throw on all faults that constitute the Glencoe relay zone. (Left) Backstripped throw for the Glencoe relay zone. Each respective 2D map is backstripped to the noted surface above. Black dots indicate a value of 0m. .

geometric centre of each of the faults defining the Thebe relay zone with throw maxima during this period reaching up to ~300 m on Fault 1 and 2, approximately 60% of the maximum throw on any fault in the Thebe relay zone (Fig. 6.12c; Table 6.2). The backstripped throw plots form the Top barrow to the Top Muderong show increasing throw along the lengths of all faults until they reach their present day throw distribution (Fig. 6.7d-f). The present day throw shows that Fault 3 has maximum throw near its geometric centre, with throw decreasing towards its tips of ~ 460m (Fig. 6.12f; Table 6.2). Throw on Fault 4 also follow this distribution with a maximum throw of ~310m (Fig. 6.12f; Table 6.2). Finally, the hangingwall relay-breaching fault increases in throw away from its branchline with Fault 3, towards its throw maximum of ~127m located at its geometric centre and then decreases along its length towards its northernmost tip (Fig. 6.12f, Table 6.2).

The Thebe relay zone throw rate analysis supports the observations shown by the backstripped throw plots in the earliest stages of the Thebe relay zone, by also showing that Fault 3 and 4 were active along their lengths during the Top Mungaroo – Top Brigadier (Fig. 6.12a and 6.13a). Faults 3 shows its highest maximum throw rate (9.4m/Myr) during this time period and Fault 4 exhibits its second highest throw rate also during this time (8.4m/Myr) (Fig. 6.9 and 6.10a; Table 6.2). Maximum throw rates for each time period reduce from those observed in the Top Mungaroo – Top Brigadier until the 141 Ma – Top Barrow period (Fig. 6.10a and 6.13b-d; Table 6.2). Despite this, by ~141 Ma, the Thebe relay zone faults had accumulated ~60% of each of their maximum throws (Fig. 6.12c, see 6.5.1). During the 141 Ma – Top Barrow period an increase in throw rates occurs on every fault (Fig. 6.10a). The maximum throw rate on any fault for the whole life of the Thebe relay zone is present on the hangingwall relay-breaching fault of 13.4m/Myr during this period which occurs on the breaching fault at its branchline with Fault 3 is present (Fig. 6.9, 6.10a and 6.13d; Table 6.2). In addition, the second highest throw rate on Fault 4 also occurs during this period. (Fig. 6.10a and 6.13d; Table 6.2). Finally, during the Top barrow – Top Muderong both

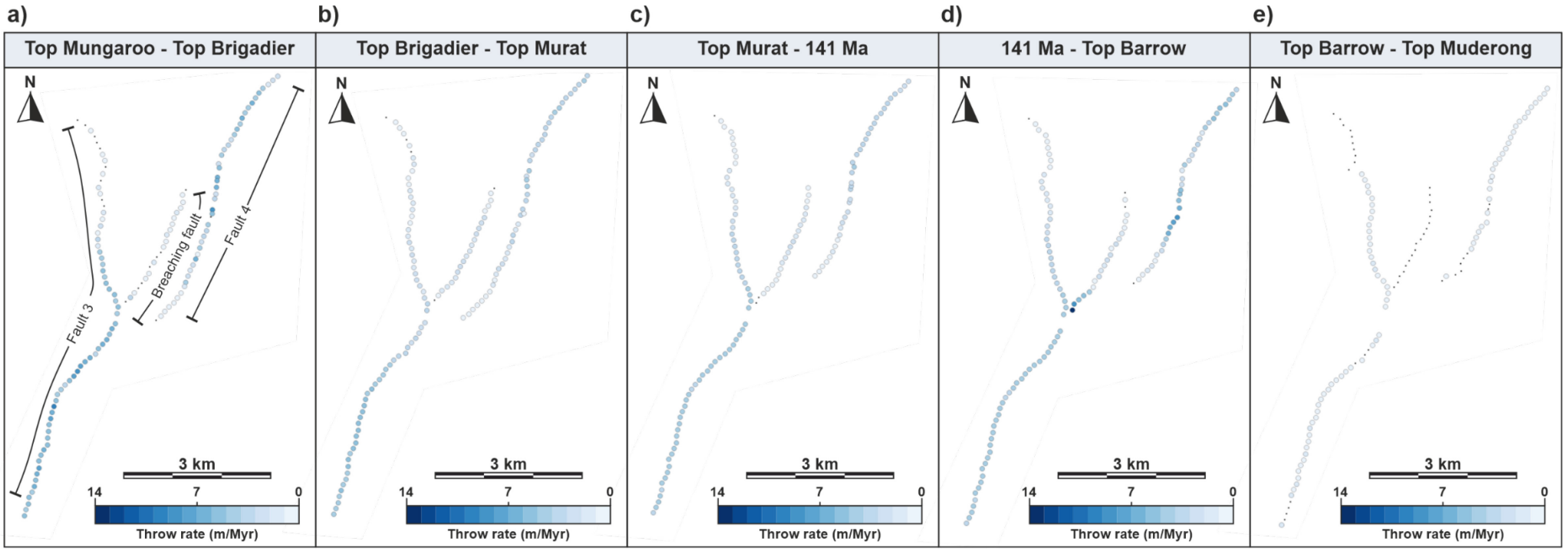


Figure 6.13. Thebe relay zone throw rate variability| 2D GIS throw rate maps showing the throw rate on the faults constituting the Thebe relay zone for each noted time period between noted key stratigraphic surfaces (a-f). Black dots indicate a value of 0 m/Myr (i.e., faults are inactive during respective time period).

tips of Fault 3 and the southern tip of Fault 4 show throw rates of 0m/Myr (Fig. 6.13e), as does the whole length of the hangingwall relay-breaching fault (Fig. 6.10b and 6.13e)

These observations clearly show that the highest throw rate for the Thebe relay zone occurred during the ~141 Ma – Top Barrow period on the hangingwall relay-breaching fault with a maximum throw rate of 13.4 m/Myr, 48% higher than the maximum throw rates on the adjacent fault segments (Fig. 6.9, 6.10a and 6.13; Table 6.2).

6.5.3 Interpretation

We interpret that all faults that constitute the Thebe Relay zone had established their near-final length early on within the first 8.2 Mry of fault activity and the first 9% of fault activity, during the Rhaetian to Earliest Jurassic (Fig. 6.3, 6.12a and 6.13a). Despite reducing throw rates from this time until the Early Cretaceous (i.e., ~141 Ma surface), we interpret that the faults established up to 60% of their final total throw by the Early Cretaceous (Fig. 6.12c). In addition, although each fault had already accrued up to 60% of their final throw maxima and ~80% of the fault life having already occurred, the highest throw rate of 13.4 m/Myr was observed on the Glencoe relay zone also during the period of Early Cretaceous (i.e., 141 Ma - Top Barrow) (Fig. 6.10a; Table 6.2). The beginning of this 3.3 Mry period (i.e., 141 Ma – Top Barrow; Table 6.1), in which the maximum throw rate on the Thebe relay zone occurs, corresponds to the phase of reactivation on the Exmouth Plateau during the Early Cretaceous. Thus, we argue that this throw rate may have been associated with this event, particularly since all throw rates on each fault increases at this period (Fig. 6.3 and 6.10a). Finally, we suggest that all three faults were active along their total length until the Early Cretaceous (Fig. 6.3a and 6.13e; i.e., Top Barrow –-Top Muderong), when the breaching fault became inactive (Fig. 6.13e; Table 6.2).

Like the Glencoe relay zone, we see that the highest throw rate is present on the relay-breaching fault, and in this case some 48% faster than the maximum throw rates on its adjacent faults. Additionally, although this throw rate is significantly higher, we do not see that it persists on the

breaching fault, this fault having the highest throw rate for no other period in the history of the Thebe relay zone (Fig. 6.10a), rather we see it persist for 3.3 Myr at most (Fig. 6.10a; Table 6.2). Thus, we suggest that this furthers our hypothesis in our interpretations for the Glencoe relay zone that relatively higher throw rates on breaching faults do not persist over the life of a fault. In fact, in the case of the Thebe relay zone the breaching fault is the highest throw rate only in this 3.3 Myr period, just 4% of the total rift period (Fig. 6.10a). Furthermore, in the case of the Thebe relay zone a throw minimum still exists across the breaching fault and relay zone in which it has a maximum throw (i.e., ~127m) some 333m (27% of Fault 3's maximum throw) and 183m (~40% of Fault 4's maximum throw) less than the maxima on Fault 3 and 4, respectively (Fig. 6.12f; Table 6.2). Thus, we suggest that like hypothesised from the Glencoe results that throw minima are not removed when throw rates do not persist and/or are not high enough on breaching faults with respective to the throw maxima on their adjacent fault segments. We suggest such is the case on the Thebe relay zone.

6.6 Discussion

6.6.1 The Role of Breaching Faults and Throw Rate

The previous work upon which we based our study on throw rate variability at relay zones and maximum throw rates being located on relay-breaching faults over geological timescales were principally conducted by Faure Walker et al. (2009), Faure Walker et al. (2015). Faure Walker et al. (2009) used geological, geomorphological, and geochemical data from the Apennines of Central Italy to explore the growth of segmented normal faults. They show that over the Late Pleistocene-Holocene (15,000 yrs.), maximum throw rates are higher (by 21%-76%) across relay-breaching faults (0.67 mm/yr) than on adjacent faults (0.55 and 0.38 mm/yr) (Faure Walker et al., 2009). They suggest that if these rates persisted over the timescales considered in our study, this would result in the removal of throw minima present on their studied faults in <1.0 Myr (Faure Walker et al., 2009). Finally, Faure Walker et al. (2009) suggests that such throw rates on relay-breaching

faults are made possible by, and dependent upon, the 3-D geometry of breaching faults (i.e., fault dip and its strike relative to adjacent faults) (Faure Walker et al., 2009).

Our study shows that irrespective of the maturity of their associated relays (i.e., fully breached, or partially breached), the relay-breaching faults had higher throw rates than their flanking segments (Fig. 6.9 and 6.10; Table 6.2). As Faure Walker et al. (2009) suggest, if these throw rates were to continue throughout the life of the faults, they would result in the removal of throw minima developed at their respective relays (e.g., Fig. 6.1b). However, this is demonstrably not the case in the Thebe Relay Zone, where the relay-breaching fault has significantly lower maximum throw than its flanking segments, a maximum throw only 27% (Fault 3) and 40% (Fault 4) of the maximum throw, such that a pronounced minima is still present (Fig. 6.12f; Table 6.2). However, there is an argument that the Glencoe Relay Zone shows such behaviour, where the footwall-breaching section has maximum throw of 840 m, just 152 m less than, and 85% of, the throw maximum on its adjacent faults(Fig. 6.7g; Table 6.2). While this is does not constitute a full removal of the throw minimum on the relay-breaching fault, it is considerably higher than the Thebe relay zone where the maximum throw on the relay-breaching fault are only 27-40% of its adjacent segments.

There are two reasons why this may be the case. Firstly, the period over which the maximum throw rate on the Glencoe breaching fault lasts 9.7 Myr, whereas they persist, at most, over a period of 3.3 Myr (Fig. 6.10; Table 6.1). Thus, higher throw rates over a longer time would reduce the throw minimum more on the Glencoe relay zone than on the Thebe relay zone. Secondly, the maximum throw rate observed on the Glencoe relay-breaching fault (47.9 m/Myr) is plainly faster than that observed on the Thebe relay-breaching fault (13.4 m/Myr) (Fig. 6.10; Table 6.2). Thus, we suggest that the Glencoe relay zone was able to reduce its minimum and achieve such a high maximum throw of 840 m because of a period of the rapid maximum throw rates of 47.7 m/Myr on the breaching segment during the Top Murat – 192.0 Ma period (17% of the ~60 Myr breaching

section faults' activity). In addition, it was able to reduce the throw minimum because throw rates over the rest of the faults life were relatively reduced (Fig. 6.8 and 6.10; Table 6.2).

Interestingly, the maximum throw rates on relay-breaching faults for both the Thebe and Glencoe relay zones only existed for short periods of the entire life of the relay zones activity (3.3 and 9.7 Myr, respectively). Thus, we propose that short periods of higher throw rates on relay-breaching faults relative to the time of complete period of fault activity, may be the reason as to why throw minima are still commonly present on ancient examples of relay zones. This hypothesis would reconcile the observations seen by Faure Walker et al. (2009) on faults in the Apennines of Central Italy that young (15,000 kyr) faults have maximum throw rates on breaching faults higher than their adjacent faults, with the observation that in the majority of cases we do not see throw minima removed from relay zones (e.g., Peacock and Sanderson, 1991, Trudgill and Cartwright, 1994, Huggins et al., 1995, Wilkins and Gross, 2002, Elliott et al., 2012, Conneally et al., 2014). Thus, it may be the case that (Faure Walker et al., 2009) simply observed breaching faults during this short (i.e., relative to geological timescales) period of high throw rates, which over geological timescales would not persist as seen in this study of ancient, seismogenic faults. Finally, Faure Walker et al. (2009) cite that breaching faults may have higher throw rates than their adjacent faults, despite being areas of lower throw, due to the 3D orientation of the breaching fault (obliquity of strike and relatively higher dip), and therefore that such faults could remove throw minima (e.g., Faure Walker et al., 2015, Faure Walker et al., 2009). This may be true in the case of the Glencoe Relay Zone which shows higher throw rates on the breaching fault than the adjacent fault segments since it strikes at oblique angles to its adjacent fault segments (30-60°). Furthermore, the Thebe Relay Zone, which does not show any evidence of its throw minima being reduced or removed but exhibits its highest throw rate on the breaching fault, strikes parallel rather than obliquely to its concomitant Faults 3 and 4; which Faure Walker et al. (2009) state is a prerequisite for the removal of throw minima at relay zones by breaching faults.

6.6.2 Implications for Fault Growth by Segment Linkage

Though the focus of this study was to constrain throw rate variability at relay-breaching faults over geological time, a consequence of our findings is that it gives insights into the fault growth models of these relay zones and their growth by segment linkage.

Our study shows two stages of fault growth for faults 1 – 2 in Glencoe. First, they establish their near-final length in the first 11% their deformation history and form the Glencoe relay zone (Fig. 6.7a-b and 6.8a-b), with characteristics most common to the constant length mode (e.g., Walsh et al., 2002, Rotevatn et al., 2019). Second, is the relay zone breaching phase in which the breaching fault at the southern tip of Fault 2 rapidly accumulates throw (i.e., 47.9 m/Myr) and length, consequently fully breaching the footwall of the Glencoe relay zone within at most 10.7 Myr and after a total of 28.2 Myr of rifting (39% of total faults 1 and 2 life) (Fig. 6.8c, 6.9 and 6.10b). The Thebe study area shows a stage of fault lengthening in which all faults establish their near-final length within the first 8.2 Myr of their fault activity (9% of total fault lives) (Fig. 6.12a and 6.13a). This is followed by throw accumulation over the each of the faults' lives, a model also most conducive to the constant-length model (e.g., Walsh et al., 2002, Jackson et al., 2017, Rotevatn et al., 2019, Lathrop et al., 2021).

These models of relay zone breaching are consistent with fault growth models in which: (i) Thebe relay zone is best represented by the constant length model due to all faults having their length established in the first 9% of rifting and; (ii) Glencoe relay zone is also best represented by the constant length model since its adjacent faults established their length early and then accumulated additional throw later (e.g.,Rotevatn et al., 2019, Lathrop et al., 2021). The Glencoe model differs in one way from that of the constant length model noted in Rotevatn et al. (2019), namely that the hangingwall relay-breaching fault established its length and throw extremely rapidly with maximum throw rates of 47.9 m/Myr at a later time during the Early Jurassic (i.e., 192 Ma – Top Murat and 25% of faults 1 and 2 lifespans), while the adjacent segments formed after just 11% of the faults 1 and 2 lifespans (Fig. 6.7 and 6.8).

6.6.3 Implications for Potential Seismic Hazards

Relay zones have been identified as sites of seismicity due to their role in fault segment linkage (e.g., Machette et al., 1991, Soliva and Benedicto, 2003, Soliva et al., 2008). Though we measure the vertical component of fault slip in our evaluation of throw rates on breaching faults, it has been widely recognised that faults grow by accumulation of slip, and with it, increased seismicity on fault surfaces (Cowie and Scholz, 1992b, Luo and Liu, 2018, Huang et al., 2018). Since faults grow by accumulation of fault slip accompanied by seismic events, our study highlights that increased throw rates on breaching faults at the site of fault linkage could impact earthquake periodicity and magnitude on the breaching fault surface, and that of the concomitant relay zone faults (e.g., Di Bucci et al., 2006, Soliva et al., 2008, Cowie et al., 2012).

6.7 Conclusions

We use 3D seismic data from offshore NW Australia to study relay-breaching faults and their throw rates with respect to their adjacent faults in two relay zones. We show that breaching faults exhibit the highest throw rates irrespective of how mature the breaching fault is. The Glencoe relay zone exhibits rapid throw rates during its initial fault activity (Fig. 6.10b; i.e., 47.9 m/Myr in first 15% of relay-breaching fault's life) and suggests that throw minima may be removed or have been being removed, given that the maximum throw value on the relay-breaching segment of ~840m is only ~150 m less than its concomitant faults' maximum throw value of ~990m (Fig. 6.7f). This may be due to the breaching faults high (30°-60°) obliquity with its concomitant fault segments. We base this on the fact that the throw minimum still exists on the Thebe Relay Zone where the breaching fault strikes parallel to its adjacent faults and findings from Faure Walker et al. (2009) that state the obliquity of relay-breaching faults with respect to their adjacent faults may control throw rates on breaching segments.

Each of our study areas show that breaching of the relay zone can occur either (i) early on in the fault life as in the case of Thebe Relay Zone (9% of total fault lifespan) or; (ii) in the case of the

Glencoe Relay Zone after 25% of the total fault lifespan, and still result in maximum throw rates that are higher than their concomitant faults (Fig. 6.9 and 6.10). The key conclusion from our study of throw rate variability on breaching faults at relay zones is that maximum throw rates are present on relay-breaching faults, but only persist for a short period of time relative to the overall fault life over geological timescales. This would explain why we do not commonly see the removal of throw minima in ancient examples of relay zones that were active over geological timescales, but do still observe periods of high breaching throw rates in modern and ancient examples (e.g., Commins et al., 2005, Faure Walker et al., 2009). Finally, since these periods occur at different stages of relay zone development between our two studied relay zones, we do not determine whether these periods of high throw rates are common to a particular stage of relay zone maturity (i.e., breaching or partially breached, initiation of breaching fault or towards the end of its activity). We thus propose that more evidence is needed to constrain whether the period of high throw rates correlates to a particular stage of relay zone breaching and that this could be an important focus of a future work.

Acknowledgements

The work contained in this study is part of work conducted during a PhD study undertaken as part of the Natural Environment Research Council (NERC) Centre for Doctoral Training (CDT) in Oil & Gas and is fully funded by NERC, whose support is gratefully acknowledged. We also would like to thank the Quake4D group at the University of Plymouth for their thought-provoking hypotheses on throw rate variability at relay zones. In particular, we note the contributions of Zoe Faure Walker to this reseach topic which have opened the discussion on such a crucial aspect of fault growth by segmetn linakge. In addition, we thank Billy Andrews for his contributions in writing the code that gave key results on throw rate variability and helping the first author of this study to understand key methods for achieving research aims. In addition, we also thank those who fund the great work done by the Quake4D group. Finally, we thank Geoscience Australia for

their ongoing commitment to making these and a plethora of other data available for academic use. We thank Schlumberger for providing access to Petrel software.

7

Conclusions and Discussion

Preamble

This chapter of the thesis summarizes the principal findings of the research chapters presented and provides an overview of how they address key research aims. In addition, it outlines the wider implications of this research and discusses them in context of existing literature. A consideration of future research directions arising from this thesis is also given.

Overview

The main aim of this thesis was to address normal fault growth and the fundamental principles that currently underpin their growth and dimensions. This research has taken the approach of investigating the controls on the growth and dimensions of *individual fault segments* and undertaken the study of how these controls can result in a deviation from the fault scaling relationships by which fault growth is often characterised (Chapter 4). This thesis built on the understanding of the controls on fault growth and dimensions by addressing a key question regarding the process by which *faults grow by segment linkage* and investigated *throw rates on relay-breaching faults during relay zone kinematics* (Chapter 6). Fault growth by segment linkage does not solely occur in ideal settings in which it can be observed, measured and tested. For this reason, this thesis presented a *novel technique* by which to observe and measure fault tip propagation in *sediment starved basins* (Chapter 5). Thus, this thesis addresses its key aims by (1) understanding controls on fault growth on a individual fault surface, (2) addresses a critical question regarding relay zone breaching during relay zone kinematics and growth by segment linkage and (3) measures fault growth in a sediment starved basin by using basin architecture and proposing a new technique.

7.1 Research Aim 1: Investigating Host Rock Properties' Control on Fault Dimensions

Chapter 4 was one of few studies to quantify the control of mechanical stratigraphy on normal faults on a seismic scale. The motivation for this work was to understand how mechanical stratigraphy controls fault growth and geometry, in order to determine why faults may deviate from established $D - L$ scaling laws. In addition, I highlighted that geometric data alone may be insufficient to determine the style of fault growth and propose fault growth models when these data do not consider the influence of mechanical stratigraphy on fault dimensions. The key findings from Chapter 4 were that: (i) aspect ratios and displacement patterns vary even on closely

spaced seismic scale faults forming in the same host rock based on their interaction with mechanical stratigraphy; (ii) the geometric data (i.e. D – L) for seismic scale faults that are controlled by mechanical stratigraphy can lie within the general scatter and even the trend of the fault scaling relationship in global $D-L$ datasets, despite not adhering to $D-L$ scaling laws during growth (e.g., Fig. 4.2); and that (iii) in the absence of extensive growth strata D – L scaling relationships must be used with caution when studying fault kinematics, given that global $D-L$ data are not controlled for local – regional host rock properties, such as mechanical stratigraphy, and may hide the significant deviations away from fault scaling laws.

7.1.1 Mechanical Stratigraphy Controls Fault Geometry and Growth

Previous studies have overwhelmingly used outcrop and numerical studies to investigate the precedence that mechanical stratigraphy and its control on normal fault growth would lead to a "breakdown in fault scaling relations thought to characterise isolated fault growth" (e.g., Gross et al., 1997, Martel, 1999, Wilkins and Gross, 2002, Ravaglia et al., 2004, Soliva et al., 2005a, Soliva et al., 2005b, Soliva et al., 2006, Ferrill et al., 2017). Chapter 4 is one of few works that take this precedence published by Gross et al. (1997) and tests it in 3D seismic reflection data and tests it using examples of large, seismogenic faults to observe mechanical stratigraphy's influence on the 3D geometry of seismic scales (Redpath et al., 2022). While our study focussed on the variability in geometry and growth within a fault array in particular geological setting, recently Roche et al. (2021) conducted a similar (i.e., large, seismic-scale faults) study using a large database of 3D fault geometry in a range of geological settings, ultimately investigating the same hypothesis that we have in Chapter 4 (i.e., Gross et al., 1997). The authors used published fault surface maps, as well as 63 newly-mapped fault zones from eight seismic reflections surveys, located in numerous basins and geological settings (Roche et al., 2021). In their results, they demonstrated that a significant component of variability in seismic-scale fault geometry was attributed to the mechanical heterogeneity of the faulted sequence and showed similar findings to

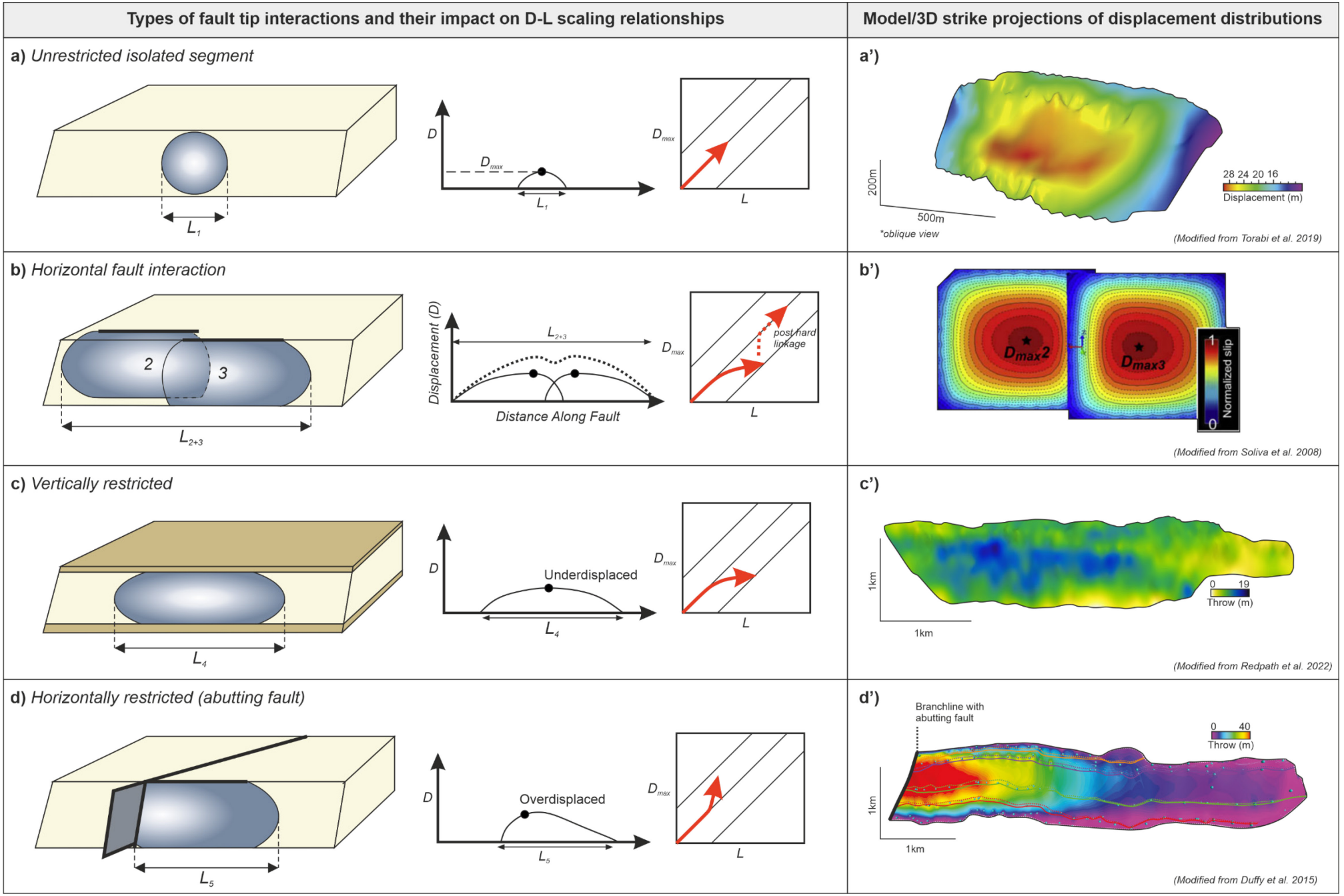

Types of fault tip interactions and their impact on D-L scaling relationships
Model/3D strike projections of displacement distributions
a) Unrestricted isolated segment
D
D_{max}
L_1
L
a')
200m
500m
*oblique view
28 24 20 16
Displacement (m)
(Modified from Torabi et al. 2019)
b) Horizontal fault interaction
2
3
L_{2+3}
Displacement (D)
Distance Along Fault
post hard linkage
b')
D_{max2}
D_{max3}
Normalized slip
1
0
(Modified from Soliva et al. 2008)
c) Vertically restricted
Underdisplaced
L_4
c')
1km
1km
0 19
Throw (m)
(Modified from Redpath et al. 2022)
d) Horizontally restricted (abutting fault)
Overdisplaced
L_5
d')
Branchline with abutting fault
0 40
Throw (m)
1km
1km
(Modified from Duffy et al. 2015)

Figure 7.1. Mechanical controls on fault growth and dimensions| (a-d) Schematic diagrams showing examples of the types of fault interactions that can occur and their respective displacement-length plots. **(a'-d')** 3-D strike projections showing the geometry and distribution of throw/displacement on the fault surface according to the type of fault interaction. **(a-a')** An unrestricted isolated segment that grows freely without interaction with other stress fields. The displacement maximum is located at the geometric centre of the fault and decreases radially towards the fault tips. The D-L scaling relationship is maintained. 3-D strike projection is from Torabi et al. (2019) **(b-b')** Horizontal fault tip interaction. The displacement maxima are skewed towards the adjacent, interacting tips and display high displacement gradients at their interacting tips. They become 'underdisplaced' until post- hard linkage occurs, after which they maintain fault scaling relationships. 3-D strike projection is from Soliva et al. (2008)**(c-c')** A vertically restricted fault. Restriction is because of mechanical stratigraphy at the faults upper and lower tips. The displacement maxima is elongate. The fault preferentially lengthens since its vertical tips are restricted and becomes 'underdisplaced'. 3-D strike projection is from Redpath et al. (2022). **(d-d')** A horizontally restricted fault. The displacement maximum is skewed towards the restricted tip. Since fault lengthening is restricted, the fault appears 'overdisplaced'. 3-D strike projection show the displacement distribution on such a fault from Duffy et al. (2015).

Chapter 4, namely: (i) mechanical stratigraphy control the dimensions of seismic-scale faults in the East African Rift and the Porcupine Basin, by imposing vertical restriction on their fault tips, resulting in high aspect ratios; and (ii) that the branchlines of bifurcating faults displayed a tendency to be preferentially located along the boundaries of mechanically heterogenous layers (e.g., Fig. 4.5, 4.10,4.13 and 4.14) (Roche et al., 2021).

Evidently, what is clear from Chapter 4 and the few studies investigating mechanical stratigraphy's control on the displacement and geometry of natural, seismic-scale faults, is that even on the larger scale of the fault dimensions in our study, mechanical stratigraphy controls fault growth and geometry (Roche et al., 2021, Redpath et al., 2022).

7.1.2 Implications from Thesis Findings On Mechanical Interactions of faults

Figure 7.1 reviews examples of how mechanical interactions control the growth and dimensions of fault growth, including mechanical stratigraphy.

Relay zones are a key site of mechanical interaction between adjacent fault segments and result in horizontal fault interactions (Fig. 7.1b). In Chapter 5, we observe mechanical controls on fault dimensions of the Thebe Fault Complex, where two relay zones resulted in displacement transfer, high displacement gradients at adjacent fault tips, and throw-length distributions in which throw is skewed towards the relay zone (e.g., Fig. 5.6 and 7.1b). Chapter 6 also shows examples of this

(see 6.4 and 6.5). A key discussion point arising from Chapter 6 regarding the control of mechanical interactions between adjacent fault segments on growth and dimensions, is that relay-breaching faults mechanically and physically link fault segments with elevated throw rates. This has implications for the development of high /displacement gradients at the interacting fault tips on fault surfaces as observed during mechanical interaction and physical linkage of faults (Fig. 7.1b).

The findings in chapter 4, thus, develop the understanding of the extent to which mechanical stratigraphy can control the dimensions of natural normal faults. In addition, this chapter furthers the understanding that was previously established by outcrop and smaller scale studies and opens enquiries as to what we might further learn by observing the effect of mechanical stratigraphy on seismic-scale faults (e.g., Gross et al., 1997, Wilkins and Gross, 2002, Soliva et al., 2005b, Soliva et al., 2005a, Soliva et al., 2006).

Chapter 4 highlights remaining questions as to (i) how we could explicitly quantify how much of the scatter present in global D - L datasets, which are typically made up of large, seismic-scale fault data, could be attributed to mechanical stratigraphy. In addition, the findings of Chapter 4 and Chapter 6 together, present a basis for the study of (ii) how elevated throw rates on relay-breaching faults may impact the short- and long- term throw/displacement gradients found at the tips of interacting faults during segment linkage. Two such studies could contribute to (i) furthering the understanding that fault growth models established on global fault geometric data (i.e., D-L) need to be proposed in context of their host-rock properties and (ii) constrain the development of throw/displacement gradients at interacting fault tips controlling for throw/displacement rate on relay-breaching faults.

7.2. Research Aim 2: Constraining Fault Growth and Segment Linkage in Sediment-Starved Basins

To date, fault growth models have predominantly been tested in ideal settings where syn-sedimentary faults are associated with the presence of near-to-complete or complete syn-kinematic sequences. Admittedly, examples of fault growth models in overfilled basins are crucial in proposing fault growth models and progressing our understanding of normal fault growth (e.g., Jackson et al., 2017, Rotevatn et al., 2019). Clearly, however, not all faults grow in such settings. Therefore, it is important to be able to understand fault growth, irrespective of whether a complete synkinematic sequence recording fault activity is present or not.

Chapter 5 focused on characterising fault growth in sediment - starved basins using footwall geomorphology, volume balancing and quantitative analysis of fault geometry and displacement. The motivation for this work was to constrain fault growth and propose fault growth models for large, basin – bounding faults in sediment-starved settings where complete records of syn-kinematic strata are often absent. Given the well-imaged nature of large (>15 km long), tectonic faults with extensive footwall erosion, the presence of footwall derived fans and high-quality 3D seismic, we used 3D seismic reflection data on the Exmouth Plateau, offshore NW Australia (e.g., Bilal et al., 2020, Barrett et al., 2021, Bilal and McClay, 2022). The main findings of this study which added to the understanding of constraining fault growth in challenging geological settings include: (i) footwall geomorphology can reveal that footwall erosion is controlled by fault throw and that erosion mimics the along-strike variability in throw; (ii) where (i) can be established by volume balancing of footwall erosion - fan volume, the temporal and spatial distribution of footwall-derived fans can be used to interpret fault lengthening and segment linkage; (iii) tectonic faults located in our study accumulated near-final length and displacement sufficient for footwall degradation in the first < 10 Myr of rifting (i.e., < 12% of the *ca.* 85.5 Myr rift history) – a fault

growth model most consistent with the hybrid growth model (Rotevatn et al., 2019).; and (iv) fault growth models can be constrained in sediment - starved settings using fan-degradation complexes.

7.2.1 A Discussion of Fault Growth, Footwall Erosion and Volume Balancing

The coupled relationship between fault throw and footwall erosion, in which it mimics the along-strike variability of throw has previously been documented in active and ancient settings (e.g., Densmore et al., 2004, Elliott et al., 2012, Whittaker and Walker, 2015). These studies established that: (i) patterns of catchment area, footwall relief, and catchment outlet spacing varied predictably with fault tip propagation (Densmore et al., 2004); (ii) a first - order control on erosional patterns and the size of drainage catchments is the fault throw distribution (Elliott et al., 2012) and; (iii) that patterns in footwall relief mimic fault segmentation (Whittaker and Walker, 2015). Similar to these authors, Chapter 5 asserts fault throw as a first - order control on footwall degradation. While the authors of previous works focused primarily on catchment areas in each case, we use this relationship only to establish the fundamental assumption that footwall erosion is coupled to fault tip propagation and throw accumulation.

Having observed fault throw as a first - order control on footwall erosion on major fault scarps along the Thebe Fault Complex on the Exmouth Plateau, offshore NW Australia, chapter 5 takes this relationship further by using it to constrain the source of hangingwall fans, using volume balancing between the volumes of footwall erosion and hangingwall fans. This novel volume balancing approach was introduced by Barrett et al. (2021), a study also conducted on the Exmouth Plateau, offshore NW Australia. The authors found that the highest values measuring $V_{\text{hangingwall fan}} / V_{\text{footwall erosion}} > 1$ revealed positions of through going sediment input points and that $V_{\text{hangingwall fan}} / V_{\text{footwall erosion}} < 1$ revealed areas of sediment bypass. These results support our findings in that we agree that areas of through going sediment input points and sediment bypass would be represented by these respective values. However, they did not balance total footwall erosion with total hangingwall fan volumes along the length of the fault. In Chapter 5, upon balancing the

sections of the Thebe Fault Complex that hangingwall fan volume exceeded that of footwall erosion ($V_{hangingwall\ fan}$ / $V_{footwall\ erosion}$ > 1) with sections of the Thebe Fault Complex where the eroded volume of the footwall exceeded that of hangingwall fans ($V_{hangingwall\ fan}$ / $V_{footwall\ erosion}$ < 1), we found that the total eroded footwall material could account for 99.6 % of the total degraded fan volumes. Thus, we concluded that the origin of hangingwall fans are likely to be completely footwall – derived and that in addition to the findings of Barrett et al. (2021) that $V_{hangingwall\ fan}$ / $V_{footwall\ erosion}$ < 1 and >1 revealed sediment bypass systems, this pattern can also be a result of along-strike transport of footwall-derived material within the fixed area of the hangingwall basin.

7.2.2 Fault Growth Models in Sediment – Starved Settings

Chapter 5 found that (i) fault throw and footwall erosion are coupled; and (ii) volume balancing reveals that footwall erosion accounts for 99.6 % of hangingwall fan volumes for the Thebe Fault Complex and (iii) presented a novel method to constrain fault growth models in sediment - starved settings, using fault - degradation complexes. The study in Chapter 5 highlights that where (i) and (ii) are true, the spatial distribution of hangingwall fans can constrain paleotip location at the time of fan deposition. Thus, by mapping the spatial and temporal distribution of footwall - derived fans, fault tip propagation and fault growth models can be constrained using the fault - degradation complexes. Other studies mentioned in 7.2.1 which link fault displacement and footwall erosion have focussed on catchment areas and have not used these methods to constrain fault growth settings (i.e., Densmore et al., 2004, Elliott et al., 2012, Whittaker and Walker, 2015). Moreover, Barrett et al. (2021) use their novel volume balancing approach to quantify sediment bypass and through - going sediment input, and do not apply it in any manner to constrain fault growth models in sediment – starved basins. In fact, at present and with best efforts of exploring the literature, there are no studies where volume balancing and the spatial and temporal distribution of footwall - derived fans are used to constrain fault growth models. We found that fans were distributed along the length of the Thebe Fault Complex. These fans all downlapped onto the same

chronostratigraphic surface with the age of the onlapping stratigraphy restricting fan deposition to the first < 10 Ma of rifting or 12% of rift history. In addition, we found that at relay zones this relationship was maintained, meaning that fault tip interaction and relay zone formation also occurred within this time period. The chapters key findings are thus that the processes required for fan deposition, namely: (i) fault throw accumulation; (ii) footwall erosion and fan deposition; and (iii) fault lengthening and relay zone formation, too, must have occurred within the first 12% of rift history and that the Thebe Fault Complex grew by the hybrid fault growth model, based on the requirement of rapid fault lengthening *and* sufficient throw accumulation within the early fault life to result in significant footwall erosion of up to 49 % of initial throw on the fault scarp.

This novel approach for constraining fault growth in sediment - starved settings requires the presence of footwall degradation, the presence of footwall - derived fans in the hangingwall and the application of volume balancing to the footwall erosion and hangingwall fans to quantify the relationship between footwall erosion and fan volumes. Without the assumption that the fans are almost completely footwall - derived, the results of this method to constrain fault growth would be unreliable, as the reasonable assumption that the timing of fan deposition is solely related to fault growth would not be reasonably validated.

7.2.3 Implications of my findings on Constraining Fault Growth in Sediment Starved Basins

In Chapter 4, we see the importance of being able to understand the fault scaling relationships underpinning fault growth and dimensions. How we adjust our observation and interpretation of fault scaling relationships and their consequent fault growth models to different geological settings is also clarified in Chapter 4, where local- to regional mechanical controls on fault growth and dimensions causes deviations from fault scaling relations (e.g., Cowie and Scholz, 1992a, Gross et al., 1997, Peacock, 2002, Wilkins and Gross, 2002, Soliva and Benedicto, 2005, Soliva et al., 2005a, Redpath et al., 2022). Chapter 5 offers a novel technique to understanding fault scaling relations

and the evolution of fault growth in geological settings where it is otherwise difficult to do so because a complete syn-kinematic sequence is absent. Thus, highlighting the need to adjust approaches taken to measure normal fault growth in context of geological setting.

Thus, Chapter 5 shows the importance of geomorphological methods when quantifying fault throw and footwall erosion. In addition, this chapter highlights how volume balancing can be a key tool when evaluating fault evolution in sediment starved basins where traditional techniques using growth strata to do so would be used with rather limited effectiveness. It was forementioned that the basis for this method was that not all faults are present as ideal growth faults on which to analyse their growth. Likewise, natural resources are not distributed in ideal settings where all aspects of the resource 'play' can be constrained. Thus, this method enhances the ability to understand the presence and distribution of natural resources, where these aspects are controlled by fault growth in sediment-starved settings.

7.3 Research Aim 3: Determining the Behaviour of Relay-Breaching Faults

Relay zone kinematics are fundamental to the process of fault growth by segment linkage and the tectono-stratigraphic evolution of extensional basins (e.g., Peacock and Sanderson, 1991, Trudgill and Cartwright, 1994, Cartwright et al., 1996, Peacock and Sanderson, 1996, Gawthorpe and Leeder, 2000, Tavarnelli and Pasqui, 2000, Mansfield and Cartwright, 2001, Jackson et al., 2002, Peacock, 2002, Moustafa and Khalil, 2016, Jackson et al., 2017, Finch and Gawthorpe, 2017, Whipp et al., 2017, Rotevatn et al., 2019, Ma et al., 2021). A well-known and distinctive characteristic of relay zones are the presence of displacement minima in displacement-length data along their length (e.g., Peacock and Sanderson, 1991, Gawthorpe and Hurst, 1993, Wilkins and Gross, 2002). The motivation for Chapter 6 was to understand the behaviour of displacement minima at relay zones over geological timescales. This interest was instigated observations that

breaching faults have higher throw rates than their adjacent faults and that this behaviour could remove displacement minima on young (15kyr), active faults in <1 Myr by Faure Walker et al. (2009). This chapter did so by focussing on throw rate variability on breaching faults by measuring the throw rate along the length of the strike of relay-breaching faults and their adjacent segments over geological timescales. Moreover, this chapter is, to the best of our search in the literature, one of the first studies to investigate breaching fault throw rates and the persistence and presence of displacement minima using ancient, large normal faults that were active over geological timescales. The key findings from Chapter 6 were that: (i) relay-breaching segments on the Glencoe and Thebe relay zones had higher throw rates by 58 and 48%, respectively, than throw rates observed on their adjacent faults; (ii) these high throw rates did not persist over the life of the relay-breaching faults, rather they were present for 13% of the total rift period in the case of the Glencoe relay and 4% of the total fault activity in the case of the Thebe relay zone; (iii) that the relay-breaching fault on the Glencoe relay zone reduced the throw minimum by up to 85% of the adjacent faults' throw maximum and; (iv) relay-breaching faults removing or reducing displacement minima may be dependent on the magnitude by which throw rates exceed their adjacent faults and the period over which throw rates persist - which we suggest may not be long enough since they were present for just 4-13% of the faults life. The findings of Chapter 6 have significant implications for our understanding of relay zone kinematics and the mechanism of relay zone breaching, by which faults grow by segment linkage (e.g., Peacock and Sanderson, 1991, Trudgill and Cartwright, 1994, Dawers and Anders, 1995, Cartwright et al., 1995, Cartwright et al., 1996, Rotevatn et al., 2019).

7.3.1 High Throw Rates Exist on Breaching Faults

The existence of breaching faults having higher throw rates than their adjacent segments has previously been documented by Faure Walker et al. (2009). The authors found that the breaching faults on young (15,000 years) active faults had a throw rate of 0.67 mm/yr, some 21-76% higher than their adjacent faults (0.38-0.55 mm/yr.). Our study agrees with these findings, insomuch that

the breaching faults in both studies are higher than those on their adjacent faults. Furthermore, Faure Walker et al. (2009) suggest that the greater the obliquity of the breaching segment (up to 90°) with respect to its adjacent faults, the higher throw rates that are able to be achieved. Our study, too, agrees with their modelling approach. It shows that the maximum throw rate on the breaching segment that was parallel (0-10°) to its adjacent faults was lower (i.e., 13.7 m/Myr and 48% of the max. throw rates on its adjacent segments) than that observed on the breaching segment (i.e., 47.9 m/Myr and 58% higher than the max. throw rates on its adjacent faults) with a more oblique orientation to its adjacent segments (i.e., ~30-60° with its adjacent segments, respectively). One discussion that is imperative is that my study is somewhat different to those previously conducted because it observes breaching throw rates on faults that were active over geological timescales, rather than just over the Holocene, and does so using 3D seismic reflection data. As such, we have been able to reconcile the two key observations from Faure Walker et al. (2009)that inspired this study, namely: (i) breaching faults have higher throw rates than their adjacent faults that would remove displacement minima in <1 Myr Faure Walker et al. (2009) and ;(ii) displacement minima are present on relay zones active over geological timescales (Torabi et al., 2019, e.g., Jackson et al., 2017, Rotevatn et al., 2019, Lathrop et al., 2020, Pan et al., 2021, Ma et al., 2021). I reconcile these two contradictory observations by showing that higher throw rates on breaching faults only persist for short periods of the total fault life. Moreover,I show that in fact, putting aside the periods in which relay-breaching faults exhibit their maximum throw rates, they have lower throw rates than their adjacent segments over geological timescales (Fig. 6.10).

Although Chapter 6 makes a significant contribution to the understanding of relay zone kinematics and their breaching faults over geological timescales, it remains unclear as to whether (i) the high throw rates are related to a specific stage of breaching or the maturity of a relay zone and (ii) periods of higher throw rate have implications for the stratigraphic architecture that may develop basin entry points.

7.4 Potential Societal Impact of Research

7.4.1 Potential Geohazard from Increased Throw Rates During Segment Linkage

Seismicity and its implications for society are widely recognised as significant geohazards (e.g., Cui et al., 2011, Kargel et al., 2016, Fan et al., 2019, Lyu et al., 2020). Relay zones have been identified as sources of potential geohazard since they are the sites of fault growth by segment linkage (Polcari et al., 2014, Soliva et al., 2008, Di Bucci et al., 2006, Soliva and Benedicto, 2003, Cowie and Scholz, 1992b) .Chapter 6 found that throw rates on active breaching normal faults increase rapidly for a period of time associated with the breaching of the relay ramp. The presence of increased throw rates implies that fault slip rates would increase and create the possibility of seismic events at both the sites of fault linkage during breaching of the relay ramp and on the breaching segment that is exhibiting the elevated throw rates (e.g., Machette et al., 1991, Soliva and Benedicto, 2003, Faure Walker et al., 2009, Luo and Liu, 2018).

7.4.2 Potential Economic Significance of Research

The ability to understand potential geohazards mentioned above certainly has economic implications in areas where populous is present. However, the more direct economic significance of this research comes from the findings in Chapter 5. Degraded footwall highs are the site of hydrocarbon accumulation not only across the Exmouth Plateau (e.g., Scarselli et al., 2015, Paganoni et al., 2019, Bilal et al., 2020, Barrett et al., 2021), but can also be found in several basins globally and in particular in the North Sea (e.g., Brent Field; Zeta Structure) (e.g., Livera, 1990, Coutts et al., 1996, BERGER and ROBERTS, 1999, McLeod and Underhill, 1999). Understanding the relationship between fault growth and scarp degradation in this sense has implications for constraining the timing of trap formation. In addition, where the products of footwall degradation are deposited as hangingwall fans as in Chapter 5, these findings show both a method for reservoir prospecting and highlight the potential of fault scarp degradation-fan complexes as reservoir facies (e.g., Alves and Cupkovic, 2018, Barrett et al., 2021). In addition to the economic implications for

hydrocarbon exploration, these exact same findings can be applied to prospecting for viable sites for the geological storage of CO_2 (e.g., Sundal et al., 2016).

7.5 Future Research Directions

7.5.1 Quantifying the influence of mechanical stratigraphy and scatter in D – L datasets

The principal conclusions of Chapter 4 were that (i) mechanical stratigraphy controls fault dimensions on seismic – scale normal faults; and (ii) its influence on fault growth can result in the breakdown of fault scaling relationships which underpin fault growth models (Redpath et al., 2022). Currently, datasets of maximum displacement and fault trace length do not typically indicate the geological setting and mechanical heterogeneity of the faulted sequences in which the measured faults propagated (Fig. 4.2). However, Chapter 4 and 7.1 clearly highlight the need to consider *D* - *L* datasets and fault scaling relationships in context of mechanical stratigraphy, to: (i) understand scatter - deviations from fault scaling relations - in *D* - *L* datasets; and (ii) quantify the extent to which mechanical stratigraphy constitutes scatter in large *D* - *L* datasets.

Future work in this area would thus be focussed on quantifying the extent to which mechanical stratigraphy is the cause of scatter in *D* - *L* global datasets. This would include creating/using existing D-L datasets and conducting fault analysis to identify fault data that are 'over'- or 'under-displaced'. Then it would include calculate the standard deviations of global D-L data and determine the parameters that would define fault data as representing scatter in the dataset (i.e., over- or under-displaced). Using those data that are predefined as scatter, it would analyse the faulted sequences of these faults and evaluate how many of them are laterally or vertically restricted at their tips by boundaries or contacts within heterogenous faulted sequences (i.e., mechanical stratigraphy). Finally, this study would quantify the percentage of the global D-L dataset that is represented by fault data that deviate from fault scaling relationships due to mechanical stratigraphy. This study would focus on seismogenic faults rather than smaller outcrop studies given this is an area yet to be investigated thoroughly for the role of mechanical stratigraphy and

that such faults constitute global D-L datasets. Thus, this work would demonstrably quantify the need to analyse geometric data (i.e., D-L) in context of their geological setting and to properly discriminate when using such D-L data to underpin other research topics.

7.5.2 Relay Zone Kinematics and Displacement Rates on Breaching Faults

The findings of Chapter 6 showed that relay-breaching faults had higher maximum throw rates than their adjacent fault segments, which had higher maximum throw values and much longer trace lengths. Future work needs to consider the implications of these findings and how to further statistically conclude that this is the case for relay zones in general and whether the maximum throw rates on relay-breaching faults are associated with specific conditions related to the maturity of the relay zone and/or their breaching faults. Future work in this area could thus be focussed on: (i) investigating if, indeed, breaching faults have higher throw rates than their concomitant faults because of specific 3D geometric parameters over geological timescales, and (ii) determining whether or not the periods of higher throw rates, which we observed did not persist over the whole life of the breaching faults, are restricted to a particular period of maturity of the relay zone and/or breaching faults. A future study could investigate (i) and (ii) by testing these hypotheses using a statistically significant dataset of faults in 3D seismic. This dataset would ideally be taken from several extensional basins, where access to 3D seismic datasets and well data allow for the observation of natural relay zones. As such, and given the plethora of data and data availability, the North Sea and the Exmouth Plateau may provide suitable locations in which to conduct this study. On the other hand, given the magnitude of observational work that would have to be conducted on relay zones in the forementioned approach, a modelling technique may also provide a good method for observing stages of relay zone breaching and if the high throw rates are associated with a particular time period. This approach would likely use numerical modelling (i.e., Imber et al., 2004, Laurent et al., 2013) to allow for the isolation of periods of high relay-breaching

fault throw rates and to allow for the comparison of when they occur, controlling for the maturity and/or geometry of the relay zone.

7.5.3 The Stratigraphic Response to High Displacement Rates at Sediment Basin Entry Points: Insights from Modelling Breaching Rates.

While a dedicated study of the structural development of breaching faults has important implications for furthering the understanding of relay zone kinematics, we did not investigate the stratigraphic implications of our findings in this study. Relay zones are key basin entry points for sedimentary systems as rifts develop. Furthermore, they are an inherent part of rifts evolving from hydrologically closed settings to open marine settings (i.e., transfer zones) (See Chapter 2) (e.g., Gawthorpe and Hurst, 1993, Gawthorpe and Leeder, 2000, Moustafa and Khalil, 2016). Building upon observation from Chapter 6, future research study would aim to determine if there is a stratigraphic response to high breaching rates at relay zones.

Future work could therefore aim to use numerical modelling to isolate the period of higher throw rates on relay-breaching faults against a background of constant throw rates on its adjacent segments. In addition, I would then introduce sedimentary systems to the relay ramp (e.g., Wiebke et al., 2010). What is particularly interesting about this future research is that it would test the stratigraphic response to varying breaching rates and observe the consequent stratigraphic architecture in the hangingwall basin. In addition, this study would seek to vary throw rates on breaching faults to compare the depositional architecture to variable throw rates. The base case in this study would be established using inputs from examples of sedimentary systems and their deposits at relay zones (e.g., Gawthorpe and Hurst, 1993, Densmore et al., 2003, Wiebke et al., 2010, Athmer and Luthi, 2011, Moustafa and Khalil, 2016).

7.6 Implications and Concluding Remarks

The research presented within this thesis has provided detailed evidence to address normal fault growth and the fundamental principles that underpin their growth, dimensions, and fault growth models. Firstly, this research has taken the approach of investigating the controls on fault growth and geometry for *individual fault segments,* by studying how these controls can cause faults to deviates from the fault scaling relationships that underpin fault growth (Chapter 4). In addition, this thesis builds on the findings from Chapter 4 by addressing how *faults grow by segment linkage* through an investigation of throw rates on relay-breaching faults during relay zone kinematics (Chapter 6). Finally, it is obvious that fault growth does not solely occur in ideal settings where it can be observed, measured, and tested. For this reason, this thesis presents a *novel technique* by which to observe and measure fault tip propagation in *sediment starved basins* (Chapter 5). Thus, this thesis addresses its key aims by (1) understanding controls on normal fault growth on a individual fault surface, (2) addressing a critical question regarding relay zone breaching during relay zone kinematics and growth by segment linkage and (3) measuring fault growth in a sediment starved basin by proposing a novel technique which uses basin architecture and geomorphological techniques.

These findings are essential to improving our understand of normal fault growth and the fault scaling relationships by which they grow, in addition to suggesting how best we can use fault geometric data to understand fault growth models. The new approach presented in this thesis to test fault growth models in sediment starved basins provides an important tool for future studies. Importantly, this thesis has addressed research topics which contribute to the proposal for future research directions and in furthering the understanding of mechanical stratigraphy's control on seismic-scale faults and relay zone kinematics which define fault growth by segment linkage.

References

ALVES, T. M., CARTWRIGHT, J. & DAVIES, R. J. 2009. Faulting of salt-withdrawal basins during early halokinesis: effects on the Paleogene Rio Doce Canyon system (Espírito Santo Basin, Brazil). *AAPG bulletin,* 93**,** 617-652.

ALVES, T. M. & CUPKOVIC, T. 2018. Footwall degradation styles and associated sedimentary facies distribution in SE Crete: Insights into tilt-block extensional basins on continental margins. *Sedimentary Geology,* 367**,** 1-19.

ANDERSON, E. M. 1905. The dynamics of faulting. *Transactions of the Edinburgh Geological Society,* 8**,** 387-402.

ATHMER, W. & LUTHI, S. M. 2011. The effect of relay ramps on sediment routes and deposition: A review. *Sedimentary Geology,* 242**,** 1-17.

BACON, M., SIMM, R. & REDSHAW, T. 2003. 3-D Seismic Interpretation. *3-D Seismic Interpretation, by M. Bacon and R. Simm and T. Redshaw, pp. 222. ISBN 0521792037. Cambridge, UK: Cambridge University Press, October 2003.*

BADLEY, M., PRICE, J. & BACKSHALL, L. 1989. Inversion, reactivated faults and related structures: seismic examples from the southern North Sea. *Geological Society, London, Special Publications,* 44**,** 201-219.

BARNETT, J. A., MORTIMER, J., RIPPON, J. H., WALSH, J. J. & WATTERSON, J. 1987. Displacement geometry in the volume containing a single normal fault. *AAPG Bulletin,* 71**,** 925-937.

BARRETT, B. J., HODGSON, D. M., JACKSON, C. A. L., LLOYD, C., CASAGRANDE, J. & COLLIER, R. E. L. 2021. Quantitative analysis of a footwall-scarp degradation complex and syn-rift stratigraphic architecture, Exmouth Plateau, NW Shelf, offshore Australia. *Basin Research,* 33**,** 1135-1169.

BASTESEN, E. & ROTEVATN, A. 2012. Evolution and structural style of relay zones in layered limestone–shale sequences: insights from the Hammam Faraun Fault Block, Suez rift, Egypt. *Journal of the Geological Society,* 169**,** 477.

BATE, R. H., CAMERON, N. R. & BRANDÃO, M. G. P. 2001. *The lower cretaceous (Pre-Salt)*
lithostratigraphy of the Kwanza Basin, Angola, Newsletter on Stratigraphy

BAUDON, C. & CARTWRIGHT, J. 2008a. The kinematics of reactivation of normal faults using high resolution throw mapping. *Journal of Structural Geology,* 30**,** 1072-1084.

BAUDON, C. & CARTWRIGHT, J. A. 2008b. 3D seismic characterisation of an array of blind normal faults in the Levant Basin, Eastern Mediterranean. *Journal of Structural Geology,* 30**,** 746-760.

BERGER, M. & ROBERTS, A. M. 1999. The Zeta Structure: a footwall degradation complex formed by gravity sliding on the western margin of the Tampen Spur, Northern North Sea. *Geological Society, London, Petroleum Geology Conference Series,* 5**,** 107-116.

BILAL, A. & MCCLAY, K. 2022. Tectonic and stratigraphic evolution of the central Exmouth Plateau, NW Shelf of Australia. *Marine and Petroleum Geology,* 136**,** 105447.

BILAL, A., MCCLAY, K. & SCARSELLI, N. 2020. Fault-scarp degradation in the central Exmouth Plateau, North West Shelf, Australia. *In:* MCCLAY, K. R. & HAMMERSTEIN, J. A. (eds.) *Passive Margins: Tectonics, Sedimentation and Magmatism.* Geological Society of London.

BLACK, M., MCCORMACK, K., ELDERS, C. & ROBERTSON, D. 2017. Extensional fault evolution within the Exmouth Sub-basin, North West Shelf, Australia. *Marine and Petroleum Geology,* 85**,** 301-315.

BODVARSSON, G., BENSON, S. & WITHERSPOON, P. 1982. Theory of the development of geothermal systems charged by vertical faults. *Journal of Geophysical Research: Solid Earth,* 87**,** 9317-9328.

BORONKAY, K. & DOUTSOS, T. 1994. Transpression and transtension within different structural levels in the central Aegean region. *Journal of Structural Geology,* 16**,** 1555-1573.

BOSWORTH, W. 1985. Geometry of propagating continental rifts. *Nature,* 316**,** 625-627.

BRICE, S. E., COCHRAN, M. D., PARDO, G. & EDWARDS, A. D. 1982. Tectonics and Sedimentation of the South Atlantic Rift Sequence: Cabinda, Angola

Studies in Continental Margin Geology. *In:* WATKINS, J. S. & DRAKE, C. L. (eds.). American Association of Petroleum Geologists.

BROWN, A. R. 2011. *Interpretation of three-dimensional seismic data*, Society of Exploration Geophysicists and American Association of Petroleum ….

BÜRGMANN, R., POLLARD, D. D. & MARTEL, S. J. 1994. Slip distributions on faults: effects of stress gradients, inelastic deformation, heterogeneous host-rock stiffness, and fault interaction. *Journal of Structural Geology,* 16**,** 1675-1690.

CAMANNI, G., ROCHE, V., CHILDS, C., MANZOCCHI, T., WALSH, J., CONNEALLY, J., SAQAB, M. M. & DELOGKOS, E. 2019. The three-dimensional geometry of relay zones within segmented normal faults. *Journal of Structural Geology,* 129**,** 103895.

CARAFA, M. M. C., DI NACCIO, D., DI LORENZO, C., KASTELIC, V. & BIRD, P. 2022. A Meta-Analysis of Fault Slip Rates Across the Central Apennines. *Journal of Geophysical Research: Solid Earth,* 127**,** e2021JB023252.

CARTWRIGHT, J. A., MANSFIELD, C. & TRUDGILL, B. 1996. The growth of normal faults by segment linkage. *Geological Society, London, Special Publications,* 99**,** 163-177.

CARTWRIGHT, J. A., TRUDGILL, B. D. & MANSFIELD, C. S. 1995. Fault growth by segment linkage: an explanation for scatter in maximum displacement and trace length data from the Canyonlands Grabens of SE Utah. *Journal of Structural Geology,* 17**,** 1319-1326.

CÉLÉRIER, B. 2008. Seeking Anderson's faulting in seismicity: A centennial celebration. *Reviews of Geophysics,* 46.

CHILDS, C., HOLDSWORTH, R. E., JACKSON, C. A.-L., MANZOCCHI, T., WALSH, J. J. & YIELDING, G. 2017a. Introduction to the geometry and growth of normal faults. *Geological Society, London, Special Publications,* 439**,** 1-9.

CHILDS, C., HOLDSWORTH, R. E., JACKSON, C. A. L., MANZOCCHI, T., WALSH, J. J. & YIELDING, G. 2017b. Introduction to the geometry and growth of normal faults. *Geological Society, London, Special Publications,* 439**,** 1.

CHILDS, C., MANZOCCHI, T., NICOL, A., WALSH, J. J., SODEN, A. M., CONNEALLY, J. C. & DELOGKOS, E. 2017c. The relationship between normal drag, relay ramp aspect ratio and fault zone structure. *Geological Society, London, Special Publications,* 439**,** 355.

CHILDS, C., NICOL, A., WALSH, J. J. & WATTERSON, J. 2003. The growth and propagation of synsedimentary faults. *Journal of Structural geology,* 25**,** 633-648.

CHOPRA, S. & MARFURT, K. J. 2005. Seismic attributes—A historical perspective. *Geophysics,* 70**,** 3SO-28SO.

CHOPRA, S. & MARFURT, K. J. 2018. Coherence attribute applications on seismic data in various guises — Part 1. *Interpretation,* 6**,** T521-T529.

CLADOUHOS, T. T. & MARRETT, R. 1996. Are fault growth and linkage models consistent with power-law distributions of fault lengths? *Journal of Structural Geology,* 18**,** 281-293.
COLLANEGA, L., JACKSON, C., BELL, R., COLEMAN, A., LENHART, A. & BREDA, A. 2018. Normal fault growth influenced by basement fabrics: the importance of preferential nucleation from pre-existing structures. *Basin Research*.
COMMINS, D., GUPTA, S. & CARTWRIGHT, J. 2005. Deformed streams reveal growth and linkage of a normal fault array in the Canyonlands graben, Utah. *Geology,* 33**,** 645-648.
CONNEALLY, J., CHILDS, C. & WALSH, J. J. 2014. Contrasting origins of breached relay zone geometries. *Journal of Structural Geology,* 58**,** 59-68.
CORBEL, S., SCHILLING, O., HOROWITZ, F., REID, L., SHELDON, H., TIMMS, N. & WILKES, P. Identification and geothermal influence of faults in the Perth metropolitan area, Australia. Thirty-Seventh Workshop on Geothermal Reservoir Engineering, 2012. Stanford University California, 8.
COUTTS, S., LARSSON, S. & ROSMAN, R. 1996. Development of the slumped crestal area of the Brent reservoir, Brent Field; an integrated approach. *Petroleum Geoscience,* 2**,** 219-229.
COWIE, P., GUPTA, S. & DAWERS, N. 2000. Implications of fault array evolution for synrift depocentre development: insights from a numerical fault growth model. *Basin Research,* 12**,** 241-261.
COWIE, P. A., ROBERTS, G. P., BULL, J. M. & VISINI, F. 2012. Relationships between fault geometry, slip rate variability and earthquake recurrence in extensional settings. *Geophysical Journal International,* 189**,** 143-160.
COWIE, P. A. & SCHOLZ, C. H. 1992a. Displacement-length scaling relationship for faults: data synthesis and discussion. *Journal of Structural Geology,* 14**,** 1149-1156.
COWIE, P. A. & SCHOLZ, C. H. 1992b. Growth of faults by accumulation of seismic slip. *Journal of Geophysical Research: Solid Earth,* 97**,** 11085-11095.
COWIE, P. A. & SHIPTON, Z. K. 1998. Fault tip displacement gradients and process zone dimensions. *Journal of Structural Geology,* 20**,** 983-997.
CRIDER, J. G. & POLLARD, D. D. 1998. Fault linkage: Three-dimensional mechanical interaction between echelon normal faults. *Journal of Geophysical Research: Solid Earth,* 103**,** 24373-24391.
CUI, P., CHEN, X.-Q., ZHU, Y.-Y., SU, F.-H., WEI, F.-Q., HAN, Y.-S., LIU, H.-J. & ZHUANG, J.-Q. 2011. The Wenchuan Earthquake (May 12, 2008), Sichuan Province, China, and resulting geohazards. *Natural Hazards,* 56**,** 19-36.
CUNNINGHAM, J. E., CARDOZO, N., TOWNSEND, C. & CALLOW, R. H. T. 2021. The impact of seismic interpretation methods on the analysis of faults: a case study from the Snøhvit field, Barents Sea. *Solid Earth,* 12**,** 741-764.
DAWERS, N. H. & ANDERS, M. H. 1995. Displacement-length scaling and fault linkage. *Journal of Structural Geology,* 17**,** 607-614.
DELOGKOS, E., SAQAB, M. M., WALSH, J. J., ROCHE, V. & CHILDS, C. 2020. Throw variations and strain partitioning associated with fault-bend folding along normal faults. *Solid Earth,* 11**,** 935-945.
DENG, H. & MCCLAY, K. 2020. Tectono-stratigraphy of the Dampier sub-basin, North West Shelf of Australia. *Geological Society, London, Special Publications,* 476**,** 259-285.
DENSMORE, A. L., DAWERS, N. H., GUPTA, S., ALLEN, P. A. & GILPIN, R. 2003. Landscape evolution at extensional relay zones. *Journal of Geophysical Research: Solid Earth,* 108.

DENSMORE, A. L., DAWERS, N. H., GUPTA, S., GUIDON, R. & GOLDIN, T. 2004. Footwall topographic development during continental extension. *Journal of Geophysical Research: Earth Surface,* 109.

DI BUCCI, D., MASSA, B. & ZUPPETTA, A. 2006. Relay ramps in active normal fault zones: A clue to the identification of seismogenic sources (1688 Sannio earthquake, Italy). *GSA Bulletin,* 118**,** 430-448.

DOCKRILL, B. & SHIPTON, Z. K. 2010. Structural controls on leakage from a natural CO2 geologic storage site: Central Utah, USA. *Journal of Structural Geology,* 32**,** 1768-1782.

DRISCOLL, N. W. & KARNER, G. D. 1998. Lower crustal extension across the Northern Carnarvon basin, Australia: Evidence for an eastward dipping detachment. *Journal of Geophysical Research: Solid Earth,* 103**,** 4975-4991.

DUFFY, O., BELL, R., JACKSON, C., L. GAWTHORPE, R. & S. WHIPP, P. 2015. *Fault Growth and Interactions in a Multiphase Rift Fault Network: Horda Platform, Norwegian North Sea*, Journal of Structural Geology

EATON, G. P. 1982. The Basin and Range province: Origin and tectonic significance. *Annual Review of Earth and Planetary Sciences,* 10**,** 409-440.

ELIET, P. & GAWTHORPE, R. 1995. Drainage development and sediment supply within rifts, examples from the Sperchios basin, central Greece. *Journal of the Geological Society,* 152**,** 883-893.

ELLIOTT, G. M., WILSON, P., JACKSON, C. A. L., GAWTHORPE, R. L., MICHELSEN, L. & SHARP, I. R. 2012. The linkage between fault throw and footwall scarp erosion patterns: an example from the Bremstein Fault Complex, offshore Mid-Norway. *Basin Research,* 24**,** 180-197.

EVANS, S. L. & JACKSON, C. A.-L. 2019. Base-salt relief controls salt-related deformation in the Outer Kwanza Basin, offshore Angola. *Basin Research,* n/a.

EXON, N. F. & WILLCOX, J. B. 1978. Geology and Petroleum Potential of Exmouth Plateau Area Off Western Australia1. *AAPG Bulletin,* 62**,** 40-72.

FAIRLEY, J. P. & HINDS, J. J. 2004. Rapid transport pathways for geothermal fluids in an active Great Basin fault zone. *Geology,* 32**,** 825-828.

FAN, X., SCARINGI, G., KORUP, O., WEST, A. J., VAN WESTEN, C. J., TANYAS, H., HOVIUS, N., HALES, T. C., JIBSON, R. W. & ALLSTADT, K. E. 2019. Earthquake-induced chains of geologic hazards: Patterns, mechanisms, and impacts. *Reviews of geophysics,* 57**,** 421-503.

FAURE WALKER ET AL., R. G., COWIE P., MCCAFFREY K., WEDMORE L., MILDON Z., GREGORY L. 2015. Long-term strain rates as a tool for understanding the mechanics of continental extension and the importance of local 3D fault geometry for local throw-rates across faults. *6th Int. INQUA Meeting on Paleoseismology, Active Tectonics and Archaeoseismology.*

FAURE WALKER, J. P., ROBERTS, G. P., COWIE, P. A., PAPANIKOLAOU, I. D., SAMMONDS, P. R., MICHETTI, A. M. & PHILLIPS, R. J. 2009. Horizontal strain-rates and throw-rates across breached relay zones, central Italy: Implications for the preservation of throw deficits at points of normal fault linkage. *Journal of Structural Geology,* 31**,** 1145-1160.

FERRILL, D. A. & MORRIS, A. P. 2001. Displacement gradient and deformation in normal fault systems. *Journal of Structural Geology,* 23**,** 619-638.

FERRILL, D. A. & MORRIS, A. P. 2008. Fault zone deformation controlled by carbonate mechanical stratigraphy, Balcones fault system, Texas. *AAPG bulletin,* 92**,** 359-380.

FERRILL, D. A., MORRIS, A. P., MCGINNIS, R. N., SMART, K. J., WIGGINTON, S. S. & HILL, N. J. 2017. Mechanical stratigraphy and normal faulting. *Journal of Structural Geology,* 94**,** 275-302.

FERRILL, D. A., STAMATAKOS, J. A. & SIMS, D. 1999. Normal fault corrugation: Implications for growth and seismicity of active normal faults. *Journal of Structural Geology,* 21**,** 1027-1038.

FINCH, E. & GAWTHORPE, R. 2017. Growth and interaction of normal faults and fault network evolution in rifts: insights from three-dimensional discrete element modelling. *Geological Society, London, Special Publications,* 439**,** 219.

FOSSEN, H. & ROTEVATN, A. 2016. Fault linkage and relay structures in extensional settings—A review. *Earth-Science Reviews,* 154**,** 14-28.

FREDERIKSEN, S. & BRAUN, J. 2001. Numerical modelling of strain localisation during extension of the continental lithosphere. *Earth and Planetary Science Letters,* 188**,** 241-251.

FREITAG, U. A., SANDERSON, D. J., LONERGAN, L. & BEVAN, T. G. 2017. Comparison of upwards splaying and upwards merging segmented normal faults. *Journal of Structural Geology,* 100**,** 1-11.

GAWTHORPE, R. L. & HURST, J. M. 1993. Transfer zones in extensional basins: their structural style and influence on drainage development and stratigraphy. *Journal of the Geological Society,* 150**,** 1137-1152.

GAWTHORPE, R. L. & LEEDER, M. R. 2000. Tectono-sedimentary evolution of active extensional basins. *Basin Research,* 12**,** 195-218.

GAWTHORPE, R. L., LEEDER, M. R., KRANIS, H., SKOURTSOS, E., ANDREWS, J. E., HENSTRA, G. A., MACK, G. H., MURAVCHIK, M., TURNER, J. A. & STAMATAKIS, M. 2018. Tectono-sedimentary evolution of the Plio-Pleistocene Corinth rift, Greece. *Basin Research,* 30**,** 448-479.

GHALAYINI, R., DANIEL, J.-M., NADER, F. & HOMBERG, C. 2016. Predicting reservoir intervals by looking at fault data: An exploration tool in frontier basins. *International Conference and Exhibition, Barcelona, Spain, 3-6 April 2016.*

GIBA, M., WALSH, J. J. & NICOL, A. 2012. Segmentation and growth of an obliquely reactivated normal fault. *Journal of Structural Geology,* 39**,** 253-267.

GIBBONS, A. D., BARCKHAUSEN, U., VAN DEN BOGAARD, P., HOERNLE, K., WERNER, R., WHITTAKER, J. M. & MÜLLER, R. D. 2012. Constraining the Jurassic extent of Greater India: Tectonic evolution of the West Australian margin. *Geochemistry, Geophysics, Geosystems,* 13.

GIBBS, A. D. 1984. Structural evolution of extensional basin margins. *Journal of the Geological Society,* 141**,** 609-620.

GOLDSWORTHY, M. & JACKSON, J. 2000. Active normal fault evolution in Greece revealed by geomorphology and drainage patterns. *Journal of the Geological Society,* 157**,** 967-981.

GROSS, M. R., GUTIE, G., BAI, T., WACKER, M. A., COLLINSWORTH, K. B. & BEHL, R. J. 1997. Influence of mechanical stratigraphy and kinematics on fault scaling relations. *Journal of Structural Geology,* 19**,** 171-183.

GUPTA, A. & SCHOLZ, C. H. 2000. A model of normal fault interaction based on observations and theory. *Journal of Structural Geology,* 22**,** 865-879.

GUPTA, S. & COWIE, P. 2000. Processes and controls in the stratigraphic development of extensional basins. *Basin Research,* 12**,** 185-194.

GUPTA, S., COWIE, P. A., DAWERS, N. H. & UNDERHILL, J. R. 1998. A mechanism to explain rift-basin subsidence and stratigraphic patterns through fault-array evolution. *Geology,* 26**,** 595-598.

GUPTA, S., UNDERHILL, J. R., SHARP, I. R. & GAWTHORPE, R. L. 1999. Role of fault interactions in controlling synrift sediment dispersal patterns: Miocene, Abu Alaqa Group, Suez Rift, Sinai, Egypt. *Basin Research,* 11**,** 167.

HONGXING, G. & ANDERSON, J. K. 2007. Fault throw profile and kinematics of Normal fault: conceptual models and geologic examples. *Geological Journal of China Universities,* 13**,** 75-88.

HOWLETT, D. M., GAWTHORPE, R. L., GE, Z., ROTEVATN, A. & JACKSON, C. A.-L. 2020. Turbidites, topography and tectonics: Evolution of submarine channel-lobe systems in the salt-influenced Kwanza Basin, offshore Angola. *Basin Research,* n/a.

HUANG, Y., WANG, Q., HAO, M. & ZHOU, S. 2018. Fault Slip Rates and Seismic Moment Deficits on Major Faults in Ordos Constrained by GPS Observation. *Scientific Reports,* 8**,** 16192.

HUDEC, M. & JACKSON, M. 2003. *Structural segmentation, inversion, and salt tectonics on a passive margin: Evolution of the Inner Kwanza Basin, Angola*.

HUDEC, M. & JACKSON, M. 2004. *Regional restoration across the Kwanza Basin, Angola: Salt tectonics triggered by repeated uplift of a metastable passive margin*, AAPG Bulletin.

HUGGINS, P., WATTERSON, J., WALSH, J. J. & CHILDS, C. 1995. Relay zone geometry and displacement transfer between normal faults recorded in coal-mine plans. *Journal of Structural Geology,* 17**,** 1741-1755.

IMBER, J., TUCKWELL, G., CHILDS, C., WALSH, J., MANZOCCHI, T., HEATH, A., BONSON, C. & STRAND, J. 2004. Three-dimensional distinct element modelling of relay growth and breaching along normal faults. *Journal of Structural Geology,* 26**,** 1897-1911.

JACKSON, C. A.-L., CARRUTHERS, D. T., MAHLO, S. N. & BRIGGS, O. 2014. Can polygonal faults help locate deep-water reservoirs? *AAPG Bulletin,* 98**,** 1717-1738.

JACKSON, C. A. L., BELL, R. E., ROTEVATN, A. & TVEDT, A. B. M. 2017. Techniques to determine the kinematics of synsedimentary normal faults and implications for fault growth models. *Geological Society, London, Special Publications,* 439**,** 187.

JACKSON, C. A. L., GAWTHORPE, R. L. & SHARP, I. R. 2002. Growth and linkage of the East Tanka fault zone, Suez rift: structural style and syn-rift stratigraphic response. *Journal of the Geological Society,* 159**,** 175-187.

JACKSON, C. A. L. & ROTEVATN, A. 2013. 3D seismic analysis of the structure and evolution of a salt-influenced normal fault zone: A test of competing fault growth models. *Journal of Structural Geology,* 54**,** 215-234.

JACKSON, J. & MCKENZIE, D. 1983. The geometrical evolution of normal fault systems. *Journal of Structural Geology,* 5**,** 471-482.

JACKSON, J. A. 1987a. Active normal faulting and crustal extension. *Geological Society, London, Special Publications,* 28**,** 3-17.

JACKSON, M. P. A. & HUDEC, M. R. 2008. Interplay of Basement, Salt Tectonics, and Sedimentation in the Kwanza Basin, Angola *AAPG International Conference and Exhibition 2008*.

JACKSON, M. P. A., HUDEC, M. R. & HEGARTY, K. A. 2005. The great West African Tertiary coastal uplift: Fact or fiction? A perspective from the Angolan divergent margin. *Tectonics,* 24.

JACKSON, P. 1987b. The corrugation and bifurcation of fault surfaces by cross-slip. *Journal of Structural Geology,* 9**,** 247-250.

JOSHI, G. R. & HAYASHI, D. 2010. Development of extensional stresses in the compressional setting of the Himalayan thrust wedge: inference from numerical modelling. *Natural Science,* 2**,** 667.

KARGEL, J. S., LEONARD, G. J., SHUGAR, D. H., HARITASHYA, U. K., BEVINGTON, A., FIELDING, E. J., FUJITA, K., GEERTSEMA, M., MILES, E. & STEINER, J. 2016. Geomorphic and geologic controls of geohazards induced by Nepal's 2015 Gorkha earthquake. *Science,* 351**,** aac8353.

KARNER, G. D. & GAMBÔA, L. A. P. 2007. Timing and origin of the South Atlantic pre-salt sag basins and their capping evaporites. *Geological Society, London, Special Publications,* 285**,** 15.

KHALIL, S. & MCCLAY, K. 2009. Structural control on syn-rift sedimentation, northwestern Red Sea margin, Egypt. *Marine and Petroleum Geology,* 26**,** 1018-1034.

KHALIL, S. M. & MCCLAY, K. R. 2017. 3D geometry and kinematic evolution of extensional fault-related folds, NW Red Sea, Egypt. *Geological Society, London, Special Publications,* 439**,** 109.

KIM, Y.-S. & SANDERSON, D. J. 2005. The relationship between displacement and length of faults: a review. *Earth-Science Reviews,* 68**,** 317-334.

KNIPE, R. J., JONES, G. & FISHER, Q. 1998. Faulting, fault sealing and fluid flow in hydrocarbon reservoirs: an introduction. *Geological Society, London, Special Publications,* 147**,** vii-xxi.

KOGAN, L., FISSEHA, S., BENDICK, R., REILINGER, R., MCCLUSKY, S., KING, R. & SOLOMON, T. 2012. Lithospheric strength and strain localization in continental extension from observations of the East African Rift. *Journal of Geophysical Research: Solid Earth,* 117.

KRISTENSEN, M., CHILDS, C. & KORSTGÅRD, J. 2008. The 3D geometry of small-scale relay zones between normal faults in soft sediments. *Journal of Structural Geology,* 30**,** 257-272.

LATHROP, B., JACKSON, C., BELL, R. & ROTEVATN, A. 2020. *The kinematics of growth faults and the role of lateral tip retreat*.

LATHROP, B. A., JACKSON, C. A. L., BELL, R. E. & ROTEVATN, A. 2021. Normal Fault Kinematics and the Role of Lateral Tip Retreat: An Example From Offshore NW Australia. *Tectonics,* 40.

LAUBACH, S. E., OLSON, J. E. & GROSS, M. R. 2009. Mechanical and fracture stratigraphy. *AAPG bulletin,* 93**,** 1413-1426.

LAURENT, G., CAUMON, G., BOUZIAT, A. & JESSELL, M. 2013. A parametric method to model 3D displacements around faults with volumetric vector fields. *Tectonophysics,* 590**,** 83-93.

LEEDER, M. R. & GAWTHORPE, R. L. 1987. Sedimentary models for extensional tilt-block/half-graben basins. *Geological Society, London, Special Publications,* 28**,** 139-152.

LIVERA, S. 1990. Brent oil field.

LONG, J. J. & IMBER, J. 2012. Strain compatibility and fault linkage in relay zones on normal faults. *Journal of Structural Geology,* 36**,** 16-26.

LONGLEY, I., BUESSENSCHUETT, C., CLYDSDALE, L., CUBITT, C., DAVIS, R., JOHNSON, M., MARSHALL, N., MURRAY, A., SOMERVILLE, R. & SPRY, T. 2002. The North West shelf of Australia–a woodside perspective. *The sedimentary basins of Western Australia,* 3**,** 27-88.

LUO, G. & LIU, M. 2018. Stressing Rates and Seismicity on the Major Faults in Eastern Tibetan Plateau. *Journal of Geophysical Research: Solid Earth,* 123**,** 10,968-10,986.

LYU, H.-M., SHEN, S.-L., YANG, J. & ZHOU, A.-N. 2020. Risk Assessment of Earthquake-Triggered Geohazards Surrounding Wenchuan, China. *Natural Hazards Review,* 21**,** 05020007.

MA, P., LIN, C., REN, L., JAHREN, J., DONG, D., YU, G., MA, C., WANG, D., LIU, L. & HELLEVANG, H. 2021. Linkage and growth of the independent and coherent faults: Insight into the effect of relay ramps on sedimentation patterns in the northern Bonan Sag, Bohai Bay Basin. *Marine and Petroleum Geology,* 127**,** 104985.

MACHETTE, M. N., PERSONIUS, S. F., NELSON, A. R., SCHWARTZ, D. P. & LUND, W. R. 1991. The Wasatch fault zone, utah—segmentation and history of Holocene earthquakes. *Journal of Structural Geology,* 13**,** 137-149.

MAERTEN, L., WILLEMSE, E. J., POLLARD, D. D. & RAWNSLEY, K. 1999. Slip distributions on intersecting normal faults. *Journal of Structural Geology,* 21**,** 259-272.

MANSFIELD, C. & CARTWRIGHT, J. 2001. *Fault growth by linkage: Observations and implications from analogue models*.

MANZOCCHI, T., CHILDS, C. & WALSH, J. 2010. Faults and fault properties in hydrocarbon flow models. *Geofluids,* 10**,** 94-113.

MARRETT, R. & ALLMENDINGER, R. W. 1990. Kinematic analysis of fault-slip data. *Journal of Structural Geology,* 12**,** 973-986.

MARSHALL, N. & LANG, S. 2013. A new sequence stratigraphic framework for the North West Shelf, Australia. *The Sedimentary Basins of Western Australia IV: Proceedings of the Petroleum Exploration Society of Australia Symposium***,** 1-32.

MARTEL, S. J. 1999. Mechanical controls on fault geometry. *Journal of Structural Geology,* 21**,** 585-596.

MARTON, L. G., TARI, G. C. & LEHMANN, C. T. 2000. Evolution of the Angolan passive margin, West Africa, with emphasis on post-salt structural styles. *Geophysical Monograph-American Geophysical Union,* 115**,** 129-150.

MCCLAY, K. R. 1990. Extensional fault systems in sedimentary basins: a review of analogue model studies. *Marine and Petroleum Geology,* 7**,** 206-233.

MCLEOD, A. & UNDERHILL, J. Processes and products of footwall degradation, northern Brent Field, Northern North Sea. Geological Society, London, Petroleum Geology Conference series, 1999. Geological Society of London, 91-106.

MCLEOD, A. E., DAWERS*, N. H. & UNDERHILL, J. R. 2000. The propagation and linkage of normal faults: insights from the Strathspey–Brent–Statfjord fault array, northern North Sea. *Basin Research,* 12**,** 263-284.

MEYER, V., NICOL, A., CHILDS, C., WALSH, J. J. & WATTERSON, J. 2002. Progressive localisation of strain during the evolution of a normal fault population. *Journal of Structural Geology,* 24**,** 1215-1231.

MIOCIC, J. M., GILFILLAN, S. M., ROBERTS, J. J., EDLMANN, K., MCDERMOTT, C. I. & HASZELDINE, R. S. 2016. Controls on CO2 storage security in natural reservoirs and implications for CO2 storage site selection. *International Journal of Greenhouse Gas Control,* 51**,** 118-125.

MORLEY, C. 2017. The impact of multiple extension events, stress rotation and inherited fabrics on normal fault geometries and evolution in the Cenozoic rift basins of Thailand. *Geological Society, London, Special Publications,* 439**,** 413-445.

MORLEY, C., NELSON, R., PATTON, T. & MUNN, S. 1990. Transfer zones in the East African rift system and their relevance to hydrocarbon exploration in rifts. *AAPG bulletin,* 74**,** 1234-1253.

MORLEY, C. K. 2007. Development of crestal normal faults associated with deepwater fold growth. *Journal of Structural Geology,* 29**,** 1148-1163.

MOSCARDELLI, L. & WOOD, L. 2008. New classification system for mass transport complexes in offshore Trinidad. *Basin Research,* 20**,** 73-98.

MOUSTAFA, A. R. & KHALIL, S. M. 2016. Control of extensional transfer zones on syntectonic and post-tectonic sedimentation: implications for hydrocarbon exploration. *Journal of the Geological Society,* 174**,** 318-335.

NALIBOFF, J. B., BUITER, S. J. H., PÉRON-PINVIDIC, G., OSMUNDSEN, P. T. & TETREAULT, J. 2017. Complex fault interaction controls continental rifting. *Nature Communications,* 8**,** 1179.

NEEDHAM, D., YIELDING, G. & FREEMAN, B. 1996. Analysis of fault geometry and displacement patterns. *Geological Society, London, Special Publications,* 99**,** 189-199.

NICOL, A., CHILDS, C., WALSH, J., MANZOCCHI, T. & SCHÖPFER, M. 2017. Interactions and growth of faults in an outcrop-scale system. *Geological Society, London, Special Publications,* 439**,** 23-39.

NICOL, A., WALSH, J., BERRYMAN, K. & NODDER, S. 2005. Growth of a normal fault by the accumulation of slip over millions of years. *Journal of Structural Geology,* 27**,** 327-342.

NICOL, A., WALSH, J., CHILDS, C. & MANZOCCHI, T. 2020a. Chapter 6 - The growth of faults. *In:* TANNER, D. & BRANDES, C. (eds.) *Understanding Faults.* Elsevier.

NICOL, A., WALSH, J., CHILDS, C. & MANZOCCHI, T. 2020b. The growth of faults. *Understanding faults.* Elsevier.

NICOL, A., WATTERSON, J., WALSH, J. J. & CHILDS, C. 1996. The shapes, major axis orientations and displacement patterns of fault surfaces. *Journal of Structural Geology,* 18**,** 235-248.

PAGANONI, M., KING, J. J., FOSCHI, M., MELLOR-JONES, K. & CARTWRIGHT, J. A. 2019. A natural gas hydrate system on the Exmouth Plateau (NW shelf of Australia) sourced by thermogenic hydrocarbon leakage. *Marine and Petroleum Geology,* 99**,** 370-392.

PAN, S., BELL, R. E., JACKSON, C. A. L. & NALIBOFF, J. 2021. Evolution of normal fault displacement and length as continental lithosphere stretches. *Basin Research*.

PEACOCK, D. & SANDERSON, D. 1994. Geometry and development of relay ramps in normal fault systems. *AAPG bulletin,* 78**,** 147-165.

PEACOCK, D. C. P. 2002. Propagation, interaction and linkage in normal fault systems. *Earth-Science Reviews,* 58**,** 121-142.

PEACOCK, D. C. P., NIXON, C. W., ROTEVATN, A., SANDERSON, D. J. & ZULUAGA, L. F. 2017. Interacting faults. *Journal of Structural Geology,* 97**,** 1-22.

PEACOCK, D. C. P. & SANDERSON, D. J. 1991. Displacements, segment linkage and relay ramps in normal fault zones. *Journal of Structural Geology,* 13**,** 721-733.

PEACOCK, D. C. P. & SANDERSON, D. J. 1996. Effects of propagation rate on displacement variations along faults. *Journal of Structural Geology,* 18**,** 311-320.

POLCARI, M., STRAMONDO, S., VANNOLI, P., CANNELLI, V., MELINI, D., SAMSONOV, S., MORO, M., BIGNAMI, C. & SAROLI, M. A possibile breached relay ramp causing the 2013 Lunigiana earthquake (Northern Italy). 2014 IEEE Geoscience and Remote Sensing Symposium, 13-18 July 2014 2014. 2397-2399.

POLIT, A. T., SCHULTZ, R. A. & SOLIVA, R. 2009. Geometry, displacement–length scaling, and extensional strain of normal faults on Mars with inferences on mechanical stratigraphy of the Martian crust. *Journal of Structural Geology,* 31**,** 662-673.

QUATTROCCHI, F., BOSCHI, E., SPENA, A., BUTTINELLI, M., CANTUCCI, B. & PROCESI, M. 2013. Synergic and conflicting issues in planning underground use to produce energy in densely populated countries, as Italy: Geological storage of CO2, natural gas, geothermics and nuclear waste disposal. *Applied Energy,* 101**,** 393-412.

RAVAGLIA, A., TURRINI, C. & SENO, S. 2004. Mechanical stratigraphy as a factor controlling the development of a sandbox transfer zone: a three-dimensional analysis. *Journal of Structural Geology,* 26**,** 2269-2283.

REDPATH, D., JACKSON, C. A. L. & BELL, R. E. 2022. Mechanical Stratigraphy Controls Normal Fault Growth and Dimensions, Outer Kwanza Basin, Offshore Angola. *Tectonics,* 41**,** e2021TC006823.

REEVE, M. T., BELL, R. E., DUFFY, O. B., JACKSON, C. A.-L. & SANSOM, E. 2015. The growth of non-colinear normal fault systems; What can we learn from 3D seismic reflection data? *Journal of Structural Geology,* 70**,** 141-155.

REEVE, M. T., JACKSON, C. A. L., BELL, R. E., MAGEE, C. & BASTOW, I. D. 2016. The stratigraphic record of prebreakup geodynamics: Evidence from the Barrow Delta, offshore Northwest Australia. *Tectonics,* 35**,** 1935-1968.

REILLY, C., NICOL, A., WALSH, J. J. & KROEGER, K. F. 2016. Temporal changes of fault seal and early charge of the Maui Gas-condensate field, Taranaki Basin, New Zealand. *Marine and Petroleum Geology,* 70**,** 237-250.

ROCHE, V., CAMANNI, G., CHILDS, C., MANZOCCHI, T., WALSH, J., CONNEALLY, J., SAQAB, M. M. & DELOGKOS, E. 2021. Variability in the three-dimensional geometry of segmented normal fault surfaces. *Earth-Science Reviews,* 216**,** 103523.

ROCHE, V., HOMBERG, C. & ROCHER, M. 2012. Fault displacement profiles in multilayer systems: from fault restriction to fault propagation. *Terra Nova,* 24**,** 499-504.

ROTEVATN, A., FOSSEN, H., HESTHAMMER, J., AAS, T. E. & HOWELL, J. A. 2007. Are relay ramps conduits for fluid flow? Structural analysis of a relay ramp in Arches National Park, Utah. *Geological Society, London, Special Publications,* 270**,** 55.

ROTEVATN, A., JACKSON, C. A. L., TVEDT, A. B. M., BELL, R. E. & BLÆKKAN, I. 2018. How do normal faults grow? *Journal of Structural Geology*.

ROTEVATN, A., JACKSON, C. A. L., TVEDT, A. B. M., BELL, R. E. & BLÆKKAN, I. 2019. How do normal faults grow? *Journal of Structural Geology,* 125**,** 174-184.

ROURE, F., BRUN, J.-P., COLLETTA, B. & VAN DEN DRIESSCHE, J. 1992. Geometry and kinematics of extensional structures in the Alpine foreland basin of southeastern France. *Journal of Structural Geology,* 14**,** 503-519.

ROWAN, M. G., HART, B. S., NELSON, S., FLEMINGS, P. B. & TRUDGILL, B. D. 1998. Three-dimensional geometry and evolution of a salt-related growth-fault array: Eugene Island 330 field, offshore Louisiana, Gulf of Mexico. *Marine and petroleum geology,* 15**,** 309-328.

SCARSELLI, N., FERRER, O., PATEN, T., GUMPRECHT, S., HAMMERSTEIN, J. & MCCLAY, K. R. 3D Seismic Analysis of Fault-Degradation Complexes, Exmouth Plateau, NW Shelf, Australia. International Conference and Exhibition, Melbourne, Australia 13-16 September 2015, 2015. Society of Exploration Geophysicists and American Association of Petroleum …, 190-190.

SCHLISCHE, R. W., YOUNG, S. S., ACKERMANN, R. V. & GUPTA, A. 1996. Geometry and scaling relations of a population of very small rift-related normal faults. *Geology,* 24**,** 683-686.

SCHÖPFER, M. P. J., CHILDS, C. & WALSH, J. J. 2006. Localisation of normal faults in multilayer sequences. *Journal of Structural Geology,* 28**,** 816-833.

SERIÉ, C., HUUSE, M., SCHØDT, N. H., BROOKS, J. M. & WILLIAMS, A. 2017. Subsurface fluid flow in the deep-water Kwanza Basin, offshore Angola. *Basin Research,* 29**,** 149-179.

SIMM, R. & BACON, M. 2014. *Seismic Amplitude: An Interpreter's Handbook,* Cambridge, Cambridge University Press.

SOLIVA, R. & BENEDICTO, A. 2003. Can normal fault segment linkage increase seismic hazard?
SOLIVA, R. & BENEDICTO, A. 2004. A linkage criterion for segmented normal faults. *Journal of Structural Geology,* 26**,** 2251-2267.
SOLIVA, R. & BENEDICTO, A. 2005. Geometry, scaling relations and spacing of vertically restricted normal faults. *Journal of Structural Geology,* 27**,** 317-325.
SOLIVA, R., BENEDICTO, A., SCHULTZ, R. A., MAERTEN, L. & MICARELLI, L. 2008. Displacement and interaction of normal fault segments branched at depth: Implications for fault growth and potential earthquake rupture size. *Journal of Structural Geology,* 30**,** 1288-1299.
SOLIVA, R., BENEDICTO, A., VERGÉLY, P. & RIVES, T. 2005a. Mechanical control of a lithological alternation on normal fault morphology, growth and reactivation. *Bulletin de la Société Géologique de France,* 176**,** 329-342.
SOLIVA, R., SCHULTZ, R. A. & BENEDICTO, A. 2005b. Three-dimensional displacement-length scaling and maximum dimension of normal faults in layered rocks. *Geophysical Research Letters,* 32.
SOLIVA, S., ANTONIO, B. & LAURENT, M. 2006. Spacing and linkage of confined normal faults: Importance of mechanical thickness. *Journal of Geophysical Research: Solid Earth,* 111.
SPATHOPOULOS, F. 1996. An insight on salt tectonics in the Angola Basin, South Atlantic. *Geological Society, London, Special Publications,* 100**,** 153.
STAGG, H. 2004. *Geological framework of the outer Exmouth Plateau and adjacent ocean basins*, Geoscience Australia.
SUNDAL, A., NYSTUEN, J. P., RØRVIK, K.-L., DYPVIK, H. & AAGAARD, P. 2016. The Lower Jurassic Johansen Formation, northern North Sea – Depositional model and reservoir characterization for CO2 storage. *Marine and Petroleum Geology,* 77**,** 1376-1401.
TAO, Z. & ALVES, T. M. 2019. Impacts of data sampling on the interpretation of normal fault propagation and segment linkage. *Tectonophysics,* 762**,** 79-96.
TAVARNELLI, E. & PASQUI, V. 2000. Fault growth by segment linkage in seismically active settings: Examples from the Southern Apennines, Italy, and the Coast Ranges, California. *Journal of Geodynamics,* 29**,** 501-516.
TAYLOR, S. K., NICOL, A. & WALSH, J. J. 2008. Displacement loss on growth faults due to sediment compaction. *Journal of Structural Geology,* 30**,** 394-405.
TORABI, A., ALAEI, B. & LIBAK, A. 2019. Normal fault 3D geometry and displacement revisited: Insights from faults in the Norwegian Barents Sea. *Marine and Petroleum Geology,* 99**,** 135-155.
TRUDGILL, B. D. & CARTWRIGHT, J. A. 1994. Relay-ramp forms and normal-fault linkages, Canyonlands National Park, Utah. *GSA Bulletin,* 106**,** 1143-1157.
TSODOULOS, I. M., KOUKOUVELAS, I. K. & PAVLIDES, S. 2008. Tectonic geomorphology of the easternmost extension of the Gulf of Corinth (Beotia, Central Greece). *Tectonophysics,* 453**,** 211-232.
TVEDT, A. B., ROTEVATN, A., JACKSON, C. A.-L., FOSSEN, H. & GAWTHORPE, R. L. 2013a. Growth of normal faults in multilayer sequences: a 3D seismic case study from the Egersund Basin, Norwegian North Sea. *Journal of Structural Geology,* 55**,** 1-20.
TVEDT, A. B. M., ROTEVATN, A. & JACKSON, C. A. L. 2016. Supra-salt normal fault growth during the rise and fall of a diapir: Perspectives from 3D seismic reflection data, Norwegian North Sea. *Journal of Structural Geology,* 91**,** 1-26.
TVEDT, A. B. M., ROTEVATN, A., JACKSON, C. A. L., FOSSEN, H. & GAWTHORPE, R. L. 2013b. Growth of normal faults in multilayer sequences: A 3D seismic case study

from the Egersund Basin, Norwegian North Sea. *Journal of Structural Geology,* 55**,** 1-20.
VERROIOS, S. & ZYGOURI, V. 2021. Geomorphological Analysis of Xilokastro Fault, Central Gulf of Corinth, Greece. *Geosciences,* 11**,** 516.
WALDRON, J. W. 2005. Extensional fault arrays in strike-slip and transtension. *Journal of structural Geology,* 27**,** 23-34.
WALSH, J., CHILDS, C., MEYER, V., MANZOCCHI, T., IMBER, J., NICOL, A., TUCKWELL, G., BAILEY, W., BONSON, C. & WATTERSON, J. 2001. Geometric controls on the evolution of normal fault systems. *Geological Society, London, Special Publications,* 186**,** 157-170.
WALSH, J. J., BAILEY, W. R., CHILDS, C., NICOL, A. & BONSON, C. G. 2003. Formation of segmented normal faults: a 3-D perspective. *Journal of Structural Geology,* 25**,** 1251-1262.
WALSH, J. J., NICOL, A. & CHILDS, C. 2002. An alternative model for the growth of faults. *Journal of Structural Geology,* 24**,** 1669-1675.
WALSH, J. J. & WATTERSON, J. 1987. Distributions of cumulative displacement and seismic slip on a single normal fault surface. *Journal of Structural Geology,* 9**,** 1039-1046.
WALSH, J. J. & WATTERSON, J. 1988. Analysis of the relationship between displacements and dimensions of faults. *Journal of Structural Geology,* 10**,** 239-247.
WALSH, J. J. & WATTERSON, J. 1991. Geometric and kinematic coherence and scale effects in normal fault systems. *Geological Society, London, Special Publications,* 56**,** 193-203.
WALSH, J. J., WATTERSON, J., BAILEY, W. R. & CHILDS, C. 1999. Fault relays, bends and branch-lines. *Journal of Structural Geology,* 21**,** 1019-1026.
WATTERSON, J. 1986. Fault dimensions, displacements and growth. *pure and applied geophysics,* 124**,** 365-373.
WEBER, K. 1987. Hydrocarbon distribution patterns in Nigerian growth fault structures controlled by structural style and stratigraphy. *Journal of Petroleum science and Engineering,* 1**,** 91-104.
WHIPP, P., JACKSON, C. L., GAWTHORPE, R., DREYER, T. & QUINN, D. 2014. Normal fault array evolution above a reactivated rift fabric; a subsurface example from the northern Horda Platform, Norwegian North Sea. *Basin Research,* 26**,** 523-549.
WHIPP, P. S., JACKSON, C. A. L., SCHLISCHE, R. W., WITHJACK, M. O. & GAWTHORPE, R. L. 2017. Spatial distribution and evolution of fault-segment boundary types in rift systems: observations from experimental clay models. *Geological Society, London, Special Publications,* 439**,** 79.
WHITTAKER, A. C. & WALKER, A. S. 2015. Geomorphic constraints on fault throw rates and linkage times: Examples from the Northern Gulf of Evia, Greece. *Journal of Geophysical Research: Earth Surface,* 120**,** 137-158.
WIEBKE, A., M., G. R., M., L. S., E., D. M., DIMITRIOS, S. & ERNST, W. 2010. Relay ramps as pathways for turbidity currents: a study combining analogue sandbox experiments and numerical flow simulations. *Sedimentology,* 57**,** 806-823.
WILKINS, S. J. & GROSS, M. R. 2002. Normal fault growth in layered rocks at Split Mountain, Utah: influence of mechanical stratigraphy on dip linkage, fault restriction and fault scaling. *Journal of Structural Geology,* 24**,** 1413-1429.
WILKINSON, M., ROBERTS, G. P., MCCAFFREY, K., COWIE, P. A., FAURE WALKER, J. P., PAPANIKOLAOU, I., PHILLIPS, R. J., MICHETTI, A. M., VITTORI, E., GREGORY, L., WEDMORE, L. & WATSON, Z. K. 2015. Slip distributions on active normal faults measured from LiDAR and field mapping of geomorphic offsets: an

example from L'Aquila, Italy, and implications for modelling seismic moment release. *Geomorphology,* 237**,** 130-141.

WILLEMSE, E. J., POLLARD, D. D. & AYDIN, A. 1996. Three-dimensional analyses of slip distributions on normal fault arrays with consequences for fault scaling. *Journal of Structural Geology,* 18**,** 295-309.

WORTHINGTON, R. P. & WALSH, J. J. 2017. Timing, growth and structure of a reactivated basin-bounding fault. *Geological Society, London, Special Publications,* 439**,** 511.

WU, N., JACKSON, C., JOHNSON, H. & HODGSON, D. 2019. *Lithological, petrophysical and seal properties of mass-transport complexes (MTCs), northern Gulf of Mexico*.

XU, S., SAMANIEGO, Á. F. N., ÁLVAREZ, S. A. A. & MARTÍNEZ, L. M. C. 2011. Structural analysis of a relay ramp in the Querétaro graben, central Mexico: Implications for relay ramp development. *Revista mexicana de ciencias geológicas,* 28**,** 275-289.

YIELDING, G. 1990. Footwall uplift associated with Late Jurassic normal faulting in the northern North Sea. *Journal of the Geological Society,* 147**,** 219-222.

YIELDING, G. & ROBERTS, A. 1992. Footwall uplift during normal faulting—implications for structural geometries in the North Sea. *Structural and tectonic modelling and its application to petroleum geology.* Elsevier.

YOUNG, M. J., GAWTHORPE, R. L. & HARDY, S. 2001. Growth and linkage of a segmented normal fault zone; the Late Jurassic Murchison–Statfjord North Fault, northern North Sea. *Journal of Structural Geology,* 23**,** 1933-1952.

ZIEGLER, P. 1992. North Sea rift system. *Tectonophysics,* 208**,** 55-75.

ZIESCH, J., ARUFFO, C. M., TANNER, D. C., BEILECKE, T., DANCE, T., HENK, A., WEBER, B., TENTHOREY, E., LIPPMANN, A. & KRAWCZYK, C. M. 2017. Geological structure and kinematics of normal faults in the Otway Basin, Australia, based on quantitative analysis of 3-D seismic reflection data. *Basin Research,* 29**,** 129-148.

“ The beginning of greater things to come ”

David Redpath BSc MSc